UNIVERSITY OF TWENTE.

ISBN: 978-90-365-4670-6
DOI: 10.3990/1.9789036546706

Running-in of metal-to-metal seals and its influence on sealing ability | Dennis Ernens

Running-In of Metal-to-Metal Seals and its Influence on Sealing Ability

With application to the design of biodegradable thread compounds

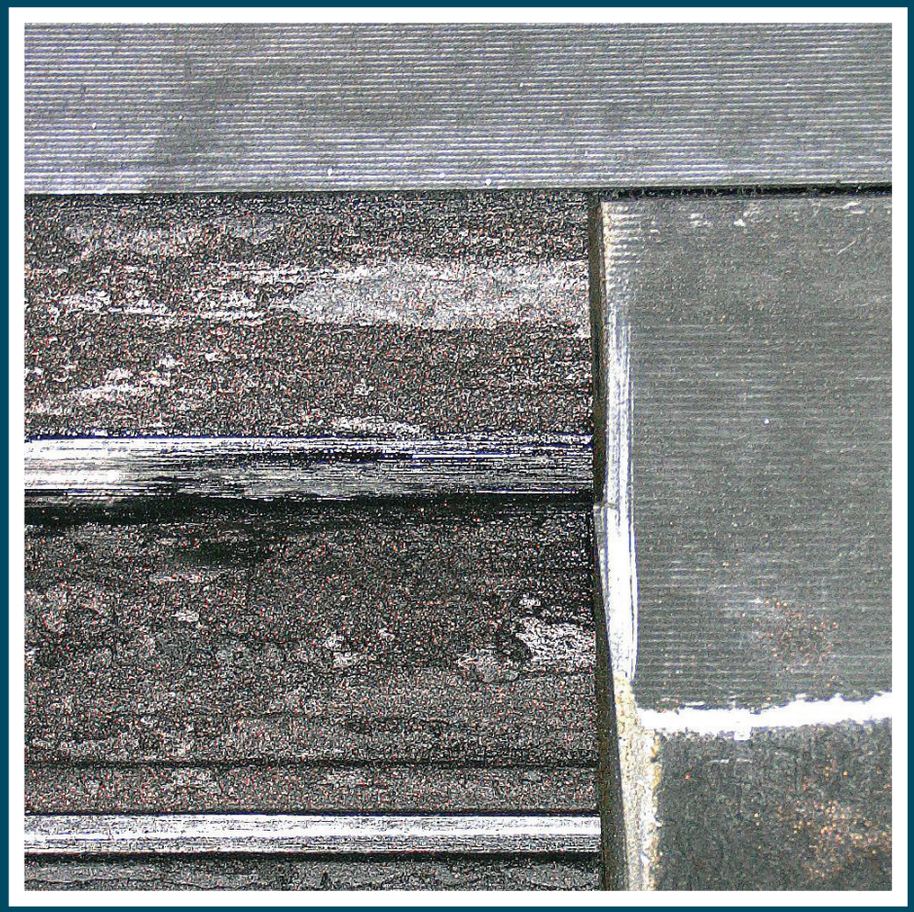

Dennis Ernens

RUNNING-IN OF METAL-TO-METAL SEALS AND ITS INFLUENCE ON SEALING ABILITY

WITH APPLICATION TO THE DESIGN OF BIODEGRADABLE THREAD COMPOUNDS

Dennis Ernens

RUNNING-IN OF METAL-TO-METAL SEALS AND ITS INFLUENCE ON SEALING ABILITY

WITH APPLICATION TO THE DESIGN OF BIODEGRADABLE THREAD COMPOUNDS

PROEFSCHRIFT

ter verkrijging van
de graad van doctor aan de Universiteit Twente,
op gezag van de rector magnificus,
prof. dr. T.T.M. Palstra,
volgens besluit van het College voor Promoties
in het openbaar te verdedigen
op donderdag 6 december 2018 om 14:45 uur

door

Dennis Ernens
geboren op 13 september 1982
te Velsen, Nederland

Dit proefschrift is goedgekeurd door:

de promotor:
dr. ir. M.B. de Rooij

de co-promotor:
prof. dr. ir. D.J. Schipper

PROMOTIE COMMISSIE:

Voorzitter/secretaris:
prof. dr. G.P.M.R. Dewulf

Promotor:

dr. ir. M.B. de Rooij	Universiteit Twente

Co-promotor:

prof.dr.ir. D.J. Schipper	Universiteit Twente

Leden (in alfabetische volgorde):

prof. dr. ir. J-P. Celis	K.U. Leuven
prof. dr. ir. J.E. ten Elshof	Universiteit Twente
prof. dr. S. Franklin	University of Sheffield
prof. dr. ir. T. Tinga	Universiteit Twente

Referent:

dr. H.R. Pasaribu	Shell Global Solutions International B.V.

The research in this dissertation was carried out at and supported by Shell Global Solutions BV in Rijswijk, The Netherlands, and the Laboratory for Surface Technology and Tribology at the University of Twente. The work was also supported by TMC Physics BV in Utrecht, The Netherlands. The support is gratefully acknowledged.

RUNNING-IN OF METAL-TO-METAL SEALS AND ITS INFLUENCE ON SEALING ABILITY
Dissertation, University of Twente, Enschede, The Netherlands, December 2018

ISBN: 978-90-365-4670-6
DOI: 10.3990/1.9789036546706

Summary

Running-in of metal-to-metal seals and its influence on sealing ability

Metal-to-metal sealing of casing connections is affected by running-in because it determines the topography of the gap between the contacting surfaces by wear and plastic deformation during assembly under the influence of the thread compound, coatings and the initial surface topography. The work in this thesis concerns the mechanisms related to these elements of the tribosystem and how they affect running-in of the metal-to-metal seal tribosystem and ultimately influence the sealing ability.

The research was driven by a need to reduce costs in particular of the qualification of premium connections. Furthermore, increased understanding of the barriers in the well is important for well engineering. Understanding was needed on galling during assembly which is an often occurring failure mechanism as well as the protective mechanisms behind the applied coatings. In addition, the Oslo-Paris Convention for the protection of the Marine Environment of the North-East Atlantic (OSPAR) demands future substitution of mineral oils and the (heavy) metal additives used in the American Petroleum Insitute (API) modified thread compound by biodegradable alternatives. To this end a combined experimental and modelling approach was applied.

The existing thread compounds were shown, with pin-on-disc, anvil-on-strip and Shell Sealing Mock-Up Rig (SSMUR) tests, to provide relatively minor protection to initiation of galling in uncoated contacts. This was shown to be because of squeeze out of the formed tribofilms, limited adsorption of the additives and the lack of replenishment by the plan parallel contact configuration coming from the turned surface topography. These mechanisms only added 60 mm of additional sliding length, before failure, with API modified thread compound compared to a plain mineral oil.

In relation to the substitution of API modified for biodegradable alternatives, the elevated temperature degradation mechanisms of (environmentally acceptable) thread compounds were studied using Thermogravimetric Analysis (TGA), Differential Scanning Calorimetry (DSC), high temperature rheometry and pin-on-disc. Thread compounds were shown to fail because of evaporation and oxidation leading to starved lubrication conditions. The system subsequently enters a severe adhesive wear regime sometimes exacerbated by abrasive action of the hard metal oxide particles present in environmentally acceptable compounds. The found failure mechanisms and the developed test protocol were validated and successfully mitigated by the development of a prototype thread compound.

The presence of phosphate conversion coatings proved to be a dominating factor in the running-in of the metal-to-metal seal. This was shown to be caused by two main mechanisms using

various tribological experiments and analytical techniques. On the uncoated counter surface a durable tribofilm was formed by physical adsorption of phosphate debris particles through a shear stress activation mechanism. From the same debris particles a smooth glaze layer was generated on the phosphated surface which possesses a substantial hardness after dry sliding. However, this hardness was much lower after lubricated sliding and was shown to be related to the particle size which generated the glaze layer. The combination of these mechanisms resulted in a wear process that could satisfactorily be described by the energy dissipated in the sliding contact.

Finally, it was shown with experimental data and a simple running-in model that the combination of plastic deformation of the waviness of the turned surface topography and wear of the phosphate coating determine the running-in behaviour. It was found that the surface runs-in within 40 mm sliding length after which the wear regime transitioned to mild wear. The combination of severe initial wear by plastic deformation of the waviness and the generation of a smooth glaze layer created a conformal sealing configuration with multiple concentrated line contacts along the circumference. This created the most robust sealing configuration compared to configurations that did not have a distinct lay.

Samenvatting

Inloop gedrag van metaal-op-metaal afdichtingen en de invloed op lekdichtheid

Metaal-op-metaal afdichting van geschroefde pijp verbindingen wordt beïnvloed door inlopen, omdat het de topografie bepaald van de spleet tussen de oppervlakken in contact, dit is het gevolg van slijtage en plastische deformatie tijdens de assemblage, onder invloed van het gebruikte smeermiddel, coatings en de initiële oppervlakte topografie. Het werk in deze thesis onderzoekt de mechanismen gerelateerd aan deze elementen van het tribosysteem en hoe deze het inloop gedrag en uiteindelijk het afdichten van de metaal-op-metaal afdichting beïnvloeden.

Het onderzoek werd gedreven door een noodzaak voor het reduceren van de kosten van het kwalificeren van premium kwaliteit geschroefde pijp verbindingen. Verder, is een verbeterd begrip van de barrières in een oliebron van belang voor het ontwerp en de constructie van toekomstige oliebronnen. Begrip was nodig van vreten (koudlassen), een veelvoorkomend faal mechanisme tijdens assemblage van de connectie, en de beschermende mechanismen van de aanwezige coatings. Daarnaast vraagt het verdrag inzake de bescherming van het mariene milieu in het noordoostelijk deel van de Atlantische Oceaan, toekomstige vervanging van minerale oliën en de (zware) metalen in het huidige American Petroleum Institute (API) modified smeermiddel door biologisch afbreekbare alternatieven. Om het bovenstaande te bereiken werd een experimentele en numerieke modelleer aanpak gecombineerd.

De bestaande smeermiddelen gaven relatief weinig bescherming tegen de initiatie van koudlassen in niet gecoate contacten, dit werd aangetoond met pin-op-disk en aanbeeld-op-strip experimenten. De oorzaak was het verwijderen van de gevormde tribofilm, gelimiteerde adsorptie van de additieven en een gebrek aan verversing van het smeermiddel door het plan parallelle contact als gevolg van de gedraaide oppervlakte topografie. Door deze mechanismes voegde API modified slechts 60 mm extra glijlengte, voor falen, toe vergeleken met een schone minerale olie.

In relatie tot de vervanging van API modified voor biologische afbreekbare alternatieven, werden de hoge temperatuur degradatie mechanismen van (milieu acceptabele) smeer middelen onderzocht gebruikmakend van thermogravimetrische analyse, dynamische differentiecalorimetrie, hoge temperatuur rheometrie en pin-op-disk. Smeermiddelen faalden door verdamping en oxidatie wat leidde tot schrale smeercondities. Vervolgens kwam het systeem in het zware adhesieve slijtage regime terecht, soms verergerd door abrasieve slijtage door de aanwezigheid van harde metaaloxide deeltjes in de milieu acceptabele smeermiddelen. De gevonden faal mechanismen en het ontwikkelde test protocol werden gevalideerd en succesvol gemitigeerd met de ontwikkeling van een prototype smeermiddel.

De aanwezigheid van fosfaat conversie coatings bleek een dominerende factor te zijn in het inloop gedrag van de metaal-op-metaal afdichting. Dit werd veroorzaakt door twee mechanismen en aangetoond met een combinatie van tribologische experimenten en analytische technieken. Op het niet gecoate tegenoppervlak vormde zich een duurzame tribofilm door fysische adsorptie van fosfaat deeltjes middels een schuifspanning gedreven activatie mechanisme. Van dezelfde fosfaat deeltjes vormde zich op het gefosfaateerde oppervlak een gladde glazuurlaag welke een substantiële hardheid heeft na droge glij condities. Deze hardheid was echter een stuk lager wanneer de glazuurlaag werd gevormd in gesmeerde condities en werd gerelateerd aan de deeltjes grootte waaruit de glazuurlaag bestaat. De combinatie van deze mechanismen resulteerde in een slijtage proces dat goed beschreven kan worden met de totale gedissipeerde energie in het glijdende contact.

Tot slot, werd met experimentele data en een simpel inloop model aangetoond dat de combinatie van plastische deformatie van de golving van de gedraaide oppervlakte topografie en slijtage van de fosfaat coating het inloop gedrag bepaald. Het oppervlak is ingelopen binnen 40 mm glijlengte en het slijtage regime veranderde vervolgens naar milde slijtage. De combinatie van zware initiële slijtage door plastische deformatie van de golving, en de vorming van een gladde glazuurlaag, creëert een conforme afdichtingsconfiguratie met meerdere geconcentreerde lijncontacten over de omtrek. Dit leidde tot de meest robuuste afdichtingsconfiguratie vergeleken met configuraties die geen specifieke oriëntatie hebben.

Acknowledgements

Writing these acknowledgements marks the end of an intensive period combining my work with my PhD studies in the exiting field of tribology. I was an Aerospace Engineer who worked on numerical mathematics applied to fluid mechanics during his master studies. After that, I started at TMC Physics on an assignment for Shell, where I worked on lubricants for pipe expansion, and brazing of casing connections. Then, this opportunity arose to study an (to me) entirely new field of research, called tribology. A field that has a richness and diversity of topics because it is at the intersection of many sciences. I turned out to like that, it suits my broad interests and it awakened a passion for experimental research.

This would not have been the case if Rihard Pasaribu, my new team lead at Shell at the time, had not asked the following question during our "get to know you" meeting: "Do you want to do a PhD?". When I, after some deliberation, answered "Yes!", he was also the driving force to make it happen. We ended up with a most unusual arrangement – the details will be left out for brevity – between Shell, TMC and the University of Twente. Which would not have happened if Gerben Kuipers, Paul Bekkers and Joeri Voets of TMC Physics BV had not given me their trust and support. At Shell, it were Jan Brakel and Henk Vasmel who gave their blessing. Finally, it was Dik Schipper, later joined by Matthijn de Rooij and Rob Bosman of the University of Twente who sealed the deal by taking me in. I owe these persons already a big thank you for setting all of this into motion. The dust settled, contracts were signed, the project started, and it was time to do some work. Delivering the project and obtaining a PhD in Surface Technology and Tribology would not have been possible without the following persons.

I want to express my gratitude to my daily supervisor and (now) promotor Matthijn de Rooij for his valuable guidance, support and motivation throughout the project. I really enjoyed our weekly discussions and random conversations. Also, thanks for your patience deciphering my theories and getting it straight in my mind.

Rihard Pasaribu, thanks for being an excellent company supervisor. I really enjoyed your enthusiasm, creative thinking and how you always made things possible. Thanks also for our many in depth discussions on the project and for being a mentor and coach.

Rob Bosman thanks for all those discussions about things related and unrelated to the project, I learned every time. Even though I do not always agree, you have given me another way of looking at things. Thanks also for giving me a good start with your contact code and making time available to teach me the operation of the AFM.

My, now, co-promotor Dik Schipper was a bit more on the background, however, always available whenever needed. Dik thanks for our conversations and for your to the point and no-nonsense advice.

The majority of the time was spent at Shell in Rijswijk. I would like to thank the project team members Egbert, Willem-Maarten, Mark, Maurice, Jan, Gerben and Yves for the great team work over the years and everything I have learned from you. In the last 2 years, the project and the team went through a lot of change and turmoil. Serge and Roel were instrumental during that time in getting it done and delivered. Thanks for the support, keeping the project going and allowing me the time to finish this thesis. Erik, your continuous interest in the project and my well being was also greatly appreciated. The "analytical guys", Frans, Huub and Marco, thanks for the support with and discussions on SEM, XRD and XPS.

I would like to thank Francesc Pérez-Ràfols of Luleå University of Technology for a great collaboration, his contributions, the many good discussions and his help on the modelling part of this thesis.

Frank Hollmann and Ralf Schneider of Chemetal GmbH are acknowledged for sharing their knowledge on phosphate conversion coatings, the fruitful discussions that sparked new ideas and their general interest in my work.

In Twente I have had the opportunity to meet a lot of interesting people on the occasions I was there. I would like to mention a few persons specifically. Erik de Vries, thanks for you advice and our interesting discussions on how to perform experiments properly. Walter thanks for helping me set-up those first scratch experiments. Aydar thank you for the discussions on the BEM and exchange of ideas. Mohammad, Tanmaya and Xavier thanks for the discussions, coffee chats and the great conference memories. Erik, Walter, Nadia, Matthijs, Michel, Belinda and many others, thanks for the great coffee breaks and making my days in university even more pleasant.

At TMC I would like to thank Elizabeth Vela and Robert van Tankeren for continuing the support after the original persons that made this possible left the company. I would also like to thank everyone who expressed an interest in the work and who came to my "pizza sessions" on tribology.

I extend my appreciation to my committee members: prof. dr. ir. Celis, prof. dr. ir. Ten Elshof, prof. dr. Franklin and prof. dr. ir. Tinga, for their time and effort.

Thanks to the bachelor, master and PDEng. students that I supervised and who supported me during the PhD work: Dennis, Maurice, Lawrence, Dimitri, Ruben, Tom, Gideon, Paul, Ezgi, Järvi and Elio. I hope you learned as much from me as I did from you.

I would like to thank my family and friends for their continued support and interest during the course of the work. I recognize that after work, PhD and private life not much time was left for you. I hope to make that up in the future.

Last but certainly not least, I want to thank you, my dear Sandra. Thank you for your continuous support, ensuring I see some sunlight, showing me there is more than research and in general our great life together. Thank you for your patience and your sacrifices that allowed me to pursue a PhD, it has not gone unnoticed.

Dennis Ernens, Delft, November 2018

Nomenclature

The symbols used in this thesis are classified in a Greek and Roman category. Some symbols appear more than once, their specific meaning follows from their context or from subscripts.

Abbreviations

AFM	Atomic Force Microscopy
API	American Petroleum Insitute
AsM	as machined
BSE	Backscatter electron
CAL	Connection Assessment Level
CCW	counter clockwise
CEFAS	Centre for Environment Fisheries and Aquaculture Science
COF	Coefficient of Friction
CW	clockwise
DSC	Differential Scanning Calorimetry
DTA	Differential Thermal Analysis
EDX	Energy-dispersive X-ray spectroscopy
FEA	Finite Element Analysis
FIB	Focused Ion Beam
HOCNF	Harmonised Offshore Chemicals Notification Format
ISO	International Organization for Standardization
MP	Manganese Phosphate, hureaulite
NEA	Norwegian Environment Agency
OSPAR	Oslo-Paris Convention for the protection of the Marine Environment of the North-East Atlantic
PAT	Ploughing Asperity Tester
RMS	Root Mean Square
RPM	Rotations Per Minute
SE	Secondary electron
SEM	Scanning Electron Microscopy
SodM	Staatstoezicht op de Mijnen
SSMUR	Shell Sealing Mock-Up Rig
TGA	Thermogravimetric Analysis
TPI	threads per inch
UTS	Ultimate Tensile Strength
VME	Von Mises Equivalent

XPS	X-ray Photoelectron Spectroscopy
XRD	X-ray diffraction
ZDDP	zinc dialkyldithiophosphate
ZP	Zinc Phosphate, hopeite

Greek Symbols

(α, β, γ)	Rotations around (x,y,z) respectively	rad
Δ	Incremental change	-
Γ	Fourier number	-
Ω	Domain	-
Φ	Temperature rise	K
κ	Thermal diffusivity	$m^2\,s^{-1}$
μ	Coefficient of friction, COF	-
ν	Poisson ratio	-
ϕ	Heat flux	$W\,m^{-2}$
σ	Stress	$N\,m^{-2}$, Pa
τ	Shear stress	$N\,m^{-2}$, Pa
v	Velocity	$m\,s^{-1}$

Roman Symbols

A	Area	m^2
E	Young's modulus	$N\,m^{-2}$, Pa
E^*	Composite elastic modulus	$N\,m^{-2}$, Pa
F	Force	N
H	Hardness	$N\,m^{-2}$, Pa
I	Index set	-
L	Length	m
M	Pixels in x-direction	-
N	Pixels in y-direction	-
P	Pressure	bar
$\mathbf{R}$	Rotation matrix	rad
$\vec{T}$	Translation matrix	m
d	Pixel pitch	m
g_{00}	Rigid body separation	m
h	Gap between two surfaces	m
k	Wear rate	$mm^3\,N^{-1}\,m^{-1}$
l	Sliding length	m
n	Sub pixel steps in y-direction	-
p	Contact stress	$N\,m^{-2}$, Pa
q	Contact intensity	$N\,m^{-1}$
r	Full cycle counter in the averaging approach	-

t	Time	s
u	Deformation	m
HV	Vickers hardness	$\mathrm{kg\,mm^{-2}}$
PI	Plasticity index	-
wt%	Weight percent	%
x, y, z	Cartesian coordinates	m

Sub- and superscripts

N	Normal to surface
c	Contact
e	Elastic, external
i	Index, internal
p	Plastic
x, y, z	In the direction of x, y, z
A	Archard
aft	After
bef	Before
D	Dissipated energy

This page has been intentionally left blank.

Contents

Appended papers

A Ernens, D., Rooij, M. B. de, Pasaribu, H. R., Riet, E. J. van, Haaften, W. M. van and Schipper, D. J. 'Mechanical characterization and single asperity scratch behaviour of dry zinc and manganese phosphate coatings'. *Tribology International* 118 (February 2018), pp. 474–483

B Ernens, D., Riet, E. J. van, Rooij, M. B. de, Pasaribu, H. R., Haaften, W. M. van and Schipper, D. J. 'The Role of Phosphate-Conversion Coatings in the Makeup and Sealing Ability of Casing Connections'. *SPE Drilling & Completion* (October 2018)

C Ernens, D., Langedijk, G., Smit, P., Rooij, M. B. de, Pasaribu, H. R. and Schipper, D. J. 'Characterization of the Adsorption Mechanism of Manganese Phosphate Conversion Coating Derived Tribofilms'. *Tribology Letters* 66.4 (December 2018), p. 131

D Ernens, D., Rooij, M. B. de, Pasaribu, H. R. and Schipper, D. J. 'On the glaze layer formation in zinc and manganese phosphate coatings'. *To be submitted to Tribology International* (2018)

E Ernens, D., Rooij, M. B. de, Pasaribu, H. R. and Schipper, D. J. 'The mechanisms leading to galling initiation during make-up of casing connections'. *In preparation* (2018)

F Ernens, D., Westerwaal, D., Riet, E. J. van, Roijmans, R., Daegling, S., Wheatley, A., Worthington, E., Kramer, H., Haaften, W. M. van, Rooij, M. B. de and Pasaribu, H. R. 'Evaluation of the Elevated Temperature Performance and Degradation Mechanisms of Thread Compounds'. *To be submitted to SPE Drilling & Completion* (2018)

Other publications

- Di Crescenzo, D., Shuster, M., Petlyuk, A., Ernens, D., Zijsling, D. H. and Pasaribu, H. R. 'Lubricants and Accelerated Test Methods for Expandable Tubular Application'. *SPE/IADC Drilling Conference and Exhibition*. London: Society of Petroleum Engineers, March 2015
- Ernens, D., Hariharan, H., Haaften, W. M. van, Pasaribu, H. R., Jabs, M. and McKim, R. 'Improving Casing Integrity by Induction Brazing of Casing Connections'. *SPE Drilling & Completion* (2018)
- Hariharan, H., Ernens, D., Haaften, W. M. van, Jabs, M., Pasaribu, H. R. and Mckim, R. 'The Use of Induction Brazing in Casing Connections to Improve Well Integrity'. *AADE National Technical Conference and Exhibition*. 2017
- Kopeć, M., Spanjers, J., Scavo, E., Ernens, D., Duvigneau, J. and Vancso, G. J. 'Surface-initiated ATRP from polydopamine-modified TiO 2 nanoparticles'. *European Polymer Journal* (July 2018)

Conference contributions

- Ernens, D., Rooij, M. B. de, Schipper, D. J., Pasaribu, H. R., Riet, E. J. van and Haaften, W. M. van. 'Mechanical Characterization and Single Asperity Scratch Behaviour of Dry Zinc and Manganese Phosphate Coatings'. *17th Nordic Symposium on Tribology*. Hämeenlinna, 2016
- Ernens, D., Riet, E. J. van, Rooij, M. B. de, Pasaribu, H. R., Haaften, W. M. van and Schipper, D. J. 'The Role of Phosphate Conversion Coatings in Make-Up of Casing Connections'. *SPE/IADC Drilling Conference and Exhibition*. Den Haag: Society of Petroleum Engineers, March 2017
- Ernens, D., Langedijk, G., Rooij, M. B. de, Pasaribu, H. R. and Schipper, D. J. 'The mechanism of lifetime enhancement by phosphate conversion coatings'. *6th European Conference on Tribology*. Ljubljana, 2017
- Ernens, D., Rooij, M. B. de, Pasaribu, H. R. and Schipper, D. J. 'On the glaze layer formation in zinc and manganese phosphate coatings'. *44th Leeds-Lyon symposium on tribology*. Lyon, 2017

Part I.

The Thesis

1. Introduction

This chapter starts with the motivation for conducting a study into the running-in of metal-to-metal seals in casing connections. Then it goes into a general introduction to well construction and the role of casing connections and their metal-to-metal seals is discussed. Subsequently a detailed dissemination of the metal-to-metal seal tribosystem is given. The need for understanding running-in is discussed and the general research objectives are stated. Finally the thesis outline is given.

1.1. Running-in of metal-to-metal seals

This thesis is concerned with the running-in of metal-to-metal seals of premium casing connections used in the oil and gas industry. Casing connections are equipped with a screw thread to connect 12 m pipes (casing) that fortify the bore hole after drilling. The screw thread and metal-to-metal seal ensure structural integrity and leak tightness respectively. They undergo friction and wear in two phases of their lifetime: the rotary assembly phase where two lengths of casing are connected using the threaded connector and the micro sliding phase perpendicular to the rotary sliding direction under influence of well loading. The rotary assembly is critical as it establishes the initial conditions for micro sliding and sealing ability.

The topic is of interest as qualification of a casing connection and its metal-to-metal seal is a mandatory but costly undertaking. Furthermore, increased understanding of the barriers in an oil and gas well is important for well engineering. Indeed, not much was known about the origin of galling during assembly, the protective mechanisms of the applied coatings and the influence of friction and wear on metal-to-metal sealing. Finally, with a suitable model, possible improvements of the metal-to-metal seal can be generated and investigated.

In order to reduce the costs associated with qualification of connections and improve understanding of the running-in phase and its influence on sealing ability a combined experimental and modelling approach was proposed. The results are presented in this thesis. After this broad description of the problem at hand, a more detailed introduction will follow hereafter.

1.2. Constructing an oil and gas well

Oil and gas wells are constructed by drilling a hole in the ground, Figure 1.1. This is done with a drilling assembly. Well control is maintained by the hydrostatic column of a drilling fluid avoiding inflow of formation fluids. The resulting cuttings are transported out of the well by circulating the drilling fluid through the drill bit. Once a certain depth is reached, a certain

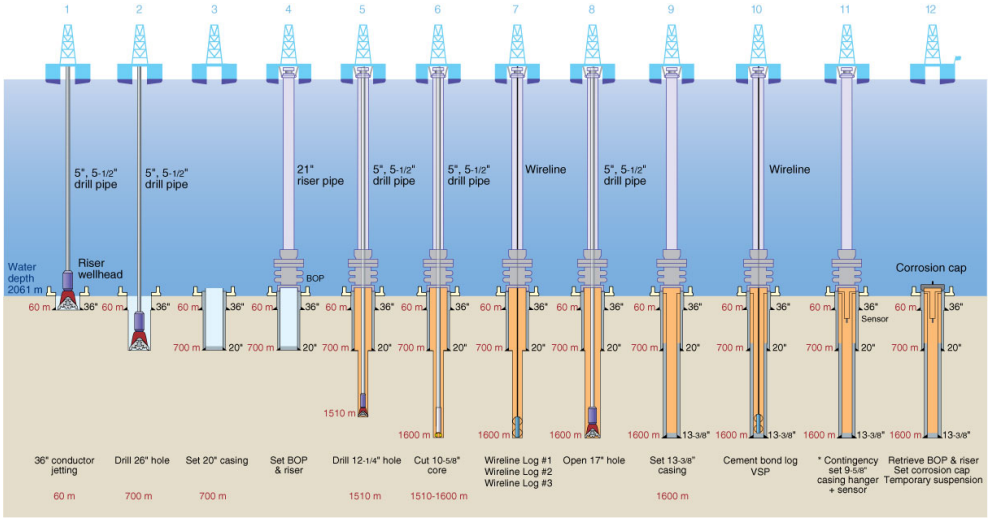

Figure 1.1.: Schematic sequence showing the construction of a well. Source [1].

subsurface lithology[1] is passed or a feature like an aquifer is crossed the drilling process is stopped and the drill is pulled up from the borehole to surface. The borehole is subsequently fortified by lowering and cementing in place steel tubular. The steel tubular is called casing when connected all the way to surface and liner if this is not the case.

The casing forms a pressure vessel withstanding the formation pressures on the outside and the drilling fluid or reservoir pressures on the inside giving a net differential pressure which puts the system under burst or collapse loading. In addition, it also needs to take up axial loading from its own weight and the thermal expansion generated compressive forces during production. Typical casing has a wall thickness starting at 8 mm up to 30 mm depending on the differential pressure and load requirements of the well. Combined with the material properties of the typically quenched and tempered steel grades, with an ultimate tensile strength (UTS) ranging from 500 to 1200 MPa, casing is designed to withstand pressures and loads in the order of > 1000 bar and > 20 MN at temperatures in excess of 180 degrees Celsius.

The casing string is build up out of sections of 12 meter length which are connected by a male (pin) and female (box) member equipped with a threaded connection and, if it entails a premium connection, a metal-to-metal seal, see Figure 1.2. Both elements have their own function and need to fulfil these over the lifetime (>20 years) of the well. The thread provides the means to convey the axial loading from one casing to the other. Under the same conditions, the metal-to-metal seal provides gas tight seal ability.

Premium casing connections are the subject of study in this thesis, particularly their metal-to-metal seal and how running in affects their seal ability performance. In the next sections the metal-to-metal seal tribosystem will be explained in detail.

[1] the general physical characteristics of a rock or the rocks in a particular area.

(a) Pin (b) Box

Figure 1.2.: Casing strings are connected by screwing together a male and female part also known as a pin shown in Figure 1.2a and a box shown in Figure 1.2b. Indicated is the location of the metal-to-metal seal.

1.3. Premium casing connections: two tribological systems rolled into one

A premium casing connection is different from regular casing connections because it has a metal-to-metal seal incorporated in the design. Therefore, a premium casing connection has two main components. As said, it has a screw thread for assembly and axial load transfer and a metal-to-metal seal for leak tightness and pressure integrity. Each are their own tribological system. The focus in this thesis is on the metal-to-metal seal which will be described in the next sections and from now on referred to as the tribosystem [2, 3].

1.3.1. Metal-to-metal seal

The metal-to-metal seal, like the casing connection, comprises two contacting members shown schematically in Figure 1.5a and Figure 1.5b. The pin (Figure 1.2a and Figure 1.5b) metal-to-metal seal has typically a rounded or cylindrical geometry and the box (Figure 1.2b and Figure 1.5a) a conical geometry. When the contact is made this gives, in its simplest form, a Hertzian line contact around the circumference. The metal-to-metal seal in typical casing connection designs, as shown in Figure 1.2, is located at the pin tip and the box base. The metal-to-metal seal is brought into contact by assembling the pin and box using the screw thread.

1.3.2. Metal-to-metal sealing

Metal-to-metal sealing is achieved by applying a sufficiently high contact stress to two surfaces in contact. The contact stress should reduce the gap between the two members far enough such that no gas molecule can pass and / or that no connecting path from the high pressure to low pressure side exists. This concept is shown schematically in Figure 1.3 for the fictitious connection of Figure 1.5. As discussed, for a flat against a round-off a Hertzian line contact stress distribution, $p(x, y)$, around the circumference is expected as shown in Figure 1.3b. This

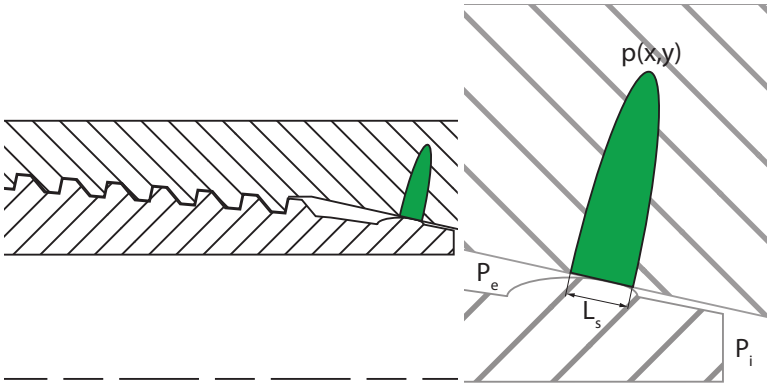

(a) (b)

Figure 1.3.: The pin and box of Figure 1.5 shown after assembly in Figure 1.3a. Indicated the Hertzian line contact stress profile in the metal-to-metal seal. The magnification in Figure 1.3b provides details on the nomenclature.

needs to create a seal such that the medium under internal, P_i, or external, P_e, pressure cannot escape. The seal contact intensity (N m^{-1}) can now be defined as

$$q(y) = \int_0^{L_s} p(x,y)dx \tag{1.1}$$

where L_s is the seal contact width.

In an ideal world a knives edge contacting a perfect flat would be sufficient to achieve this. However, in the normal world the metal-to-metal seal undergoes sliding (Section 1.3.3) affecting the seal ability. The sliding phase runs-in the sealing surface because of plasticity and wear and is influenced by a thread compound (Section 1.3.4), coatings (Section 1.3.5) and surface topography (Section 1.3.6). In addition, in the well the system needs to operate in high temperatures and is thus affected by thermal degradation (Section 1.3.4). Hence having an understanding of the complex interactions of these parameters and the influence on sealing ability would be beneficial and is the topic of this thesis.

1.3.3. Assembly, micro sliding and lubrication regimes

After application of the thread compound (Section 1.3.4), the connection threads are engaged by "hand" and subsequently a torque tool called a power tong, shown in Figure 1.4, takes over to torque up the connection to a pre-described assembly or make-up torque. This tool grabs and holds the casing on the box side and grabs and rotates the casing on the pin side. The assembly phase is fully dictated by the applied rotational velocity, the screw thread pitch, P, and the pin and box taper and diameter yielding a net interference. Figure 1.5 shows this schematically and defines the relevant nomenclature. If required, the connection can also be disassembled or broken out by the reverse procedure.

Figure 1.4.: A power tong for assembly of casing connections. The lower part is stationary and grabs the box and the top part grabs the pin and is driven by hydraulics. Picture: Universe Machine Corporation.

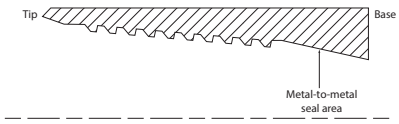

(a) Box

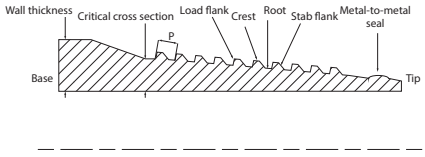

(b) Pin

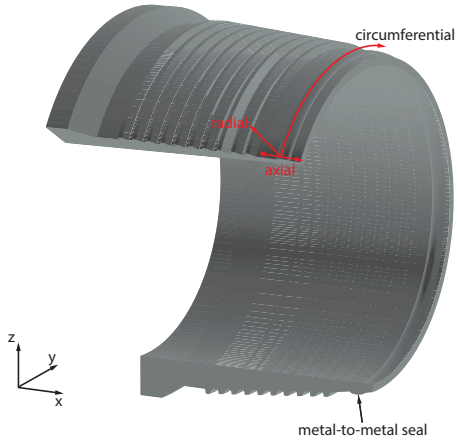

(c)

Figure 1.5.: Figure 1.5a shows a box cross section and Figure 1.5b shows a pin cross section. A reference frame that can be attached to the pin (and box) metal-to-metal seal surface is shown on a 3D representation of a pin in Figure 1.5c.

Typical rotational velocities are 2 - 5 rotations per minute (RPM) and thread pitches are in the order of 5 mm rev^{-1}. This results in circumferential and axial velocities in the order of 10 mm s^{-1} and 0.1 mm s^{-1} respectively. As such the pin progresses into the box with a velocity vector mainly pointed in the circumferential direction. It means further that the pin is always contacting on the same surface area while the box surface sees the pin sliding past in axial direction. The seal engages at the final moments of assembly giving a short sliding length of about 0.2-0.6 m in circumferential direction. In this short length a peak contact stress in the order of 1 GPa is build up by the increasing interference of the pin and box seal area. Given these velocities and contact stresses it is clear that the metal-to-metal seal operates in the boundary/mixed lubrication regime depending on the chosen surface finish and thread compound.

After assembly the casing is lowered into the well bore to start its job of fortifying the drilled

hole. During this lifetime the casing will see several stress states. For instance, when the well is started it will heat up and the casing moves from tensile to compressive loading because of thermal expansion, this will lead to small movements in the metal-to-metal seal in axial direction which will be defined as micro sliding. The micro sliding is typically in the order of 0.5 mm and operates at extremely low velocities i.e. $\ll 0.1\,\mathrm{mm\,s^{-1}}$ and thus fully in the boundary lubrication regime. As typical contact widths are approximately 1.0 mm this can also be characterised as fretting.

Cold welding and subsequent material transfer also known as galling is an often occurring failure mechanism of the connections in the assembly phase. It is of great interest because, as said in Section 1.3.2, the initial seal ability of the metal-to-metal seal is determined here. It was known from previous studies that even at mild loads galling initiation happened on uncoated surfaces lubricated with a thread compound. The mechanisms, however, were poorly understood and are important as design input for the development of environmentally friendly thread compounds as discussed in Section 1.3.4. This thesis provides the galling initiation mechanisms which were mitigated by the prototype thread compound developed in this thesis.

1.3.4. Grease or thread compound

The assembly of (casing) connections is performed with grease, also called thread compound. The base greases are typically made with a mineral base oil and metal soaps or metal complex soaps. Additives are subsequently added in the form of metallic, mineral or metallic oxide based particles. Thread compounds are thus relatively simple grease formulations. What is special about them is the high solids content of up to 50-60 wt% [4].

The function of the grease and the added particles was said to be threefold: it provides repeatable friction for a predictable assembly torque response, it forms a film during assembly to protect the mating surfaces and aids in the seal ability of the system by blocking or bridging potential leak channels.

As discussed in the previous sections, the casing string and connections are subjected to substantial loads under high temperature conditions. The seal ability of the system needs to be guaranteed under the micro sliding conditions described earlier. Meaning that lubricity needs to be guaranteed to avoid cumulative damage leading to seal failure. Therefore, the long term thermal stability of the grease and related tribofilms is of great importance for the metal-to-metal seal tribosystem. This is the reason why the de facto standard thread compound, API modified [4], still uses metallic lead in its formulation.

Initiatives are under way to ban the use of heavy metals in thread compounds and to push the industry to formulate fully biodegradable alternatives. These initiatives are led by the Norwegian and British regulatory bodies, the Norwegian Environment Agency (NEA) and the Centre for Environment Fisheries and Aquaculture Science (CEFAS) respectively. They execute the outcomes of the OSPAR by implementing the Harmonised Offshore Chemicals Notification Format (HOCNF) [5]. HOCNF is a scheme to harmonise the regulation of chemicals used in the offshore industry in the North Sea and the North-East Atlantic. The aim is to minimize the risk of serious spills and damage to the local marine environment. The

regulators both define a environmental friendliness scale to categorise the chemicals for use offshore. The scale runs from readily biodegradable and non-bioaccumulative, designated as E or Green, to non-biodegradable and bioaccumulative, designated as A or Black by CEFAS and NEA respectively. API modified belongs in the A or black category. The goal of CEFAS and NEA is to push developments in the direction of E or green category thread compounds.

However, to replace API modified the lubrication and sealing mechanisms needed to be understood. Next to that, limited information was available about high temperature degradation of thread compounds and how it ultimately leads to failure of the metal-to-metal seal. These mechanisms were investigated and are described in this thesis. In addition, current thread compound qualification and test procedures are not pushing manufacturers enough to bridge the gap from black to green dope. A proposal for a test method which incorporates high temperature degradation is done in this thesis. The found mechanisms and test method were validated by successfully developing a prototype thread compound that remedies the found thermal degradation issues with current yellow thread compounds.

1.3.5. Coatings

Coatings are applied to casing connections to protect the surface from corrosion during storage and galling during assembly, as discussed in the previous section. To this end, zinc and manganese phosphate conversion coatings are applied to carbon steels and copper plating is applied to stainless steel grades. The focus in this thesis is on carbon steels because they are most widely used in the application.

For carbon steels corrosion protection is achieved by combining the phosphate coated steel with a corrosion inhibitor also known as a storage compound. The storage compound is removed from the connections and replaced by thread compound shortly before it is used in a drilling campaign. Coating thickness's are in the order of 10 µm. In most cases only one of the contacting members is coated, however, if carbon steel casing needs to be stored for extended periods of time both members are phosphated. The Scanning Electron Microscopy (SEM) micrographs in Figure 1.6 show the surface of a zinc and manganese phosphate coating. The images indicate why these coatings are applied. They provide almost full surface coverage which provides already a basic corrosion protection. Next to that, these coatings provide a porous structure which is beneficial for absorption of a corrosion inhibitor or a lubricant. In the oil and gas industry, phosphate conversion coatings are mainly seen as carrier for the corrosion inhibitor and therefore not much care is taken in the quality and consistency of the coatings. The tribological benefits are recognized but seen more as an added bonus. However, in other industries phosphate conversion coatings full-fill an important role in long running machine elements, e.g. gearboxes, where the coating facilitates and completely wears off in the running-in phase.

However, how phosphate conversion coatings protect the surfaces from for instance galling was not known. The work in this thesis provides the mechanisms that lead to the protective properties of these coatings. In addition, a compelling case is made to include these coatings as part of the thread compound and metal-to-metal seal design process which could lead to biodegradable thread compounds and improved metal-to-metal sealing.

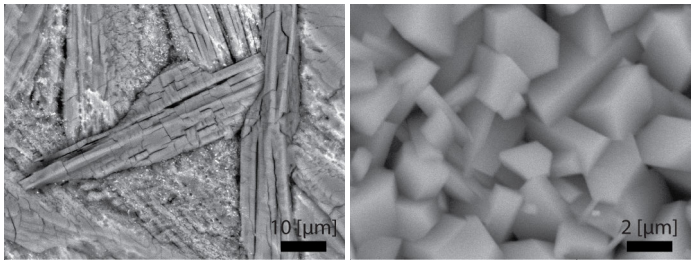

(a) (b)

Figure 1.6.: SEM Backscatter electron (BSE) (20 kV) images of a zinc (Figure 1.6a) and manganese (Figure 1.6b) phosphate coating. Note the difference in magnification when comparing.

1.3.6. Surface topography

Casing connections are manufactured on a lathe, resulting in a metal-to-metal seal with a characteristic spiralling turning profile around the circumference. The surface topography thus has a certain directionality or lay. The pitch and amplitude are determined by the cutting insert geometry, feed rate and cutting depth [6]. When taking a cross section in axial direction a line profile emerges as shown in Figure 1.7a. This profile with round-off radius 80 mm was cut with a carbide insert with a tip radius of 0.8 mm at a feed rate of 120 µm rev^{-1}.

The metal-to-metal seal surface topography therefore consists of a hierarchy of scales as shown in Figure 1.7. In this thesis the surface topography (Figure 1.7a) is defined to be the sum of form (Figure 1.7b), waviness (Figure 1.7c) and roughness (Figure 1.7d). Hence, form is associated with the seal round-off radius or conicity and determines the Hertzian contact stresses. Waviness is associated with the manufacturing process, in this example coming from the combination of the carbide insert geometry, depth of cut and axial feed rate. Roughness is the result of the removal of material by the cutting action of the insert.

Figure 1.8 shows a comparison of the contact stress distribution before and after make-up sliding at a contact intensity of 136 N m^{-1} using the contact model implemented for this thesis. Yellow indicates contact. This illustrates that the turned surface topography of Figure 1.7 gives rise to very localized contact stresses at the peaks of the waviness. Comparing the before and after states it can be observed that running-in widens the localized contact zones. In addition, some contact lines seem to have a more intermittent contact compared to the before state because of the wear process during sliding.

How the micro geometry changes and what the influence of these changes is on sealing ability was unknown. In extension, it was also unknown how a suitable geometry for sealing should look like or could be realized. This thesis will show that the surface topography and particularly its orientation is important as it plays a role, combined with the thread compound and coating, in its friction and wear characteristics, its galling susceptibility and ultimately its seal ability.

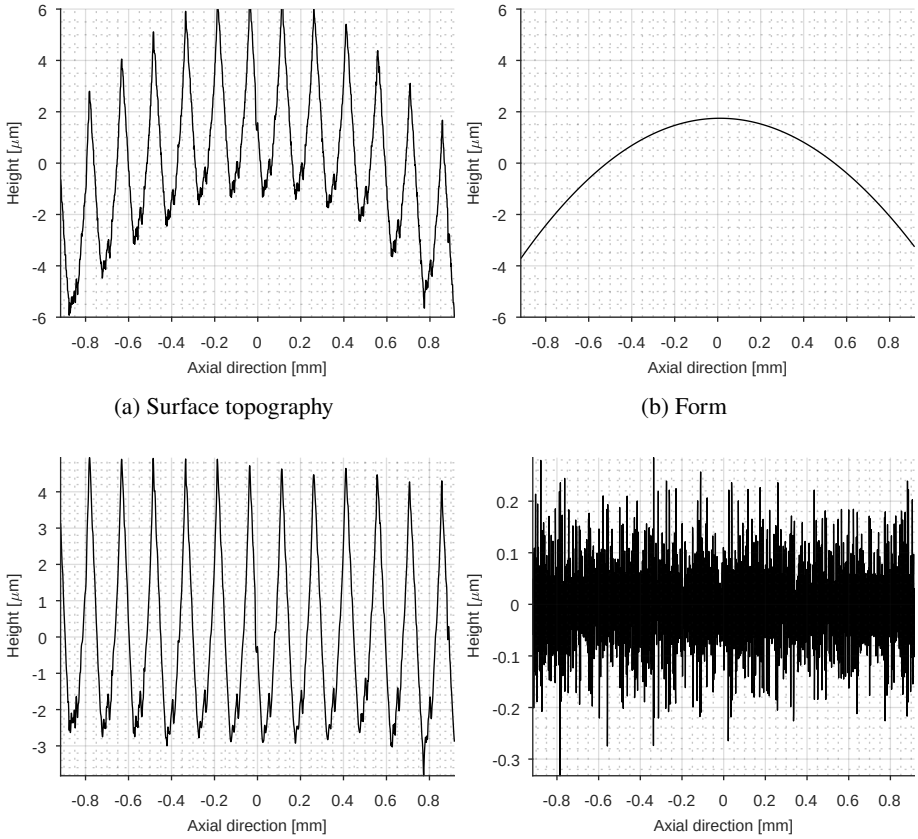

(a) Surface topography

(b) Form

(c) Waviness

(d) Roughness

Figure 1.7.: Overview of the hierarchy of scales present in the metal-to-metal seal which together are affected by the running-in and ultimately determine the seal ability performance. Note: height axes are not set to the same scale. Figure 1.7a shows the complete surface topography which is defined in this thesis to be the sum of form, Figure 1.7b, waviness, Figure 1.7c, and roughness, Figure 1.7d.

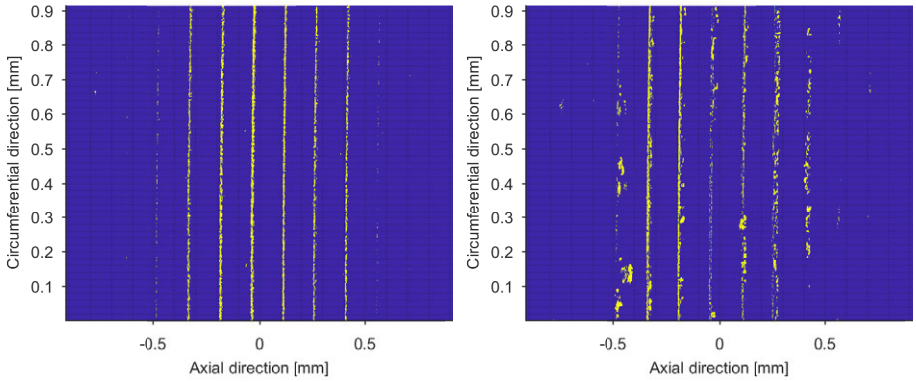

(a) Before (b) After

Figure 1.8.: Contact stress distribution before, Figure 1.8a, and after, Figure 1.8b, make-up sliding of a metal-to-metal face seal. Contact is indicated by yellow. The localised contact widens because of running-in of the surface during make-up sliding.

1.4. The need for prediction of connection qualification outcomes

A (new) connection needs to tested and qualified before it can be used in well construction. Connection testing is done according to the ISO 13679 standard [7]. The standard defines four Connection Assessment Level (CAL)s indicated with an increasing Roman numeral corresponding to increasing severity. CALI is used to qualify connections for well designs which only see moderate internal pressures and axial loads. Whereas CALIV is used to qualify connections for demanding high pressure high temperature applications which push the system to its limits. Once a qualification is obtained it is only for that CAL or lower and tribosystem (material grade, connection type, wall thickness, thread compound, coating and surface topography) combination. Rules do exist for extrapolation/interpolation to another material grade or wall thickness, however, typically at least a single specimen test needs to be performed to proof the new combination [7].

The CAL tests entail simulation of several well scenarios (e.g. the thermal expansion discussed in Section 1.3.3) that are imposed on the full scale connection by assembly tests in a power tong and structural performance tests in a specialized load frame. The latter is best illustrated by the Von Mises Equivalent (VME) stress diagram in Figure 1.9. The casing connection undergoes combined loading, internal (P_i) or external (P_e) pressure and tensile (F_T) or compressive (F_C) axial load, while load, displacement and seal ability is monitored. The example is for a connection that is limited to 70% of pipe compression and 80% pipe tension because of its reduced critical cross section (Figure 1.5b). A failure is defined if any of the following occurs: the metal-to-metal seal shows galling in the assembly tests, the connection fails structurally (exceeds yield strength) or the connection leaks at a sustained rate of >1.2 ml min^{-1} [7].

The qualification according to CALIV comes down to approximately 6 months of testing and

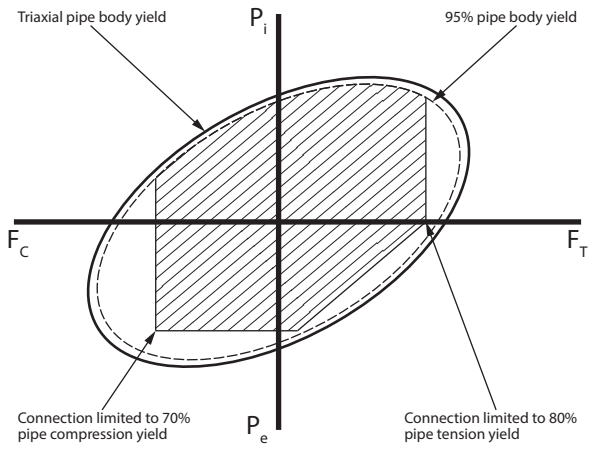

Figure 1.9.: Von Mises equivalent stress diagram for the pipe body. The connection is represented by the hatched area. Artistic impression by the author reproduced from [7].

an investment in the order of a million US dollar, if successful. Further as the test is decisive if the connection can be used in operations, it will steer connection design. Therefore, it is interesting to have a method developed to screen connection sealing performance before the actual qualification tests are done avoiding unnecessary tests and costs. In addition, such a method can provide insights in the design of metal-to-metal seals that can help to improve them. An idea is to use finite element analysis to do the screening by calculating the contact stress to applied pressure ratio of the metal-to-metal seal. However, as discussed in Section 1.3.2, success or failure of a metal-to-metal seal is governed by other parameters than only contact stress acting on a perfectly flat and round surface.

For the connection testing and subsequently the lifetime of the well it is therefore important to understand how these (changing) parameters affect the sealing ability of the metal-to-metal seal. The work was therefore subdivided in a running-in model and a sealing ability model. For the sealing ability model see the work by Francesc Pérez-Ràfols [8]. A summary of the work will be given in Section 2.5. The work presented in this thesis is related to the running-in of the metal-to-metal seal.

1.5. The need for a running-in model of metal-to-metal seals

As discussed every metal-to-metal seal undergoes at least one assembly which transitions the initial surface topography because of friction and wear to a run-in surface topography. If successful (e.g. no galling was observed), the connection is subsequently lowered in the well and the run-in topography becomes the initial condition for the sealing ability and micro sliding phase. Therefore, to come to a predictive model of metal-to-metal sealing this part needs to be

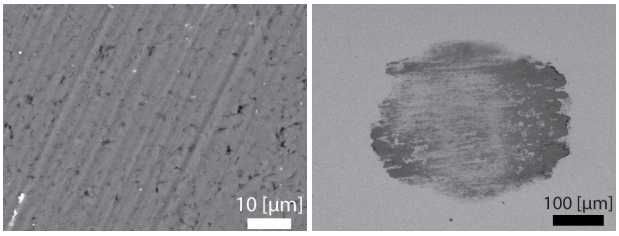

(a) (b)

Figure 1.10.: SEM BSE images of pin-on-disc experiments showing a glaze layer formed on a manganese phosphated disc (Figure 1.10a at 20 kV) and a manganese phosphate derived tribofilm formed under lubricated conditions on the ball (Figure 1.10b at 10 kV)).

taken into account. With the model it can then be investigated what is required for a successful assembly and what part of the tribosystem affects the sealing ability the most.

1.6. The need for a deeper understanding of phosphate conversion coatings

Knowledge on the behaviour of phosphate conversion coatings in short running systems is scarce. In the case of a metal-to-metal seal the coating is present during the complete operational lifetime. It was found in this thesis that during running-in a smooth glaze layer is formed on the phosphated side and a strong tribofilm on the non-phosphated side as shown in Figure 1.10. The mechanism behind the glaze layer formation relies on crushing and subsequent compaction of the phosphate crystal debris. The tribofilm is formed by adsorbing the debris particles through a shear stress activated mechanism. Together these mechanisms dominate the friction and wear and thus running-in behaviour of the metal-to-metal seal and ultimately the sealing ability.

1.7. Objectives

The running-in behaviour of a metal-to-metal seal tribosystem and its resulting sealing ability is generally determined by the combination and interaction of thread compound, phosphate conversion coatings and surface topography. The interaction is a result of contact stresses generated by the increasing interference between pin and box during assembly. After assembly the tribosystem undergoes additional sliding as a consequence of external loading. The aim of this research is to investigate the role of running-in on the seal ability of premium casing connection metal-to-metal seals. The principal objectives of the thesis were as follows:

- Determine the mechanism of galling initiation in premium casing connection metal-to-metal seals.

- Determine the protective mechanisms and influence on running-in of the metal-to-metal seal surface of thread compound and phosphate coatings.
- Develop a running-in model for a metal-to-metal seal.
- Validate the running-in model.

1.8. Outline of the thesis

The thesis is constructed as follows. Chapter 2 provides an overview of the relevant literature and based on that defines the gaps that will be addressed by the research questions posed at the end of the chapter. The main body of the work starts in Chapter 3 with the characterisation of the lubrication mechanism of API modified, the related galling initiation mechanisms and the role of the thread compound in sealing. The failure mechanisms related to thermal degradation of API modified and selected environmentally acceptable thread compounds was investigated in Chapter 4. This resulted in a new proposal for a test methodology that was validated with the successful development of a thread compound that mitigates the high temperature degradation and galling issues. Chapter 5 then turns to the phosphate conversion coatings and explains the mechanisms leading to the dominating influence on the running-in of a metal-to-metal seal. The observations and mechanisms of the preceding chapters are subsequently used in Chapter 6 to develop a running-in model and together they are used to explain the role of running-in on metal-to-metal sealing. Finally, the overall conclusions and recommendations are given in Chapter 7.

This page has been intentionally left blank.

2. Setting direction: Literature review and exploratory testing

This chapter gives an overview of the relevant literature in relation to the influence of running-in on metal-to-metal sealing and how this is affected by the various components of the tribosystem. It should have become clear in the introduction that the metal-to-metal seal operates in two regimes: close to uni-directional sliding during the assembly stage and fretting during the micro sliding stage. An attempt is made here to relate those to the existing literature. Part of the exploratory work discussed in this chapter is reproduced from Paper B

2.1. Introduction

As discussed in Chapter 1 the focus in this work is on metal-to-metal seals of casing connections and mainly the factors during assembly and micro-sliding that influence the performance of the metal-to-metal seal. An overview of the relevant literature will be given in the following.

2.2. A short history of casing connections

Casing connections are as old as the oil and gas industry. They are needed to connect tubular extending into the oil and gas bearing zone such that it can be extracted. As discussed in Section 1.2 the casing and the casing connection together form a pressure vessel that needs to withstand the down-hole axial and pressure induced forces [9]. This is by no means an extensive review of the history of casing connections. For such a review the reader is referred to the thorough overview by [10].

The first record of a connection intended for connecting pipes dates back to 1876 by O'Neill [11]. Soon after, Allison [12] filed the first metal coating treatment for such a connection and the coupling was invented in 1882 by Morse [13]. The first record defining a pin and box as it is known today is the coupling by Bole [14]. Examples of modern day coupled connections are shown in Figure 2.1a and Figure 2.1b, here a Hunting TKC CLTC and TenarisXP Buttress respectively named after the API 8-round and buttress thread forms used in the connections. It should be noted for these designs that there is no clear way of knowing when it is properly made-up. Therefore, a position based system was implemented to get repeatable assembly.

However, this was still unreliable because of for example varying tolerances or unknown Coefficient of Friction (COF), which resulted in unwanted loosening of the connections. This

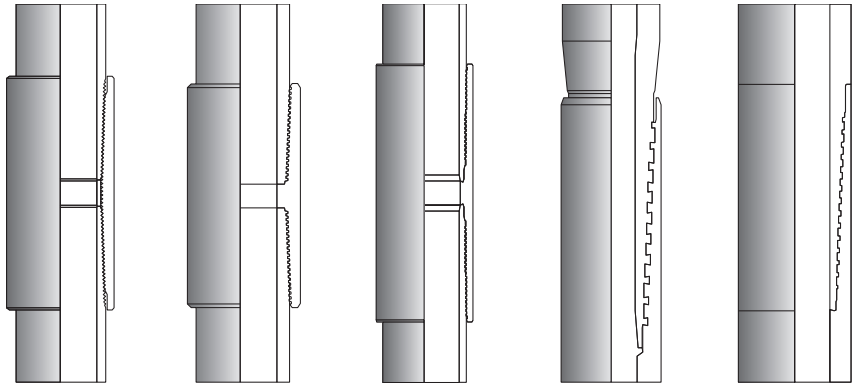

(a) Hunting TKC CLTC (b) TenarisXP Buttress (c) VAM Connection VAM 21 (d) TenarisHydril Wedge 511 (e) VAM Connection VAM MUST

Figure 2.1.: Examples of various thread forms and connection designs. Two coupled non-premium type connections are shown in Figure 2.1a with API 8-round thread and Figure 2.1b with API buttress thread. Figure 2.1c shows a coupled premium connection with internal metal-to-metal seal [20]. Integral premium connections are depicted in Figure 2.1d with wedge thread and Figure 2.1e internal metal-to-metal seal. Adapted from [21].

resulted in the introduction of the torque shoulder [15] such as the one shown in Figure 2.1c providing a clear end point for the assembly of the connection and a way to introduce additional pre-tension in the connection. The final innovation was the addition of a metal-to-metal sealing element to the connection by Reimschissel [16] to separate the functionality of axial load transfer and sealing ability as is known today.

Sealing ability research subsequently shifted back to thread sealing [17]. The standard triangular API 8-round (Figure 2.1a) and trapezoidal API buttress (Figure 2.1b) thread form have clearances when made-up [18]. The clearances were closed with a thread compound. This was achieved by adding particles to the thread compound and worked best when a particle was at least two times larger than the gap they needed to pass through. In addition, a broad distribution of particle size yielded the best sealing [17]. API modified was designed with this in mind [4] with particles measuring 43-173 µm. With this an API 8-round thread could withstand 69 bar pressure.

The increasing well depths and demand for connections with good compressive strength, high tensile efficiency, repeatable make-up performance and minimal diameter loss by the coupling finally led to the invention of the first premium connection in 1965 by Blose et al. [19]. This contained all the elements of the premium connections we know today. Figure 2.1c shows a modern premium coupled connection with internal metal-to-metal seal and torque shoulder. Two variants of premium integral[1] connections are shown in Figure 2.1d and Figure 2.1e where the former has a wedge thread and the latter an internal and external metal-to-metal seal.

[1] Meaning pin and box are both cut from the pipe wall thickness giving a joined connection with the same diameter as the pipe as opposed to a coupled connection which add 2 times the pipe thickness to the diameter.

Despite the availability of this technological superior design, the limited pressure ($\leq$1034 bar) and temperature levels at the time still allowed the use of much cheaper polymer or elastomer sealing elements. When pressures and temperatures went up in the late 70s, these sealing elements became unreliable and were replaced by metal-to-metal sealing [17].

The advent of improved manufacturing capability and more precise carbide cutting inserts at the start of the 80s allowed ever tighter tolerances and manufacturing of the complex shapes needed for proper metal-to-metal sealing. Initially these seals were frustoconically shaped. Meaning a sequence of two cones with different taper. These surfaces were energized by placing them near the torque shoulder and applying a negative shoulder angle to generate an outward force on the sealing surface [22] similar to the design in Figure 2.1c which is detailed in [23].

At the same time the higher pressures and temperatures together with the improved manufacturing sparked a new series of investigations into thread sealing. The higher precision machining allowed for smaller clearances in API 8-round and buttress thread and improved sealing ability when combined with the right thread compound [17]. In addition, Asbill et al. [24–26] and later Schwind et al. [27] showed with Finite Element Analysis (FEA) and physical testing that API 8-round sealing ability is compromised by tension loading while API buttress is not. This is the reason that all premium connection nowadays use an API buttress (inspired) thread design.

Finally, to get around the challenges with (metal-to-metal) sealing all together an alternative technology based on brazing was recently developed [28]. The technology entails applying a brazing material on the pin and the box by flame spray and subsequently making them up while applying heat using an induction heater. This metallurgically binds the pin and box together yielding a leak tight connection.

In the review hereafter the items related to casing connections and metal-to-metal sealing will be discussed in more detail using the available literature. From the review the gaps in the literature will be identified and incorporated in the research objectives.

2.3. Boundary conditions: testing a casing connection

As discussed in the introduction (Section 1.4) the casing connection needs to pass a qualification test program according to International Organization for Standardization (ISO) 13679 before it can be used in operations [7, 29]. Before continuing, it is good to address this with more detail as it will determine the boundary conditions for the experimental and modelling work.

The requirement was that the work reflects the most stringent CALIV as this is typically the operational condition for connections equipped with metal-to-metal seals. In addition, all other CALs will be covered as they are a subset of CALIV. The results obtained below are summarized in Table 2.1.

The selection of CALIV entails the following in condensed form based on the 2002 version of the ISO13679 standard [7] as this is most widely used [29]. For this test program 8 specimens

Table 2.1.: Summary of the metal-to-metal seal tribosystem properties used as input for experimental and model work.

Contact conditions	
Contact stress	800-2000 MPa
Contact width	1-3 mm
Make-up/Break-out	
Cumulative pin sliding length	1.0-2.4 m
Cumulative box sliding length	0.15-1.44 m
Linear velocity	0.3-100 mm s^{-1}
Sealing ability tests	
Micro-sliding stroke length	0.22-0.4 mm
Cumulative micro-sliding length	11-19 mm

are required with a variation (within the bounds of the tolerances) in the pin/box diameter, taper angle and final torque level. This will ensure that the product is tested at the worst case performance configurations. For instance, combining a pin with a small taper angle with a box with a large taper angle will lead to a low seal contact stress and thus a worst case for sealing ability. The loading program will be performed in counter clockwise (CCW) and clockwise (CW) direction along the Von Mises ellipse of Figure 1.9.

For 8 specimens with different tolerance configurations perform [7, Fig. 1]:

- Galling evaluation: up to 2x make-up/break-out tests per specimen.
- Final make-up.
- Connection bake-out at 180 °C for 12h.
- Sealability testing
  - Specimens 1, 3, 5, 7 Series A: loading spanning all quadrants of the Von Mises Ellipse (Figure 1.9). Internal pressure is applied with gas and external pressure with water. Run CCW-CW-CCW.
  - Specimens 2, 4, 6, 8 Series B: loading spanning quadrant 1 and 2 of the Von Mises Ellipse (Figure 1.9) and bending. Internal gas pressure. Run CCW-CW-CCW.
  - Specimens 1, 3 from Series A and specimens 2, 4 from Series B move to Series C: 5x mechanical cycling at ambient, 5x thermal cycling at 180 °C, 5x mechanical cycling at 180 °C, 5x thermal cycling at 180 °C, 5x mechanical cycling at ambient under tension and internal gas pressure.
- 8 specimens failure test: either tension, compression, internal pressure or external pressure to failure or selected combinations of pressure and axial loading to failure

This means that at the end of the test program, based on a best guess estimate 0.2-0.6 m circumferential sliding length (Section 1.3.3), the metal-to-metal seal has seen a maximum of 2 make-ups + 2 break-outs + final make-up = 1.0-2.4 m cumulative sliding length. Note that break-out reverses the sliding direction and pin and box will see different cumulative sliding lengths. The pin has a stationary contact, hence the calculation above is correct, while the box sees a moving contact because the pin progresses inwards as a consequence of the thread pitch. The cumulative box sliding length is thus proportional to the ratio between thread pitch and contact width.

The thread pitch is dependent on pipe diameter and can be determined from the amount of threads per inch (TPI) as $P = \frac{25.4}{TPI}$ mm. The TPI values are reported in the manuals [30, 31]. A general number is 4 - 5 TPI for casing diameters of 100-300 mm resulting in a pitch of 5.08-6.35 mm which is in line with the results reported in [32].

The contact width is a function of the increasing interference between pin and box, the contact geometry, contact stiffness and the onset of plasticity or surface hardness [33]. Unfortunately this is considered proprietary information. Therefore an estimation was made based on literature giving a contact width of 1-3 mm [34, 35]. This results in a cumulative sliding length ratio of $\frac{l_{box}}{l_{pin}} = 0.15 - 0.6$ or $l_{box} = 0.15$-1.44 m.

In addition, the load cycling will introduce micro-sliding in axial direction. The amount of tensile and compressive cycles (zero to maximum axial load) adds up to 24 and 9 respectively [7, Sec. 7.3]. The seal stroke length depends on the relative movement between pin and box as a consequence of the box elongation during axial loading. The elongation was determined using the make-up loss [30, 31], which is equal to the engaged length of the connection, and the fact that at maximum load the material is close to yield. The make-up loss depends on the casing diameter and is 112-200 mm. The elongation is 0.2% at yield and thus the seal stroke length is 0.22-0.4 mm. The cumulative sliding length assuming a torque shoulder (hence movement is restricted in compression direction) is 2 times the stroke length times the amount of cycles which amounts to 11-19 mm.

Contact stresses, like the contact width, for premium casing connection metal-to-metal seals are proprietary. Therefore, an estimation was made based on numbers disclosed in the available literature reporting contact stresses of up to 800 MPa for nominal configurations [34, 35]. Variations in seal tolerances, taper and material yield can increase the *contact intensity* by a factor of 2 to 6 according to [20]. As for line contacts $p \propto \sqrt{q}$ [33, Eq. 4.45] an estimation of seal contact stresses in the range of 800-2000 MPa was obtained.

The assembly speed follows from the running manual of the manufacturer and is typically 2-5 RPM with a strong advice to use 2 RPM [30, 31]. Combined with the casing diameter, this results in linear velocities in the range of 0.3-100 mm s^{-1} as shown in Figure 2.2.

2.4. Studies focused on the oil and gas application

Most recently, work by Stewart et al. [36] and Stewart [37] investigated the lubrication regime and running-in behaviour of casing connections when a solid lubricant is applied. The focus was on the performance and prediction of the COF of the solid lubricant against shot peened

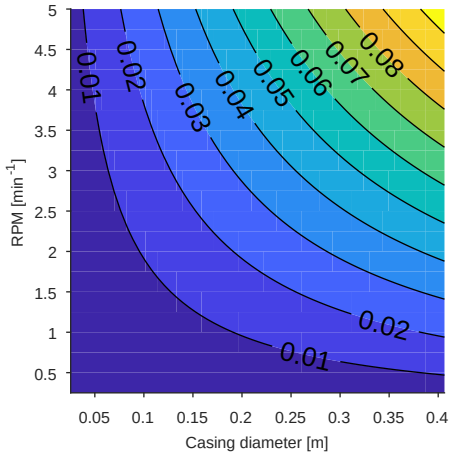

Figure 2.2.: Contour plot of make-up linear velocity as function of casing diameter and make-up RPM. Isolines in m s^{-1}.

chrome steel surfaces. They showed, Figure 2.3, experimentally that most of the surface evolution happens in the first 50 mm of sliding. The mechanism of running-in, however, was not discussed. This work was followed up by Le et al. [38] with an asperity based running-in model by Christensen [39] to account for asperity plasticity and a simplified flow factor approach to model lubricant entrapment and flow by Patir et al. [40]. The model produced a reasonable prediction of the statistical changes in surface topography and COF. They showed that the bronze plated against ceramic shot peened chrome steel system operates in the severe wear regime with a wear coefficient in the order of 10^{-4} or converted to wear rate 10^{-14} m^3 N^{-1} m^{-1} [41]. This meant that the system was run-in after only 50 mm of sliding. The model assumptions, however, prohibited any deterministic predictions on the surface topography. The need for a deterministic prediction, however, is evident because most casing connections have a turned surface topography as discussed in Section 1.3.

Earlier studies, as discussed in Section 2.2, focused mainly on the behaviour and interaction of the connection with thread compound. Thread compounds are made according to API specifications [4] and are different from normal greases [42] because of their high solids content of up to 60%. They need to give repeatable friction for the torque based assembly [43], avoid galling during assembly [44–47] and help in sealing ability once the casing connection is assembled [18, 48–50]. In addition, the thread compound needs to perform under the conditions present in the well. This means under elevated temperatures and exposure to well fluids or gasses [48, 49, 51]. Both are known to degrade the sealing performance of the thread compound because of evaporation and dissolving of the base oil. This was confirmed in later works which will be highlighted hereafter. The exact degradation mechanisms are, however, not given.

As discussed the standard thread compound is API modified [4]. The compound was formulated over 70 years ago [17] and is still the most widely used thread compound in the oil and gas industry [4]. It contains a base grease made with a heavy mineral oil and a metal soap

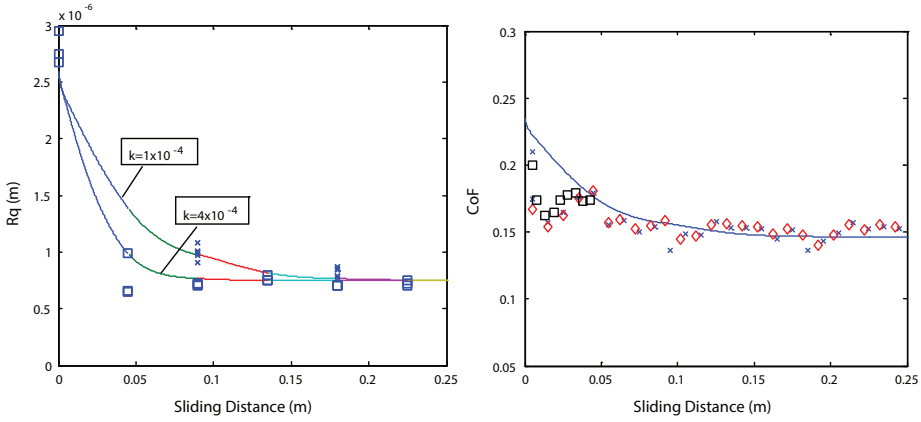

(a) (b)

Figure 2.3.: Running-in behaviour of a bronze plated versus shot peened chrome steel surface. Figure 2.3a shows the evolution of Root Mean Square (RMS) roughness and Figure 2.3b the evolution of COF both as function of sliding length. Adopted from [38].

thickener combined with graphite, lead, zinc and copper. Several explanations for its success in protecting the surface during assembly and sealing ability are given. Ertas [47] attributes it mainly to the lead particles that form a protective film. While zinc and copper are said to be added to control the friction coefficient. In addition, the copper particles are the largest and probably aid in thread sealing [17, 18]. Finally the graphite is not of lubrication grade and therefore acts mainly as filler [47]. This, together with the broad particle size distributions of the metallic additives [17], should help in the sealing ability [47]. Carper et al. [46] found that this protection is limited to the rather low contact stress of 303 MPa in typical oil industry steel grades (Section 1.2). Nowadays a contact stress of up to 2000 MPa is common. This is probably because API modified was originally designed as a thread sealing compound [17]. This is an often occurring failure mechanism in casing connections. However, the mechanism behind the failures has not been explained. Therefore, this needs to be understood as API modified is the most widely used thread compound. In addition, it will provide insight in what is needed for an environmentally friendly thread compound.

In addition, the work of [43, 45, 47] indirectly assesses the influence of phosphate conversion coatings on the galling behaviour of connections during make-up. The coating was applied on the specimens to be able obtain sensible results in their screening tests. Implicitly they show that all the fully formulated lubricants sustain no galling with phosphated surfaces up to extremely high contact stresses. Whereas, as said before, some of these lubricants show galling on bare metal surfaces at very low contact stresses [43, 46]. No explanations as to why the phosphate conversion coating improved performance dramatically were given. This was identified as another gap because of the dominating influence of these coatings on the running-in behaviour as will be discussed in Section 2.10.

It was shown by [50] that the thread compound, when considered for its seal ability alone, makes a large difference when gas seal ability is considered. The onset of leakage was much later and

instantaneous compared to experiments without thread compound. There is, however, a large difference in the sealing performance between the different commercial thread compounds as shown by [49]. This was mainly attributed to imposed variations of the applied internal pressure, the type of gas and the temperature cycling. Still, API modified holds up well against recently developed thread compounds. Particularly under high temperature conditions.

Inose et al. [48] show that thermal degradation of the thread compounds plays a significant role in reduction of the sealing performance of metal-to-metal seal. They exposed API modified and an environmentally acceptable thread compound with inorganic particles to temperatures of 180 °C and monitored sealing ability. It was concluded that API modified performed better compared to the plant based oil and inorganic particles of the environmentally acceptable thread compound. This was attributed to the mineral oil which performed better under elevated temperature conditions and its soft metallic particles helped sealing ability because they closed potential leak paths. They thus show that a connection can be successfully made-up but fail during load cycling because of thermal degradation of the lubricant. This exposed the surface directly to the hard inorganic particles contained in the environmentally acceptable thread compound. The particles subsequently abraded the surface leading to formation of scratches and/or galling in the seal area reducing its sealing performance. These works suggest that the choice for base oil, thickener and additives needs to be balanced between tribology and sealing ability. How this needs to be done is not discussed and needed to be identified to understand the running-in during the micro-sliding phase.

In light of the above it is interesting to discuss the API 5A3 standard [4] and what it dictates in relation to the performance of the thread compound. A set of standardized tests characterizing the physical and chemical properties of the compound is included, like worked penetration, evaporation, copper corrosion, etc [52]. However, a test relating this to make-up performance or sealing ability does not (really) exist. For make-up performance a 1 inch nut and bolt assembly test is specified also known as the "nut buster". This subjects the thread compound to a rather low contact stresses of 200-400 MPa on the loading collar and 260 MPa on the threads. For (high temperature) sealing ability the only reliable way of testing is according to the ISO13679 (Section 2.3). Hence no simple and cost effective test methodology exists that is predictive of thread compound performance in full scale connections. Proposals have been made over the years [36, 43, 46, 47, 49], but none have been taken up into the standard. On the basis of the work in this thesis a proposal is made for a simpler and more cost effective screening method.

Finally, casing connection manufacturers are spending considerable effort to avoid the environmental concerns related to the heavy metallic contents of the thread compound. One approach is to run without any thread compound and instead apply a solid lubricant coating to ensure smooth make-up [53, 54]. An added benefit is increased productivity on the well site because the lubrication prior to assembly can be skipped. However, this is offset by added costs in manufacturing because of the need for an additional step and the related quality assurance and control.

2.5. Metal-to-metal sealing

As discussed in the introduction (Section 1.3.2) metal-to-metal sealing is achieved by applying a sufficiently high contact stress to two surfaces in contact. If surfaces would posses no surface topography and limited form error (unflatness or unroundness) [55] this would be the end of the discussion. However, engineering surfaces do have a surface topography, often with a certain orientation, which affects their sealing performance. Pérez-Ràfols et al. [56] and Pérez-Ràfols et al. [57–59] expanded the work of Sahlin et al. [60, 61] for steel contacts and showed with a deterministic and stochastic sealing model that the surface topography and its lay plays an important role in the sealing ability of a metal-to-metal seal. The results of a comparison between a turned and a shot blasted surface are shown in Figure 2.4 and Figure 2.5.

Instead of a smooth Hertzian contact stress profile (Section 1.3.2), a localized contract stress distribution is found when roughness is accounted for with a deterministic contact model (Section 2.7). For a turned surface this results in a gap shown in Figure 2.4a with the fluid meandering over the resulting castellated gap topography. For a shot blasted surface, however, the result in Figure 2.4b is completely different with fluid flow over the full contact length.

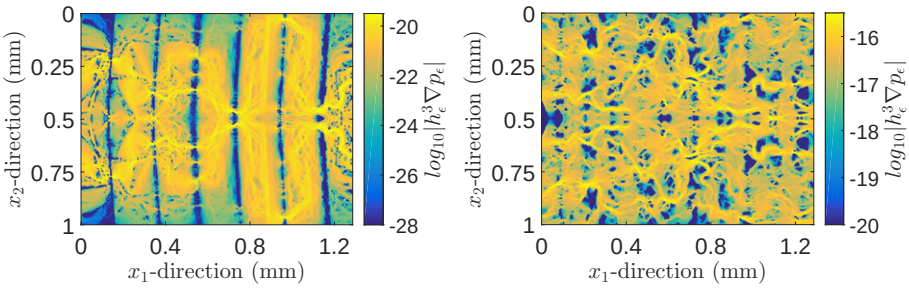

(a) (b)

Figure 2.4.: Flow patterns for a turned and shot blasted surface for the pressure driven flow through the gap using the deterministic sealing model presented in [62]. The unitary pressure differential acts from left to right. Shown in Figure 2.4a and Figure 2.4b is the absolute value of deterministic flux, in logarithmic scale, at a total applied load of 200 MPa. Reproduced with permission [62].

This qualitative behaviour is made quantitative by computing the permeability of the gap as function of load in Figure 2.5a and Figure 2.5b for the turned and shot blasted surface respectively. The difference is several orders of magnitude in favour of the turned surface. Hence it is clear that the type of surface topography and also its orientation plays an important role in the sealing performance of a metal-to-metal seal.

In a casing connection metal-to-metal seal the surface topography works in conjunction with the thread compound as discussed earlier (Section 2.4). Next to the experimental studies (Section 2.4), no modelling attempts incorporating the sealing mechanism of a thread compound have been found in the literature.

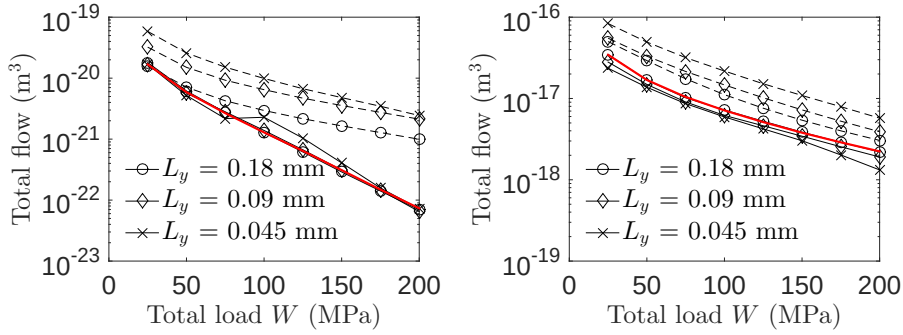

Figure 2.5.: Permeability for a turned and shot blasted surface as function of load for the pressure driven flow through the gap using the deterministic sealing model presented in [62]. Figure 2.5a shows the permeability as function of load. Reproduced with permission [62].

The role of the surface topography and lay is supported by earlier work by [63–65]. It is then not a big stretch to conclude that the running-in of said surface topography also plays an important role. This will be discussed next by covering the literature related to the various elements and building blocks needed to understand the running-in of a metal-to-metal seal tribosystem.

2.6. Phosphate conversion coatings

The standard work for phosphate conversion coatings is the book by Rausch [66]. Many of the later results discussed in this review can already, maybe with less detail, be found in this book. The review by Narayanan [67] is another excellent starting point. In the oil and gas industry phosphate conversion coatings are mainly used as corrosion protection of casing connections during storage. However, as will be discussed in Section 2.10, they play an important role in the running-in of the metal-to-metal seal. The mechanisms of surface protection, however, were poorly understood which became a large part of the work in this thesis.

A phosphate conversion coating belongs to the family of chemical conversion coatings. The coating forms under a topochemical reaction which incorporates part of the base metal into the coating. The coating is deposited on a steel surface by submerging it in a solution of phosphoric acid and (alkali) metal ions. The free acid will dissolve the iron which leads to the formation of soluble primary ferrous phosphate. This will alter the pH at the metal-solution interface which changes the equilibrium between primary phosphates and insoluble metal tertiary phosphates. This subsequently leads to precipitation of the latter and formation of a phosphate conversion coating on the steel surface [67].

Phosphate conversion coatings provide a chemically incompatible (towards steel) and porous surface [67]. The porosity facilitates the absorption of a lubricant and/or corrosion inhibitor to protect the surface [68–71]. The coating can deform slightly to even out high pressure peaks in the contact and improve conformity of the surfaces [71]. Furthermore, because of

the properties mentioned it can also serve as a base layer for paint and organic coatings [69, 72, 73]. In tribology these properties make them ideal to facilitate the running-in phase of machine elements like gears [74].

Typical zinc and manganese coatings consist of respectively hopeite ($Zn_3(PO_4)_2 \cdot 4\,H_2O$) [75], and hureaulite ($Mn_5^{2+}(PO_3OH)_3(PO_4)_2 \cdot 4\,H_2O$) [76] crystals. Hence a phosphate conversion coating is crystalline. The crystal hardness is reported by [77] to be 3.2 and 5 on the Mohs scale. Others report 2.5 - 3 Mohs and 3.5 Mohs respectively [66]. As the Mohs scale is ordinal, this only says that hureaulite is harder than hopeite. Several investigators have tried to characterise these coatings with other means than the Mohs scale.

Kumar et al. [78] characterized zinc phosphate using micro hardness indentations, wear experiments and corrosion experiments. They determined the micro hardness of the layer to be 50 HV and found that the needle structure of zinc phosphate crystals plays an important role in the wear behaviour of medium alloy low carbon steel. The experimentally observed wear increase was attributed to the roughening of the surface and the subsequent increase in local contact stress. They found that the phosphate process introduces considerable compressive residual stresses in the substrate which was deemed positive for fatigue life. However, this means tensile stresses in the coating, reducing fretting resistance of the coating [79]. Furthermore, they observed an increase in the COF compared to bare steel attributed to the increased contact area due to the softer layer. Based on this, they concluded that zinc phosphate is not effective in increasing wear resistance.

For the characterization of manganese phosphate coatings the work by Hivart et al. [80] is of interest. They derived a bulk behaviour law for manganese phosphate based on micro hardness indentations combined with a finite element model. The finite element analysis is used to match the experimental indentation data to provide the stress – strain curves assuming a non-layered material. The combined data is fitted to a modified Ludwick model. The procedure yields a continuous material model that incorporates the coating to bulk transition. The surface hardness was measured to be 125 HV.

The author attributes the introduction of compressive stresses in zinc phosphate to epitaxy. In [66] a misfit of -7 % between the hopeite lattice and α-Fe lattice is reported which indeed leads to tensile stresses in the coating and thus compressive stresses in the substrate. The misfit of hureaulite is -1 % and should thus lead to less issues with wear resistance of the coating. It is also suggested in [66, 77] that the phosphate layers have a certain directionality or anisotropy owing to the crystal growth and aforementioned epitaxy leading to slight differences in deformation behaviour.

The friction behaviour of zinc phosphate has been investigated by [81] in dry and lubricated conditions. Here, lubrication was provided by a paraffinic oil and a sodium stearate soap. The soap resulted in the lowest COF because of its high durability attributed to chemical adherence to the phosphate layer. This is the main reason why zinc phosphates are heavily used as a chemical reaction layer in combination with soaps to lubricate deep drawing processes [82]. The first friction and wear investigation in dry and lubricated condition of manganese phosphate is by [77, 83, 84]. They characterized manganese phosphated grey cast iron as having hybrid properties between that of a soft metal coating and a rock salt. Inheriting similar abrasive properties of the rock salt. It was concluded that manganese phosphate reduces the COF and

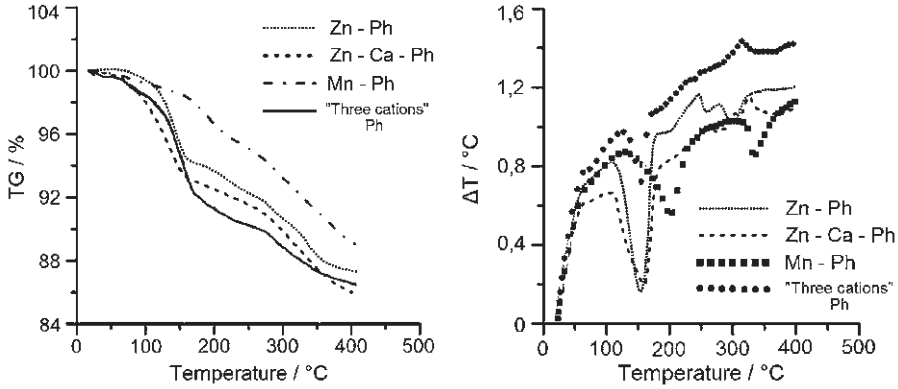

(a) TGA (b) DTA

Figure 2.6.: TGA/DTA results for hopeite (Zn - Ph) and hureaulite (Mn - Ph) reproduced from [72].

increases the wear resistance. It reduces the likelihood of adhesive wear under lubricated conditions and the wear properties are a function of surface finish and substrate. Further they found that phosphating offers no advantage in dry sliding on grey cast iron.

The quality of the phosphate coating and its aforementioned properties are strongly influenced by the process conditions during phosphating. The wear characteristics as function of the applied phosphating process were first investigated by [71]. The findings were that a thin fine grained coating gives superior wear performance. A more elaborate study on the relation between the coating process and the seizure behaviour of manganese phosphate was done by [85]. Considerable improvements were obtained by fine tuning the cleaning, refining and phosphating parameters. They also showed that the carbon content of the substrate plays a significant role. Next to that they found that annealing the coating yields considerable improvements in seizure resistance related to improved oil retaining properties and increased surface hardness from 125 HV to 300 HV [86].

The thermal properties of the phosphate conversion coatings are of interest for discussions related to galling induced by thermal breakdown of the protective films [87, 88]. For this the work by [72] is reproduced in Figure 2.6. This shows TGA (Figure 2.6a) and Differential Thermal Analysis (DTA) (Figure 2.6b) results of several phosphate conversion coatings. In the figures Zn-Ph and Mn-Ph correspond to hopeite and hureaulite respectively. The DTA results show the first endothermic peaks at 110 °C for hopeite and 150 °C for hureaulite. The peaks were attributed to dehydration of crystal water contained in the respective crystals and thus not breakdown of the phosphate coating.

As discussed in this section, the beneficial properties of phosphate conversion coatings for running-in of tribological systems is recognized in literature. The mechanisms that lead to these properties were, however, not described yet or phenomenologically. Therefore, this was identified as an important gap in the understanding of the running-in behaviour of a metal-to-metal seal.

2.7. Contact mechanics

The prerequisite for tribology is contact between two or more surfaces. The recently published outcomes of the contact mechanics challenge set up by Müser et al. [89] show that there is a proliferation of contact mechanics models [90].

Statistical or asperity based contact models [91, 92] go back to the pioneering work of Greenwood et al. [93]. The premise is that if one knows or determines the mechanical behaviour of a single asperity one can calculate the behaviour of a whole ensemble of asperities. In essence the asperity becomes the discrete element on which the computation is performed. In the case of [93] the shape of such an asperity was idealized to have one radius and chosen to be hemispherical. Later, they were generalized by Bush et al. [94] to paraboloids. Others derived the equations for elliptical [95], triangular [96], sinusoidal [97], wedge and cone shaped [98, 99], asymmetric wedge shaped [100] and rounded wedge shaped [101]. These relative simple shapes allow an analytical treatment of the asperity contact based on elasticity theory [33]. Furthermore it allows parametrization of a single asperity based on a few inputs which can be obtained from a surface topography measurement.

The assumption is that the asperity is in contact with a perfectly flat rigid counter surface. Hence only the asperity is deforming. The transition from elastic to plastic deformation is determined by a suitable yield criterion [93]. The extension to full plastic deformation goes back to [102] who defined the fully plastic regime based on the surface hardness. The intermediate or elastic plastic regime, was later added by work by [103–105]. The calibration or validation of these models is done by single asperity versus rigid flat indentation experiments as carried out by for instance [95, 106–108].

Fractal surfaces are interesting because they can be constructed to resemble real surface topographies. The mathematical theory of distribution functions subsequently lends itself for the development of contact models [109, 110]. The theory is particularly suited to compute the real area of contact up to the atomistic scale. This is of particular interest for problem involving adhesion [111]. Extensions have been made to incorporate the effect of plasticity [109] and asperity interaction [112]. Statistical models have low computational cost as they only require statistical analysis of the measured surfaces and subsequent solution of the closed form equations [113].

The most popular approach for deterministic (measured) roughness is based on the Boussinesq-Cerruti half-space assumption [33]. The work by Polonsky et al. [114] implements this approach for elastic rough contact using a multi-level multi-summation technique [115] and minimizes the energy [116] in the system by a conjugate gradient method solution strategy. Accelerated by a fast Fourier transform based solution technique (DC-FFT) developed by [117], this method is able to quickly and accurately solve elastic contact on real rough surfaces as shown by [90]. The method was further expanded to solve elastic-perfect plastic contact problems implementing an additional constraint by setting the maximum contact stress to the material hardness [118]. Full elastic-plastic behaviour was implemented using a return mapping algorithm [119] based on strain [120] or stress [121].

The finite element method can also be utilized, however, the needed mesh resolution for rough surfaces becomes prohibitive quite quickly [122]. Next to that, tuning of the contact stiffness

with a Hertzian contact solution and then applying the model to an unknown (rough) problem is questionable. Still, it a popular choice when studying smooth engineering surfaces [123] or fundamental questions on the true area of contact and the role of plasticity [122] because it is relatively easy to incorporate the effects of the elastic-plastic regime including strain hardening [124].

The contact mechanics of the turned surfaces in a metal-to-metal seal needed to be modelled in a numerically cost effective way. As this entails a surface topography with a clear lay or deterministic features (Figure 1.7) the choice was made for the boundary element method. This allows the computations to be performed directly on the as measured surface topography. Furthermore, it made linking the running-in model with the sealing model of [8] easy as it uses the same contact mechanics model.

2.8. Running-in

Running-in is defined as the transitional period between start-up of the (fresh) tribosystem and a steady state situation which can be defined by constant COF, wear, or other measures [125, 126]. This means that during running-in these measures can vary wildly according to eight patterns as identified by [127], Figure 2.3 is an example of one of those. In addition, the system can spiral out of control and move into a severe wear regime that will be discussed later. If the system is properly designed, however, the running-in period is where tribofilms get formed [128, 129] and contacting surfaces increase their conformance because of plastic deformation [130] and/or mild wear [131]. These processes allow contact stresses to go down and moves the system towards said steady state regime.

The aim in this thesis is to develop a running-in model of a metal-to-metal seal. This means a relatively short sliding length, although long enough to reach a steady state as discussed earlier (Section 2.4) according to the work of [36, 38]. This showed that both plastic deformation and wear needs to be taken into account in the boundary/mixed lubrication regime. As discussed in the previous section, there was a need for using measured roughness as input and a deterministic outcome as the output because of the turned surface topography which also includes form (Figure 1.7). A wide variety of models exist according to the recent review by Vakis et al. [132], which is an excellent overview of the state-of-art in multi-scale tribological modelling.

For running-in in the pure rolling regime, capturing plastic deformation is sufficient as shown with the deterministic running-in model by [95, 130, 133]. Modelling of running-in in a sliding contact is typically accomplished by combining a suitable contact model (Section 2.7) for the plastic deformation with an appropriate wear law to modify the surface topography while stepping forwards in time or space. The approaches in literature mainly differ in the type of contact model used. This can be asperity based [38, 130], half space based [121, 134–136] or finite element based [137–139]. When the elastic-plastic regime is considered in the model, the size of the wear particles can be determined from the subsurface stresses directly and the surface updated accordingly [135, 136, 140]. However, because of the computational complexity, the contact model is typically combined with a wear law to determine the amount of material removal which will be discussed in the following. The choice of combining a contact model with a wear law was made for this reason. In this thesis the contact width exceeds 1 mm

(Section 2.3) leading to rather large computational domains on which the contact mechanics (Section 2.7) needs to be solved every time step.

The most familiar and most used description of wear is by Archard [141] for adhesive wear of ductile materials. This predicts a linear relationship between the volume of wear and the applied normal load times sliding length times a wear rate. The theory is based on statistical reasoning at the asperity level, stating that generation of a wear particle is a rare event. Most asperities will interact elastically or plastically and go their merry way, only a few, represented by the wear factor K, will have an interaction leading to a wear particle. Whereas [142–145] applied a perhaps more intuitive concept of the amount of energy dissipated by the frictional contact to be proportional to the volume of (coating) material removed. Both concepts have been recently shown to be true by the fundamental numerical study by Aghababaei et al. [146, 147] using multimillion-atom simulations of colliding asperities. It turned out that there is a critical junction size at which debris is formed and once formed directly determines the size of the wear particle as predicted by [141]. It was shown that the generated wear volume is best modelled by the dissipated energy in the contact as predicted by [142–145].

The attractiveness of both wear models is the ease of implementation and the presence of one calibration factor. However, a large diversity of wear models exists. Meng et al. [148] presented an overview of wear models in the literature in 1995 and found 182 different descriptions of wear. Earlier, Lim et al. [149] came to a similar conclusion when construction their wear map for metals. Kato [150] constructed such a map for abrasive wear using the approach of ploughing, cutting and wedging developed earlier [151]. Later Kato [152] published an attempt at classification by defining three wear types: mechanical, chemical and thermal. This is complemented with the description of seven wear modes: abrasive, adhesive, flow, fatigue, corrosive, melt and diffusive wear. However, the conclusion was that most wear is a mix of the different wear modes and is therefore hard to classify uniquely.

The most recent attempt at coming up with a unifying classification is by Varenberg [153]. He suggests a classification system based on the three questions: Why?, How?, Where? This resulted in a 3D classification space defined by 5 types of relative motion (fretting, sliding, rolling, impact, flow), 4 mechanism of surface damage (physical interaction, chemical interaction, motion of defects, storage of defects) and 2 surface states (normal, pathological). The resulting scheme is simple, three inputs give a wear mechanism, and seems to fit already known wear types as defined by the earlier investigators. Using this classification scheme the wear (Figure 2.3) can be characterised as (severe) abrasive and/or adhesive. This motivated the initial choice in this work for an Archard type of wear law.

2.9. Boundary lubrication

As discussed in Section 2.3 the connection sees two sliding phases. For assembly, sliding is predominantly parallel to the line contact and hence no wedge effect is present to build pressure in the lubricant [41]. This means that the system runs in the boundary lubrication regime as discussed by the work presented earlier in Section 2.4 [36]. For micro-sliding the direction is perpendicular and the sliding velocities are even lower. This also gives the boundary lubrication regime.

The formation of tribofilms is important in contacts running in the boundary or mixed lubrication regime. The tribofilm separates the contacting surfaces and if it fails the system transitions from mild wear to severe wear [154]. The film is formed by adsorption on and / or chemical reaction at the surfaces of the contacting members [41, 155]. According to a recent review there is a wide range of additives employing one or a combination of these mechanisms to form the tribofilm [156]. Fatty acids, amides and functionalised polymers for instance are physically adsorbed. Stearic acid forms iron stearate with iron oxide by chemical adsorption. The simplest chemical reaction derived film is formed by sulphur which reacts with freshly exposed iron once the oxide layer is removed by wear [157]. The formation of tribofilms can be initiated and accelerated by shear or thermal influences or a combination thereof also known as mechanochemistry [158, 159]. He et al. [160] showed for instance that the physisorption yield of hydrocarbon precursors was dependent on contact stress which could be described by an Arrhenius-type equation. Still, boundary lubrication is poorly understood judging from the many review articles over the years [128, 129, 158, 161–165]. This is because of the complex and overlapping nature of the interaction mechanisms at the interface. There is, however, a glimpse of unification by the concept of stress-augmented thermal activation advocated by Spikes [158].

The interaction of phosphate chemistry with steel surfaces is of interest in this thesis because of the presence of phosphate based coatings (Section 2.6). A well-known example of stress-augmented thermal activation and phosphate chemistry is zinc dialkyldithiophosphate (ZDDP) which is widely used as anti-wear additive and spans an enormous body of work [166, 167]. The formation of ZDDP relies on contact between the sliding members and stops when the film thickness is significantly greater than the roughness i.e. the contact operates in the elastohydrodynamic lubrication (EHL) regime [168]. The molecule reacts with steel [169] and other substrate chemistries like DLC [170], silicon [171, 172] and other metals [173] to form a protective boundary film. The growth rate is governed by the applied (shear) stress [171], base oil polarity [174, 175], and bulk temperature which could be satisfactorily described by an Arrhenius growth model [171]. Recently the activation was definitively shown to be because of shear stress by Zhang et al. [173]. They explained that shear lowers the activation energy barrier by stretching or deforming a dialkyldithiophosphate group. However, the influence of the directionality of the stress is not fully understood (yet) and requires the study of well-defined model systems as recently discussed by Tysoe [161].

The running-in and wear models discussed earlier (Section 2.8) can be combined with a model of tribofilm formation to come to a tribochemical model describing the growth and removal of tribofilms which can predict when equilibrium between growth and removal or the steady state regime is reached [154, 176–179].

2.10. Exploratory testing and refining the research direction

Early on in the project it became clear that the phosphate conversion coating has a dominating role in the running-in of a metal-to-metal seal. This was investigated with pin-on-disc (Appendix II.5.2) and anvil-on-strip (Appendix II.5.3) tests in Figure 2.7. A COF of 1 indicates

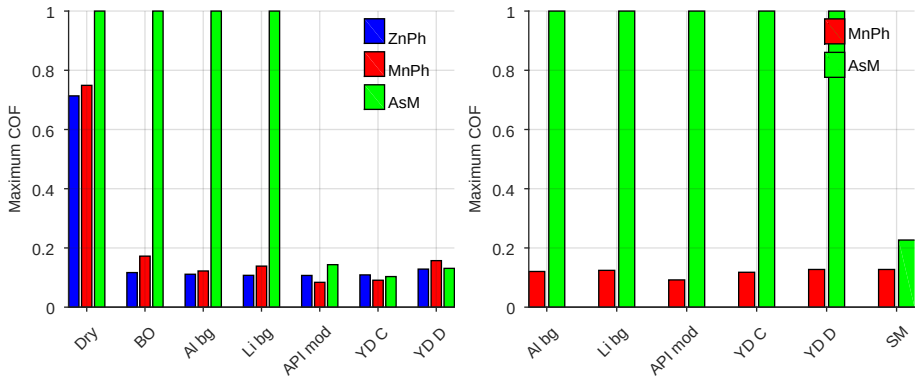

(a) Pin-on-disc (b) Anvil-on-strip

Figure 2.7.: Summarized results for pin-on-disc and anvil-on-strip tests. Figure 2.7a shows the results of the pin-on-disc tests for as machined (AsM), and zinc (ZnPh) and manganese (MnPh) phosphated discs. Note that a COF of 1 indicates galling which was determined with light microscopy after the test. Figure 2.7a shows the results of the striptests for as machined and manganese phosphated anvils. Reproduced from Paper B.

galling, which is the case for all tested commercial thread compounds in the bare-bare anvil-on-strip system. Coating one side with phosphate resolved this even when only using a base oil. As discussed, this was also observed by earlier investigators [43, 46, 47] and confirmed in face seal and tapered seal configurations (Appendix I.1) in Chapter 3 and Chapter 5. The mechanisms explaining this performance, however, were not described in literature. It was further unclear why galling happened despite the (metallic) additives in the thread compounds. At the same time regulatory changes demanded an investigation into the possibility of a environmentally friendly thread compound. This led to an adjustment of the objectives as listed in Chapter 1.

2.11. Conclusions

The initial configuration (turned vs. sand blasted) and subsequent evolution because of friction and wear of the tribosystem is important for successful sealing. The contact modelling needs to be able to take into account the lay of the surface topography of the contacting members. This means a deterministic contact model needs to be implemented to construct a running-in model. In all the previous works no link has been made between running-in and the subsequent seal ability performance of a metal-to-metal seal. Therefore, the goal of this thesis was to understand the mechanisms and influence of the separate components of the tribosystem on the seal ability of the metal-to-metal seal with the additional aim of removing heavy metals from thread compound formulations by developing an environmentally friendly thread compound.

Gaps in the literature and outcomes of exploratory testing:

- The mechanism initiating galling in casing connections is unknown.
- The friction mechanisms behind thread compounds at ambient and elevated temperature are unknown and need to be understood in order to formulate an environmentally friendly alternative.
- The mechanisms giving rise to the dominating influence of phosphate conversion coatings on the running-in of a tribological system are not described.
- No studies have been made on the running-in of a casing connection metal-to-metal seal and its effect on seal ability.

The goals will be achieved by answering the following research questions (RQ):

RQ1 What are the mechanisms of protection of the thread compound and what is the galling initiation mechanism in the metal-to-metal seal tribosystem?

RQ2 How does elevated temperature affect the thread compound protective mechanisms and how does this affect sealing ability?

RQ3 What are the mechanisms that give phosphate conversion coatings their protective properties?

RQ4 How does a casing metal-to-metal seal run in and how does it affect sealing ability?

3. The mechanism leading to galling initiation during make-up

The mechanism leading to galling initiation in (casing) connections and their metal-to-metal seals was poorly understood as discussed in Chapter 2. A study was initiated to gain understanding of the friction and wear mechanisms of thread compounds and the initiation of galling with emphasis on API modified. The understanding of the mechanism was needed to reduce the future occurrence of these failures in the field and based on that develop environmentally friendly thread compounds which will be discussed in Chapter 4. This chapter summarizes the work published in Paper B and E.

3.1. Introduction

As discussed in the introduction (Section 1.3.4) the standard thread compound in the oil and gas industry is API modified which contains amorphous graphite, lead, copper and zinc particles as additives, see Appendix II.4 for the formulation. It was further discussed using the literature (Section 2.4) that despite the high concentration of soft metallic particles the galling susceptibility is high. However, what the exact mechanisms of galling initiation are and why the thread compound is failing to provide protection was not known.

In order to understand the mechanisms a pin-on-disc, anvil-on-strip and Shell Sealing Mock-Up Rig (SSMUR) (Appendix I) program was set up to investigate the role of the components present in API modified. In addition, a hypothesis revolving around local flash temperatures leading to desorption [87, 88] of the lubricant was tested and discarded as possible galling initiation mechanism using the thermal model of [180]. See summarized results in Figure VI.3 for carbon and stainless steel. To study the mechanisms of API modified, a thread compound manufacturer kindly provided the full formulation thread compound, and variations on this formulation with single particle compounds to study their effect on friction and wear. An overview is presented in Appendix II.4.

The focus in this chapter is on the observations in SSMUR, an overview of these tests is presented in Table I.6 for the face seal set-up and Table I.7 for the interference seal set-up. In the table and the following, sets are indicated with F for face seal and I for interference seal. The G indicates dedicated galling tests, whereas RS is running-in followed by sealing. Hence FRS## is a face seal test which is first made-up and subsequently tested for sealing ability, the ## will be its unique set number. Supplemental materials for this chapter can be found in Appendix III which entails SEM Energy-dispersive X-ray spectroscopy (EDX) results of the various cross sections and additional light microscopy and interferometer results of the

pin-on-disc wear scars. Results of the anvil-on-strip test (Appendix II.5.3) can be found in Figure 2.7 and Paper B.

A follow-up investigation was carried out using reciprocating (500 µm stroke) pin-on-disc (Bruker UMT-3) tests with a 10 mm AISI52100 ball on AISI4130 flat configuration to fill in the blanks. The flat was polished or ground, see Figure II.1 for surface topography. On the ground disc the sliding was either parallel or perpendicular to the ground surface texture. The maximum Hertzian contact stress was 1 GPa, the sliding velocity 0.5 mm s^{-1} and the test was performed for 1000 cycles resulting in a cumulative sliding length of 1 m. See Appendix II.5.2 for details.

Real connections salvaged from the field were finally used to validate the scaled test findings.

3.2. Galling initiation mechanism

The results of [46] were reproduced in the SSMUR (Appendix I) with both specimen configurations using as machined (AsM) vs AsM surfaces and API modified as the lubricant. Make-up was performed with a contact intensity of 136 N mm^{-1} resulting in a maximum Hertzian contact stress of 0.25 GPa (Section I.3.1). The specimens were rotated stepwise with the following sequence 2.5-5-10-20-40-70.4-70.4 mm. In between steps the specimen was cleaned, surface replicas were taken, and fresh lubricant was applied for the next sliding step. The interference seal specimen was made-up in 2 steps of 58 mm. Important for later reference is that the sliding direction was parallel (face seal) or predominately parallel (interference seal) respectively to the turned roughness. The end result was severe galling in both cases after only 77.5-87 mm. As an example the end states for the face seal configuration with set FG01 is shown in Figure 3.1a and Figure 3.1b for pin and box respectively. Severe plastic deformation was observed on both sides as a consequence of galling. However, at some locations a tribofilm was found as shown in Figure 3.1b which coincided with the locations of lowest average contact stress. The Focused Ion Beam (FIB) cross section in Figure 3.1c and subsequent SEM/EDX analysis in Appendix III and Appendix V revealed that the film consists of the constituents of the thread compound. These could be individually observed, indicating minimal churning or shearing of the compound. This indicated that the film was formed by squeezing during the initial closing of the contact. The film is subsequently worn and squeezed out of the concentrated line contacts (Figure 1.8) during sliding. In addition, the plan parallel configuration at the peaks of the waviness does not allow replenishment of the contact, giving rise to the limited sliding length till failure. Therefore, the hypothesis was that the thread compound plays a minor role in galling prevention because of these observations and the ones with other thread compounds in Paper B.

Follow-up work with a clean mineral oil (Shell Ondina 933, O933) as lubricant was performed to find the initiation mechanism. Care was taken to stop the test at onset of galling, which happened after 17.5 mm. The difference in sliding length till failure with API modified was thus 60 mm. The result is shown in Figure 3.2 for set FG03 with a wide view of the scratch in Figure 3.2a and the initiation point in Figure 3.2b. Which reveals that galling initiates at the peaks of the waviness. This provided additional evidence for the hypotheses stated above. The missing link was why this initiated after 17.5 mm.

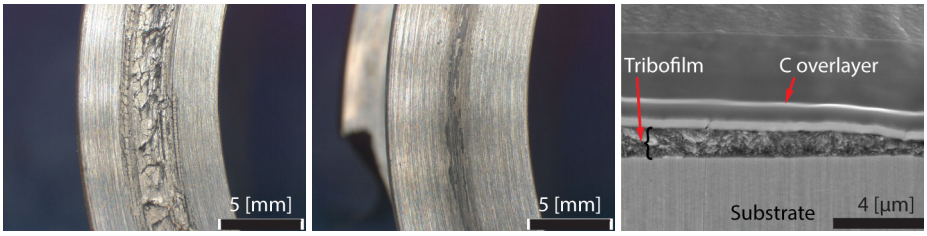

(a) FG01 pin detail (b) FG01 box detail (c) FIB cross section box film

Figure 3.1.: LM and SEM images of the contact area of a face seal specimen that failed during make-up sliding with API modified because of galling. Figure 3.1a shows a macroscopic view of the galled area. Figure 3.1b shows a tribofilm on another part of the same surface. FIB cross sectioning results imaged by Secondary Electron (SE) at 20 kV in Figure 3.1c on the tribofilm shown from the top in Figure 3.1b, here taken from the pin of FRS06. The EDX mapping results can be found in Figure III.6 and Table III.1.

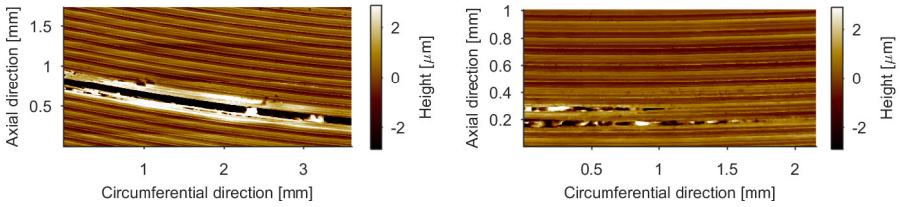

(a) (b)

Figure 3.2.: Interferometer measurement of the surface damage on the box of set FG03. Figure 3.2a shows an overview of the scratch and Figure 3.2b a detail of the initiation location. Initiations happens at the peaks of the waviness.

The reason that the mineral oil could still provide some sliding length before failure was because of the presence of an (always present) oxide layer on the steel surface. Fretting tests (stroke 50 µm) were used as an analogy for the concentrated contact at the peak of the waviness. Discs were prepared with different oxide thickness to confirm this hypothesis. Initiation was delayed with O933 on discs with a thicker oxide layer as shown in Figure 3.3. API modified, when relying only on the additives present in the contact at initial contact could only delay the failure by a limited amount. In agreement with the observations in SSMUR and anvil-on-strip in Paper B.

The influence of sliding orientation relative to the lay of the surface topography, the role of the metallic particles and the mechanisms of galling initiation was subsequently investigated. A summary of the results for sliding orientation and metallic particles is given in Figure 3.4 in terms of COF vs cumulative sliding length. The results are split according to surface topography and orientation, Figure 3.4a shows polished, Figure 3.4b perpendicular to ground roughness and Figure 3.4c parallel, see Figure II.1 in Appendix II for surface topography. It became clear that the orientation of the roughness plays an important role in this tribosystem.

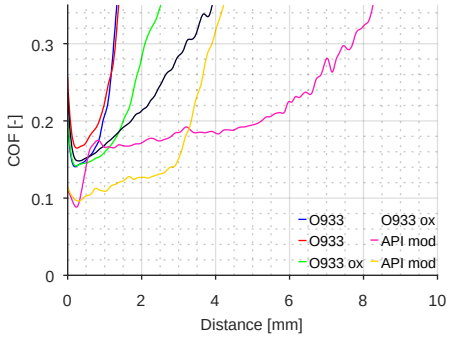

Figure 3.3.: Fretting experiments with 50 µm stroke at 0.05 mm s^{-1} to investigate the effect of oxide thickness on the initiation of galling with Ondina 933 and API modified. Initiation was delayed by increasing the oxide thickness using tempering at 80 °C.

The copper and lead single particle systems both resulted in galling parallel to the lay of the ground roughness with the same result on the polished disc. The exception was zinc which performed well in all cases. It was found that the copper and lead particles were not entering the contact. This was related to the limited affinity of these materials with the substrate [181] and by a particle entrapment model inspired by the work of [182, 183] in Paper E.

The observations in the scaled tests were confirmed with a real connection, in paper F, that was salvaged from the field after >10 years of operation. The box was phosphated in this case as per standard practise to avoid corrosion and galling. Only a limited amount of particles were found in the metal-to-metal seal contact as shown in Figure 3.5. With SEM/EDX only lead and copper was found on the contacting surfaces, see Figure III.8 in Appendix III. This is in line with the observations presented above. In addition, the areas before and after the contact contained high concentrations of particles.

Together this gives the following galling initiation mechanism in AsM-AsM contacts when using typical thread compounds (Paper B) and API modified in particular (Paper E). Thread compound is applied and upon initial contact compressed into a protective film. The film is worn and squeezed from the contact during sliding and not replenished because of the plan parallel gap. Once the film is removed, the oxide layer provides surface separation until it is worn out which subsequently exposes fresh steel leading to galling initiation at the peaks of the waviness. The atmosphere under the thread compound is oxygen starved such that no oxide layer regeneration can occur. In addition, the thread compounds do not have surface active additives. Cold welding and the subsequent material transfer results then in galling. In Chapter 4 and Paper F a thread compound will be designed which mitigates these mechanisms.

The thread compound and its particles thus play a relatively minor role in the running-in of the metal-to-metal seal contact and therefore sealing ability of the metal-to-metal seal. As shown with the real connection, the phosphate plays a crucial role here which will be explained in Chapter 5 and Paper A-D. However, large amounts of particles were observed in front of the contact. It thus seems that the contact acts as a barrier against which the thread compound

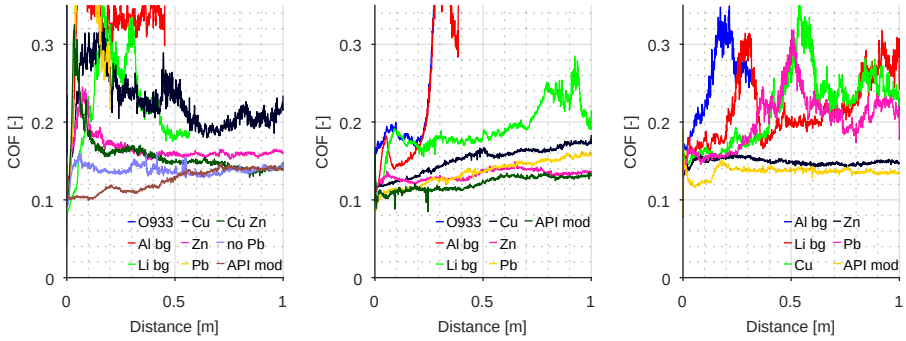

(a) Polished (b) Ground perpendicular (c) Ground parallel

Figure 3.4.: Comparison of the COF versus cumulative sliding length for all tested base greases. The y-axis is truncated at COF = 0.35 for clarity of the presentation. Figure 3.4a shows the evolution of COF versus cumulative sliding length on a polished disc. Figure 3.4b shows a comparison of the COF when sliding perpendicular to the roughness versus cumulative sliding length for all tested (base) greases. Figure 3.4c shows a comparison of the COF when sliding parallel to the roughness versus cumulative sliding length for all tested (base) greases.

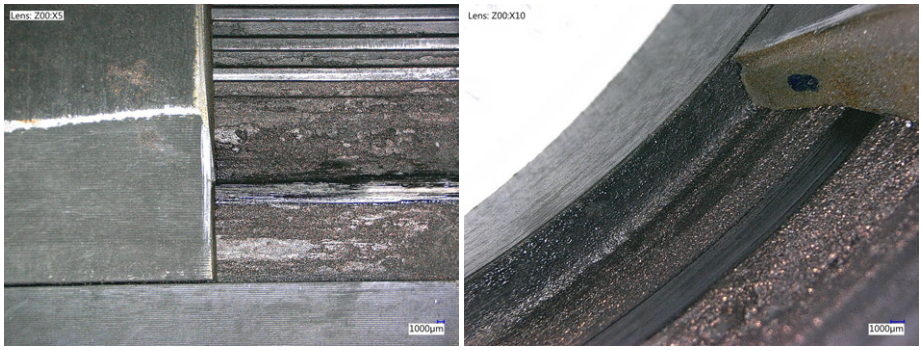

(a) (b)

Figure 3.5.: Macroscopic images of the metal-to-metal seal area of a section cut from a salvaged VAM®21 connection. The contact was opened gently to show the distribution of the thread compound (here API modified). The contact area has a much lower concentration of particles compared to the surrounding non-contact area. The accompanying SEM/EDX results can be found in Figure III.8.

can form a seal. Similar to the thread sealing based on particles bridging the gaps that was employed in the past (Section 2.2).

The mechanisms above also explains why stainless steel grades are so problematic with the lubricants used in the oil and gas industry. There is no additional barrier present in the form of an oxide layer and they will thus cold weld readily. In addition, it is well known that shot blasting alleviates these problems [Shell connection QA/QC team, pers. comm.] which can now be explained by the locking mechanism.

3.3. Conclusions

It was shown that a soft metallic tribofilm is formed by the initial contact which squeezes the particles into a film. This film is subsequently squeezed out of and rubbed off the concentrated contact on the waviness. The tribosystem then wears off the oxide layer until fresh steel is exposed initiating cold welding, material transfer and ultimately galling.

- Desorption of the lubricant because of exceeding local flash temperatures is not the initiation mechanism of galling.
- Galling was induced at a relatively moderate maximum Hertzian contact stress of 250 MPa. It was shown this happens because of interacting mechanisms which can be generalized to other thread compounds:
    1. Squeeze out and wear of at initial contact formed soft (metallic) tribofilms.
    2. Lack of strong adsorption of the thread compound or its tribofilm to the steel.
    3. Particle size.
    4. Waviness/roughness orientation with respect to the dominating sliding direction.
    5. Affinity of the particle towards the substrate.
    6. Creation of an inert atmosphere by the thread compound combined with the continuous contact such that no oxide layer recovery can happen.
    7. Wearing out the oxide layer which subsequently exposes bare steel initiating galling.
- As a consequence API modified or thread compounds in general only add about 60 mm of additional sliding length till failure compared to a plain mineral oil.
- Sealing ability might for a large part be attributed to the particles forming a seal in front of the metal-to-metal seal contact.

4. High temperature degradation mechanism of thread compound

This chapter summarizes the work on high temperature (environmentally acceptable) thread compound testing. The performance of commercially available environmentally acceptable thread compounds is investigated with TGA/DSC, high temperature rheometry and high temperature pin-on-disc tests. The compounds are assessed on their high temperature stability, high temperature consistency, high temperature lubricity, and the resulting wear. The results indicated that without exception the commercially available thread compounds fail by adhesive and/or abrasive wear around 150 degrees Celsius because of thermal degradation. To remedy this a prototype thread compound was developed which exhibits strong film forming. The conclusion is that a successful high temperature resistant environmentally acceptable thread compound can be developed if it is able to form a tribofilm which protects the surface after the lubricant lost its consistency. In addition it allows galling free make-up on non-coated steels solving the issues identified in Chapter 3. The work in this chapter is reproduced from a patent application, a report for the Staatstoezicht op de Mijnen (SodM) and Paper F.

4.1. Introduction

As discussed (Section 2.4), sealing performance of contacting elements has been shown to be determined by the surface texture and changes thereof [48, 59, 62], the shape distortion [55], the interaction with the lubricant [50] and degradation thereof [48]. The initial configuration and subsequent evolution because of friction and wear of the tribosystem is thus important for successful sealing. Moreover the wear should be minimum to stay as close as possible to the intended design contact stresses of the connection manufacturer. A metal-to-metal seal can for instance be successfully made-up but fail during load cycling because of thermal degradation of the lubricant [48] at the temperatures imposed during testing (Section 2.3). However, the current thread compound testing methodologies [4] will not reveal this behaviour as discussed in Section 2.4.

Therefore, screening of environmentally acceptable thread compounds was performed at elevated temperatures and a methodology developed that can be performed in a pin-on-disc apparatus. The methodology revolves around investigating the thermal stability of the thread compound and relating it to the tribological behaviour and ultimately sealing ability. In order to do so a combination of TGA/DSC, rheology and tribometer characterisation was performed at elevated temperatures up to 250 °C. The main property to test for was sustained lubricity at elevated temperatures to minimize damage to the sealing surface during the micro-sliding

phase over the lifetime of the connection. These tests continued the work on room temperature behaviour of thread compounds in Chapter 3 and Paper B and F.

The compounds listed in Appendix IV were investigated in Paper F with the following techniques. Thermal stability was assessed with TGA/DSC. This was followed up by rheometer tests at increasing temperature to investigate the changes in consistency as a consequence of the thermal degradation. The rheometer tests were performed by imposing a shear stress sweep to also investigate yielding behaviour. The outcomes of TGA/DSC and rheometer were subsequently used to explain the high temperature pin-on-disc tests. The pin-on-disc tests are designed to investigate make-up sliding and micro-sliding in a single test and the same as Chapter 3 except for the addition of elevated temperatures. The used drive is open to atmosphere, so components in the grease can evaporate or react with oxygen. This is not or to a lesser extend the case in a real connection as observed in Figure 3.5. Therefore, the test is accelerating degradation and can be seen as a worst case scenario for the thread compound. The tests are summarized in Table 4.1, more detail is given in Appendix II.

Table 4.1.: Summary and overview of the used test protocol for the various screening methods.

Test type	Measurement geometry	Protocol	Atmosphere
TGA/DSC	100 µL Al open cup, 60 µL Au closed cup	Dynamic 30-250 °C at 10 °C min^{-1}, iso hold 30 min at 250 °C, dynamic 250-30 °C at -10 °C min^{-1}	open cup 80 mL min^{-1} air or N_2
Rheometer 1	coaxial cylinder (PZ38) 50 mL	Perform shear stress sweep 1.5-800 Pa at 20-50-100-150-200 °C with 30 min temperature hold per step	Closed pressure vessel N_2
Rheometer 2	coaxial cylinder (Z10)	Perform shear rate sweep 1.0-100 s^{-1} at 20-40-70-100-140-180-200 °C with 30 min temperature hold per step, hold for 3 hours, perform another sweep at 180 °C	Open cup air
Pin-on-disc	10 mm AISI52100 ball on AISI4130 disc	Perform 250 reciprocating cycles at 1 GPa with stroke 500 µm at 30-70-100-150-200-250 °C	Half-open drive air

Based on the correlations between sealing and surface quality and the role of the thread compound [48, 59, 62], the results of the tests are assessed according to the following criteria:

1. High temperature stability (e.g. dropping point).
2. High temperature consistency (e.g. shear/temperature thinning behaviour).
3. High temperature lubricity (COF).
4. Surface damage (wear).

The assessment was done by combining observations on the change in consistency, appearance and surface texture after the tests. In addition, the resulting wear scars were investigated with a digital light microscope and a scanning electron microscope (Section II.8.1).

The results indeed showed premature failure by adhesive and/or abrasive wear for all environmentally acceptable thread compounds because of thermal degradation. However, this was not always supported by the TGA/DSC or rheology data and only revealed in the pin-on-disc tests. To remedy the issues observed in commercial environmentally acceptable thread compounds a hypothesis was formulated. This stated that improved film forming can mitigate the issues with loss of lubricity at elevated temperatures. This was confirmed by a prototype thread compound developed with the methodology described in Paper F.

4.2. High temperature degradation mechanism

The results of the comparative screening work performed in Paper F are shown in Figure 4.1. The TGA/DSC tests indicated large differences in thermal behaviour between the tested compounds. Where YD B showed large weight losses and permanent phase transitions in the TGA (Figure 4.1a) and DSC (Figure 4.1b) test respectively. The phase transitions were mainly attributed to evaporation of the base oil as the onset of weight loss and the endothermic peaks coincided. The two other environmentally friendly compounds were more stable, with relatively low weight losses. However, endothermic peaks were observed which became more pronounced when iron oxide (hematite, designated with H in the legend) was added indicating oxidation.

In the rheology tests (Figure 4.1c and Figure 4.1d) the evaporation and oxidation translated into an increase of consistency for YD B and C turning both in a (dry) clay like substance (Figure 4.2). For YD B this was observed at 150 °C and for YD C after the test. No extreme changes in consistency were found for API mod and YD A.

The high temperature tribological experiments, however, showed that the environmentally acceptable thread compounds (YD A-C) all showed degradation of their lubrication performance on or shortly after the 150 °C step. This can be observed in Figure 4.1e from the increase in mean COF, its standard deviation and the maximum COF. The reason is different for each compound and to be discussed in a moment, however, it resulted for all in failure of the tribosystem leading to scratched surfaces as shown in Figure 4.2. Which is not a desirable situation for a metal-to-metal seal. YD A shows the earliest indications of imminent failure at 100 °C followed by YD C at 150 °C and then YD B at 250 °C. Hence good performance in TGA/DSC and rheometer does not ensure good tribological performance.

The reason for the tribological failures can be ascribed to either evaporation leading to a completely dried out compound for YD B as shown in Figure 4.2b. When the compound dries up, lubricity is lost and the contact cannot be replenished. In fact it becomes easier to remove compound from the contact. This also means that the mineral particles (e.g. TiO_2) become abrasive and start to wear out any tribofilm (as in Figure 4.2e) that was formed which finally leads to damage to the surface as shown in Figure 4.2. The initial abrasive wear can subsequently spiral further out of control by adhesive wear which was observed for YD C in Figure 4.2f.

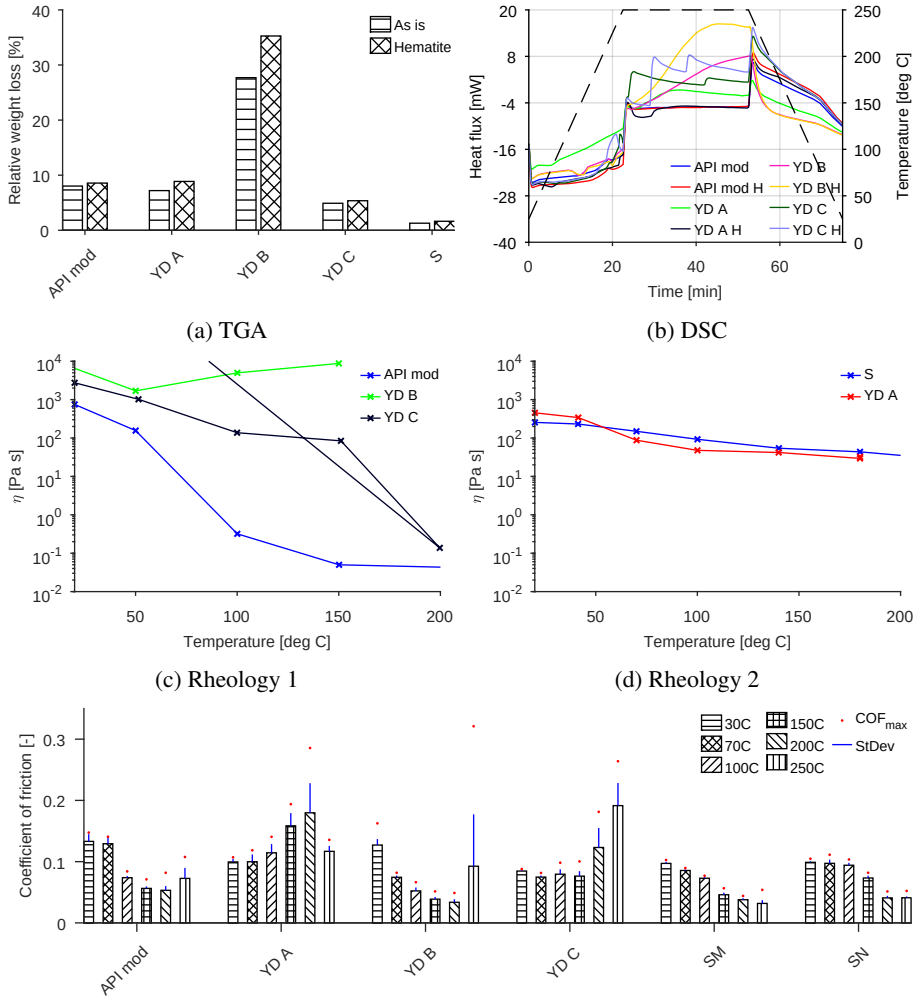

(a) TGA

(b) DSC

(c) Rheology 1

(d) Rheology 2

(e) High temperature pin-on-disc

Figure 4.1.: Overview summarizing the test results obtained with the protocols in Table 4.1, for details see paper G. The TGA results for open cup in air is presented in Figure 4.1a. The weight is normalized with the starting weight for each experiment. The corresponding DSC results are shown in Figure 4.1b. The H indicates the addition of hematite. The rheology results are summarized by showing viscosity versus temperature at $\tau = 50$ Pa in Figure 4.1c and $\dot{\gamma} = 1\ \mathrm{s}^{-1}$ in Figure 4.1d. The high temperature pin on disc results are shown in Figure 4.1e, experiments are summarized by mean COF (bars), standard deviation (vertical lines) and maximum COF (red dots).

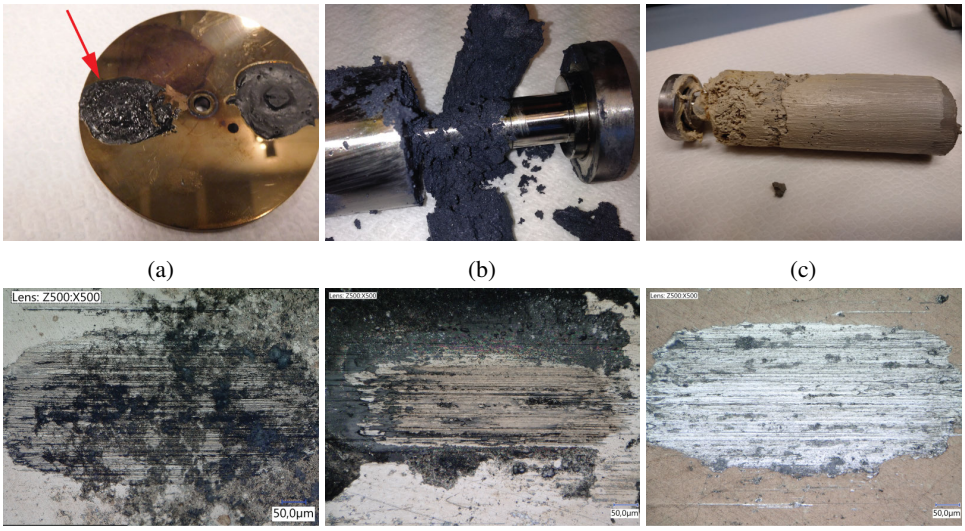

(a) (b) (c)

(d) YD A (e) YD B (f) YD C

Figure 4.2.: Observations after the tests which are representative for TGA/DSC, rheology and pin-on-disc. Figure 4.2a shows the relative little change in consistency of YD A after the pin-on-disc test. Figure 4.2b shows the completely dried out YD B and Figure 4.2c the observed thickening of YD C after rheology testing. Corresponding wear scars after the pin-on-disc tests are shown on the second row. All three environmentally thread compounds failed because of adhesive and/or abrasive wear as evidenced by the wear scars in Figure 4.2d, Figure 4.2e and Figure 4.2f.

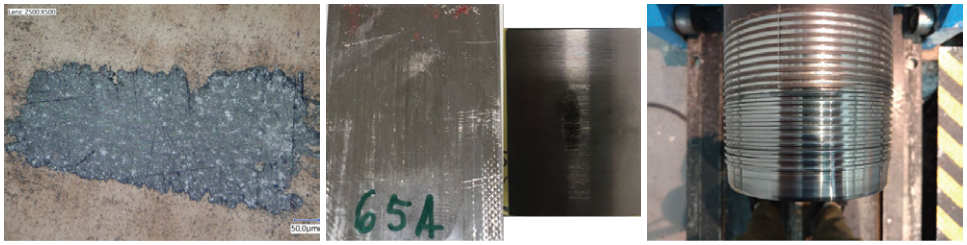

(a) SM and SN (b) SM (c) SN

Figure 4.3.: Prototype compound combining SA, SB and SG. Figure 4.3a shows pin-on-disc results after 250 reciprocating cycles per temperature step for a total of 1500 at 1 GPa with a 10 mm AISI52100 ball on a AISI4130 flat. Strong film forming was observed providing successful surface protection. The performance in the strip tests was equally good with no galling observed in an AsM-AsM P110 tribosytem in Figure 4.3b. Finally the performance was confirmed by assembly tests of a 5.5" 23# L8013Cr VAM®TOP HT connection which showed no galling after multiple make-up and break-outs as shown in Figure 4.3c.

4.3. Prototype thread compound

To validate the above understanding of the mechanisms leading to failure and the high temperature pin-on-disc protocol a lubricant was designed that mitigates the observed failure modes. The rationale revolved around generating a thick tribofilm before the high temperature exposure (in the make-up phase) and using relatively soft particle additives which fall, ideally, in the green category. Once the film is formed the system is protected and the absence of abrasive particles will ensure low wear even when the thread compound disintegrates.

This was achieved by combining a thermally stable base oil designated as "S" in Figure 4.1 with a clay thickener and testing multiple iterations of single particle prototypes with the pin-on-disc protocol. The best performing particles were subsequently combined into multi particle prototype compounds, see for compositional details Appendix IV. The best performer in pin-on-disc consisted of calcium phosphate, graphite and methyl metacrylate and is shown in Figure 4.3a. Strong film (>4 µm thick) forming was observed. This compound was designated "SM and "SN" in Figure 4.1e, where "SN" has the same composition but is produced in a grease plant. Subsequent tests in the anvil-on-strip confirmed its performance with no galling observed in an AsM-AsM contact in Figure 4.3b. Hence the film forming mitigated the failure mechanism found in Chapter 3.

Confirmation was obtained in a multiple assembly-disassembly test of a VAM TOP casing connection manufactured from a high chromium steel grade (13wt% Cr) as shown in Figure 4.3c. Finally, using SSMUR interference seal tests (Appendix I.3.2 and Table I.7) it was shown with a series of five tests that gas sealing ability was maintained to a Hertzian contact stress of 325 MPa on average over the 5 tests. Which is very low compared to the results of [49, 50].

4.4. Conclusion

A simple high temperature tribological test protocol was developed and validated using cross testing with TGA/DSC, high temperature rheometry, anvil-on-strip, SSMUR and full scale make-up/break-out tests. The protocol was developed by using it to investigate the high temperature failure mechanisms of commercially available thread compounds. The protocol and mechanisms were subsequently successfully validated by designing a prototype thread compound. The results indicate the following:

- Relying on just TGA/DSC or rheometry or even a combination thereof is not sufficient for the development of thread compounds for high temperature (>150 °C) applications. That also means that current methods of testing are not sufficient (Section 2.4).
- The commercial environmentally acceptable thread compounds fail at elevated temperatures because of evaporation of the base oil combined with oxidation of the compound. This increases consistency, which leads to starved lubrication conditions. The remaining tribofilm is worn till the system fails because of adhesive wear. This is sometimes further enhanced by abrasive action coming from the inorganic particle additives.
- The found mechanisms were validated by solving these issues with a prototype thread compound developed using the methodology described. This was achieved by increasing the film forming tendency of the lubricant before the base oil is evaporated. This thicker film is then able to protect the surface long after the lubricant lost its consistency.
- The performance of the thread compound was successfully validated using anvil-on-strip tests on P110 material and full scale make-up and break-out test on L8013Cr material.

This page has been intentionally left blank.

5. The mechanisms of protection of phosphate conversion coatings

The role of phosphate conversion coatings turned out to be a dominating factor in the metal-to-metal seal tribosystem. The reason for this is the formation of a tribofilm on the uncoated side of the tribosystem and a glaze layer on the coated side of the tribosystem. Together it results in a robust tribosystem allowing freedom in the choice of thread compound. Therefore, taking the presence of a phosphate conversion coating into account in the design of thread compounds could make the transition to environmental friendly compounds easier. The tribofilm and glaze layer formation mechanisms and the resulting wear mechanism are discussed in this chapter. The work in this chapter is reproduced from Paper A-D.

5.1. Introduction

The role of phosphate conversion coatings in casing connections was investigated using pin-on-disc, anvil-on-strip and the SSMUR (Paper B). This was complemented with observations in real connections. Figure 5.1 summarizes the most important observations from the experimental program with the face seal set-up (Section I.3.1) summarized in Table I.6 and the connection analysed in Chapter 3. The following observations were made:

1. Formation of a transfer film on the uncoated member, for both Zinc Phosphate (ZP) in Figure 5.1b and Manganes Phosphate (MP) in Figure 5.1d.

2. Formation of a smooth and shiny glaze layer on the phosphated member, Figure 5.1a and Figure 5.1c.

These mechanisms provided a lot of robustness to the tribosystem as shown in Figure 5.2 for pin-on-disc and anvil-on-strip tests without and with phosphate coating. In the phosphated case any lubricant (even base oils) can be used to obtain a system that can run for considerable time till failure. This can also be concluded upon comparison of the results in Chapter 3 with Figure 5.1 and the successful sealing ability tests with base oil (O933) in Table I.6. For more details see Paper B.

In order to understand the mechanisms behind the tribofilm formation and the glaze layer formation a pin-on-disc program was set up. The results will be summarized in the following.

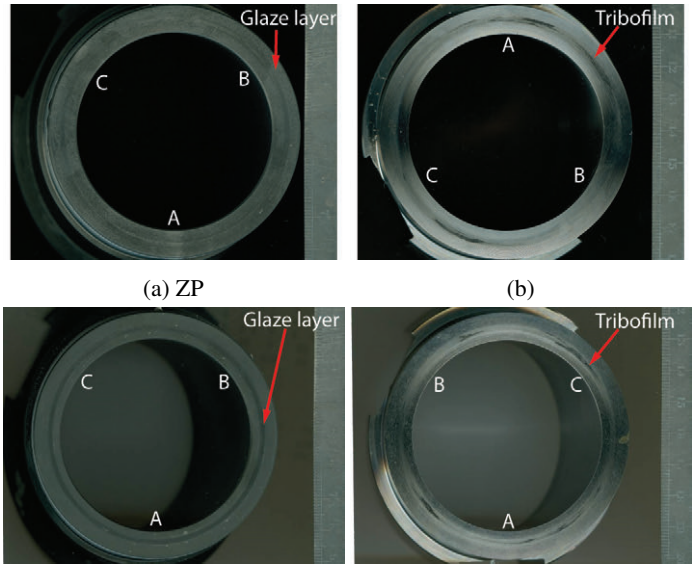

(a) ZP (b)

(c) MP (d)

Figure 5.1.: Surface after make-up sliding with phosphate specimens FRS06 and FRS07 lubricated by API modified. Letters indicate orientation of specimen to match with the counter surface. Figure 5.1a and Figure 5.1b show the result of a zinc phosphate box against an as machined pin (FRS07). Figure 5.1c and Figure 5.1d show the results of a manganese box against an as machined pin (FRS06). Sliding conditions were the same: 1 full revolution at 24 mm/s. No galling is observed. Image reproduced from Paper B.

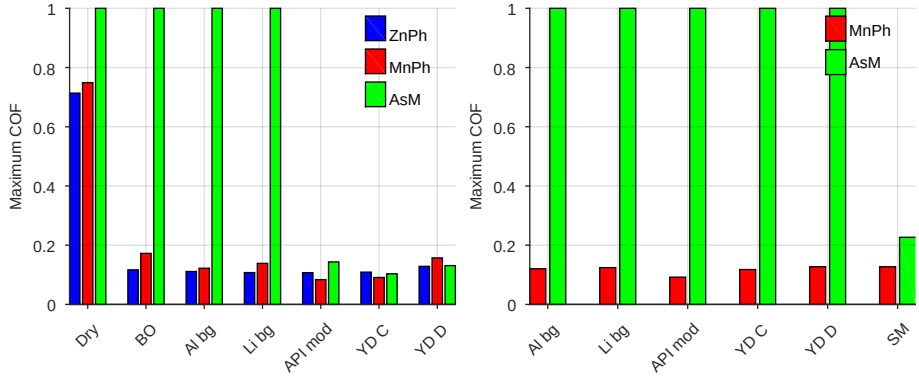

(a) Pin-on-disc (b) Anvil-on-strip

Figure 5.2.: Summarized results for pin-on-disc and strip tests. Figure 5.2a shows the results of the pin-on-disc tests for as machined (AsM), and (ZP) and (MP) discs. Note that a COF of 1 indicates galling. Figure 5.2b shows the results of the striptests for as machined and manganese phosphated anvils. Figure 5.2b is adapted from Paper B to incorporate comparison with prototype compound SM.

5.2. Tribofilm formation

The tribofilm was investigated to understand the mechanisms behind its formation in paper C. The working hypothesis was that the tribofilm growth is governed by a chemical reaction and influenced by base oil polarity. To understand the mechanisms behind its growth the thickness of the tribofilm was monitored as function of the normal load, sliding length, velocity, bulk temperature, substrate chemistry and base oil polarity. Figure 5.3 shows the results for 10 mm AISI52100 balls as function of sliding length and base oil polarity.

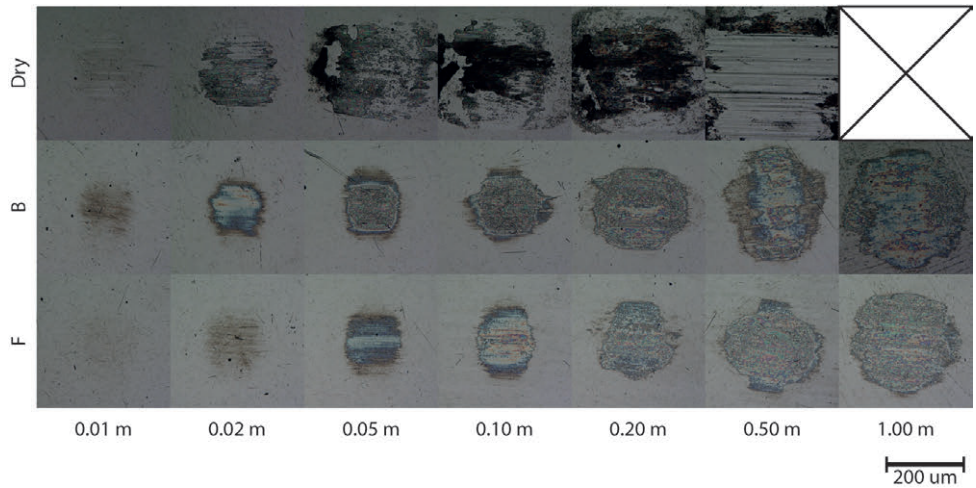

Figure 5.3.: Excerpt of the overview of tribofilm formation as function of cumulative sliding length and base oil at a sliding velocity of 0.5 mm s^{-1} and temperature of 22 °C. Reciprocating sliding direction is horizontal. Here the base oils with the lowest and the highest tribofilm growth rate are shown versus dry sliding. For the full overview see Paper C.

With XRD, XPS and FIB/SEM small crystallites of hureaulite were shown to be transfered to the ball surface yielding an amorphous but durable tribofilm as shown in Paper C. No indications of chemical reactions were found. This was further elaborated with experiments on different substrate chemistries on which the tribofilm also readily grew and at high temperatures (up to 200 °C) which did not accelerate the growth. It was therefore concluded that the tribofilm adheres to the ball by a physisorption mechanism. In addition, no correlations were found between base oil polarity and tribofilm growth rate. Instead the tribofilm formation was fully explained by a stress activation mechanism and shown to be driven by shear stress as shown in Figure 5.4.

Using the slope of Figure 5.4 following the work of [173] an activation volume could be found using the stress-augmented thermal activation paradigm by [158], according to

$$Rate = A \exp\left(\frac{-(E - N\tau\Delta v)}{RT}\right). \tag{5.1}$$

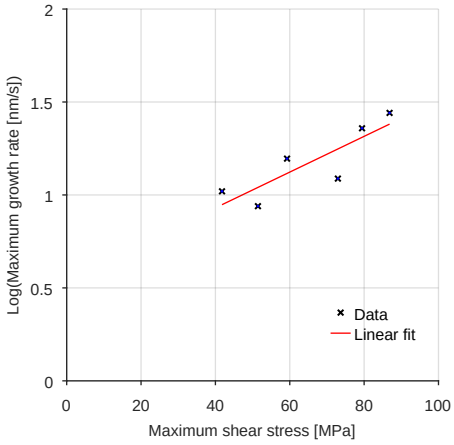

Figure 5.4.: Correlation of the logarithm of the maximum growth rate with maximum shear stress. The slope was used to fit an activation volume in equation (5.1). Taken from Paper C.

Where A is the pre-constant, E the molar thermal activation energy, N Avogadro's constant, τ the shear stress, Δv the activation volume, R the gas constant, and T the temperature. The activation volume was calculated to be 0.052 nm^3. If a typical bond length of 0.2 nm is considered, the molecular area over which the shear stress acts is 0.26 nm^2. The most plausible functional groups in the hureaulite molecule are the phosphate group, PO_4^{3-}, and the hydroxide group, OH^-. Using the bond lengths reported in [76] and the Van der Waals radii of the atoms these groups yield a molecular area of roughly 0.29 nm^2 and 0.23 nm^2 respectively. For adsorption to happen particles need to be generated first. A crystal has a tendency to split along crystallographic structural planes because of relative weakness in the crystal which is known as cleavage. In other words, a preferential fracture plane. For hureaulite this is perpendicular to the a-axis [76] which will expose phosphate groups. Hence the most plausible explanation for the adsorption of hurealite was deformation or stretching of (a bond in) the exposed phosphate group. This will make the non-polar phosphate group slightly more polar leading to adsorption on the ball surface.

5.3. Glaze layer formation

Glaze layer formation was investigated with SEM, Atomic Force Microscopy (AFM), nano-indentation and scratch tests in paper A and D. In paper C glaze layer formation was investigated at the macroscopic level and linked to sealing ability in SSMUR face seal tests. An overview of the initial phosphate coatings and the generated glaze layers after dry uni-directional sliding are shown for zinc phosphate in Figure 5.5 and manganese phosphate in Figure 5.6 using backscatter electron imaging (BSE). The results on an untouched section of the phosphated discs are shown in Figure 5.5a and Figure 5.6a (Note the difference in magnification when comparing). The crystal surface of zinc phosphate (Figure 5.5a) shows a rough texture coming from the needle shape which is typical for hopeite crystals [75]. The needle can grow well

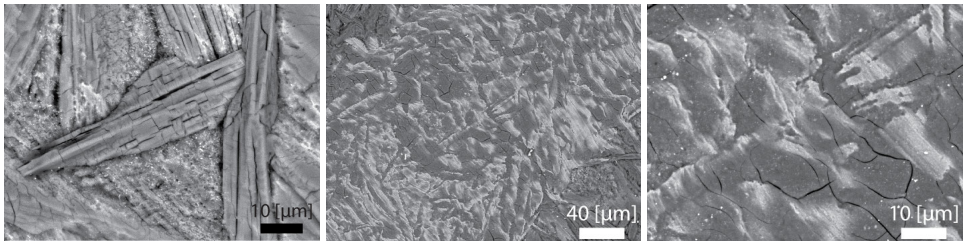

(a) (b) (c)

Figure 5.5.: SEM BSE (20 kV) images of the initial crystalline zinc phosphate coating in Figure 5.5a and the resulting glaze layer at two levels of magnification in Figure 5.5b and Figure 5.5c respectively. Reproduced from Paper D.

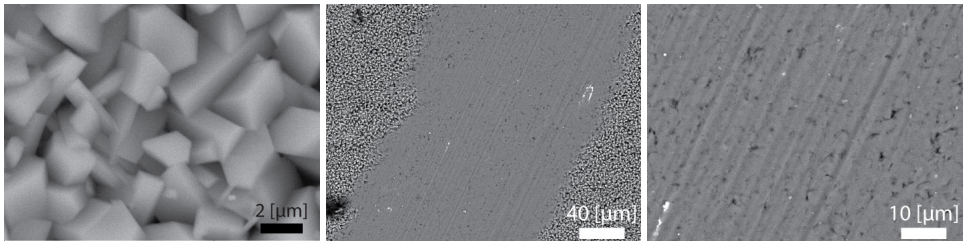

(a) (b) (c)

Figure 5.6.: SEM BSE (20 kV) images of the initial crystalline manganese phosphate coating in Figure 5.6a and the resulting glaze layer at two levels of magnification in Figure 5.6b and Figure 5.6c respectively. Reproduced from Paper D.

over 50 µm in length with a width of 10 µm. The crystal surface of manganese phosphate (Figure 5.6a) is smooth, its shape is jagged typical for hureaulite crystals [76]. An individual crystallite is approximately 2 µm in size in all directions.

Upon comparison with the untouched phosphate (Figure 5.5a, Figure 5.6a) the formation of a glaze layer can be observed in Figure 5.5b and Figure 5.6b. The glaze layer forms because of the crushing and compaction of the crystals in the sliding contact as observed in earlier investigations [184] and Paper A and B.

Zooming in on the center of the glaze layers in Figure 5.5c and Figure 5.6c it is clear that the zinc phosphate glaze layer has a different character compared to manganese phosphate. This is attributed to the difference in precursor material (hopeite vs hureaulite crystals). Flattened needles can be observed in zinc phosphate with the valleys next to them filled with crushed debris. Manganese phosphate shows a much smoother surface mainly because it starts with much smaller crystals which are all crushed and compacted into a smooth layer.

It was shown that after dry sliding because of crushing and compaction of the phosphate crystals a hard ($>$3 GPa) glaze layer (Figure 5.7b) is formed with a low shear strength (Paper A). The hardness, however, turned out to be much lower when the glaze layer is formed under

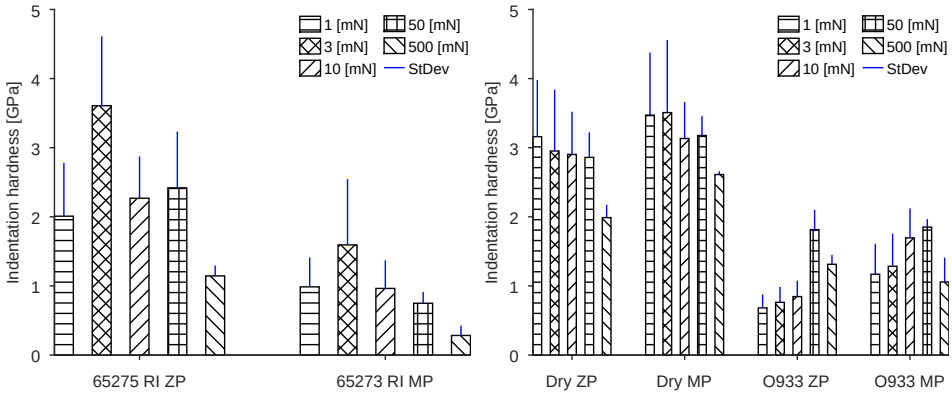

(a) Ring-on-ring (b) Pin-on-disc

Figure 5.7.: Nano-indentation results using a Berkovich indenter at increasing normal loads. Figure 5.7b shows the results for the glaze layer hardness after dry sliding (Paper A) and lubricated sliding with Ondina 933 (Paper D). Figure 5.7a shows the results after lubricated sliding in the ring-on-ring tests from Paper B.

lubricated conditions (Figure 5.7b). This was discovered first in SSMUR (Figure 5.7a) and reproduced in pin-on-disc (Figure 5.7b) (Paper D).

The mechanism behind the difference in glaze layer hardness was explained to be because of the formation of glaze layers that consist of larger phosphate particles Figure 5.8 in Paper D. The particle size was shown to be governed by the shear stress in the system. Figure 5.8 shows the phase images of the zinc phosphate glaze layer formed in dry (Figure 5.8a) and lubricated (Figure 5.8b) sliding conditions. Judging by the AFM results the glaze layer consists of tightly packed nano-particles. A clear difference in size can be observed between the dry and lubricated sliding conditions. The dry condition shows much smaller particles compared to lubricated conditions. The same observations were made for the manganese phosphate glaze layers shown in Figure 5.8. Also here a distinct difference in particle size could be observed. Again, the dry condition in Figure 5.8c shows a smaller particle size than the lubricated condition in Figure 5.8d. This was confirmed to be the same on the SSMUR specimens.

Dry sliding produced the smallest particles. This is predominantly because of the stronger adhesion of the particles to the AISI52100 ball (Paper C) and as a consequence a higher amount frictional energy available in the contact to break up the crystals. In short, the grinding was more effective compared to the lubricated condition. The observations were further explained using considerations from inter particle interactions. It was shown (Paper D) that the tensile strength is considerably lower for the lubricated condition because of the difference in the particle size generated. The larger particles cause weaker inter particle bonding and thus lower glaze layer hardness.

Glaze layer formation at the macroscopic level was investigated using SSMUR face seal specimens. At intermediate steps during make-up replica's were taken of the surfaces. Figure 5.9

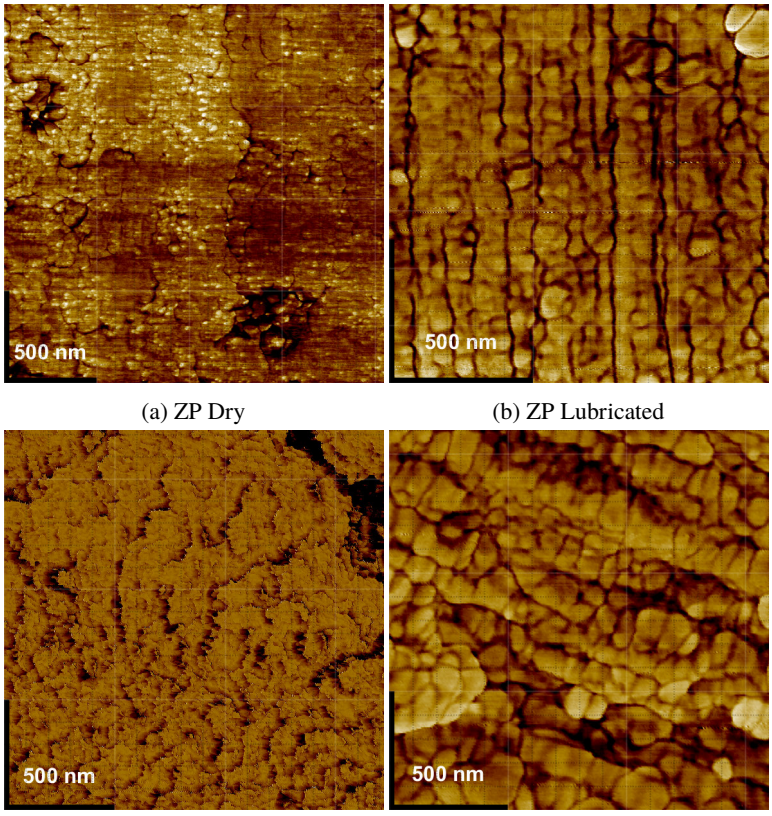

(a) ZP Dry (b) ZP Lubricated

(c) MP Dry (d) MP Lubricated

Figure 5.8.: AFM phase images of the glaze layer at high magnification. Zinc phosphate: Figure 5.8a shows the result after dry sliding and Figure 5.8b after lubricated sliding. Manganese phosphate: Figure 5.8c shows the result after dry sliding and Figure 5.8d after lubricated sliding. Reproduced from Paper D.

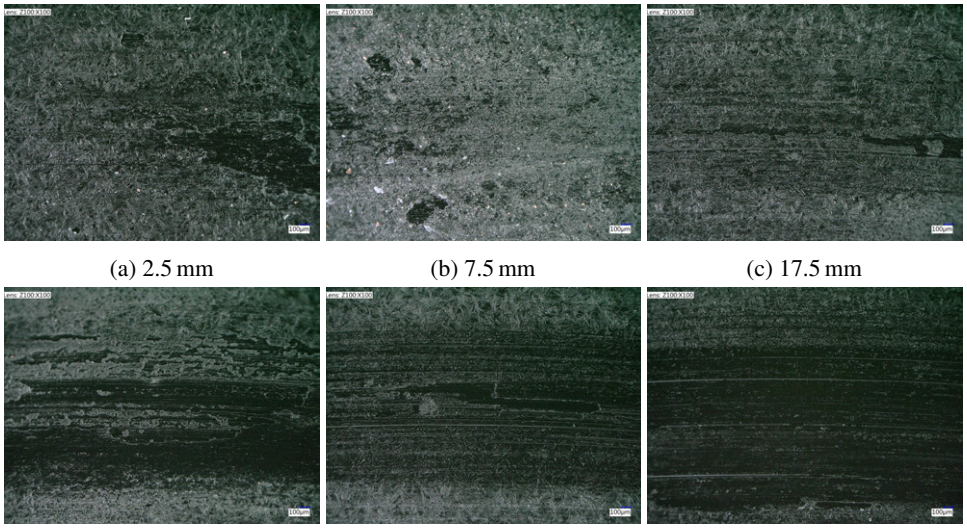

(a) 2.5 mm (b) 7.5 mm (c) 17.5 mm

(d) 37.5 mm (e) 77.5 mm (f) 155.5 mm

Figure 5.9.: Formation of the glaze layer in a face seal experiment. The formation is captured by surface replication, hence this is a negative of the real surface. The cumulative sliding length is reported under each micrograph. Reproduced from Paper B.

shows micrographs of those intermediate replica's to illustrate the glaze layer formation. The cumulative sliding length is reported underneath the micrographs. It can be clearly observed that at each successive micrograph the surface becomes smoother as a result of the glaze layer formation.

5.4. Thread compound interaction

The interaction with the thread compound was investigated following the procedure of Chapter 3 using pin-on-disc, anvil-on-strip and SSMUR. As discussed in Section 2.6 the phosphate coating facilitates the absorption of a lubricant. In the SSMUR experiments presented in Paper B (Figure 5.1) a patchy film was found on the surface of the glaze layer. Figure 5.10 shows a FIB cross section of a patch on FRS06. The film morphology and composition (Figure V.1) was found to be the same as the film found on the AsM surfaces in Section 3.2. Therefore, it was concluded the the film is formed upon initial contact, like the film in Chapter 3.

5.5. Wear mechanism of phosphate conversion coatings

The wear mechanism of the phosphate coatings was investigated with pin-on-disc and SSMUR face seal tests followed-up by FIB cross sections, interferometry, SEM/EDX and nano-

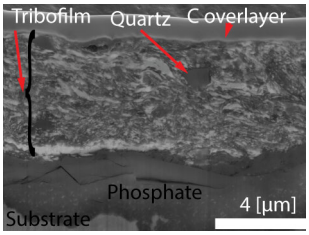

Figure 5.10.: SE (20 kV) images of the FIB cross sections of the tribofilm present on the manganese phosphated box of FRS06. Shown is a cross section of the tribofilm adsorped on manganese phosphate. Similar to the tribofilm adsorbed on bare steel of Figure 3.1c. The EDX mapping results can be found in Figure V.1.

indentation[1]. Wear volumes were determined in pin-on-disc experiments and divided by the dissipated energy [143, 145] or the normal load times the sliding length [185]. This gave the proportionality factors as shown in Figure 5.11. These rates are quite high but not unexpected for a coating with a low shear strength (Paper A). The dissipated energy approach gave a linear relation between the wear volume and energy for which all the experiments collapsed onto a single line. The Archard wear law gave a distinct coefficient for each experiment. This was particularly the case for the high velocity experiment with the high viscosity base oil. The dissipated energy approach neatly takes this into account.

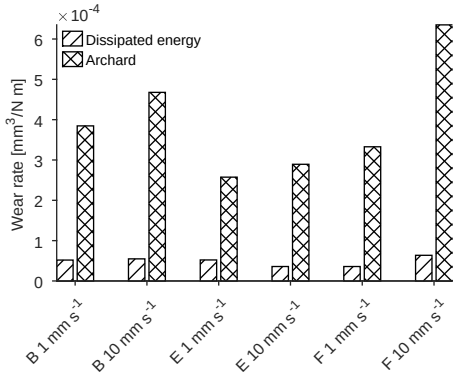

Figure 5.11.: Proportionality of the wear rate versus dissipated energy and normal load times sliding length for the various base oils.

The wear mechanism was further investigated using FIB cross sections analysing the untouched and worn phosphate coating. Shown in Figure 5.12 is a cross section of the manganese phosphated box of Figure 5.1c. Comparing before with after, redistribution of material and the creation of a smooth top surface can be observed confirming the earlier work on glaze layer formation (Paper A, D). Next to that, the surface is worn from the top. No indication

[1] A paper reporting these results is in preparation, entitled: "A dissipated energy based approach for modelling the wear of phosphate conversion coatings".

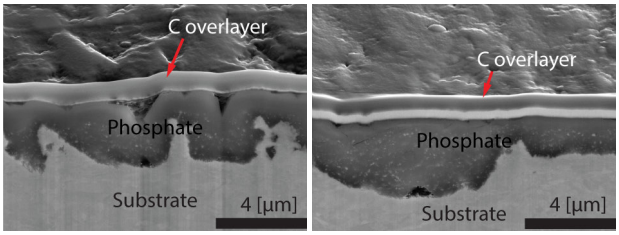

(a) (b)

Figure 5.12.: SE images of the FIB cross sections for the manganese phosphated box (65273). Figure 5.12a shows a cross section of the untouched area and Figure 5.12b shows a cross section in the wear track.

of disturbance of deeper layers can be observed. It is further observed that the acid attack of the phosphating process has created rather sharp "pillars" of substrate material. These were speculated to induce failure by generating high localized contact stresses in a steel-steel contact once the phosphate coating is worn out.

5.6. Summarizing discussion

With the above in mind the wear mechanism of phosphate conversion coatings can be summarized as follows in Figure 5.13. The initial rough phosphate coated surface was defined to have a coating thickness, t_{coat}, and a critical thickness, t_{crit}, corresponding to the localized amount of material removal where the first substrate starts to protrude. Upon initial sliding a glaze layer is formed because of crushing and compaction of phosphate debris (Paper A, B, D). At the same time, on the counter surface, a tribofilm is formed (Paper B, C). Wear and formation of the glaze layer continues from the top until the critical thickness is reached. The system is now only protected by the tribofilm. This could be described by the dissipated energy approach. From this point the system transitions to the severe wear regime and becomes susceptible to galling.

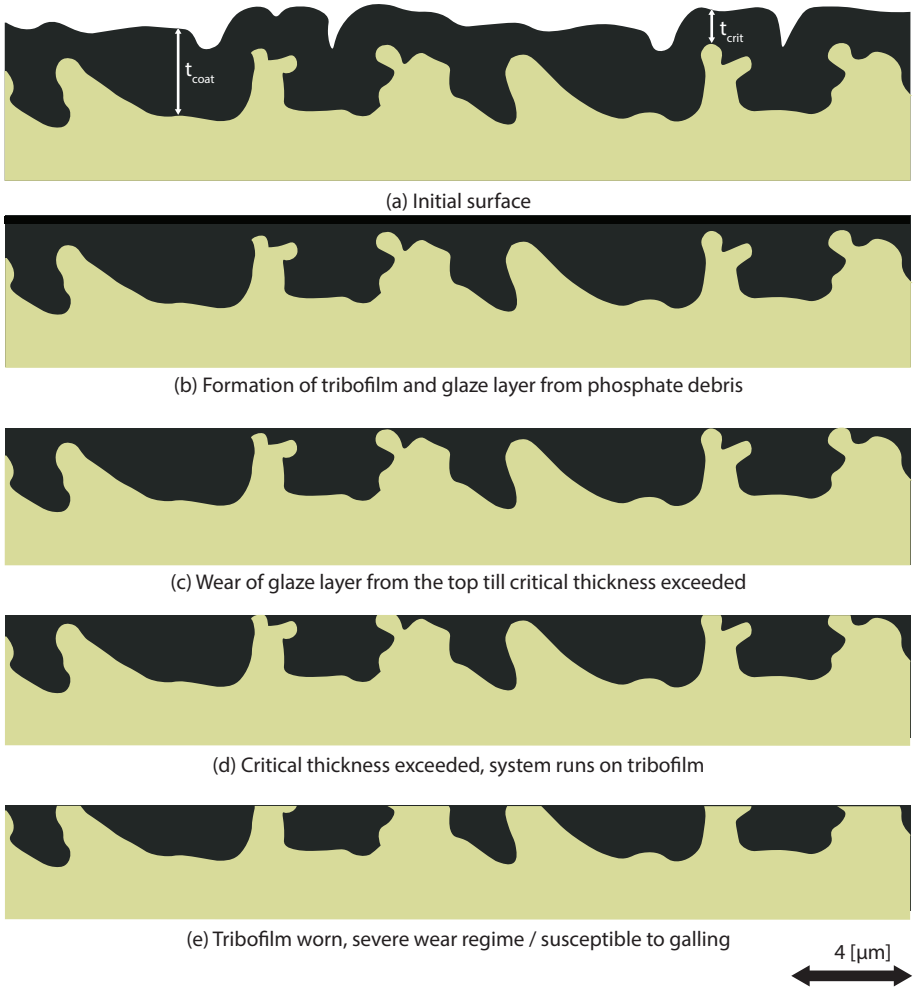

Figure 5.13.: Wear mechanism of phosphate conversion coatings and the definition of the critical thickness.

5.7. Conclusions

It was shown that the phosphate conversion coatings play a dominating role in the metal-to-metal seal tribosystem. The coatings achieve this by the following mechanisms:

- A durable tribofilm is generated on the uncoated counter surface. The tribofilm growth mechanism was shown to be activated and driven by shear stress. The tribofilm requires generated phosphate particles with exposed functional groups and therefore only happens in situ.
- No tribofilm formation was observed on thick phosphate coatings.

- A smooth glaze layer is generated on the phosphated surface. The mechanism was found to be by crushing the crystals and compacting the generated particles in the sliding contact. In dry sliding this leads to a relatively hard layer, whereas in lubricated sliding the hardness was considerably lower. The hardness difference was shown to be driven by the particle size and the related interaction forces. A small particle gives a hard glaze layer. Smaller particles are generated under high shear forces.
- The phosphate coating wears from the top. Five sequential phases could be identified: glaze layer and tribofilm formation, glaze layer wear till critical thickness, wear of tribofilm, severe adhesive wear, failure of the system because of galling.
- The wear of the coated system could be satisfactory described by a model based on the energy dissipated in the sliding contact.

These mechanisms together create a favourable tribosystem configuration which:

- Prevents galling regardless of the lubricant.
- Reduces the importance of the lubricant formulation, making the formulation of environmentally thread compounds easier.
- Provides a mild wearing wavy counter surface contacting a flat smooth phosphate surface leading to concentrated line contacts and an optimal sealing configuration.

6. Running-in and its influence on sealing ability

This chapter combines the previous chapters by presenting a numerical model validated with the experimental results. Based on the validation results further refinements of the model are discussed. Together the experiments and the model are used to explain the role of running-in during assembly and micro-sliding in sealing ability of casing connection metal-to-metal seals. It will be shown that running-in is governed by plastic deformation on the uncoated turned surface topography and severe wear of the phosphate conversion coatings. This results in an optimal sealing configuration because of the conformal contact situation with concentrated line contact which will be shown with the deterministic sealing ability model by [8].

6.1. Introduction

The influence of the thread compound and the phosphate conversion coatings was investigated in the preceding chapters. The interactions described result in a certain running-in behaviour which will be discussed in this chapter. Some conclusions on running-in have already been drawn in Chapter 5 because of the dominating role of phosphate conversion coatings. The experimental results will be further disseminated by investigating the surface evolution using all the intermediate replica's (Figure 5.9) taken during the experiments listed in Table I.6.

The observations will be further explained using a deterministic running-in model that was implemented to investigate and predict the running-in behaviour of the metal-to-metal seal. This also entailed the inclusion of a thermal model [180] to investigate if lubricant desorption was the reason for the observed galling as already discussed in Chapter 3.

The modelling approach in this chapter is based on the work of [186] with further extensions taken from the work of [61, 118, 178] for the plastic deformation and wear. Inspiration was also drawn from [130] even though this entails a rolling contact. The focus in this chapter is therefore on the modifications and additions to these models to make them suitable for simulating the running-in behaviour of a metal-to-metal seal. For reference a short summary of the models is given in Appendix VI. The model is subsequently validated with measured data from indentation and running-in experiments obtained in pin-on-disc and SSMUR.

Finally the running-in model is used to investigate the running-in behaviour of metal-to-metal seals taking into account the plastic deformation and wear of the substrate and phosphate conversion coatings. It will be shown that running-in is dominated by plastic deformation on the as-machined side while wear of phosphate is dominating on the phosphated side. In

addition, the model's short comings are laid bare. The chapter is concluded with the influence of running-in on sealing ability.

6.2. Experimental running-in results

The measured surface topography results were processed according to Appendix II.8.5. The average roughness S_a, RMS roughness S_q, skewness S_{sk} and kurtosis S_{ku} were subsequently computed. These results are plotted against the cumulative sliding length in Figure 6.1 and Figure VI.1 to visualize the running-in behaviour of the pin (Figure 6.1a) and the box (Figure 6.1b) respectively. Here S_q is used to discuss the running-in behaviour. The pin and box were separated because of the different nature of the surfaces (predominantly turned vs phosphated respectively) which can be observed in the line profile overview in Figure 6.2. The exceptions on this rule were highlighted in the graphs by their own symbol marked "Ph" in the pin data set and "AsM" in the box data set. There are 3 other subsets marked in the graphs, FRS07 and FRS09 as the only tests with ZP on the box, FRS09 again because of much higher pin roughness and FRS08 the only test with phosphate on both sides (ZP pin vs MP box).

The results for the pins hardly show running-in behaviour compared to observations in literature [125]. The S_q is hardly changing over the cumulative sliding length. This is because of the deterministic nature of the surface topography, the large waviness causes very local contact (Figure 1.8) and therefore also the changes are very localized as shown in Figure 6.2. See for instance FRS11. This leaves the waviness mostly in tact and overwhelms the S_q, resulting in a minor impact. Hence, as discussed in Section 2.4, a statistical approach is not suited for the deterministic surface topography of a metal-to-metal seal. Investigating the surfaces by matching the intermediate states with the initial states revealed that the turned roughness does not undergo major changes after the first 40 mm as shown in Figure 6.8, which will be discussed later.

The box results show running-in behaviour for the ZP coated surfaces. This is because of the relatively high initial roughness of ZP compared to MP coming from the crystal size differences as discussed in Paper A and Chapter 5. From the ZP results it can be observed that it takes approximately 40 mm to reach a steady situation with no further (large) changes to the surface topography. Similar running-in behaviour was observed by [36] as reproduced in Figure 2.3.

To explain and investigate this, a running-in model was developed which will be discussed in the following sections.

6.3. Elastic-perfect plastic contact model

A short overview of the validation of the contact model is given here, for details of implementation please consult the work of [61, 118, 186]. A short summary is given in Appendix VI.

The code was verified with Hertzian solutions for point, elliptical and line contact [33]. A result of this is shown in Figure I.5a for the charcterization of the contact stresses in SSMUR

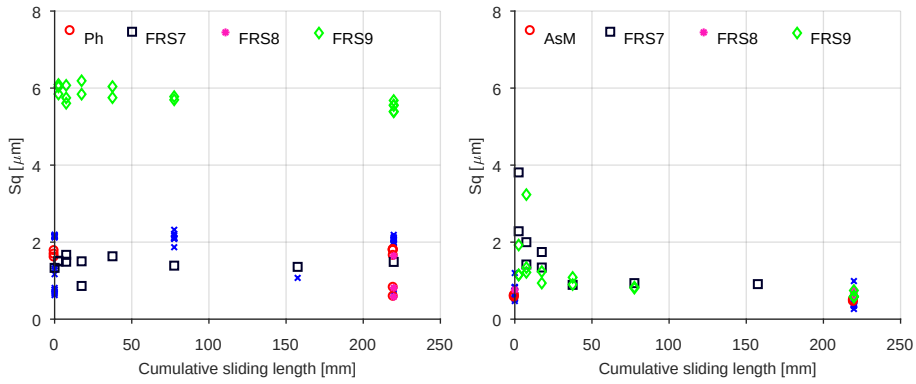

(a) Pin (b) Box

Figure 6.1.: Evolution of S_q versus cumulative sliding length for the SSMUR face seal data set in Table I.6. Pin (Figure 6.1a) and box (Figure 6.1b) results were considered separately because of the different nature of the surfaces.

(Appendix I). Validation of the contact model was done with indentation experiments using a 3 mm 700 HV AISI52100 ball on 192 HV quenched and tempered AISI4130. The result of the 35 N indentation is shown in Figure 6.3 and compared to the prediction of the elastic-perfect plastic contact model ("fine" in the legend). At this load the maximum Hertzian contact stress is 3.44 GPa which exceeds the surface hardness of the material. Hence plasticity is expected and can be observed after the experiment. The results were found to be in good agreement, the plastic deformation is satisfactorily predicted by the model. Also the shape of the plastic region is captured faithfully. This is in line with the material properties as quenched and tempered AISI4130 exhibits minimal strain hardening [187].

As a consequence of the hardness cut-off (equation (VI.10)) the roughness is completely removed in the model which is clearly shown in Figure 6.3b. This is not the case in the experiment, certain roughness wavelengths persist even under high contact stresses. The persistence of roughness was investigated with sinusoidal surfaces by [188, 189] which showed that complete flattening can only be achieved when the contact stress exceeds the yield stress by up to 15 times. This directly exposes the short coming of the contact model. In plastic contact it will act as an arbitrary low pass filter for the high frequency components of the roughness. Prediction of the final roughness is, however, important for the subsequent sealing ability model [8]. To account for this a simple interpolation method was developed which will be discussed in Section 6.4.4.

6.4. Modelling running-in

Running-in was modelled by employing the contact model in a quasi static approach. Movement was introduced by making sub pixel steps and solving a static contact problem (Section 6.3) at each step. The contact stresses and plastic deformation were subsequently used to modify the contacting surfaces between the steps to simulate running-in. The running-in

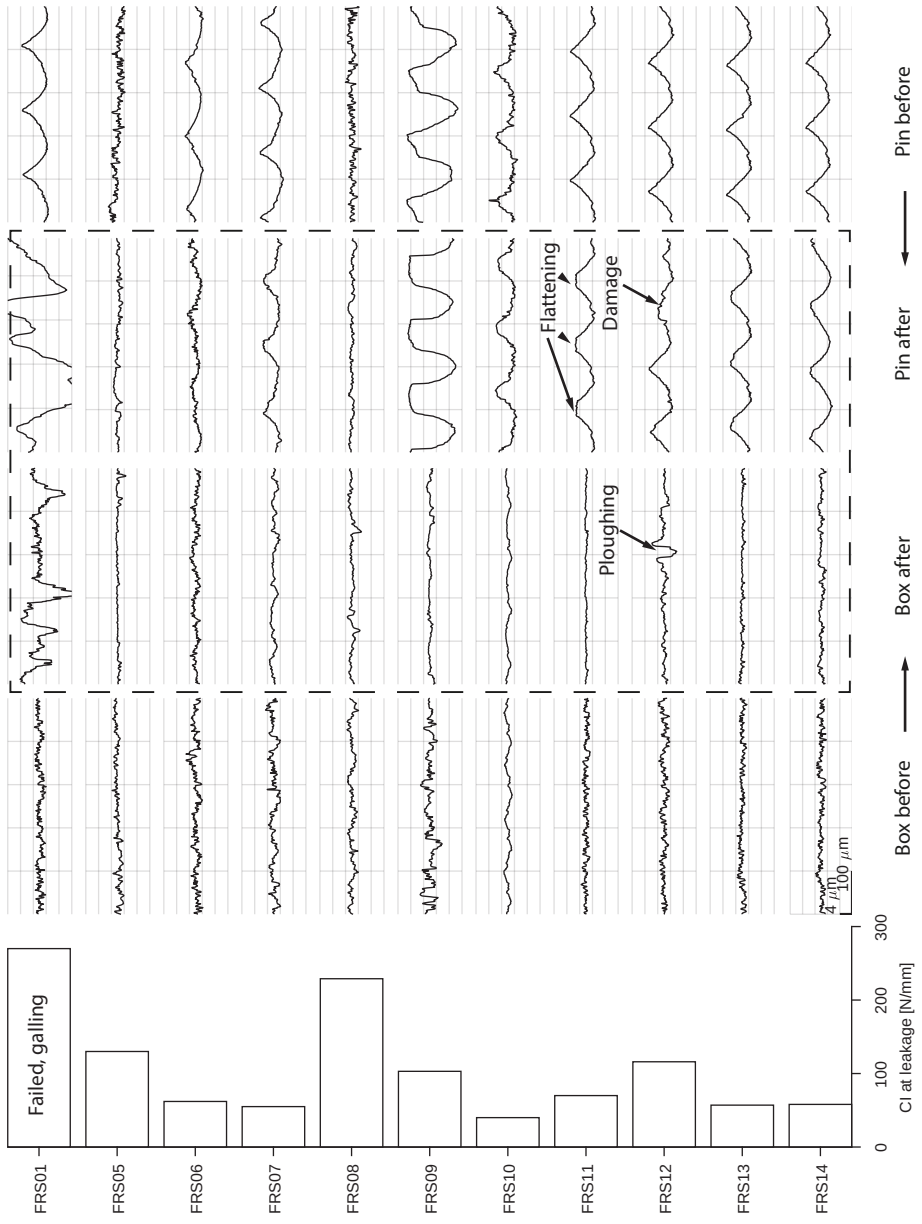

Figure 6.2.: Overview of the face seal test outcomes, refer to Table I.6 for the specimen configuration and assembly lubricant used. Rows represent an experiment as numbered on the left. Columns compare the topography before and after the test as indicated at the bottom. Presented are a bar chart with the contact intensity at leak. The lower the contact intensity at leak the better the performance of the metal-to-metal seal. Connected to these results: a cross section in radial direction of the surface topography of pin and box before and after the test for a matching location on the circumference. The pressure differential acts from left to right. A visual correlation can subsequently be made between onset of leakage and surface topography after make-up sliding. Part of these results have been presented in Paper B.

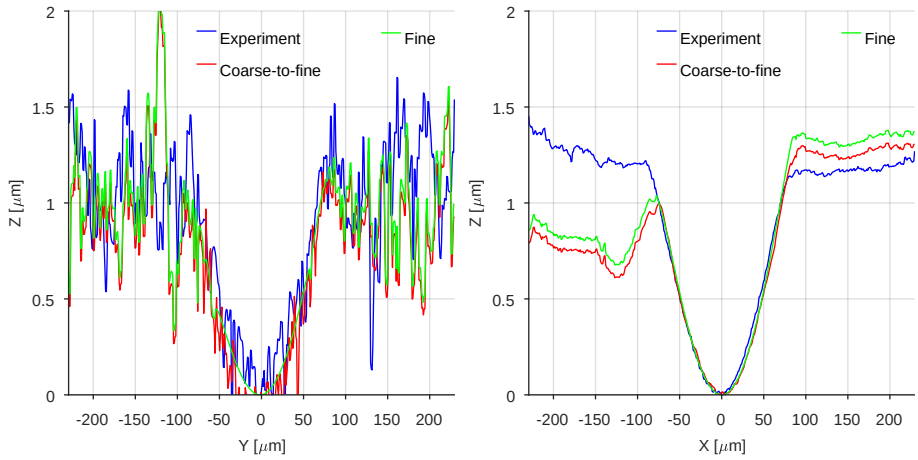

(a) (b)

Figure 6.3.: Validation of the contact model by indenting a ground AISI4130 surface (Figure II.1b) with a 3 mm AISI52100 ball. Results shown are for a 35 N normal load. Cross section through the center in X-direction shown in Figure 6.3a and Y-direction in Figure 6.3b. The surface hardness of the plate was measured with Vickers indentation at 1960 MPa and used to set the hardness cut-off according to equation (VI.10).

model follows closely the works by [134, 186]. A short overview of the implemented model is given hereafter and in the acompanying flow chart in Figure 6.7.

6.4.1. Movement

Movement is imposed on one of the contacting members, here z_2 for the sake of example. The movement is cyclic or periodic, meaning, for instance, what exits at the top or the right side of the domain enters on the bottom and left side of the domain respectively.

The step size is denoted as $\Delta x, \Delta y$, in x, y-direction respectively. To adhere to the quasi static assumption, the step size is typically smaller than the pixel size d_x, d_y of the surface topography measurement. These sub pixel movements of the surface were performed using the Fourier shift theorem,

$$\mathcal{F}\{f(x-\Delta x, y-\Delta y)\} = \exp^{-i(\omega_1 \Delta x + \omega_2 \Delta y)} F(\omega_1, \omega_2), \tag{6.1}$$

where $\omega_1 = \dfrac{2\pi k}{N}, \omega_2 = \dfrac{2\pi k}{M}$ and $\Delta x, \Delta y$ the sub pixel step in x and y respectively. This implicitly assumes a semi-periodic or periodic domain. This is a lossless operation, however, there is build up of a finite numerical error when the operation is applied many times because modes do not cancel perfectly even though conjugate symmetry is imposed. This is shown in Figure 6.4 for increasing sub pixel step size where 0.1 corresponds to $\Delta y = 0.1 d_y$. The relative error in z_2 in the L_∞-norm stabilizes at 0.9^{-9} for a cumulative sliding length of 0.6 m.

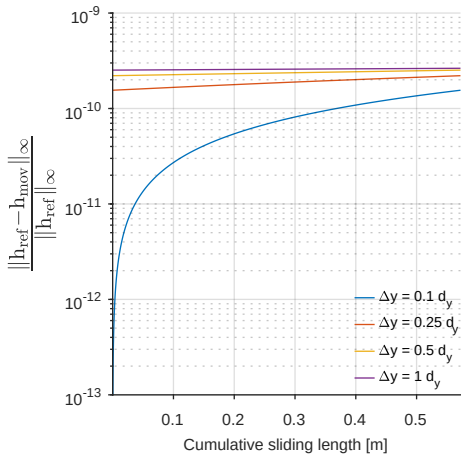

Figure 6.4.: Evolution of the relative error in the L_∞-norm versus cumulative sliding length on a semi-periodic domain as function of sub pixel step size Δy. For instance, 0.1 means a step is 10% of the pixel pitch d_y.

Note that the use of the Fourier shift theorem is not restricted to periodic domains and unidirectional sliding, also non-periodic domains and oscillating sliding for instance for fretting type of simulations can be handled in this fashion by extending the domain by its mirror image.

6.4.2. Wear

The wear in the system is determined by applying Archard's wear law [141] or the dissipated energy approach [143–145] using the local (contact) stresses [134, 186]. The wear model converts the local contact stresses to a height loss using a wear rate and the incremental sliding length. For a generalized wear model this becomes,

$$\Delta h_w(x,y) = k\sigma(x,y)\Delta l, \tag{6.2}$$

where $h_w(x,y)$ is the worn height, $\sigma(x,y)$ an applied stress, Δl an incremental sliding length, and k a wear factor in units of $\mathrm{m}^3\,\mathrm{N}^{-1}\,\mathrm{m}^{-1}$ determined by experiments. To obtain an Archard wear law $\sigma(x,y) = p(x,y)$ or for a dissipated energy approach $\sigma(x,y) = \mu p(x,y)$ with $k = k_A$ or $k = k_D$ for each choice respectively. Note further that a casing connection metal-to-metal seal moves in both x and y-direction or axial and circumferential direction, Figure 1.5, hence $\Delta l = \sqrt{(\Delta x)^2 + (\Delta y)^2}$.

6.4.3. Averaging

As discussed the brute force algorithm uses sub pixel steps to solve for the moving system. This becomes unwieldy for the combination of relative large surfaces and the related sliding

lengths that are investigated in this thesis. Therefore, the averaging approach of [178] was implemented (Figure 6.7) to reduce the computational burden while keeping a high resolution representation of the contacting surfaces.

The basic idea is to sum the localized contact stresses over one full cycle (Section 6.4.1) of sub pixel steps (Δx and/or Δy, such that for instance $N_a veraged = \frac{L_y}{\Delta y}$, and average them at the end of the cycle. This averaged contact stress is subsequently used to progress the solution for a multiple, r, full cycles. After the averaged full cycles the solver builds a new averaged contact stress by reverting back to sub pixel shifting for one cycle. The choice for the amount of averaged cycles depends on the dynamics of the system at that moment. For instance, at the start of the computation the system is running-in, hence large changes are to be expected. Thus the contact stress changes rapidly and therefore needs re-computation often. This means, that at the start the amount of averaged steps is minimal and will be increased once the system is past the running-in regime. During the averaged steps, only wear is applied like the original approach of [178].

To determine if the system is undergoing rapid change the plasticity index of the system is tracked which is defined as, [190],

$$\mathrm{PI} = \frac{I_p}{I_c}, \tag{6.3}$$

where I_p is the amount of plastic points in contact defined by $p(x, y) > H$ and I_c the total amount of points in contact defined by $p(x, y) > 0$.

6.4.4. Coarse-to-fine extrapolation to remedy shortcomings of the plasticity model

Another method that was used to decrease the complexity was to reduce the degrees of freedom by using a coarse representation of the fine scale surface through spline interpolation. The problem here is that coarsening will remove higher order roughness from the surface, hence it acts as a low pass filter. These frequencies, however, are important for the sealing ability calculation to be performed later [8]. This brings about an interesting possibility though by using the following approach.

The running-in is simulated on a coarse scale representation of the original surface. The initial high resolution version is stored. At the end of the simulation the deformation and wear results will be interpolated to the finer scale mesh and subtracted from the initial fine scale representation. This way the high frequency content of the original surface is retained while the deformation and wear is correctly applied. Next to that, this also solves the issues discussed in Section 6.3 with the elastic-perfectly plastic assumption flattening the surface topography.

As shown in Figure 6.2 these frequencies will be mainly determined by the phosphated surface. In addition, the final surface topography needs to be similar to the initial surface topography. Which means that for a ZP surface this will not work because of the clearly visible crystals that are on the surfaces which get formed into a glaze layer leading to considerable changes as shown in Figure 6.1. For a MP surface, however, the initial and final surface roughness is similar as shown in Figure 6.1.

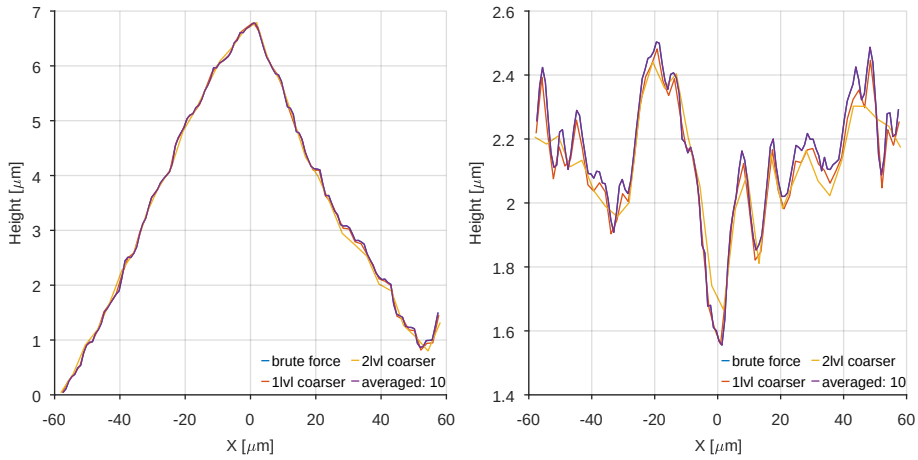

(a) Pin (b) Box

Figure 6.5.: Comparison of brute force solutions with coarsening and averaging approaches. Shown is an average line profile in Y-direction. Figure 6.5a shows the worn pin surface and Figure 6.5b the worn box surface.

An example of this approach for static indentation is shown in Figure 6.3 for the same validation case as Section 6.3 designated as "coarse-to-fine". The contact problem was solved on a 4x coarser discretization, interpolated to the finer mesh and subtracted from the initial fine scale topography. As expected, higher frequency dynamics of the original surface topography are now accounted for.

6.4.5. Comparison of approaches

The acceleration approaches described above are compared to the brute force solution. A summary of the various approaches is given with the flow chart in Figure 6.7. A single waviness is taken from the centre of the measurement in Figure 1.7a with the form removed. For the brute force solution, the full resolution is used and stepped through at half pixel step size. The coarsening approach and averaging approach also use half a pixel step size, however, for the coarsening approach this means a bigger step because of the coarser mesh. Thus a speed-up is obtained by reduced computational complexity and increased step size. The results for running-in with just plastic deformation are shown in Figure 6.5. Here the worn pin and box surface are compared for the coarsening and averaging approaches. The brute force approach is not visible as it overlaps with the averaging approach because plastic deformation is only applied during subpixel stepping. In general the results are in good agreement, it is clear that excessive coarsening leads to loss of high frequency information.

This is reflected in the cumulative plastic displacement in Figure 6.6a and plastic volume in Figure 6.6b. The averaged solution produces the same results, as expected. The coarsened approach underestimates the amount of plastic deformation in the system. This is because the

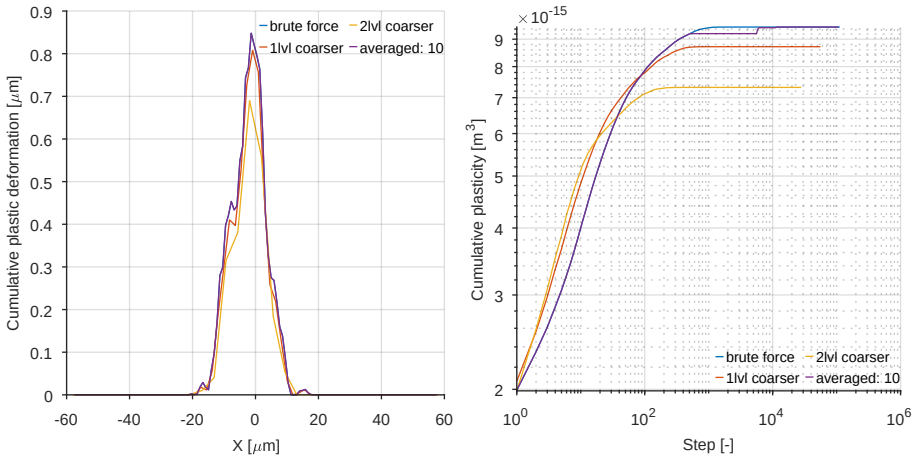

(a) (b)

Figure 6.6.: Comparison of brute force solutions with coarsening and averaging approaches. For Figure 6.6a an average line profile in Y-direction is shown. Note that the results in Figure 6.6b are on a double log-scale.

cumulative plastic displacement is lower as the surface is smoother at the start. This means less plasticity and thus the solution converges to a fully elastic solution faster. It should be noted though that this can also be the case for averaging. An elastic solution should be reached within the sliding length, otherwise plasticity will be underestimated.

6.5. Validation and discussion

The validation of the running-in model was done using SSMUR face seal experiments (Table I.6). Make-up sliding was performed for a full revolution or 220 mm at 30 kN. To track the surface evolution for the validation, the surface topography of pin and box were measured prior to the test. During the tests, the contact was opened, the surface cleaned and a replica was taken at 40 mm to get an intermediate data point. After that, thread compound was re-applied and the specimen was made up a full revolution. The surface topography after a full revolution was measured after the test on the steel surfaces. This is compared to the model by only taking into account the plastic deformation of the surface while sliding. Hence, wear is not (yet) taken into account here and thus the experiments are compared to the same model run.

The three measurements (initial, 40 mm and 220 mm) were de-trended (Section II.8.5) and subsequently matched using the algorithm presented in Section II.8.6. The result of the matched measurements was compared to the model outcome at 50 mm in Figure 6.8 for the tests with API modified and YD D. Similar to the work of [36, 38], most of the surface topography changes because of running-in happen in the first 40 mm of sliding. Upon comparison of Figure 6.8a and Figure 6.8b a change of lubricant did not show a large effect on the resulting surface topography evolution. A good correspondence was found between the model and the

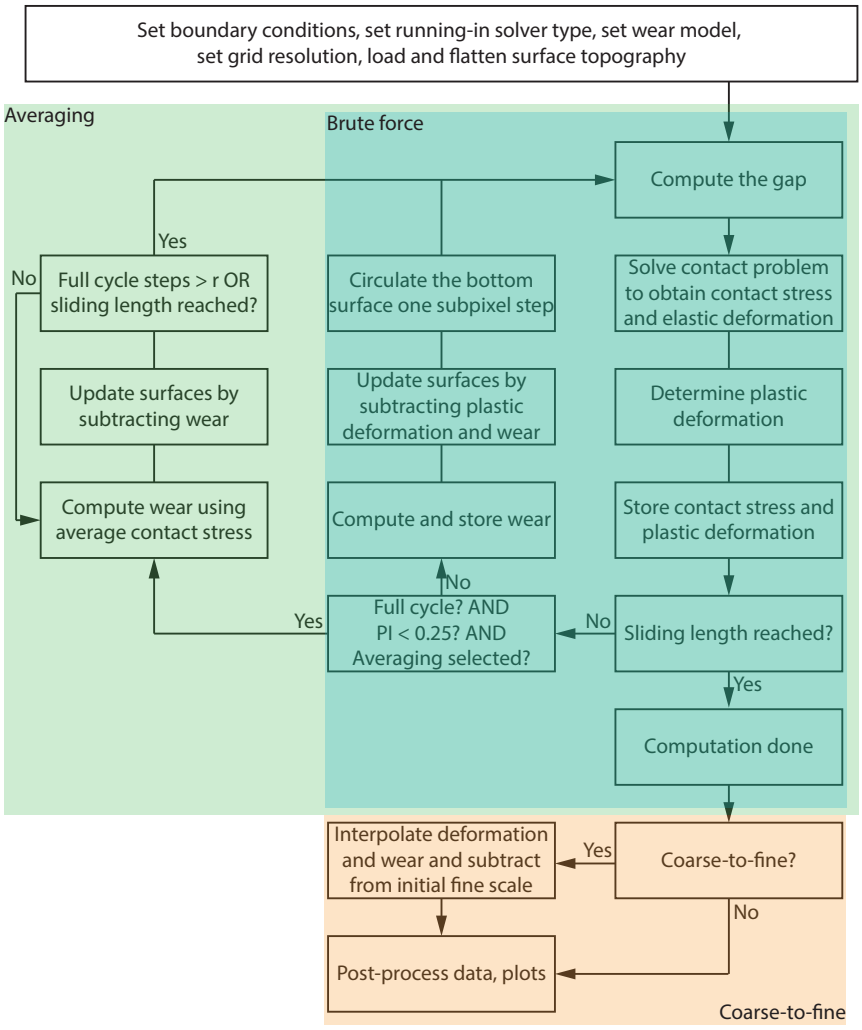

Figure 6.7.: Flowchart summarizing the model and the various approaches available.

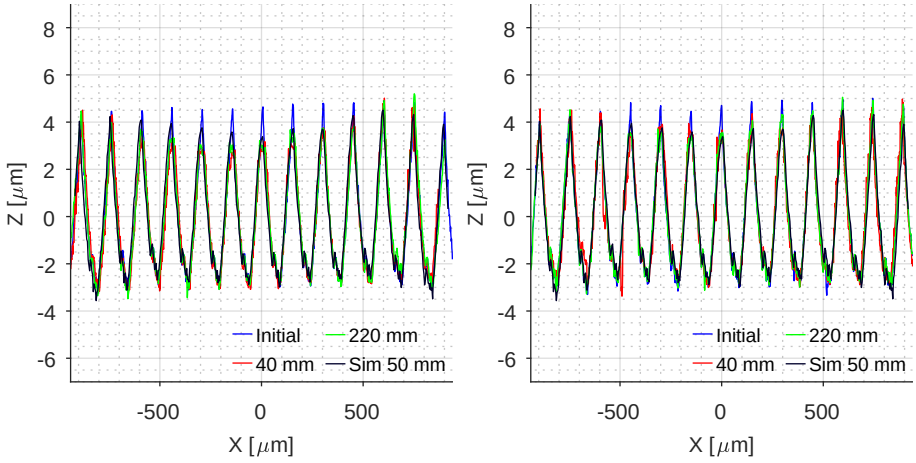

(a) API mod (b) YD D

Figure 6.8.: Running-in model validation results for the pin side of the face seal tribosystem. The experimental results for sliding 40 mm and 220 mm are compared to the simulation using the coarse-to-fine approach. Figure 6.8a shows the comparison to sliding with API mod and Figure 6.8b the compares against sliding with YD D.

experiments. This indicates that for the uncoated pin plasticity (using the measured surface hardness reported in Table I.2) dictates the running-in phase and wear is only of secondary importance.

The averaging model was used to combine plasticity and the dissipated energy to determine the phosphate wear to predict the failure for the rotation to failure experiments FRS01-04 (Table I.6). Boundary conditions were set according to the reported test conditions, wear rates were obtained from Figure 5.11 and surface hardness from Table I.2. Also a lower hardness material was simulated. The result is shown in Figure 6.9 and lays bare the shortcomings of the current model. It is clear that the critical thickness (Figure 5.13) is exceeded much earlier, after 1-2 revolution(s) depending on the surface hardness, in the model compared to the experiments as shown in Figure 6.9a. This is mainly because the presence of a tribofilm is not taken into account. In addition, the system will transition to a different and lower wear rate which is also not taken into account. The total plastic volume is determined in the first millimetres of sliding as shown in Figure 6.9b and Figure 6.8.

The results indicate that the transition from plastic to elastic behaviour of the bare surface goes hand-in-hand with the transition from severe to mild wear of the phosphate coating (Figure 6.1 and Figure 6.8). The reduction of the localized contact stresses because of plastic deformation drives the reduction of the phosphate wear and the phosphate wear improves conformity resulting in further reduction of the contact stresses and wear. This is a self enforcing loop leading to a stable system until the phosphate coating and its derived tribofilm is completely worn as discussed with Figure 5.13.

The combined experimental and numerical results thus indicate severe initial wear which

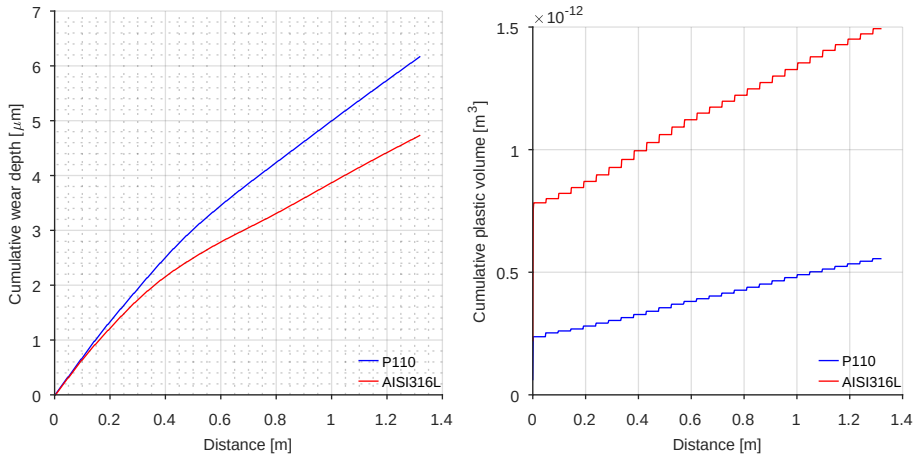

Figure 6.9.: Running-in model validation results to the rotation to failure experiments FRS01-04. The experimental results are compared to the simulation using the averaging approach with the dissipated energy wear law. The used wear rates for the phosphate coatings were taken from Figure 5.11. Figure 6.9a shows the cumulative wear depth and Figure 6.9b the cumulative wear volume.

transitions to mild wear for the remainder of the assembly phase. The experiments with sets FRS01-04 show that this steady state is kept until the phosphate wear reaches the critical thickness as discussed in Chapter 5. This transitions the system back to a severe wear regime which ultimately leads to galling because of the mechanisms described in Chapter 3.

The coarse-to-fine approach was further investigated using the sealing ability model of Pérez-Ràfols [8] (Section 2.5) by comparing the run-in experimental surface with the outcome of the model using a brute force solver and the coarse-to-fine solver. This is done by computing the permeability of the gap during loading and unloading of the run-in seal surface. The result is a permeability versus contact stress curve as shown in Figure 6.10. The experimental obtained surface shows the expected increase in permeability with lower load. The results of the brute force solver indicated almost zero permeability under all normal loads. This was because of the, unrealistic, perfect conformity of the surface. It would, however, be a desired configuration for a metal-to-metal seal. This was removed by the coarse-to-fine approach by applying the plasticity at a coarser scale. It is clear that the result is much closer to the experimentally obtained run-in surface confirming the hypothesis that the initial and final surface topography are close. However, this result is still obtained with an arbitrary choice for the coarsening. More work is needed to justify a choice for this cut-off.

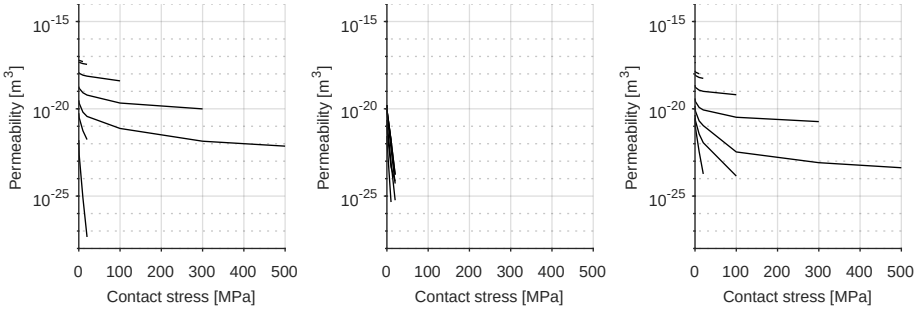

(a) Run-in experiment (b) Run-in brute force (c) Run-in coarse-to-fine

Figure 6.10.: Permeability curves for run-in single waviness ridges using the deterministic model of [59]. Here a comparison is made between the run-in surface topography of the experimental outcome (FRS13), the brute force solution and the coarse-to-fine solution.

6.6. Influence of running in on metal-to-metal sealing

From the previous sections and chapters it is clear that the metal-to-metal seal runs in relatively quickly. On the uncoated side (here pin) this is, for the largest part, driven by local plasticity (Section 6.2 and Section 6.5). On the coated side (here box) a smooth glaze layer is generated (Chapter 5). The question that remains is: How does running-in affect the sealing ability of the metal-to-metal seal?

An overview of the phosphated face seal experiments was given in Figure 6.2 which relates sealing ability to a qualitative overview of the surface topography cross sections. The bar chart shows the contact intensity at the onset of leakage for the various test configurations. Connected to the bar chart are cross sectional profiles of the pin and box specimen before and after the test. Comparing the surface textures before and after the test, the following is observed. Galling and double sided phosphate (test FRS01 and FRS08) are both resulting in poor sealing ability performance of the metal-to-metal seal. The same goes for a contact set without waviness (FRS05). An ideal configuration, as discussed earlier in Chapter 5 and Paper B, is a phosphated surface against a bare turned surface. The phosphate becomes smoother because of glaze layer formation as shown earlier with Figure 5.9. The uncoated side shows localized deformation and mild wear at the peaks of the waviness because of tribofilm formation. This results in an outcome that a base oil (O933: FRS05, 09, 11) can come close to the sealing performance of a fully formulated thread compound (API mod: FRS06, 07, 12; YD A: FRS14; YD D: FRS10, 13). Still, the wavy topography combined with the thread compound and its particle additives adds robustness to the system as can be observed from the relative good performance with the damage on the pin of FRS12.

Finally, the model is not yet ready to predict the outcomes including all the complexity above. This will be discussed as one of the recommendations of this thesis in Chapter 7.

6.7. Conclusions

The role of running-in in seal ability of metal-to-metal seals was investigated in this chapter. With experimental results a running-in model was validated. Together the experimental and numerical results indicate the following.

- The phosphated surfaces were run-in in less than 40 mm cumulative sliding distance.
- The bare and wavy counter surface only required a few millimeter to come to the run-in state because of severe plastic deformation.
- A simple running-in model combining plastic deformation and wear was developed and successfully validated with pin-on-disc and face seal experiments.
- The running-in model based on a simple hardness cut-off currently lacks the fidelity to accurately predict the surface topography of the surfaces after wear. A coarse-to-fine approach was proposed to remedy this and needs further development.
- The experimental and numerical results together indicate that running-in is dominated by plastic deformation on the uncoated surface and wear of the phosphate conversion coating on the phosphated side.
- Best seal ability was achieved with surface combinations that generate highly localized contact stress profiles, i.e. the waviness from as machined surfaces vs the generated smooth glaze layer on phosphated surfaces.
- The combination of glaze layer, tribolayer and synergy with the lubricant results in a low wearing system providing, when combined with an as machined counter surface, an ideal configuration for sealing.

7. Conclusions and recommendations

The overall conclusions and recommendations are presented here and based on the work in the preceding chapters and the appended papers A-F. The conclusions are addressed by answering the research questions posed in Section 2.11 *with the work presented in this thesis. For more detail the reader will be referred to the relevant chapter(s).*

7.1. Conclusions

7.1.1. The mechanisms of protection of thread compounds and galling initiation

RQ1 What are the mechanisms of protection of the thread compound and what is the galling initiation mechanism in the metal-to-metal seal tribosystem?

This question was answered in Chapter 3. It was shown that in an uncoated metal-to-metal seal tribosystem galling is initiated after relatively short sliding lengths with API modified thread compound. In fact, API modified only added 60 mm of additional sliding length till failure compared to a plain mineral oil at a maximum Hertzian contact stress of only 250 MPa. This was shown to be because of the waviness giving rise to concentrated line contacts leading to squeeze out and removal of the soft metallic tribofilms. These tribofilms get formed in the initial contact and were not replenished because of the plan parallel gap. With a developed particle entrapment model it was shown that some particles are not entering the contact based on their size and friction between ball, disc surface and particle. In all cases zinc entered the contact and generated a tribofilm. This is because of the high affinity of zinc towards the steel surface compared to lead and copper. The role of the thread compound and its additives was shown to be mainly in aiding metal-to-metal sealing by forming a plug of particles in front of the metal-to-metal seal.

7.1.2. High temperature degradation mechanisms of thread compound

RQ2 How does elevated temperature affect the thread compound protective mechanisms and how does this affect sealing ability?

With a newly developed accelerated test protocol and a prototype high temperature thread compound this question was answered in Chapter 4. It was found that environmentally acceptable thread compounds degrade mainly by loss of consistency. This was found to be caused by evaporation of the base oil leading to thickening or by exceeding the dropping point leading to collapse of the thickener network and bleeding of base oil. This made it easier to remove the remaining thread compound from the contact. The system then needs to rely on tribofilms that were formed at make-up or micro sliding. The tribofilms are not replenished because the thread compound has no consistency and removal was accelerated by abrasive wear by the metal oxide particles present in the formulations. Finally, the system failed because of severe adhesive and/or abrasive wear resulting in a heavily scratched surface. This will affect the sealing performance of the metal-to-metal seal negatively. The issues presented were mitigated by a prototype thread compound designed as part of this thesis using the newly proposed method. This thread compound relies on strong film forming, which negates the thermal degradation by separating the surfaces long after the compound has lost its consistency. It was shown with anvil-on-strip and make-up and break-out test that the prototype surpassed the performance of the commercial thread compounds. This also showed the effectiveness of the newly proposed screening method.

7.1.3. The dominating role of phosphate conversion coatings

RQ3 What are the mechanisms that give phosphate conversion coatings their beneficial properties?

The answer to this question was given in Chapter 5. It was found that the interaction with phosphate conversion coatings in the tribosystem leads to the formation of a smooth glaze layer on the phosphated side and a durable tribofilm on the bare side. The glaze layer and tribofilm were characterised and the mechanisms of formation explained. The glaze layer was formed under sliding conditions by crushing and compacting the phosphate crystals. In dry conditions this gave rise to a hard layer (3 GPa) which could be satisfactorily described by models for metallic films. In lubricated conditions the hardness was substantially lower. This was shown to be related to the size of the particles generated because of less effective grinding in lubricated conditions leading to larger particles and lower hardness. The particles are generated by cleavage of the Hopeite or Hureaulite crystals and because of bond stretching of the phosphate group adsorb on the bare surface. This was shown to be the mechanism of tribofilm formation and is shear stress activated. Together these mechanisms give rise to wear of the phosphated tribosystem that was best described by a dissipated energy approach. With this the phosphate coatings dominated the friction and wear of the tribosystem and allowed successful assembly and sealing ability with unformulated lubricants (base oils). This was though up to the removal of a critical thickness of the phosphate and subsequent wearing out of the tribofilm after which the system transitions to a severe wear state ultimately leading to galling.

7.1.4. The running-in of metal-to-metal seals and its influence on sealing ability

RQ4 How does a casing metal-to-metal seal run in and how does it affect sealing ability?

The final chapter, Chapter 6, answers this question using a numerical running-in model and the preceding chapters. It turned out to be the combination of plastic deformation and the wear of the phosphate coating that determined the running-in behaviour. The dominating influence of phosphate was addressed in the previous section. The plasticity of the counter surface is also an important factor in the running-in behaviour. It was found that the run-in of the phosphate coating and the plastic deformation were finished within 40 mm of sliding. This was found to be by severe wear, subsequently transitioning to mild wear. The combination of severe initial wear, waviness and the generation of a smooth glaze layer created a conformal metal-to-metal seal with multiple concentrated line contacts along the circumference. It was found that this gave rise to a robust sealing configuration, even when the sealing surface was damaged. Sealing configurations that did not have a distinct orientation of the surface topography performed worse.

7.2. Recommendations for future research

There are several aspects in which the research can be further developed which will be defined as recommendations for future work.

- The increased surface hardness of the formed glaze layer when sliding in dry conditions on phosphate conversion coatings is an interesting property to exploit. The application of this could be to improve the wear resistance of phosphate conversion coatings by applying a dry sliding pre-burnishing step. The hard glaze layer that is formed can subsequently reduce the coating wear in lubricated sliding. The efficacy of the wear reduction can be measured with the dissipated energy approach as shown in this thesis.
- The formation, growth and removal of a tribofilm was shown to be an important mechanism in both the thread compounds and the phosphate conversion coatings. This part is missing in the running-in model and should be added to come to a realistic prediction of the transition to severe wear. This can for instance be implemented by following the approaches of [154, 176–179].
- The coarse-to-fine modelling and acceleration approach needs a stronger foundation and back-up by experimental observations to decide which scales can be ignored in the modelling of running-in of the surface topographies in this thesis. Currently the cut-off is placed rather arbitrarily at a cell size that is four times the original pixel size. However, it should be related to a physical scale, for instance with a frequency component that cannot be flattened [189, 191].
- Ultimately, to come to a realistic prediction of the surface topography for subsequent sealing ability modelling [8], a high(er) fidelity wear model should be implemented which takes into account the random walk of the wear process generating scratches on the surfaces. A starting point could be the work by [140] which tries to predict the size of the generated wear particles. This already gives a way to modify the surface topography as a consequence of wear.

I. Experimental methods: emulating a metal-to-metal seal

This appendix introduces the Shell Sealing Mock-Up Rig. A set-up that was developed for the project and dedicated to metal-to-metal sealing research in a face seal and an interference seal configuration. The developed set-up is the result of a collaboration between Shell Global Solutions International BV, The Netherlands and OCAS NV, Belgium. For clarity, the author is not the designer of the set-up, I am partly responsible for the experimental design of the described experiments and merely used the results generated by the apparatus. Part of the face seal work has been presented in Paper B. The set-up, the results generated and subsequent validation of the models will be presented in an upcoming publication[1].

I.1. Introduction

In this work experiments were performed at several scales to get insight in the mechanisms of the metal-to-metal seal tribosystem. From single asperity scratch tests in the Ploughing Asperity Tester (PAT), thread compound behaviour in a pin-on-disc tester, galling susceptibility tests in the anvil-on-strip test to full scale connection make-up and break-out tests in a bucking unit. As this entails standard equipment an overview can be found in Appendix II.

A new set-up, however, was developed for this project which will be explained here including the related specimen preparation to come to a representative specimen. For consistency, these methods were also applied to prepare the specimens for the scaled tribosystems in PAT, pin-on-disc and anvil-on-strip tests.

The scaled surface evolution and sealing ability tests were performed in an in-house developed test set-up called the Shell Sealing Mock-Up Rig (SSMUR). See Figure I.1 for a schematic of the specimens and load frame. Table I.1 lists the technical specifications. In this set-up, assembly, micro sliding and sealing ability can be investigated with scaled (100 mm diameter) metal-to-metal seal specimens at (gas) pressures up to 1000 bar.

Two configurations are possible: a load controlled face seal configuration (Figure I.1a, Figure I.1c) and a position controlled interference seal configuration (Figure I.1b, Figure I.1d). The interference seal configuration is a scaled version of a real connection metal-to-metal seal and can be modified to test a wide variety of seal geometries. Both were designed according to the boundary conditions stated in Table 2.1.

[1] Title: On the Sealability of Metal-to-metal Seals with Application to Premium Casing Connections

Table I.1.: Shell sealing mock-up rig technical specifications and limits.

Property	Maximum	Resolution
Z-movement	500 mm	0.5 µm
Z-force	120 kN	1200 N
Z-torque	1 kN m	10 N m
Rotational velocity	0.1-100 mm s^{-1}	-
Temperature	200 °C	1 °C
Internal pressure (gas or liquid)	1500 bar	1 bar
Leak detection	-	1 mg
Specimen diameter	1-100 mm	-

The set-up and experimental design is aimed at mimicking the conditions during an ISO13679 CAL IV test program including multiple make-up and break-out cycles and micro-sliding to weaken the metal-to-metal seal (Section 2.3). The impact on the sealing ability can subsequently be quantified by a leakage test using gas or fluid pressure. The main difference with the CAL tests is that the SSMUR is used to deliberately find a leak to validate models with, whereas the CAL is aimed at qualification for leak tightness. Models which can subsequently be used to predict sealing ability of premium casing connection metal-to-metal seals [8].

Care has been taken that the actual conditions in a metal-to-metal seal, as discussed above, are well represented. An overview of the test set-up and testing methodology to achieve these goals is given in the following sections.

I.2. General specimen preparation and data collection

The repeatability of the tests and related procedures were assured and refined by multiple pilot tests prior to a test campaign or whenever changes were made to the set-up. In addition, checks were in place by measuring prior to each test the form and surface topography of the specimen seals using a white light interferometer (Appendix II.8.1). Consistency was further ensured by batch wise manufacturing for a single test campaign and phosphating under controlled lab conditions.

The specimens were prepared by the following procedures discussed in more detail hereafter.

1. Cut to size a piece of tubular from the mother material.
2. Manufacture the specimens on a lathe according to specifications on drawings.
3. Quality control of applied surface topography by white light interferometry.
4. Assign unique 5-digit number to each specimen.
5. Mark specimens with A-B-C at 120 degrees intervals. Location A marks the 0 degree position. In earlier tests pin and box would match as follows (pin on box): AA-BC-CB.

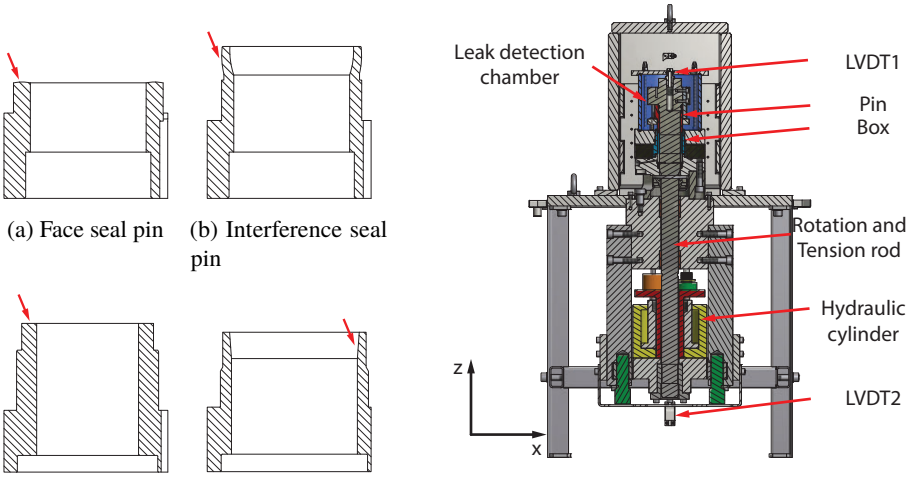

(a) Face seal pin (b) Interference seal pin

(c) Face seal box (d) Interference seal box

(e) Load frame

Figure I.1.: Figure I.1a shows a pin cross section and Figure I.1c shows a box cross section for the face seal specimens. Figure I.1b shows a pin cross section and Figure I.1d shows a box cross section for the interference seal specimens. The contact locations are indicated with an arrow. Figure I.1e shows the load frame that is used to execute the experiments on these specimens with the most important parts indicated.

This was later corrected to be: AA-BB-CC to avoid confusion and will be made clear when discussing results.

6. Cleaning (general protocol in Appendix II.3) and subsequent phosphating of specimens (all in same batch). Only the box was typically phosphated in agreement with the situation in the field.

7. Surface topography measurement or surface replica(s) before the test(s).

I.2.1. Specimen manufacturing

Specimens were manufactured from thick walled P110 tubing using a lathe. The properties of the material are given in Table I.2. This material was used for all the SSMUR specimens discussed in this thesis. To ensure repeatable surface topography for the test campaign, special attention was given to the metal-to-metal seal area. This was achieved by specifying the dimensions of the carbide cutting element, setting a fixed feed rate and depth of cut and using a new cutting element for each specimen.

Table I.2.: Properties of the mother material used for manufacturing the SSMUR specimens presented in this thesis. Properties were obtained according to ISO6892-1:2009.

Pipe ID	Yield stress Rp0.2 [MPa]	Ultimate tensile strength Rm [MPa]	Uniform plastic elongation Ag [%]	Fracture elongation A5 [%]	Hardness HV10
51876	861	947	6.3	18.8	306

Table I.3.: Overview of the phosphate conversion coating processes for the AISI4130 and P110 substrate.

Step	Treatment	Zinc phosphate	Manganese phosphate
1	Degreasing	Gardoclean® 349, 50 g L^{-1}, 75 °C, 10 min dip	
2	Rinsing	cold water	
3	Activation	Gardolene® V6522, 2 g L^{-1}, 40 °C, 1 min dip	Gardolene® V6563, 4 g L^{-1}, 40 °C, 1 min dip
4	Phosphating	Gardobond® Z3300, 75 °C, 5 min dip time, Free acid: 18, Total acid: 112, Fe++: 0.9 g L^{-1}	Gardobond® G4098 + 5 g L^{-1} Gardobond®Additive H7050, 90 °C, 5 min dip time, Free acid: 18; Total acid: 119; Fe++: 1 g L^{-1}
5	Rinsing	cold water & demineralized water	
6	Drying	oven 95 °C	
-	Coating weight	4.5 g m^{-2}	10.95 g m^{-2}

I.2.2. Phosphating

After manufacturing, the specimens were cleaned, degreased and water rinsed before they were dipped in the zinc or manganese phosphate bath. The process was carried out under laboratory conditions to ensure maximum uniformity and repeatability for the specimens. Industrial scale phosphating unfortunately gave to much variability as discussed in conference contribution [192]. See Table I.3 for an overview of the process parameters. The resulting coating weights are reported in the final row. Note, however, that because of the morphology a coating thickness is difficult to define [66]. Therefore, weight per unit area is reported in the table.

Typical SEM micrographs of the coating are shown in Figure I.2. Note the difference in magnification. The morphology for the zinc phosphate is the distinct needle shape in agreement with its orthorhombic dipyramidal unit cell [66, 75]. The morphology for manganese phosphate is the characteristic plate structure coming from its monoclinic prismatic unit cell [66, 76]. The manganese phosphate process produces a much denser and more refined coating compared to zinc phosphate because of its smaller crystal size [66].

X-ray diffraction (XRD) measurements were performed to characterize the phosphate crystal

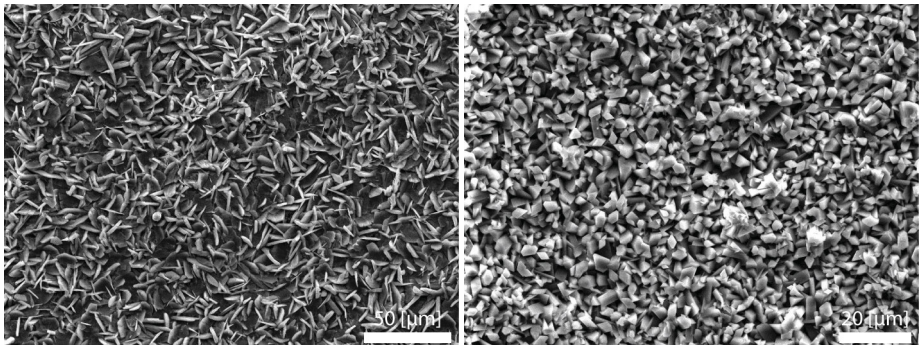

(a) ZP (b) MP

Figure I.2.: SEM micrographs of the phosphate coatings and the crystals that they contain. Figure I.2a shows zinc phosphate with is characteristic needle structure. Figure I.2b is manganese phosphate with its characteristic plate structure. Note the difference in magnification between the zinc and manganese phosphate specimens. Reproduced from paper A.

type. The measurements were performed on 2 different positions on the sample surface. For the manganese phosphate coatings, an additional measurement with a measurement time of 3600 s/frame was performed. The measurement settings are reported in Paper A. The XRD characterization of the specimens confirms that the crystal structure for zinc phosphate is predominantly hopeite [75] while for manganese phosphate it is hureaulite [76], see Figure I.3.

I.2.3. Surface topography before and after the test

To track the changes to the surface topography by plastic deformation and wear during the test all specimens were measured before the test using a Bruker NP-FLEX white light interferometer (Appendix II.8.1). Measurements were taken at locations spaced by 120 degrees over the circumference marked by A-B-C, see for instance Figure 3.1 for an example. To track the surface evolution of the specimen surface replica's were taken at intermediate steps during the assembly phase at locations A-B-C using the surface replication technology provided by Struers (RepliSet-T3). Finally, after the test the part was measured to capture the end state of the micro geometry. In order to do this, an area of 2x3 mm was captured using the matching and stitching capabilities of the Bruker NP-FLEX and the Bruker Vision64 software.

For the specimens with a seal on the inner diameter another procedure was followed. Using the Struers RepliSet-T3 and a specially designed mould replica's were taken from the inner diameter seal surfaces and stored for measurement at a later stage. The same procedure was followed for intermediate steps during the assembly for both pin and box and after the test for the box.

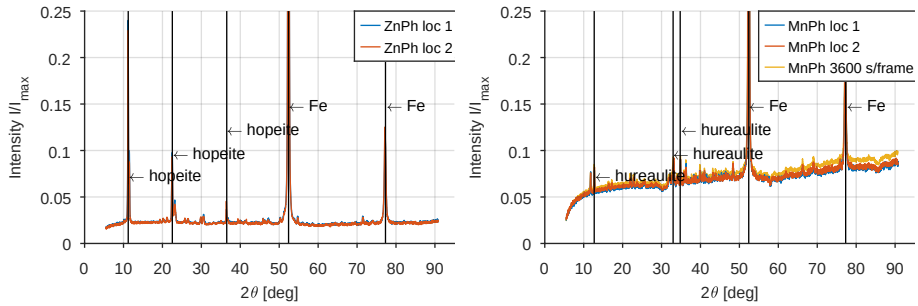

(a) ZP (b) MP

Figure I.3.: X-ray diffractograms for zinc and manganese phosphate coated specimens. The intensity is normalized by the maximum intensity. The peaks at $52.4\,\mathrm{deg}$ and $77.3\,\mathrm{deg}$ are from the iron in the substrate. The remaining diffractogram is in agreement with hopeite for zinc phosphate and hureaulite for manganese phosphate. Reproduced from Paper A.

I.2.4. Contact stress distribution before and after the test

Prior to and after each face seal test the contact stress distribution was determined using FUJiFILM Pressure Measurement Film by applying 10 kN normal force with the film between the contacting surfaces. The resulting distribution was analysed with the accompanying software to obtain the contact stress in MPa from the colour intensity of the pressure sensitive chemistry. Based on this result the initial flatness of the contact could be characterised and changes because of wear detected. Next to that, correlations could be made with the location of the onset of leakage. Note that this was not possible for the interference seal specimens as the applied shear because of the axial movement affects the measurement or would tear the film apart.

I.2.5. Roundness before and after the test

For the interference seal specimens, instead of measuring the contact stress directly, the roundness was measured before and after the test using a Mitutoyo Roundtest® RA-1600.

I.3. Test set-up, specimen and test protocol overview

As mentioned in the introduction two specimen types can be used in the SSMUR. These will be discussed in detail below. Before that an overview of the set-up is given in the as build state in Figure I.4 with the most important elements indicated to aid in the explanation below. The detailed test protocols can be found in Appendix I.7.

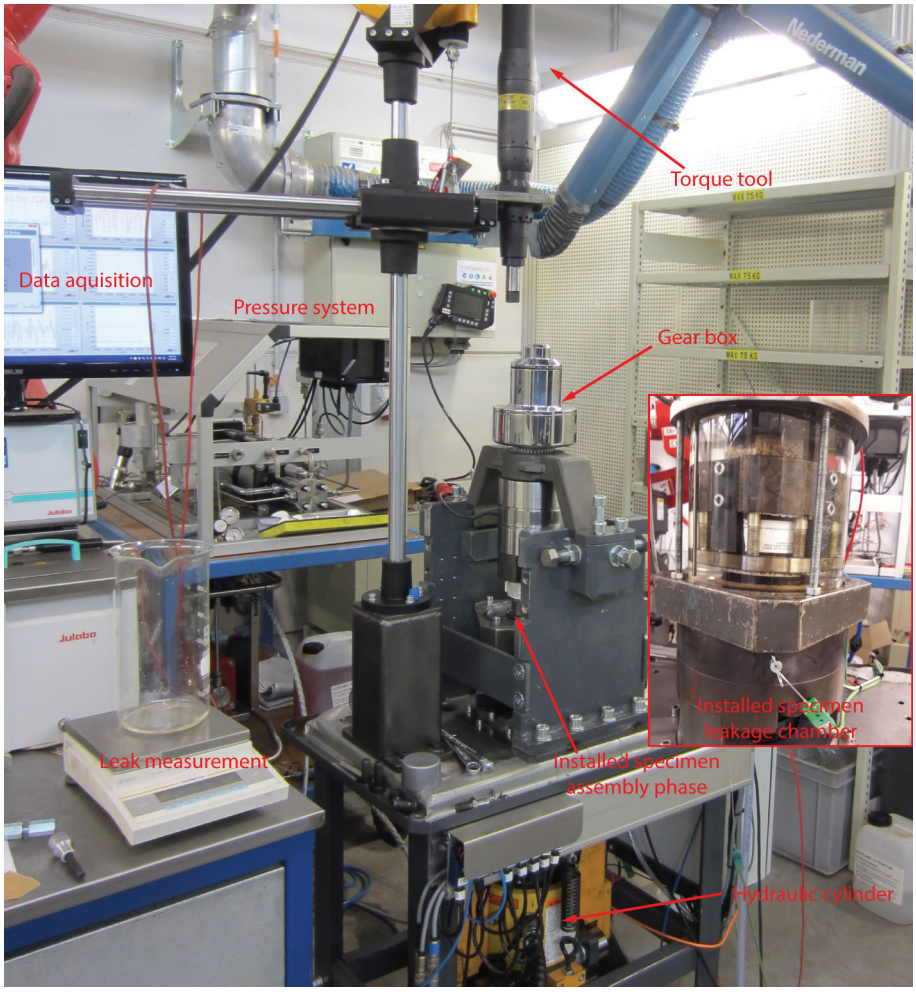

Figure I.4.: Overview of the Shell Sealing Mock-up Rig in the lab as build according to the schematic in Figure I.1e. Shown are: the data acquisition build in Labview® , Resato pressure unit for application of internal gas/liquid pressure, Torque tool for rotational make-up and break-out, gear box to reduce rotational velocity to 24 mm s^{-1}, installed face seal specimen, Enerpac hydraulic cylinder for application of normal force and axial displacement and Mettler Toledo balance for leak detection and rate measurement. Inset image shows the sealing ability mode with glass leakage chamber installed around the specimen and filled with glycol.

Table I.4.: Summary of face seal experimental conditions.

Geometry	
Round-off radius pin	10-80 mm
Contact line mean diameter	70 mm
Make-up/break-out	
Normal load	30-60 kN
Contact intensity	136-272 kN m^{-1}
Hertzian contact stress (max)	0.25-0.36 GPa
Hertzian contact width (max)	1.4 mm
Linear velocity	24 mm s^{-1}
Sealing ability	
Maximum normal load	120 kN
Contact intensity	546 kN m^{-1}
Hertzian contact stress (max)	0.5 GPa
Hertzian contact width (max)	1.4 mm
Temperature	ambient conditions
Internal pressure (liquid)	700 bar
Pressurizing medium	Julabo Thermal HS

I.3.1. Face seal set-up

The face seal set-up or ring-on-ring test provides circumferential line contact at equivalent contact stresses, sliding lengths and sliding velocities as they occur in metal-to-metal seals (Section 2.3). Sliding tests are performed with continuous contact equivalent to the assembly of a casing connector. After "assembly" a seal ability test can be performed. The experimental conditions will be described hereafter and are summarized in Table I.4.

The contact configuration is flat against a round-off of R = 80 mm line contact. The contact line diameter is approximately 70 mm and the contact width approximately 1 mm. The sliding tests are performed at a contact intensity of 136-273 N mm^{-1} or a maximum Hertzian contact stress of 0.25-0.36 GPa by applying 30-60 kN normal force as shown in Figure I.5a. The sliding velocity is 24 mm s^{-1}. The total sliding length is 1 revolution or 220 mm. At predefined sliding lengths, the contacts are separated and a surface replica of the surface topography is taken to monitor surface evolution. The lubricant is removed and reapplied at each of these steps.

After assembly the specimen inner diameter was filled with glycol, assembled, and subjected to a 60-120 kN normal force corresponding to a 273-546 N mm^{-1} contact intensity or a 0.5 GPa maximum Hertzian contact stress. On the outside the specimen was submerged in a glass chamber filled with thermal oil which acted as leak detection fluid. The glass chamber was connected with a tube to a beaker on a balance to monitor displacement of the thermal oil by the glycol. Then an internal fluid (Julabo Thermal HS) pressure of 700 bar was applied using a pump (Resato BMS). When a steady state was reached the load was gradually lowered

Table I.5.: Summary of interference seal experimental conditions.

Geometry	
Round-off radius pin	39 mm
Contact line mean diameter	73.7 mm
Make-up/break-out	
Axial interference (max)	2 mm
Contact intensity (max)	546 kN m^{-1}
Hertzian contact stress (max)	0.7 GPa
Hertzian contact width (max)	1 mm
Linear velocity	24 mm s^{-1}
Sealing ability	
Axial interference (max)	2 mm
Contact intensity (max)	546 kN m^{-1}
Hertzian contact stress (max)	0.7 GPa
Hertzian contact width (max)	1 mm
Temperature (bake-out)	180 °C
Bake-out duration	12 h
Temperature (sealability)	ambient
Internal pressure (gas)	700 bar
Pressurizing medium	N_2

in a stepwise manner and leakage was monitored for 15 minutes per step until a leak was observed.

I.3.2. Interference seal set-up

The interference seal set-up provides a radial line contact at equivalent contact stresses, sliding lengths and sliding velocities as they occur in metal-to-metal seals (Section 2.3). The specimen is 3x assembled-disassembled and finally assembled using a position controlled process by mounting it on a threaded rod which screws into a nut. The screw thread has a pitch of 3 mm rev^{-1}. The experimental conditions will be described hereafter and are summarized in Table I.5.

The contact configuration is a round-off of 39 mm against a conical flat with a taper angle of 4 degrees. Assembly is performed over approximately 0.5 revolution resulting in a monotonically increasing contact stress according to Figure I.5. At the maximum interference position a contact stress of 700 MPa is generated as determined by finite element analysis (FEA) with Abaqus and the contact model in this thesis Chapter 6. The sliding velocity is 24 mm s^{-1}. The total circumferential sliding length is approximately 1100 mm on the pin and approximately 363 mm on the box.

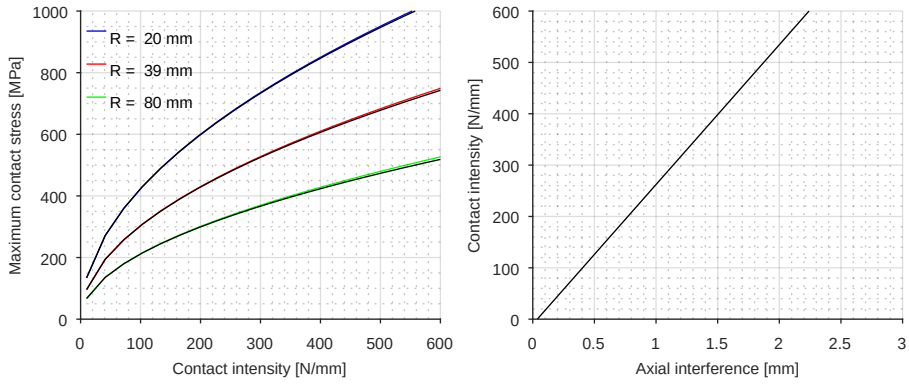

(a) (b)

Figure I.5.: Characterisation of maximum Hertzian contact stress versus contact intensity for the face seal and interference seal specimen. Results were obtained with the implemented contact model producing the same results as the Hertz solution for line contacts [33] shown in black. The contact intensities for the interference seal were obtained with an axi-symmetric FEA model in Abaqus as shown in Figure I.5b and used as boundary condition in the contact model of Chapter 6.

After each assembly-disassembly, for selected specimens, a full circumferential replica of the surface topography is taken to monitor surface evolution. The lubricant is removed and reapplied at each of these steps. After the assembly-disassembly's and final assembly the specimen is baked out for 12h at 180 °C. This is to stress the thread compound to investigate its performance after exposure to subsurface temperatures in the subsequent seal ability tests at ambient conditions (Section 2.3).

The seal ability tests comprised of two parts: performance under micro sliding and performance under progressively lower interference or contact stress. The micro sliding tests were performed by reciprocating the specimen up by 500 µm for 10 cycles using the hydraulic cylinder and a nut restricting the movement. After 10 cycles the specimen was pressurized to 700 bar internal gas (N_2) pressure and seal ability monitored for 15 minutes. If no leak was observed the next 10 cycles were applied. This was repeated 4 times. If still no leak was observed the second part started by gradually reducing the interference by moving the pin up in steps of 100 µm. At each step the seal ability was monitored for 15 minutes. This continued until a leak was found. The remaining interference was recorded as the failure point.

I.4. Analyses after the test

After the test the specimens were inspected using digital light microscopy. If it was necessary, additional analysis was performed. This could entail scanning electron microscopy (SEM) combined with energy-dispersive X-ray spectroscopy (EDX), broad and focused ion beam cross sectioning (BIB, FIB) which were subsequently analysed in the SEM, X-ray Diffractometry

(XRD) and nano-indentation. This will be indicated in the text when applicable. For an overview of the used equipment see Appendix II.8.1.

I.5. Supporting experimental work

To better understand observations made in the SSMUR set-up supporting experimental work was performed in a pin-on-disc tribometer (Bruker UMT-3), the ploughing asperity tester (PAT) and a strip tester or Quiri tribometer (Hydromecanique). To support this work analyses were performed using Confocal Microscopy (CM), atomic force microscopy (AFM), SEM/EDX, FIB/SEM, XRD, X-ray Photoelectron Spectroscopy (XPS), rheometry, ThermoGravimetric Analysis (TGA), Differential Scanning Calorimetry (DSC) and nano-indentation. For brevity the details of the experimental methods are given in Appendix II and will be summarized in the text when relevant.

I.6. SSMUR: Overview tests performed

An overview with the most important outcomes of the tests performed in the SSMUR that will be discussed in this thesis is shown in Table I.6 for the face seal set-up and Table I.7 for the interference seal set-up respectively.

I.7. SSMUR: step-by-step test execution

The step-by-step test execution following the summaries given in Section I.3 is listed in this section for each specimen type.

I.7.1. Face seal

In general the following consecutive steps are taken during the experiment:

1. Mount sample set
2. Verification of contact pressure distribution before rotation test using pressure sensitive foil.
3. Apply lubrication.
4. Apply constant force on sample and rotate sample over a certain angle.
5. Remove constant force, lift specimens apart, clean surfaces, inspect for damage and take replica's at position A, B and C.
6. Go to step 3 again according to test schedule.

Table I.6.: Overview of the experiments performed with the face seal set-up. Sealing ability tests were performed with Julabo Thermal HS as pressurizing medium.

Set #	Box	Coating	Pin	Coating	Thread compound	Average COF (-)	CI make up ($N\,mm^{-1}$)	Sliding length (mm)	CI at leak ($N\,mm^{-1}$)
Galling									
FG01[a]	65282	AsM	65248	AsM	API mod	0.08	136	220	136
FG02[b]	65300	AsM	65298[b]	AsM	O933	0.2	136	37.5	-
FG03[c]	65270	AsM	65258	AsM	O933	0.23	136	20	68
Running-in followed by sealing ability									
FRS01[d]	65297	MP	65251	AsM	O933	0,15	273	1543	270
FRS02[e]	65279	AsM	65262	ZP	API mod	0,1	273	665	-
FRS03[f]	65280	AsM	65263	ZP	API mod	0,1	273	1160	-
FRS04[g]	65265	MP	65277	ZP	API mod	0,14	273	1105	-
FRS05	65272	MP	65256	AsM	O933	0,15	136	220	130
FRS06	65273	MP	65259	AsM	API mod	0,15	136	220	62
FRS07	65275	ZP	65267	AsM	API mod	0,15	136	220	55
FRS08	65276	MP	65264	ZP	API mod	0,15	136	220	229
FRS09	65274	ZP	65260	AsM	O933	0,15	136	220	103
FRS10	65289	AsM	65266	ZP	YD-D	0,1	133	220	40
FRS11	65284	MP	87935	AsM	O933	0,15	136	220	70
FRS12	65287	MP	87936	AsM	API mod	0,15	136	220	116
FRS13	87923	MP	87938	AsM	YD-D	0,1	136	220	57
FRS14	87925	MP	65252	AsM	YD-A	0,07	136	220	58

a Galling observed in friction data after 77.5 mm.
b Turning pitch/feed rate 0.25 mm instead of 0.125 mm; Galling observed in friction data after 20 mm.
c Rotated in one step to reported sliding length, small galling spot observed.
d To failure, galling observed in friction data after 1323 mm.
e To failure, galling observed in friction data after 592 mm.
f To failure, galling observed in friction data after 1032 mm.
g Test stopped because of mishap, no galling observed.

Table I.7.: Overview of the experiments performed with the interference seal set-up. Sealing ability tests were performed with N_2 as pressurizing medium.

Set #	Box	Coating	Pin	Coating	Thread compound	Average COF (-)	Sliding length (m)	Interference make-up (mm)	Interference leak (mm)
Galling									
IG01	64726	AsM	64715	AsM	API mod	0.15	116	0.75[a]	N/A
IG02	64716	AsM	64728	MP	API mod	0.1	97	1.05	0.2
Running-in followed by sealing ability									
IRS01	64730	MP	87885	AsM	SM	0.08	1109	1.85	0.2
IRS02	64729	MP	87884	AsM	SM	0.08	1109	1.89	0.6
IRS03	64731	MP	87890	AsM	SM	0.09	1435[b]	1.85	0.4
IRS04	64732	MP	87892	AsM	SM	0.08	1272	2.11[c]	0.4
IRS05	64733	MP	87893	AsM	SM	0.1	1272	2.1[c]	1.0

a Interference was lower because of galling.
b Additional disassembly was needed to place forgotten seal ring for sealing ability tests.
c Increased interference test.

7. After the last step, rotate further to the same relative pin-box position as at the end of the rotation test and apply CI according to test schedule.
8. Install leak detection set-up.
9. Perform leak test schedule by stepwise lowering of normal force until leakage is observed.
10. Clean surfaces, inspect for damage.
11. Verify contact pressure distribution after test.

I.7.2. Interference seal

The interference seal tests are more involved and entail the following consecutive steps:

1. Mounting of specimen set.
2. Apply lubrication.
3. Bring pin and box sample in contact and rotate sample over a certain angle to the desired axial displacement.
4. Check resulting axial displacement with LVDT.
5. If not sufficiently in contact yet, rotate further to obtain the target axial displacement.
6. Break out using the same sub-steps in reverse order.
7. Clean sample and inspect for damage.
8. Repeat steps 2 to 7 two times.
9. Perform final make-up by repeating steps 2 to 5.
10. Engage lock nut and install leak detection setup.
11. Set clearance of the lock nut to obtain the correct amount of release of the axial interference during the subsequent pressurizing step.
12. Install safety cover and pressurize to 700 bar. Check axial displacement.
13. Increase cylinder pressure to 100 bar (axial displacement changes).
14. Decrease cylinder pressure to 60 bar (axial displacement changes).
15. Repeat steps 13 and 14 until the released position is reached for the tenth time, in this case increase the cylinder pressure to bring the axial position in the middle of the axial stroke during the cycling and perform a leak test for 15 min.
16. Repeat step 15 four times.

17. Release internal pressure; if necessary apply a little pressure in the cylinder, lift up and secure safety cover and increase special lock nut clearance to next level in order to reduce the axial interference. Lower safety cover and pressurize to 700 bar, check axial displacement and perform a leak test for 15 min.
18. Repeat step 17 for all the required axial displacement levels until a leak is observed.
19. Disassemble, clean surfaces and inspect for damage.

I.8. Conclusion

A newly designed test set-up for metal-to-metal sealing investigations was presented. The set-up can perform make-up and break-out sliding to run-in the sealing surface under controlled conditions including the axial progression of the thread pitch. Subsequently, it allows studies of face seal and interference seal sealing ability behaviour including the effects of running-in and thread compound bake-out under internal fluid or gas pressure. The sealing ability performance of a specimen is determined by gradually lowering the contact stress by controlling normal force or axial interference respectively until leakage is observed.

This page has been intentionally left blank.

II. Materials, lubricants, small scale test methods and analyses

II.1. Introduction

As discussed in the introduction in Chapter 1, a connection sees two types of relative motion. Make-up (circumferential direction) resulting in a velocity vector oriented parallel to the waviness and micro-sliding (axial direction) resulting in a velocity vector perpendicular to the waviness. This was mimicked in these tests.

The design of the scaled tests and related cumulative sliding lengths is in accordance with ISO13679 [193] CALIV dictated assembly-disassembly tests and load cycling as discussed in Section 2.3. To give an indication of the contact conditions, the (Hertzian [194]) contact stresses were calculated using the mechanical properties of the substrate with a Young's modulus of 210 GPa and Poisson ratio of 0.3.

II.2. Materials

Casing is manufactured with quenched and tempered steel grades. The grades are designated by a letter and a number. The number represents the yield strength of the material in kilo pounds per square inch (ksi). See Table II.1 for an overview of the API standardized grades and their chemical composition [193]. Note that these grades are chemically quite close which means the mechanical properties are mostly controlled with the heat treatment. The chemistry is close to that of AISI 4130 and 4140 steel. This material was used as substitute for the oil field grades as it can be obtained in standard shapes such as rod and flat.

Scratch tests were performed with a sharp indenter made of quenched and tempered Sverker21 steel with a round-off radius, r, of 100 µm which connects in a continuous manner to a 90° conical section [196]. The surface hardness is 700 HV and the surface finish is polished with an $\mathrm{S_a} = 0.01\,\mu\mathrm{m}$.

The pin on disc tests were carried out using an R = 5 mm bearing steel (AISI52100) ball against a quenched and tempered steel (AISI4130) disc. The chemical composition is reported in Table 1. The ball is polished and has a surface roughness of $\mathrm{S_a} = 0.01\,\mu\mathrm{m}$ and a surface hardness of 700 HV. The disc surface is polished, ground or turned and has a surface roughness of $\mathrm{S_a} = 0.01\,\mu\mathrm{m}$, $\mathrm{S_a} = 0.10\,\mu\mathrm{m}$ or $\mathrm{S_a} = 1.60\,\mu\mathrm{m}$ respectively. The surface hardness was 240 - 320 HV. See Figure 2 for a measurement of the surface topography. The disc is subsequently zinc or manganese phosphated.

Table II.1.: Chemical composition by wt% of API casing material grades. Reproduced from [195].

Gr.	Grade	Type	C	Mn	Mo	Cr	Ni	Cu	P	S	Si
1	H40	-	-	-	-	-	-	-	≤0.03	≤0.03	-
	J55	-	-	-	-	-	-	-	≤0.03	≤0.03	-
	K55	-	-	-	-	-	-	-	≤0.03	≤0.03	-
	N80	1	-	-	-	-	-	-	≤0.03	≤0.03	-
	N80	Q	-	-	-	-	-	-	≤0.03	≤0.03	-
	R95	-	≤0.45	≤1.9	-	-	-	-	≤0.03	≤0.03	≤0.45
2	M65	-	-	-	-	-	-	-	≤0.03	≤0.03	-
	L80	1	≤0.43	≤1.9	-	-	≤0.25	≤0.35	≤0.03	≤0.03	≤0.45
	L80	9Cr	≤0.15	0.3 - 0.6	0.9 - 1.1	8.0 - 10.0	≤0.5	≤0.25	≤0.02	≤0.01	≤1
	L80	13Cr	0.15 - 0.22	0.25 - 1	-	12.0 - 14.0	≤0.5	≤0.25	≤0.02	≤0.01	≤1
	C90	1	≤0.35	≤1.2	0.25 - 0.85	≤1.5	≤0.99	-	≤0.02	≤0.01	-
	T95	1	≤0.35	≤1.2	0.25 - 0.85	0.4 - 1.5	≤0.99	-	≤0.02	≤0.01	-
	C110	-	≤0.35	≤1.2	0.25 - 1	0.4 - 1.5	≤0.99	-	≤0.02	≤0.005	-
3	P110	-	-	-	-	-	-	0.03	≤0.03	-	-
4	Q125	1	≤0.35	1.35	0.85	1.5	≤0.99	-	≤0.02	≤0.01	-

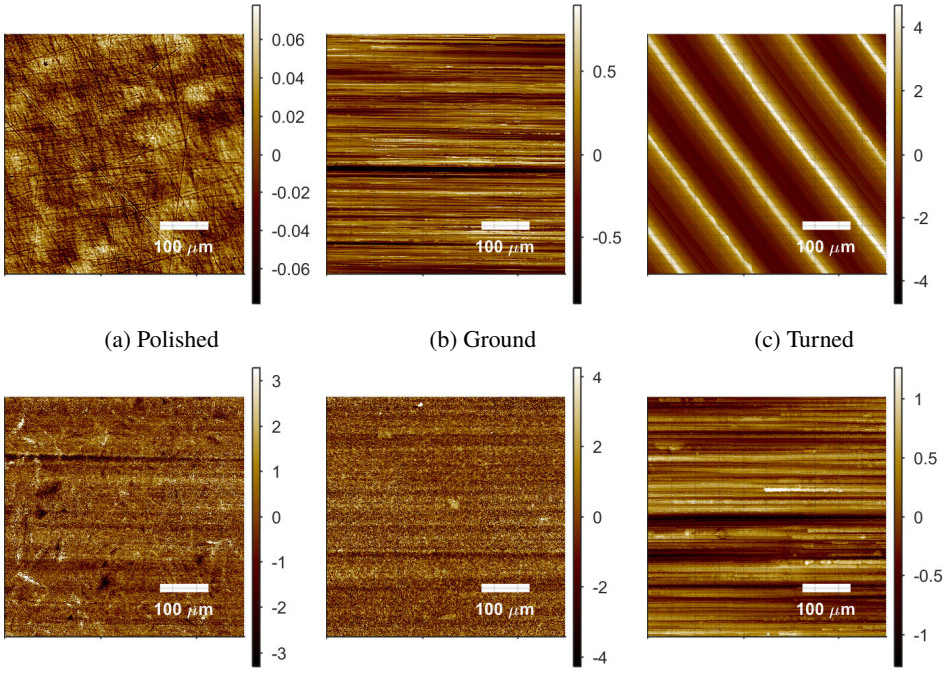

(a) Polished (b) Ground (c) Turned

(d) Zinc phosphate (e) Manganese phosphate (f) Copper plating

Figure II.1.: Sampling of surface topographies investigated in this work. Mean height is set to zero, height in µm.

The strip tests are done using a steel anvil against a steel strip. The anvils and strips are manufactured from the same 4" diameter P110 tubing as the SSMUR specimens in Appendix I. The anvil is turned and has a surface roughness of $S_a = 1.6\,\mu m$. The strip has the waviness applied by planing (mimicking a turned surface finish) with a cutting element in sliding direction and has a surface roughness of $S_a = 1.6\,\mu m$. Both surfaces have a slightly higher surface hardness of 320 HV becuase of the manufacturing process compared to Table I.2. The anvil is subsequently manganese phosphated using the process reported in Section I.2.2.

An overview of the various surface topographies is given in Figure II.1. The measurement have been performed with white light inferometry, see Section II.8.1.

II.3. Specimen preparation before and after the experiments

Specimens were cleaned prior to the tests using the following protocol. For bare steel specimens cleaning was done for 5 minutes in an ultrasonic bath using acetone as the solvent, it was subsequently blown dry using nitrogen gas and wiped clean from residue after evaporation of

Table II.2.: Overview particle properties and solids content by weight in the general API modified formulation, taken from [4].

Material	Compatibility Fe [181]	UTS MPa	Morphology	Mesh size µm [4]	wt% Total solids	wt% Compound
Amorphous graphite	-	-	Flake	<44	28.0	18.0 ± 1.0
Lead powder	0.125	18	Sphere	<44	47.5	30.5 ± 0.6
Zinc dust	0.5	$28 - 246$	Flake	<44	19.3	12.2 ± 0.6
Copper flake	0.32	$210 - 360$	Flake	<44	5.2	3.3 ± 0.3

the solvent by lens cleaning paper. For phosphate specimens cleaning was done by flushing with acetone and subsequently blowing dry with nitrogen. This was done to avoid removal of phosphate as a result of the sonication process.

To ensure maximum retention of generated surface layers the specimens were prepared for microscopy after the test by flushing the grease from the surface with heptane. Final rinsing was done by flushing with acetone and drying to air. For the subsequent measurement of the wear scars with the interferometer the specimens are ultrasonically cleaned in acetone for 5 minutes and wiped dry.

II.4. API modified

API modified was used as the reference. Details on the solid content are given in Table II.2. The variations on the full formulation are given in Table II.3. These variations are created by adding the same weight percent of an additive as listed in Table II.3 to the base grease and balancing the formulation to come to the same consistency as the full product. The particle properties are also listed in Table II.2.

II.5. Tribometry

This section will give an overview of the tribometers that were used over the coarse of this research. Figure II.2 gives an overview of the set-ups that will be discussed in detail hereafter.

Table II.3.: Overview composition and basic properties base greases.

Sample #	1	2	3	4	5	6	7
Short hand	API mod	bg	bg Cu	bg Zn	bg Pb	bg Zn Cu	API mod no Pb
Base oil	Mineral oil						
Thickener	Aluminium complex						
Penetration	310 -330	265 - 285	343	356	408	383	300
Graphite	X	-	-	-	-	-	X
Copper	X	-	X	-	-	X	X
Zinc	X	-	-	X	-	X	X
Lead	X	-	-	-	X	-	-

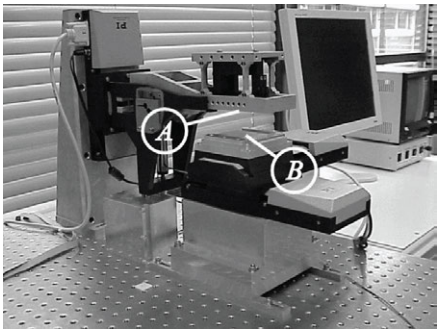

(a) Ploughing Asperity Tester

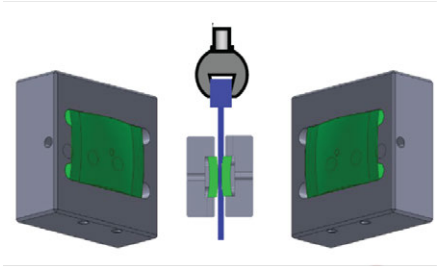

(b) Quiri tribotester

(c) Bruker UMT-3

Figure II.2.: Overview of the test set-up used in this work. Figure II.2a shows the ploughing asperity tester (reproduced from [197]). Figure II.2b shows the Quiri Hydromecanique tribotester. Figure II.2c shows the Bruker UMT-3.

Table II.4.: Ploughing asperity tester (PAT) technical specifications and limits [198].

Property	Maximum	Resolution
XY-movement	50 mm	1 µm
Z-movement	50 mm	9 nm
X-force	50 N	0.5 mN
Z-force	50 N	2 mN
Lateral/traversal velocity	0.001-50 mm s^{-1}	-
Specimen size	50 mm	-

II.5.1. Ploughing Asperity Tester

The ploughing asperity tester [196] is a dedicated test set-up for single asperity tests shown in Figure II.2a. The machine was used for the single and multiple unidirectional scratch tests. The capabilities are listed in Table II.4.

II.5.2. Pin-on-disc tribometer

The pin-on-disc experiments were performed with a UMT-3 (Bruker) shown in Figure II.2c. The UMT-3 is a modular universal mechanical tester capable of applying a normal load, F_N, of up to 1000 N. The load range and measurement accuracy are determined by the installed load cell. In this case a six degrees of freedom load cell (TFH-50) is installed. The capabilities are listed in Table II.5. The low velocity (0.05 – 0.5 mm s^{-1}) and high temperature (up to 250 °C) reciprocating tests were performed with the slider of the tribometer combined with the high temperature module (S35HE-350). Or, when under ambient conditions, with the low speed rotary drive (S20HE). The high velocity (>0.5 mm s^{-1}) reciprocating tests were performed with a dedicated reciprocating drive module (RF33FE), see Figure II.3 for an overview.

In addition to room temperature tests, elevated temperature tests were performed. The temperature set points were 30–70–100–150–200–250 °C. Once the temperature set point was reached a 15 minute hold period followed to ensure the disc surface temperature also reached the set-point. Then 250 reciprocating cycles were made with a stroke of 500 µm. Hence a total of 1500 cycles are made for an equivalent sliding length of 1.5 m. The location on the disc, ball and lubricant are not changed or refreshed during the temperature steps.

II.5.3. Anvil-on-strip tribometer

The strip test was used for contact stresses and sliding velocities equivalent to those in the connection metal-to-metal seal. The contact is elliptical which is closer to the circumferential line contact in the seal area. The test was designed, however, to be limited to unidirectional sliding parallel to the waviness.

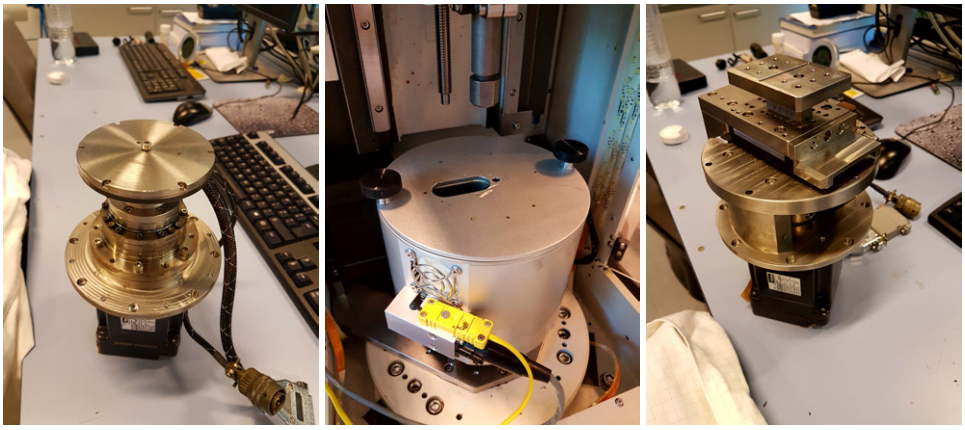

(a) (b) (c)

Figure II.3.: Overview of the used drive modules in the UMT-3. Figure II.3a shows the low speed drive (S20HE), Figure II.3b shows the high temperature (350 °C) drive S35HE-350 and Figure II.3c the reciprocating drive RF33FE.

Table II.5.: Bruker UMT-3 technical specifications and limits

Property	Maximum	Resolution
X-movement	120 mm	0.25 µm
Z-movement	150 mm	0.5 µm
XY-force	180 N	20 mN
Z-force	550 N	65 mN
XYZ-moment	22.5 N m	1.25 mN m
Lateral/traversal velocity	0.002-10 mm s^{-1}	-
Rotational velocity	0.001-80 min^{-1}	-
Temperature	350 °C	1 °C
Specimen diameter	15-90 mm	-

Table II.6.: QUIRI tribometer technical specifications and limits

Property	Maximum	Resolution
X-movement	20 mm	0.02 mm
Z-movement	500 mm	0.5 mm
X-force	15 kN	15 N
Z-force	25 kN	25 N
Lateral/traversal velocity	0.15-100 mm s^{-1}	-
Temperature	200 °C	1 °C
Specimen width	10-50 mm	-
Specimen thickness	0.5-5 mm	-

The strip tests are performed with a Quiri tribometer (Hydromecanique), see Figure II.2b for a schematic of the set-up and Table II.6 for its capabilities. In this case, unidirectional sliding tests are performed. The strip is mounted in a tensile tester. On each side of the strip an anvil is pressed at a prescribed load. The strip is then pulled up at a prescribed velocity while measuring the resultant friction force. The sliding tests are performed at a maximum Hertzian contact stress of 1.4 GPa by applying 20 kN normal load. For the as machined tests, a load ramp is applied over the first 5 strokes. The reason for this was the difficulty of distinguishing the performance of the different thread compounds when applying a constant load, i.e. they were all equally bad. The load ramp and thus milder conditions provided better differentiation. The contact spot is elliptic and approximately 5.7 mm x 1.1 mm. The sliding velocity is 24 mm s^{-1}. Up to 50 strokes were made with a sliding length of 31 mm which sums up to 1550 mm cumulative sliding length for the anvil.

II.6. Thermogravimetric analysis and differential scanning calorimetry

The thermal stability of compounds was investigated using a Mettler Toledo TGA/DSC 1 system shown in Figure II.4a. The device enables simultaneous TGA and DSC measurements over a temperature range from ambient to 1600 °C.

The thermal stability test entails a temperature sweep from ambient temperature (25 °C) to 250 °C, at a temperature increase rate of 10 °C min^{-1}, followed by a hold period of 30 minutes at the same temperature (250 °C). At the end of the hold period, a cooling rate of 10 °C min^{-1} was imposed to reduce the temperature from 250 °C back to room temperature. For the thread compounds the resistance to oxidation and their general thermal behaviour was investigated using:

1. Open cup vs. closed cup.
2. Air vs. nitrogen.
3. Mixing in iron oxide (hematite) to simulate wear particles.

All cups were loaded with approximately 60 mg of product.

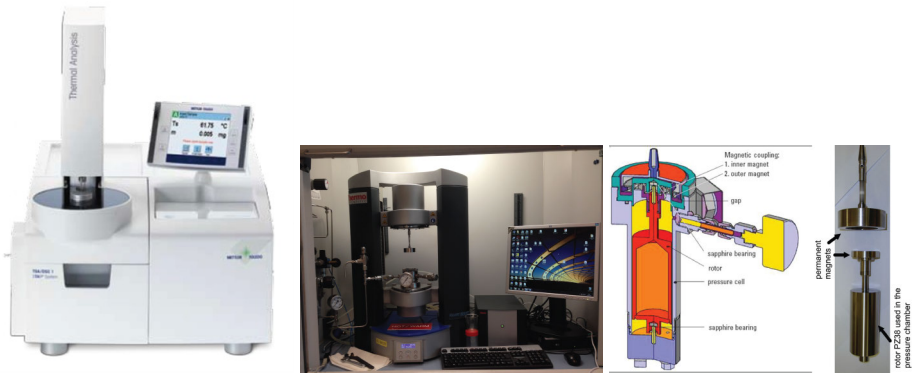

(a) (b) (c)

Figure II.4.: Mettler Toledo TGA/DSC 1 in Figure II.4a. Overview of Haake Mars III in Figure II.4b and used test geometry PZ38 in Figure II.4c.

II.7. Rheometry

The base oil and thread compound dynamic viscosities were measured using a Haake Mars III rheometer Figure II.4b with the PZ38 in Figure II.4c and Z10 coaxial cylinder geometry. Temperature was controlled using the Peltier module (TM-PE-C).

Two protocols were used. For protocol rheometer 1, the measurement geometry was a coaxial cylinder (PZ38) allowing measurements in a closed environment under N_2 conditions. The rheology measurements were carried out on a sample volume of 50 mL. Temperature was controlled using the Peltier module (TM-PE-C) up to a maximum temperature of 200 °C. The temperature set-points were 20-50-100-150-200 °C. At each set-point a 30 min hold was followed by a stress-controlled test over the range 1.5-800 Pa. The sample was not refreshed between the temperature steps. Protocol rheometer 2 used an open coaxial cylinder (Z10) performing a shear rate sweep 1.0-100 s^{-1} at 20-40-70-100-140-180-200 °C with 30 min temperature hold per step. This was followed with a 180 °C hold for 3 hours and another sweep at 180 °C to investigate the degradation.

II.8. Analyses

The following analytical techniques were used to analyse the specimens before and/or after the experiments.

II.8.1. Analytical equipment

The specimens were investigated using digital light microscopy (LM, Keyence VHX-5000) and measurements were taken with the accompanying software. When necessary additional

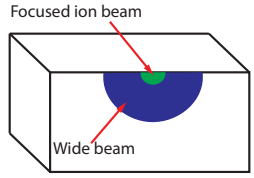

Figure II.5.: Schematic of the cross sectioning process. Initial cross section (blue) with broad ion beam. Final cross section (green) after initial broad beam polishing with focused ion beam.

analysis was performed with (a subset of) the following analytical techniques. Confocal Microscopy (CM, Keyence VK-9700), White Light Interferometry (WLI, Bruker NP-FLEX), Scanning Electron Microscopy (SEM, Tescan Vega 3, Jeol JSM-7001F SHL) combined with Energy-dispersive X-ray spectroscopy (EDX), Atomic Force Microscopy (AFM, NanoSurf Flex-Axiom in tapping mode with ACLA or ACTA cantilever), X-ray Diffractometry (XRD, PANalytical Empyrean diffractometer, Cu anode, focusing optics: 0.1 & 0.3 mm monocapillary), X-ray Photoelectron Spectroscopy (XPS, Kratos Axis Nova with 15kV Al Kα source), SEM on cross sections prepared with Focused Ion Beam (FIB, FEI Helios NanoLab 650, SII NanoTechnology Inc. SMI3000TB) and Broad Ion Beam (BIB, Jeol IB-19510CP) and nano-indentation (UNAT, Asmec).

II.8.2. Broad and focused ion beam cross sectioning

The ion beam cross sectioning of the specimens is performed with a broad ion beam (Jeol IB-19510CP) followed by a focused ion beam (SII NanoTechnology Inc. SMI3000TB). The broad ion beam is used to create a large flat cross section in one shot. This is done by applying a mask over the specimen regions that do not need to be cross sectioned. The cross section is then made by a broad Gallium ion beam. However, the cross section surface finish was not smooth enough for SEM purposes. Therefore focused ion beam was used in a subsequent step to polish a much smaller region within the broad ion beam cross section. This is done by a Gallium beam and finished with an Argon beam. See Figure II.5 for a schematic overview of the broad beam cross sectioning and subsequent focused ion beam polishing.

II.8.3. Nano-indentation

The nano-indentation was carried out using a diamond Berkovich tip. The loads applied ranged from 1 - 500 mN. Each test was repeated 15 times, tests with fracture events were discarded. The load was applied in 10 s, the hold time was 15 s and unloading was performed in 4 s. The tip geometry and measurement set-up were validated prior to the measurements using a sapphire reference. To establish a datum for the indentation tests, an indentation at 0.1 mN is made prior to the measurement. Processing of the force-displacement curves to become an indentation hardness is done according to the method of [199].

II.8.4. Tracking surface evolution using surface replication

Intermediate states of the surface topography were captured with a Struers RepliSet-T3.

II.8.5. De-trending surface topography measurements

Before plotting or determining the surface roughness areal values surfaces were prepared by removing form information as follows:

1. Read measurement data.
2. Fill in non-measured points by nearest neighbor interpolation.
3. Cut selection from measurement data: choice made was 570 µmx430 µm which corresponds to a single shot measurement at 11x magnification on the Bruker NP-flex.
4. If replica: invert data (all elements times -1) and flip left hand side to right hand side and vice versa to get "original surface" representation.
5. Remove tilt in measurement by subtracting the least squares plane.
6. Apply median filter to remove noise.
7. Remove form by line-wise de-trending the data by subtracting a least squares cubic spline.

This gives a surface which only includes waviness and roughness information.

II.8.6. Matching of before and after states using an iterative closest point algorithm

In order to match surface topography measurements before and after the tests an Iterative Closest Point (ICP) algorithm was modified that normally is used for image registration [200–202]. An example of the output is shown in Figure 6.8. The state before, z_{bef}, and the state after, z_{aft}, are matched as follows

$$z_{bef} = f(x, y, z) \tag{II.1}$$
$$z_{aft} = f(x, y, z) \tag{II.2}$$
$$\mathbf{R} = \mathbf{R}_z(\gamma)\mathbf{R}_y(\beta)\mathbf{R}_x(\alpha) \tag{II.3}$$
$$\vec{T} = \begin{pmatrix} x \\ y \\ z \end{pmatrix}. \tag{II.4}$$

Where z_{bef} is the point cloud in the Cartesian reference frame (x, y, z) that will be transformed till best alignment with the model points z_{aft}, $\mathbf{R}$ is a rotation matrix for the angles (α, β, γ)

around the axes in the direction of (x, y, z) and $\vec{T}$ ia a translation vector. Using the definition of equations (II.1)-(II.4) the following minimization problem is solved,

$$E = \sum_{i=1}^{N} \left\| \mathbf{R} z_{\mathrm{bef},i} + \vec{T} - z_{\mathrm{aft},i} \right\|^2, \tag{II.5}$$

to find the best alignment between z_{bef} and z_{aft}.

III. Supplemental materials: Chapter 3

Supplemental results for Chapter 3.

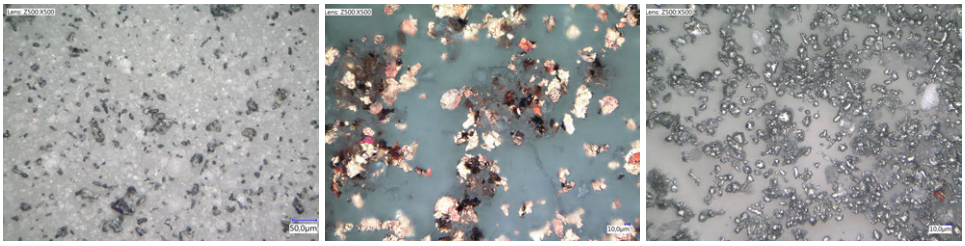

(a) Lead (b) Copper (c) Zinc

Figure III.1.: Overview of particle present in the single particle base greases after washing and decanting the base oil and thickener from the grease.

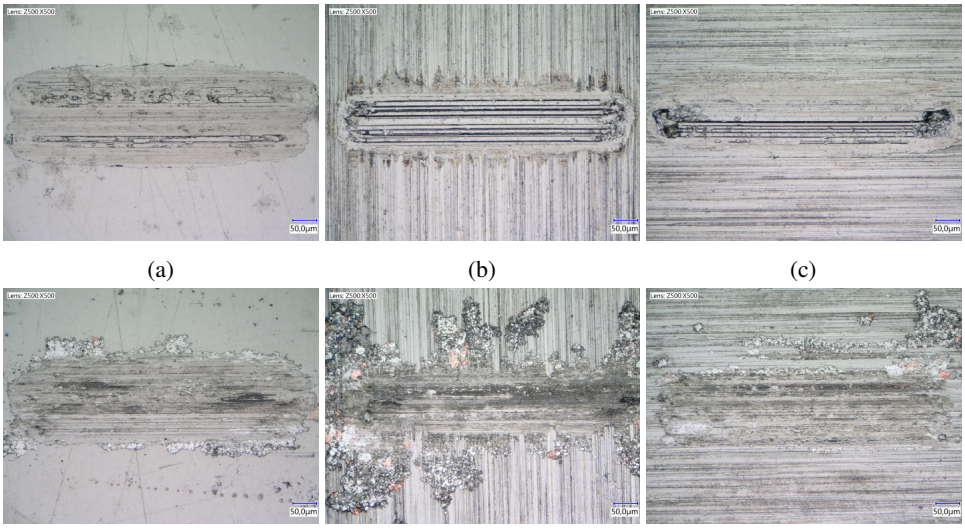

(a) (b) (c)

(d) Polished (e) Perpendicular (f) Parallel

Figure III.2.: Comparison of wear scars on a polished and ground disc perpendicular and parallel to the waviness with 500 µm stroke after 1 m cumulative sliding length with a 10 mm AISI52100 ball at 1 GPa. First row: base grease. Second row: API modified.

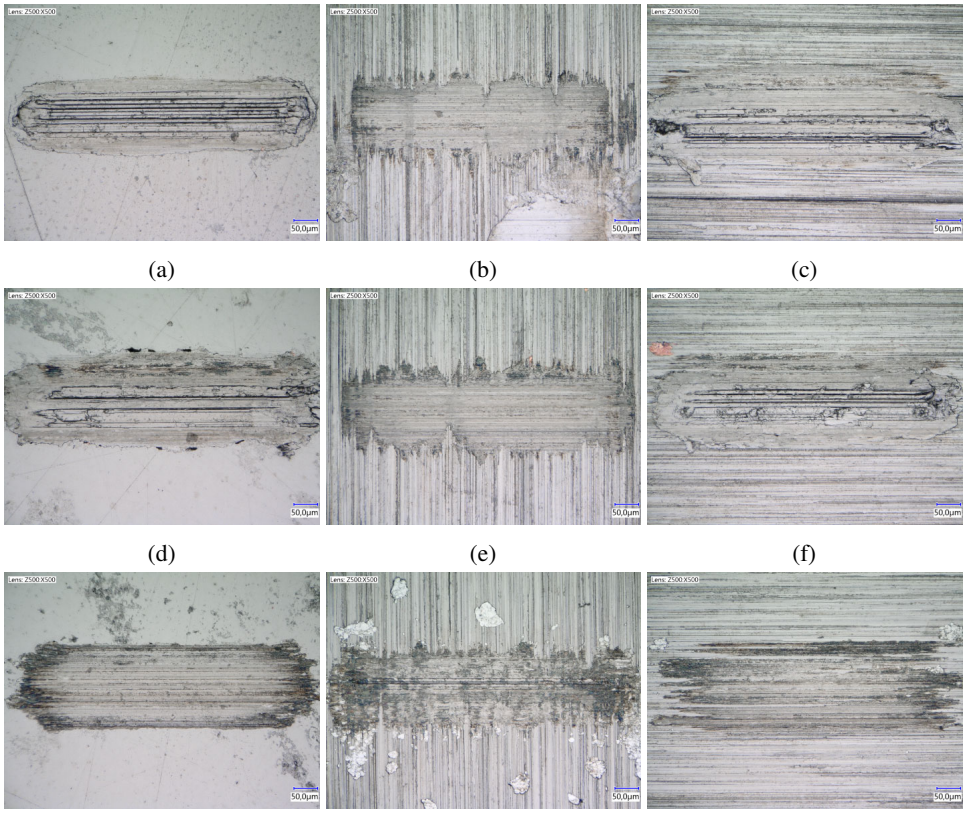

(a) (b) (c)

(d) (e) (f)

(g) Polished (h) Perpendicular (i) Parallel

Figure III.3.: Comparison of wear scars on a polished and ground disc perpendicular and parallel to the waviness with 500 µm stroke after 1 m cumulative sliding length with a 10 mm AISI52100 ball at 1 GPa. First row: base grease with lead. Second row: base grease with copper. Third row: base grease with zinc.

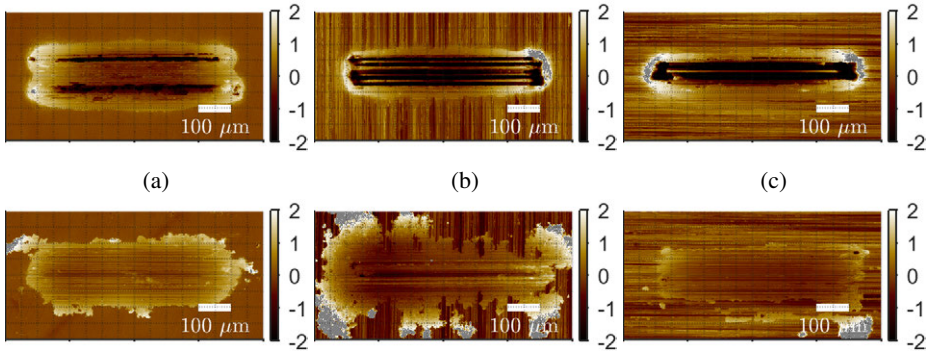

(a) (b) (c)

(d) Polished (e) Perpendicular (f) Parallel

Figure III.4.: Comparison of wear scars on a polished and ground disc perpendicular and parallel to the waviness with 500 µm stroke after 1 m cumulative sliding length with a 10 mm AISI52100 ball at 1 GPa. First row: base grease. Second row: API modified. Supplemental interferometer result for Figure III.2.

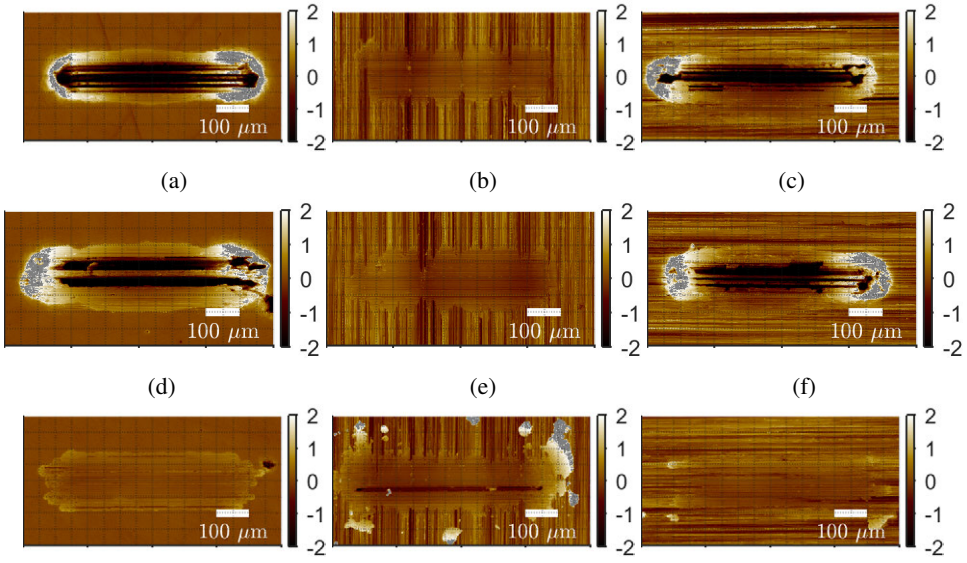

(a) (b) (c)

(d) (e) (f)

(g) Polished (h) Perpendicular (i) Parallel

Figure III.5.: Comparison of wear scars on a polished and ground disc perpendicular and parallel to the waviness with 500 µm stroke after 1 m cumulative sliding length with a 10 mm AISI52100 ball at 1 GPa. First row: base grease with lead. second row: base grease with copper. Third row: base grease with zinc. Supplemental interferometer result for Figure III.3.

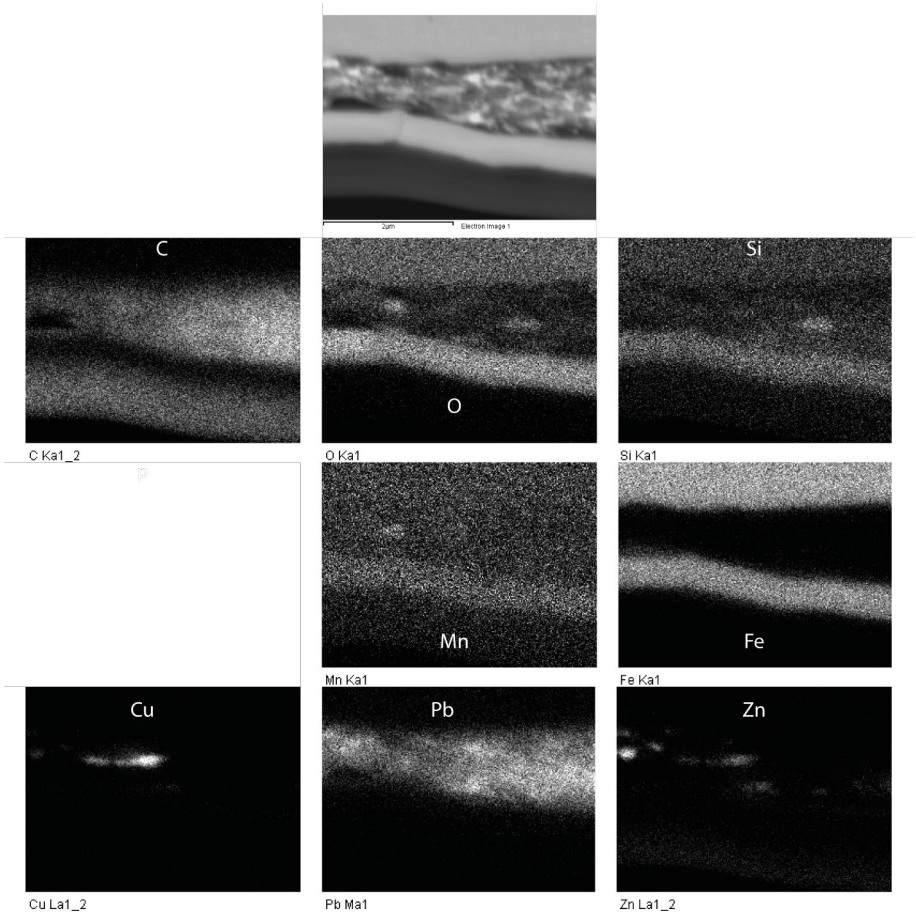

Figure III.6.: BSE image and EDX mapping corresponding to the SE image of Figure 3.1c for set FRS06 pin. Note that compared to Figure 3.1c the image is upside down because of remounting in a different SEM.

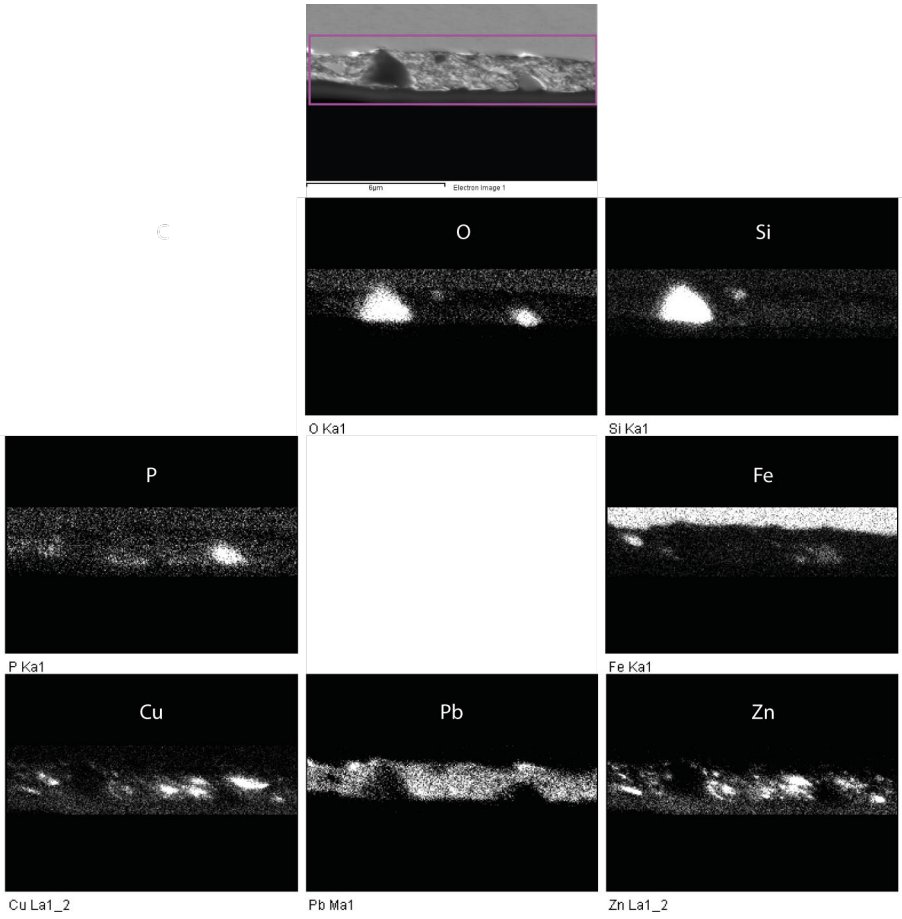

Figure III.7.: BSE image and EDX mapping corresponding to set FRS07 pin.

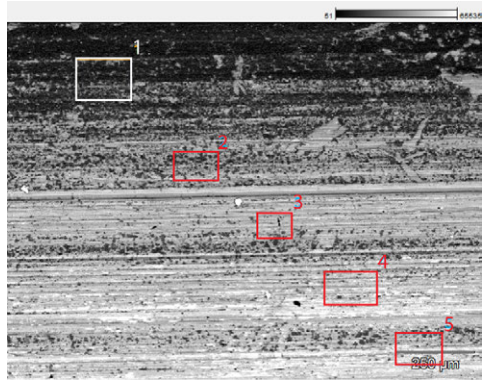

Figure III.8.: BSE image at 20 kV of the metal-to-metal seal area of a section cut from a salvaged VAM 21 connection shown in Figure 3.5. The image belongs to the EDX results in Table III.1.

Table III.1.: EDX results in wt% for presented figures. Trace elements like Si, Al and Ca have been left out for clarity of the presentation without recalculating the wt%.

					wt%				
Figure / location	C	O	Cr	Mn	Fe	Co	Cu	Zn	Pb
Figure 3.1a base metal	2.7		0.9	0.8	94.6	0.7			
Figure 3.1a	4.2		1.0	0.9	93.0	0.6			
Figure 3.1b	32.9	2.6			4.6		3.2	6.3	50.6
Figure III.8 1	10.2	35.1	0.9		33.9		0.1	10.6	1.4
Figure III.8 2	11.5	19.4	1.0		54.9			5.1	2.9
Figure III.8 3	12.7	8.0	0.7		68.9		0.1	2.2	4.7
Figure III.8 4	13.4	4.8	0.9		64.4		0.2	2.1	11.4
Figure III.8 5	15.9	8.0	0.9		62.5		0.2	2.6	7.5

IV. Supplemental materials: Chapter 4

The screened lubricants consist of off the shelve environmentally acceptable thread compounds that were compared to the reference API mod. Next to that, a clay based base grease was mixed with various additives to explore the feasibility of formulating a high temperature environmentally acceptable thread compound based on the film forming hypothesis that will be developed in this chapter. The lubricants are listed in Table IV.1, because of trade secrets most commercial compounds have undisclosed compositions except for ingredients that need to be mentioned in the material safety data sheet (MSDS) or that are mentioned with a general description on the technical data sheet (TDS).

Table IV.1.: Overview of the commercial thread compounds that were screened and the subsequent prototype compounds that were designed using the methods described in this chapter. Data obtained from TDS and MSDS.

Short hand	Base oil	Thickener	Additives based on MSDS (particles)	Dropping point °C
		Commercial thread compounds		
API mod	Mineral oil	Undis-closed	Lead, copper, zinc, graphite	>204
YD A	Synthetic PAO and ester	Undis-closed	Calcium fluoride, calcium sulphate, calcium carbonate, etc.	>288
YD B	Synthetic oil	Calcium complex	Calcium fluoride, titanium dioxide, calcium carbonate, etc.	>288
YD C	Synthetic ester	Undis-closed	Mineral fillers	>200
YD D	Undisclosed	Polyurea	Undisclosed	>270
		Shell prototype thread compounds		
SA	Mineral oil	Clay	Methyl metacrylate	>288
SB	Mineral oil	Clay	Lubrication grade graphite	>288
SG	Mineral oil	Clay	Calcium phosphate	>288
SJ	Mineral oil	Clay	SA + SB	>288
SK	Mineral oil	Clay	SB + SG	>288
SL	Mineral oil	Clay	SB + SG diff. ratio	>288
SM	Mineral oil	Clay	SA + SB + SG	>288
SN	Mineral oil	Clay	SA + SB + SG mixed in grease plant	>288

This page has been intentionally left blank.

V. Supplemental materials: Chapter 5

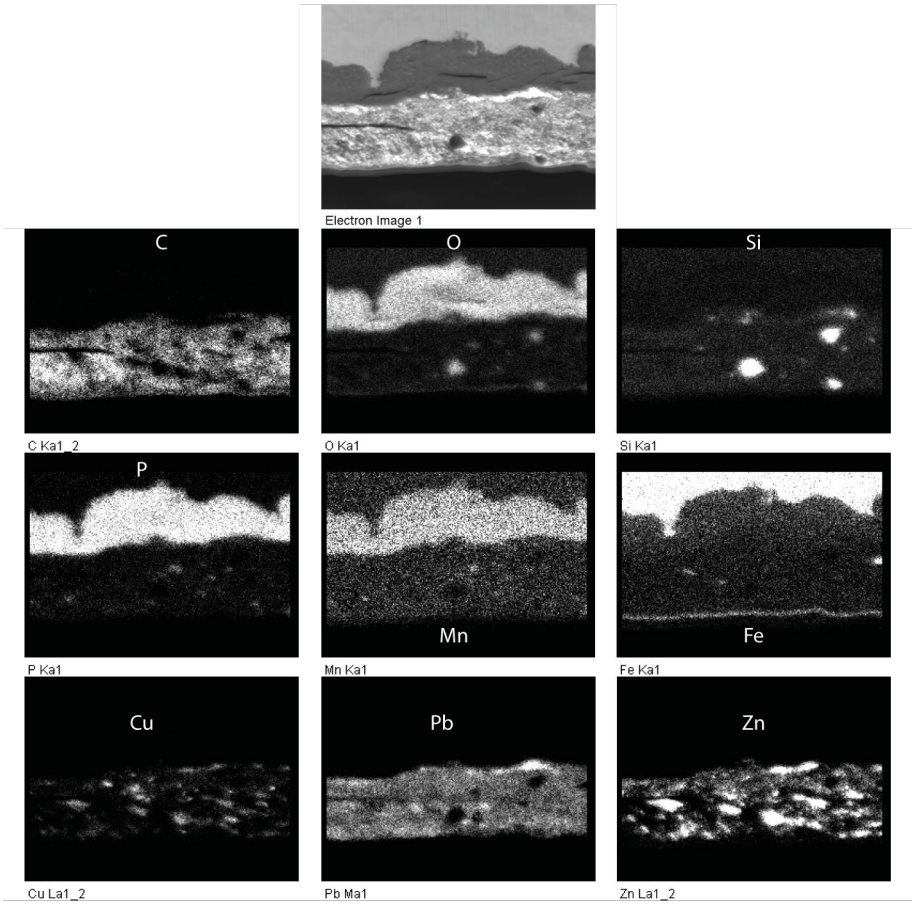

Figure V.1.: BSE image and EDX mapping corresponding to the SE image of Figure 5.10 for set FRS06. Note that compared to Figure 5.10 the image is upside down because of remounting in a different SEM.

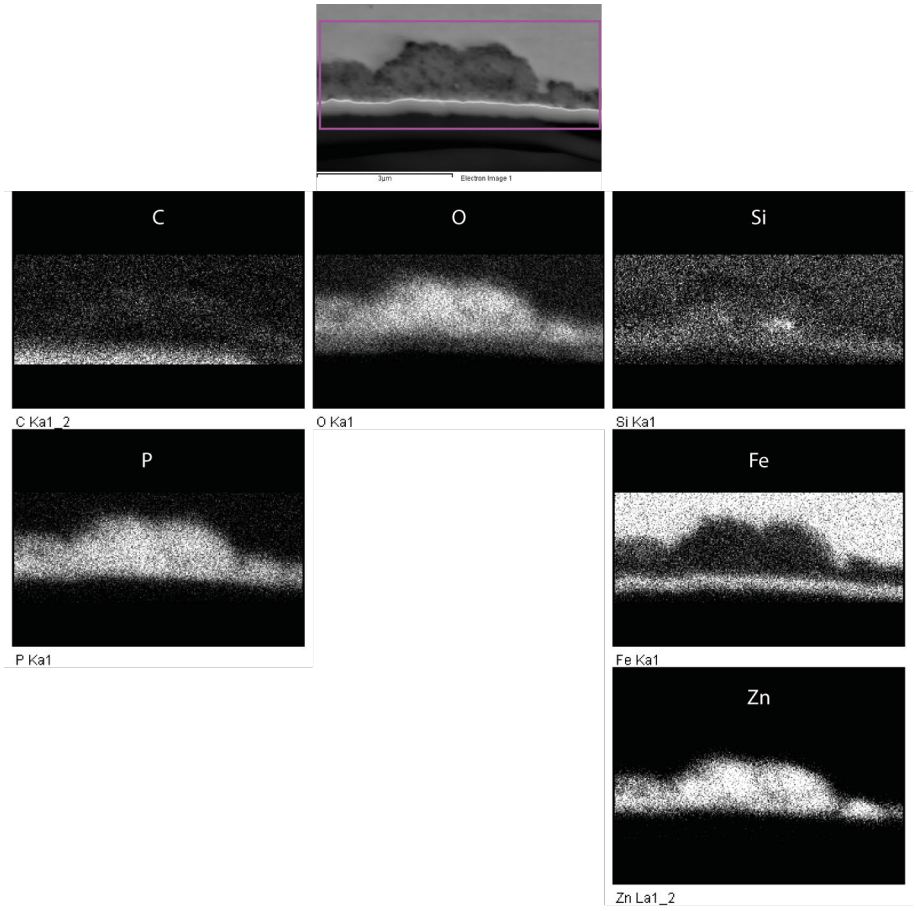

Figure V.2.: BSE image and EDX mapping corresponding to set FRS07 box.

VI. Supplemental materials: Chapter 6

Supplemental results for Chapter 6. Additional surface topography statistics as function of sliding length are shown in Figure VI.1.

VI.1. Contact model

A short overview of the contact model is given here, for details consult the work of [61, 118, 186]. Consider two surface topography measurements, $z_1(x, y)$ and $z_2(x, y)$ living in the domain

$$\Omega = \left\{(x, y) \in \mathcal{R}^2 | 0 \leq x \leq L_x, 0 \leq y \leq L_y\right\}. \tag{VI.1}$$

This could be for instance the pin seal area and the box seal area in Figure VI.2a and Figure VI.2b respectively. Then x is associated with the axial direction and y with the circumferential direction of the metal-to-metal seal (Figure 1.5). The domain size is defined by L_x and L_y and subdivided into elements defined by the pixel pitch in both directions denoted as d_x and d_y respectively. Hence the domain size in pixels is $M \times N$ and thus the physical domain size is $L_x = Md_x$ and $L_y = Nd_y$. Note that for most optical surface topography measurement techniques $d_x = d_y$ and depends on the used CCD and magnification. Next, an index set can be associated with the elements of Ω such that the set I is an index set of Ω like $\Omega = \cup_{i \in I} \Omega_i$.

To study the deformation of the surface under loading the model of [203] was implemented. The model is based on the Boussinesq-Cerruti half-space assumption [33]. For this the undeformed gap is defined as,

$$h_1(x, y) = z_1(x, y) + z_2(x, y), \tag{VI.2}$$

which is subsequently used to define the deformed gap as,

$$h(x, y) = h_1(x, y) + g_{00} + u(x, y), \tag{VI.3}$$

where g_{00} is the rigid body separation between pin and box and $u(x, y)$ is the elastic deformation.

The elastic deformation can be determined using the Boussinesq-Cerruti theory as [33],

$$u(x, y) = \frac{1}{\pi E^*} \iint_{-\infty}^{\infty} \frac{p(\bar{x}, \bar{y}) d\bar{x} d\bar{y}}{\sqrt{(x - \bar{x})^2 + (y - \bar{y})^2}}. \tag{VI.4}$$

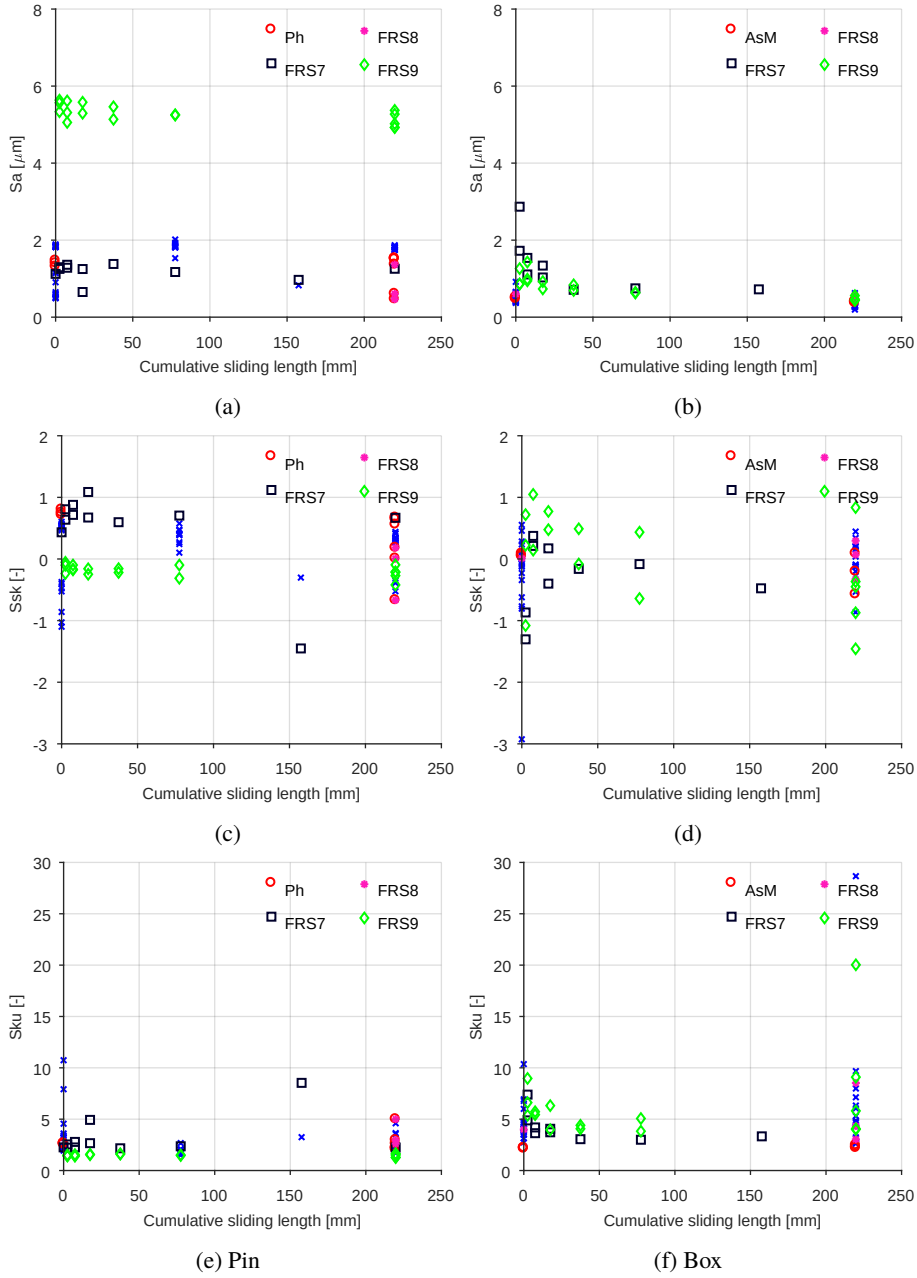

Figure VI.1.: From top to bottom, evolution of S_a, S_{sk} and S_{ku} versus cumulative sliding length for the SSMUR face seal data set in Table I.6. Pin and box results were considered separately because of the different nature of the surfaces. Supplemental results for Figure 6.1.

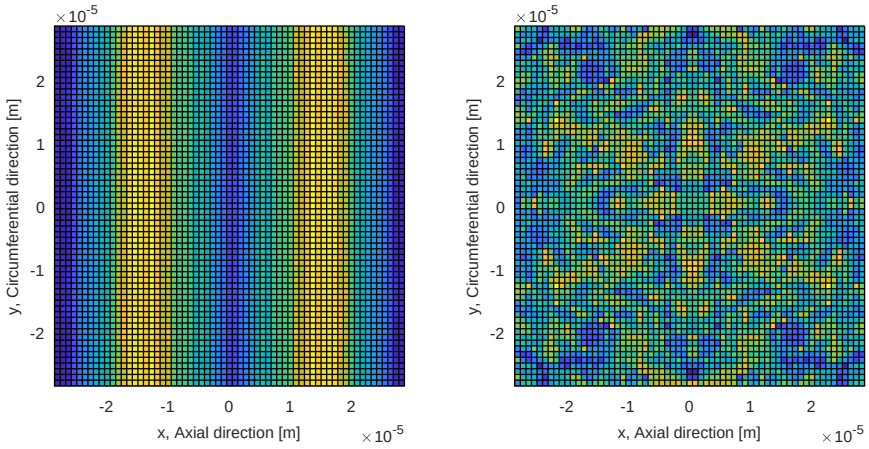

(a) z_1, Pin surface

(b) z_2, Box surface

Figure VI.2.: Surface topography measurements of SSMUR set FRS13 showing a single waviness for pin and the corresponding box area. Zoom in of 32x32 pixels region to illustrate pixel pitch, here 0.895 µm, and discretisation.

Where p is the contact stress and E^* the composite elastic modulus or contact stiffness defined as

$$\frac{1}{E^*} = \frac{1-\nu_1^2}{E_1} + \frac{1-\nu_2^2}{E_2} \tag{VI.5}$$

with E_i and ν_i the elastic modulus and Poisson ratio of contacting body i.

This system of equations needs to adhere to the following constraints for the deformed gap, h, with respect to the contact stress, p,

$$h(x,y) > 0, p(x,y) = 0, \qquad \forall (x,y) \notin \Omega_c \tag{VI.6}$$

$$h(x,y) = 0, p(x,y) > 0, \qquad \forall (x,y) \in \Omega_c \tag{VI.7}$$

$$0 \leq p(x,y) \leq H, \qquad \forall (x,y) \in \Omega, \tag{VI.8}$$

where H is defined as the surface hardness of the softest material in contact and Ω_c is defined as the subset of Ω in which the surfaces are in contact. The generated contact stresses need to balance the externally applied load according to

$$F = \int_{\Omega_c} p(x,y) dx dy. \tag{VI.9}$$

The solution of the model is obtained by minimizing the energy in the system [116] using a single loop Conjugate Gradient method [204] which is accelerated by the DC-FFT method [117]. Convergence is monitored using the force balance (VI.9) and the elastic contact plane (VI.3). For all computations the convergence criterion for the force balance (equation

(VI.9)) needed to be within a relative error of 10^{-6} and for the elastic contact plane, $h_e = h(x,y)\,\forall(x,y) \in \Omega_c$, within 10^{-10} m.

The plastic deformation, u_p, is defined at the locations where plasticity occurs, $p(x,y) > H$ in equation (VI.8). According to the perfect plasticity assumption, these points lay on the contact plane and are taken out of Ω_c and move to Ω_p, namely

$$u_p(x,y) = h(x,y) \qquad \forall(x,y) \in \Omega_p, p(x,y) > H, \tag{VI.10}$$

otherwise,

$$u_p(x,y) = 0. \tag{VI.11}$$

Hence these points float unconditionally.

VI.2. Thermal model

To investigate if desorption of the lubricant by thermal effects [87, 88] was (part of the) mechanism initiating galling a thermal model was implemented [180]. A detailed description of the model can be found in [180, 203]. The model is based on a semi-analytical approach by considering a uniform square heat source taken from Carslaw et al. [205].

For the transient temperature field the following can be written [205],

$$\begin{aligned}\Phi(\acute{x},y,z,t) = \int_0^t \int_{-b}^{b} \int_{-a}^{a} \frac{1}{\tilde{t}^{\frac{2}{3}}} \frac{\phi(\tilde{x},\acute{y})}{8(\pi\kappa)^{\frac{2}{3}}} \\ \exp\left(\frac{-\left((\acute{x}-\tilde{x}+v\tilde{t})^2+(y-\acute{y})^2+z^2\right)}{4\kappa\tilde{t}}\right) d\tilde{x}d\acute{y}d\tilde{t},\end{aligned} \tag{VI.12}$$

where Φ is the temperature rise at $(\acute{x},y)$ because of a heat flux ϕ at $(\tilde{x},\acute{y})$ moving with velocity v. The target location in the moving reference frame is denoted by $\acute{x}$ and $\tilde{x}$ is the heat source location. Thermal diffusivity is denoted with κ. This is integrated with respect to the inverse contact time $\tilde{t} = t - t_0$ on a square contact patch of $2a \times 2b$. This is a convolution integral and can be solved with a similar strategy as the contact problem of Section 6.3.

Combining the thermal model with the contact model allows the heat flux in equation (VI.12) to be computed from the COF, contact stress distribution and the sliding velocity as,

$$\phi(x,y) = \mu p(x,y) v. \tag{VI.13}$$

This is done using a decoupled solution strategy by first computing the contact stress and using the result as input for the thermal model. This means that influence of, for instance, thermal softening of the material on the contact stress is not taken into account. As will be shown, this is a reasonable assumption for the system considered here. To determine if the system is operating in a thermal transient or steady state regime it is good to define the Fourier number,

$$\Gamma = \frac{\kappa t}{A}, \tag{VI.14}$$

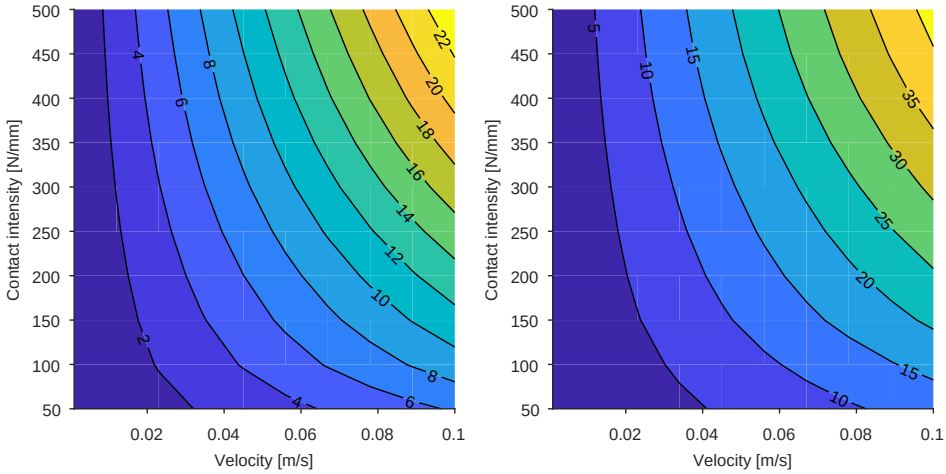

(a) P110 (b) AISI316

Figure VI.3.: Steady state thermal model results over representative make-up velocities and contact intensities for a typical oil field quenched and tempered steel grade (P110) and a stainless steel (AISI316L).

where A is a characteristic area of contact, if $\Gamma > 100$ is chosen a steady state solution will be obtained.

Computations were performed for steady state conditions over a range of contact intensities and sliding velocities. The results are shown for a quenched and tempered P110 steel and a stainless steel in Figure VI.3. Now remembering the typical sliding velocity and contact intensity for the metal-to-metal seal (Section 1.3.3) it is clear that the system is two orders of magnitude away from being at risk because of thermal failure with a typical mineral oil [87]

Therefore, the mechanisms discussed in Chapter 3 and Paper F were considered the most plausible explanation for the initiation of galling in a casing connection metal-to-metal seal including the high wt% chrome materials as used in Chapter 4.

This page has been intentionally left blank.

Bibliography

[1] Araki, E., Byrne, T., Mcneill, L., Saffer, D., Eguchi, N., Takahashi, K. and Toczko, S. *Expedition 319 Scientific Prospectus NanTroSEIZE Stage 2 : NanTroSEIZE riser / riserless observatory*. Tech. rep. 2009.

[2] Salomon, G. 'Application of Systems Thinking to Tribology'. *A S L E Transactions* 17.4 (January 1974), pp. 295–299.

[3] Czichos, H. and Winer, W. O. *Tribology: A Systems Approach to the Science and Technology of Friction, Lubrication and Wear (Tribology Series, 1)*. Vol. 100. Elsevier, 1978, p. 513.

[4] API. *Recommended Practice on Thread Compounds for Casing, Tubing, and Line Pipe*. Tech. rep. Washington: American Petroleum Institute, 2015.

[5] OSPAR. *Guidelines for Completing the Harmonised Offshore Chemical Notification Format (HOCNF)*. Tech. rep. OSPAR, 2015.

[6] Beek, A. van. *Advanced engineering design : lifetime performance and reliability*. 2006.

[7] API. *Petroleum and natural gas industries - Procedures for testing casing and tubing connections (ISO 13679:2002) Industries*. Tech. rep. Geneva: International Organization for Standardization, 2002.

[8] Pérez-Ràfols, F. 'Two-Scale Stochastic Modelling and Analysis of Leakage Through Metal-To-Metal Seals'. PhD thesis. Luleå University of Technology, 2018.

[9] Bommer, P. *A Primer of Oilwell Drilling*. 7th. Austin: The University of Texas at Austin, 2008.

[10] Galle, T. 'Development of a Numerical Framework to Assess the Influence of Connection Characteristics on the Performance-Rating of OCTG Threaded Connections'. PhD thesis. Ghent University, 2016.

[11] O'Neill, A. *Pipe Joints*. 1876.

[12] Allison, W. C. *Screw-Threaded Pipe Joint and Coupling*. 1879.

[13] Morse, J. O. *Wrought-iron coupling for pipe-sections*. 1882.

[14] Bole, W. A. *Pipe Coupling*. 1885.

[15] Montgomery, G. A. *Interior shoulder single piece tool joint*. 1932.

[16] Reimschissel, C. A. *Tubular joint seal*. 1939.

[17] API. *WI 2317 : Tech Report on LTC / BTC Performance Properties and Leak Resistance*. Tech. rep. American Petroleum Institute, 2006, pp. 1–14.

[18] Teodoriu, C. and Badicioiu, M. 'Sealing Capacity of API Connections–Theoretical and Experimental Results'. *SPE Drilling & Completion* 24.01 (March 2009), pp. 96–103.

[19] Blose, T. L. and Beckert, H. J. *Threaded Tube Joint having a Metal-to-metal Seal*. 1965.

[20] Sugino, M., Ugai, S., Nakamura, K., Yamaguchi, S. and Hamamoto, T. *VAM ® 21, an Innovative High-performance Premium Threaded Connection for OCTG*. Tech. rep. 107. Nippon Steel & Sumitomo Metal Corporation, 2015.

[21] Oil, W. '2015 Casing Reference Tables'. *World Oil* (January 2015), p. 64.

[22] Matsuki, N. *Threaded tube joint structure for casing, particularly oil well tubing*. 1975.

[23] Sugino, M., Nakamura, K., Yamaguchi, S., Daly, D., Briquet, G. and Verger, E. 'Development of an Innovative High-performance Premium Threaded Connection for OCTG'. *Proceedings of Offshore Technology Conference*. Society of Petroleum Engineers, May 2010.

[24] Asbill, W. T., Pattillo, P. D. and Rogers, W. M. 'Investigation of API 8 Round Casing Connection Performance—Part I: Introduction and Method of Analysis'. *Journal of Energy Resources Technology* 106.1 (March 1984), p. 130.

[25] Asbill, W. T., Pattillo, P. D. and Rogers, W. M. 'Investigation of API 8 Round Casing Connection Performance—Part II: Stresses and Criteria'. *Journal of Energy Resources Technology* 106.1 (March 1984), p. 137.

[26] Asbill, W. T., Pattillo, P. D. and Rogers, W. M. 'Investigation of API 8 Round Casing Connection Performance—Part III: Sealability and Torque'. *Journal of Energy Resources Technology* 106.1 (March 1984), p. 144.

[27] Schwind, B., Chappell, J. and Katsounas, A. 'Threaded Connection Limit State Equations for Use in LRFD Tubular Design'. *Offshore Technology Conference*. Offshore Technology Conference, April 1995.

[28] Ernens, D., Hariharan, H., Haaften, W. M. van, Pasaribu, H. R., Jabs, M. and McKim, R. 'Improving Casing Integrity by Induction Brazing of Casing Connections'. *SPE Drilling & Completion* (2018).

[29] Grijalva, O., Perozo, N., Holzmann, J., Paz, C. and Oppelt, J. 'Well Integrity in the Times of ISO 13679 and Premium Connections: Experiences and Way Forward'. *SPE Kuwait Oil & Gas Show and Conference*. Society of Petroleum Engineers, October 2017.

[30] Vallourec Oil and Gas. *VAM® book*. 2017.

[31] TenarisHydrill. *TenarisHydril Running Manual*. 2017.

[32] Oku, Y., Sugino, M., Ando, Y., Makino, T., Komoda, R., Takazaki, D. and Kubota, M. 'Fretting fatigue on thread root of premium threaded connections'. *Tribology International* 108.April 2017 (April 2017), pp. 111–120.

[33] Johnson, K. L. *Contact Mechanics*. Cambridge University Press, 1987, p. 452.

[34] Dvorkin, E. N. and Toscano, R. G. 'Finite element models in the steel industry Part II: Analyses of tubular products performance'. *Computers & Structures* 81.8-11 (May 2003), pp. 575–594.

[35] Assanelli, A. and Dvorkin, E. 'Finite element models of octg threaded connections'. *Computers & Structures* 47.4-5 (June 1993), pp. 725–734.

[36] Stewart, F., Le, H., Williams, J., Leech, A., Bezensek, B. and Roberts, A. 'Characterisation of friction and lubrication regimes in premium tubular connections'. *Tribology International* 53 (September 2012), pp. 159–166.

[37] Stewart, F. 'Tribological characterisation and modelling of premium tubular connections'. PhD thesis. Plymouth University, 2014.

[38] Le, H. R., Stewart, F. and Williams, J. A. 'A Simplified Model of Surface Burnishing and Friction in Repeated Make-Up Process of Premium Tubular Connections'. *Tribology Letters* 59.2 (August 2015), p. 35.

[39] Christensen, H. 'Stochastic Models for Hydrodynamic Lubrication of Rough Surfaces'. *Proceedings of the Institution of Mechanical Engineers* 184.1 (June 1969), pp. 1013–1026.

[40] Patir, N. and Cheng, H. S. 'An Average Flow Model for Determining Effects of Three-Dimensional Roughness on Partial Hydrodynamic Lubrication'. *Journal of Lubrication Technology* 100.1 (January 1978), p. 12.

[41] Stachowiak, G. and Batchelor, A. W. *Engineering Tribology*. Butterworth-Heinemann, 2013, p. 884.

[42] Lugt, P. M. *Grease Lubrication in Rolling Bearings*. Oxford, UK: John Wiley & Sons Ltd, December 2012.

[43] Carper, H. J., Ertas, A., Issa, J. and Cuvalci, O. 'Effect of Some Material, Manufacturing, and Operating Variables on the Friction Coefficient in OCTG Connections'. *Journal of Tribology* 114.4 (October 1992), p. 698.

[44] Ekwaro-Osire, S. and Karpat, F. 'Experimental Studies on Galling Onset in OCTG Connections: A Review'. *Journal of Energy Resources Technology* 130.1 (March 2008), p. 014502.

[45] Cuvalci, O., Sofuoglu, H. and Ertas, A. 'Effect of surface coating and tin plating on friction characteristics of P-110 tubing for different thread compounds'. *Tribology International* 36.10 (October 2003), pp. 757–764.

[46] Carper, H. J., Ertas, A. and Cuvalci, O. 'Rating Thread Compounds for Galling Resistance'. *Journal of Tribology* 117.4 (October 1995), p. 639.

[47] Ertas, A. 'Experimental Investigation of Galling Resistance in OCTG Connections'. *Journal of Manufacturing Science and Engineering* 114.1 (February 1992), p. 100.

[48] Inose, K., Sugino, M. and Goto, K. 'Influence of Grease on High-Pressure Gas Tightness by Metal-to-Metal Seals of Premium Threaded Connections'. *Tribology Online* 11.2 (2016), pp. 227–234.

[49] Hoenig, S. and Oberndorfer, M. 'Tightness Testing of Environmentally Friendly Thread Compounds'. *SPE Europec/EAGE Annual Conference and Exhibition*. Vol. 1. Society of Petroleum Engineers, April 2006, pp. 473–480.

[50] Murtagian, G. R., Fanelli, V., Villasante, J. A., Johnson, D. H. and Ernst, H. A. *Sealability of Stationary Metal-to-Metal Seals*. July 2004.

[51] Bollfrass, C. 'Sealing Tubular Connections'. *Journal of Petroleum Technology* 37.06 (June 1985), pp. 955–965.

[52] Lugt, P. M. 'Modern advancements in lubricating grease technology'. *Tribology International* 97 (May 2016), pp. 467–477.

[53] Leech, A. and Roberts, A. 'Development of Dope-Free Premium Connections for Casing and Tubing'. *SPE Drilling & Completion* 22.2 (June 2007), pp. 106–111.

[54] Tsuru, E., Tsukano, Y., Maruyama, K., Sato, N., Okamura, K., Nagayoshi, H. and Oka, M. *Dope-free type premium connection for oil country tubular goods*. Tech. rep. 81. Nippon Steel, 2000, pp. 69–73.

[55] Ledoux, Y., Lasseux, D., Favreliere, H., Samper, S. and Grandjean, J. 'On the dependence of static flat seal efficiency to surface defects'. *International Journal of Pressure Vessels and Piping* 88.11-12 (December 2011), pp. 518–529.

[56] Pérez-Ràfols, F., Wall, P. and Almqvist, A. 'On compressible and piezo-viscous flow in thin porous media'. *Proceedings of the Royal Society A: Mathematical, Physical and Engineering Science* 474.2209 (January 2018).

[57] Pérez-Ràfols, F., Larsson, R., Riet, E. J. van and Almqvist, A. 'On the loading and unloading of metal-to-metal seals: A two-scale stochastic approach'. *Proceedings of the Institution of Mechanical Engineers, Part J: Journal of Engineering Tribology* (February 2018).

[58] Pérez-Ràfols, F., Larsson, R., Riet, E. J. van and Almqvist, A. 'On the flow through plastically deformed surfaces under unloading: A spectral approach'. *Proceedings of the Institution of Mechanical Engineers, Part C: Journal of Mechanical Engineering Science* 232.5 (March 2018), pp. 908–918.

[59] Pérez-Ràfols, F., Larsson, R. and Almqvist, A. 'Modelling of leakage on metal-to-metal seals'. *Tribology International* 94 (February 2016), pp. 421–427.

[60] Sahlin, F., Larsson, R., Almqvist, A., Lugt, P. M. and Marklund, P. 'A mixed lubrication model incorporating measured surface topography. Part 1: theory of flow factors'. *Proceedings of the Institution of Mechanical Engineers, Part J: Journal of Engineering Tribology* 224.4 (January 2010), pp. 335–351.

[61] Sahlin, F., Larsson, R., Marklund, P., Almqvist, A. and Lugt, P. M. 'A mixed lubrication model incorporating measured surface topography. Part 2: roughness treatment, model validation, and simulation'. *Proceedings of the Institution of Mechanical Engineers, Part J: Journal of Engineering Tribology* 224.4 (January 2010), pp. 353–365.

[62] Pérez-Ràfols, F., Larsson, R., Lundström, S., Wall, P. and Almqvist, A. 'A stochastic two-scale model for pressure-driven flow between rough surfaces'. *Proceedings of the Royal Society A: Mathematical, Physical and Engineering Science* 472.2190 (June 2016).

[63] Geoffroy, S. and Prat, M. 'On the Leak Through a Spiral-Groove Metallic Static Ring Gasket'. *Journal of Fluids Engineering* 126.1 (2004), p. 48.

[64] Marie, C., Lasseux, D., Zahouani, H. and Sainsot, P. 'An integrated Approach to Characterize Liquid Leakage Through Metal Contact Seal'. *European Journal of Mechanical and Environmental Engineering* 48.2 (2003), pp. 81–86.

[65] Nakamura, T. and Funabashi, K. 'Effects of directional properties of roughness and tangential force on pressure flow between contacting surfaces'. *Lubrication Science* 4.1 (October 1991), pp. 13–23.

[66] Rausch, W. *The phosphating of metals*. Metals Park, Ohio, USA; Teddington, Middlesex, England: ASM International; Finishing Publications Ltd., 1990, p. 406.

[67] Narayanan, T. S. N. S. 'Surface pretreatment by phosphate conversion coatings - A review'. *Reviews on Advanced Materials Science* 9.2 (2005), pp. 130–177.

[68] Totik, Y. 'The corrosion behaviour of manganese phosphate coatings applied to AISI 4140 steel subjected to different heat treatments'. *Surface and Coatings Technology* 200.8 (January 2006), pp. 2711–2717.

[69] Burke, D. 'The Sliding Friction of Bonded Solid Lubricants'. PhD thesis. University of central Lancashire, 2005.

[70] Weng, D., Jokiel, P., Uebleis, A. and Boehni, H. 'Corrosion and protection characteristics of zinc and manganese phosphate coatings'. *Surface and Coatings Technology* 88.1-3 (January 1997), pp. 147–156.

[71] Khaleghi, M., Gabe, D. and Richardson, M. 'Characteristics of manganese phosphate coatings for wear- resistance applications'. *Wear* 55.2 (August 1979), pp. 277–287.

[72] Pokorny, P., Szelag, P., Novak, M., Mastny, L. and Brozek, V. 'Thermal stability of phosphate coatings on steel'. *Metalurgija* 54.3 (2015), pp. 489–492.

[73] Pokorny, P., Brozek, V. and Mastny, L. 'Improving Bond Strenght between Carbon Steel and Plasma Sprayed Ceramic Coatings through a Phosphating Process'. *International Conference on Metallurgy and Materials*. 1. 2012, pp. 1–6.

[74] Westberg, H. J., Nilsson, P. H., Rosén, B.-G. and Stenbom, B. 'Manganese Phosphating of Gears and Surface Roughness Consequence'. *Proceedings of the 26th Leeds-Lyon Symposium on Tribology*. 2000, pp. 145–153.

[75] Hill, R. and Jones, J. 'The crystal structure of hopeite'. *American Mineralogist* 61 (1976), pp. 987–995.

[76] Moore, P. B. and Araki, T. 'Hureaulite: lts Atomic Arrangement'. *American Mineralogist* 58.3-4 (1973), pp. 302–307.

[77] KozŁowski, A. 'Dry friction of manganese phosphate coatings on steel and cast iron'. *Electrodeposition and Surface Treatment* 2.2 (January 1974), pp. 109–122.

[78] Kumar, A., Bhola, S. and Majumdar, J. D. 'Microstructural characterization and surface properties of zinc phosphated medium carbon low alloy steel'. *Surface and Coatings Technology* 206.17 (April 2012), pp. 3693–3699.

[79] Holmberg, K., Matthews, A. and Ronkainen, H. 'Coatings tribology—contact mechanisms and surface design'. *Tribology International* 31.1-3 (January 1998), pp. 107–120.

[80] Hivart, P., Hauw, B., Dubar, L. and Bricout, J. P. J. 'Numerical identification of bulk behavior law of manganese phosphate coatings. Comparison with tribological properties'. *Journal of Coatings Technology* 75.942 (July 2003), pp. 37–44.

[81] Farias, M., Santos, C., Panossian, Z. and Sinatora, A. 'Friction behavior of lubricated zinc phosphate coatings'. *Wear* 266.7-8 (March 2009), pp. 873–877.

[82] Burokas, V., Martušienė, A. and Bikulčius, G. 'The influence of hexametaphosphate on formation of zinc phosphate coatings for deep drawing of steel tubes'. *Surface and Coatings Technology* 102.3 (April 1998), pp. 233–236.

[83] Perry, J. and Eyre, T. 'The effect of phosphating on the friction and wear properties of grey cast iron'. *Wear* 43.2 (June 1977), pp. 185–197.

[84] KozŁowski, A. and Czechowski, W. 'Wear resistance of manganese phosphate coatings'. *Electrodeposition and Surface Treatment* 3.1 (January 1975), pp. 55–63.

[85] Hivart, P., Hauw, B., Bricout, J. and Oudin, J. 'Seizure behaviour of manganese phosphate coatings according to the process conditions'. *Tribology International* 30.8 (July 1997), pp. 561–570.

[86] Hivart, P., Hauw, B., Crampon, J. and Bricout, J. 'Annealing improvement of tribological properties of manganese phosphate coatings'. *Wear* 219.2 (September 1998), pp. 195–204.

[87] Drogen, M. van. 'The Transition to adhesive wear of Lubricated Concentrated Contacts'. PhD thesis. University of Twente, 2005.

[88] Heide, E. van der and Schipper, D. J. 'Galling initiation due to frictional heating'. *Wear* 254 (2003), pp. 1127–1133.

[89] Müser, M. H. and Dapp, W. B. 'The contact mechanics challenge: Problem definition'. 2 (December 2015), pp. 1–5.

[90] Müser, M. H., Dapp, W. B., Bugnicourt, R., Sainsot, P., Lesaffre, N., Lubrecht, T. A., Persson, B. N. J., Harris, K., Bennett, A., Schulze, K., Rohde, S., Ifju, P., Sawyer, W. G., Angelini, T., Ashtari Esfahani, H., Kadkhodaei, M., Akbarzadeh, S., Wu, J.-J., Vorlaufer, G., Vernes, A., Solhjoo, S., Vakis, A. I., Jackson, R. L., Xu, Y., Streator, J., Rostami, A., Dini, D., Medina, S., Carbone, G., Bottiglione, F., Afferrante, L., Monti, J., Pastewka, L., Robbins, M. O. and Greenwood, J. A. 'Meeting the Contact-Mechanics Challenge'. *Tribology Letters* 65.4 (December 2017), p. 118.

[91] Kogut, L. and Jackson, R. L. 'A Comparison of Contact Modeling Utilizing Statistical and Fractal Approaches'. *Journal of Tribology* 128.1 (2006), p. 213.

[92] Jackson, R. L. and Green, I. *On the Modeling of Elastic Contact between Rough Surfaces*. 2011.

[93] Greenwood, J. A. and Williamson, J. B. P. 'Contact of Nominally Flat Surfaces'. *Proceedings of the Royal Society A: Mathematical, Physical and Engineering Sciences* 295.1442 (December 1966), pp. 300–319.

[94] Bush, A., Gibson, R. and Thomas, T. 'The elastic contact of a rough surface'. *Wear* 35.1 (November 1975), pp. 87–111.

[95] Jamari, J., Rooij, M. B. de and Schipper, D. J. 'Plastic Deterministic Contact of Rough Surfaces'. *Journal of Tribology* 129.October (2007), p. 957.

[96] Rabinowicz, E. *Friction and Wear of Materials*. Wiley, 1995, p. 315.

[97] Westergaard, H. M. 'Bearing pressures and cracks'. *Journal of Applied Mechanics* 61 (1939), A49–A53.

[98] Truman, C., Sackfield, A. and Hills, D. 'Contact mechanics of wedge and cone indenters'. *International Journal of Mechanical Sciences* 37.3 (1995), pp. 261–275.

[99] Aleksandrov, V. and Pozharskii, D. 'On a contact problem for an elastic wedge'. *Journal of Applied Mathematics and Mechanics* 52.4 (1988), pp. 506–511.

[100] Adibnazari, S., Sharafbafi, F. and Ghanati, P. 'Contact of an asymmetrical rounded apex wedge with a half plane'. *International Journal of Engineering Science* 50.1 (2012), pp. 192–197.

[101] Ciavarella, M., Hills, D. and Monno, G. 'Contact problems for a wedge with rounded apex'. *International Journal of Mechanical Sciences* 40.10 (October 1998), pp. 977–988.

[102] Abbott, E. J. and Firestone, F. A. 'Specifying surface quality: a method based on accurate measurement and comparison'. *Journal of Mechanical Engineering* 55 (1933), pp. 569–572.

[103] Chang, W. R., Etsion, I. and Bogy, D. B. *Static Friction Coefficient Model for Metallic Rough Surfaces*. January 1988.

[104] Zhao, Y., Maietta, D. M. and Chang, L. 'An Asperity Microcontact Model Incorporating the Transition From Elastic Deformation to Fully Plastic Flow'. *Journal of Tribology* 122.1 (January 2000), p. 86.

[105] Kogut, L. and Etsion, I. 'Elastic-Plastic Contact Analysis of a Sphere and a Rigid Flat'. *Journal of Applied Mechanics* 69.September 2002 (2002), p. 657.

[106] Chaudhri, M. M., Hutchings, I. M. and Makin, P. L. 'Plastic compression of spheres'. *Philosophical Magazine A* 49.4 (October 1984), pp. 493–503.

[107] Chaudhri, M. M. 'The Plastic deformation of single asperities by hard flats'. *Proceedings of the Institution of Mechanical Engineers*. 1987, pp. 1003–1012.

[108] Johnson, K. 'An experimental determination of the contact stresses between plastically deformed cylinders and spheres'. *Engineering Plasticity* (1968), pp. 341–361.

[109] Persson, B. 'Elastoplastic Contact between Randomly Rough Surfaces'. *Physical Review Letters* 87.11 (August 2001), p. 116101.

[110] Majumdar, A. and Bhushan, B. 'Role of fractal geometry in roughness characterization and contact mechanics of surfaces'. *Journal of Tribology* 112.April (1990), pp. 205–216.

[111] Persson, B. 'Contact mechanics for randomly rough surfaces'. *Surface Science Reports* 61.4 (June 2006), pp. 201–227.

[112] Ciavarella, M., Greenwood, J. A. and Paggi, M. 'Inclusion of "interaction" in the Greenwood and Williamson contact theory'. *Wear* 265 (2008), pp. 729–734.

[113] Paggi, M. and Ciavarella, M. 'The coefficient of proportionality κ between real contact area and load, with new asperity models'. *Wear* 268.7-8 (March 2010), pp. 1020–1029.

[114] Polonsky, I. and Keer, L. 'A numerical method for solving rough contact problems based on the multi-level multi-summation and conjugate gradient techniques'. *Wear* 231.2 (July 1999), pp. 206–219.

[115] Brandt, A. and Lubrecht, A. A. 'Multilevel matrix multiplication and fast solution of integral equations'. *Journal of Computational Physics* 90.2 (October 1990), pp. 348–370.

[116] Kalker, J. J. 'Numerical calculation of the elastic field in a half-space'. *Communications in Applied Numerical Methods* 2.4 (July 1986), pp. 401–410.

[117] Liu, S., Wang, Q. and Liu, G. 'A versatile method of discrete convolution and FFT (DC-FFT) for contact analyses'. *Wear* 243.1-2 (2000), pp. 101–111.

[118] Almqvist, A., Sahlin, F., Larsson, R. and Glavatskih, S. 'On the dry elasto-plastic contact of nominally flat surfaces'. *Tribology International* 40.4 (April 2007), pp. 574–579.

[119] Fotiu, P. and Nemat-Nasser, S. 'A universal integration algorithm for rate-dependent elastoplasticity'. *Computers & Structures* 59.6 (June 1996), pp. 1173–1184.

[120] Nélias, D., Antaluca, E., Boucly, V. and Cretu, S. 'A Three-Dimensional Semianalytical Model for Elastic-Plastic Sliding Contacts'. *Journal of Tribology* 129.4 (2007), p. 761.

[121] Bosman, R., Hol, J. and Schipper, D. 'Running-in of metallic surfaces in the boundary lubrication regime'. *Wear* 271.7-8 (July 2011), pp. 1134–1146.

[122] Yastrebov, V. A., Durand, J., Proudhon, H. and Cailletaud, G. 'Rough surface contact analysis by means of the Finite Element Method and of a new reduced model'. *Comptes Rendus Mécanique* 339.7-8 (2011), pp. 473–490.

[123] Wriggers, P. 'Finite element algorithms for contact problems'. *Archives of Computational Methods in Engineering* 2.March (1995), pp. 1–49.

[124] Pei, L., Hyun, S., Molinari, J. F. and Robbins, M. O. 'Finite element modeling of elasto-plastic contact between rough surfaces'. *Journal of the Mechanics and Physics of Solids* 53.11 (November 2005), pp. 2385–2409.

[125] Blau, P. J. 'On the nature of running-in'. *Tribology International* 38.11-12 (November 2005), pp. 1007–1012.

[126] Ludema, K. C. 'A review of scuffing and running-in of lubricated surfaces, with asperities and oxides in perspective'. *Wear* 100.1-3 (December 1984), pp. 315–331.

[127] Blau, P. J. 'Interpretations of the friction and wear break-in behavior of metals in sliding contact'. *Wear* 71.1 (September 1981), pp. 29–43.

[128] Hsu, S. 'Boundary lubrication: current understanding'. *Tribology Letters* 3.1 (March 1997), pp. 1–11.

[129] Spikes, H. A. 'Boundary Lubrication and Boundary Films'. In: *Tribology Series*. Vol. 25. C. 1993, pp. 331–346.

[130] Jamari, J. 'Running-in of rolling contacts'. PhD thesis. University of Twente, 2006, pp. —184.

[131] Lim, S., Ashby, M. and Brunton, J. 'Wear-rate transitions and their relationship to wear mechanisms'. *Acta Metallurgica* 35.6 (June 1987), pp. 1343–1348.

[132] Vakis, A. I., Yastrebov, V. A., Scheibert, J., Nicola, L., Dini, D., Minfray, C., Almqvist, A., Paggi, M., Lee, S., Limbert, G., Molinari, J. F., Anciaux, G., Aghababaei, R., Echeverri Restrepo, S., Papangelo, A., Cammarata, A., Nicolini, P., Putignano, C., Carbone, G., Stupkiewicz, S., Lengiewicz, J., Costagliola, G., Bosia, F., Guarino, R., Pugno, N. M., Müser, M. H. and Ciavarella, M. 'Modeling and simulation in tribology across scales: An overview'. *Tribology International* 125.November 2017 (September 2018), pp. 169–199.

[133] Jamari, J. and Schipper, D. J. 'Deterministic repeated contact of rough surfaces'. *Wear* 264 (2008), pp. 349–358.

[134] Andersson, J., Almqvist, A. and Larsson, R. 'Numerical simulation of a wear experiment'. *Wear* 271.11-12 (September 2011), pp. 2947–2952.

[135] Boucly, V. 'Semi-Analytical Modeling of the Transient Thermal-Elastic-Plastic Contact and its Application to Asperity Collision , Wear and Running-in of Surfaces'. PhD thesis. INSA de Lyon, 2008, pp. 1–206.

[136] Nélias, D., Boucly, V. and Brunet, M. 'Elastic-Plastic Contact Between Rough Surfaces: Proposal for a Wear or Running-in Model'. *Journal of Tribology* 128.2 (2006), p. 236.

[137] Mattei, L. and Di Puccio, F. 'Influence of the wear partition factor on wear evolution modelling of sliding surfaces'. *International Journal of Mechanical Sciences* 99 (August 2015), pp. 72–88.

[138] Öqvist, M. 'Numerical simulations of mild wear using updated geometry with different step size approaches'. *Wear* 249.1-2 (April 2001), pp. 6–11.

[139] Põdra, P. and Andersson, S. 'Simulating sliding wear with finite element method'. *Tribology International* 32.2 (February 1999), pp. 71–81.

[140] Akchurin, A., Bosman, R. and Lugt, P. M. 'A Stress-Criterion-Based Model for the Prediction of the Size of Wear Particles in Boundary Lubricated Contacts'. *Tribology Letters* 64.3 (December 2016), p. 35.

[141] Archard, J. F. 'Single Contacts and Multiple Encounters'. *Journal of Applied Physics* 32.8 (1961), p. 1420.

[142] Ramalho, A. and Miranda, J. 'The relationship between wear and dissipated energy in sliding systems'. *Wear* 260.4-5 (February 2006), pp. 361–367.

[143] Fouvry, S., Liskiewicz, T., Kapsa, P., Hannel, S. and Sauger, E. 'An energy description of wear mechanisms and its applications to oscillating sliding contacts'. *Wear* 255.1-6 (August 2003), pp. 287–298.

[144] Huq, M. and Celis, J.-P. 'Expressing wear rate in sliding contacts based on dissipated energy'. *Wear* 252.5-6 (March 2002), pp. 375–383.

[145] Fouvry, S., Kapsa, P., Zahouani, H. and Vincent, L. 'Wear analysis in fretting of hard coatings through a dissipated energy concept'. *Wear* 203-204.96 (March 1997), pp. 393–403.

[146] Aghababaei, R., Warner, D. H. and Molinari, J.-F. 'On the debris-level origins of adhesive wear'. *Proceedings of the National Academy of Sciences* 114.30 (July 2017), pp. 7935–7940.

[147] Aghababaei, R., Warner, D. H. and Molinari, J.-F. 'Critical length scale controls adhesive wear mechanisms'. *Nature Communications* 7.May (2016), p. 11816.

[148] Meng, H. C. and Ludema, K. C. 'Wear models and predictive equations: their form and content'. *Wear* 181-183.PART 2 (March 1995), pp. 443–457.

[149] Lim, S. and Ashby, M. 'Wear-Mechanism maps'. *Acta Metallurgica* 35.1 (January 1987), pp. 1–24.

[150] Kato, K. 'Micro-mechanisms of wear — wear modes'. *Wear* 153.1 (March 1992), pp. 277–295.

[151] Hokkirigawa, K. and Kato, K. 'An experimental and theoretical investigation of ploughing, cutting and wedge formation during abrasive wear'. *Tribology International* 21.1 (February 1988), pp. 51–57.

[152] Kato, K. 'Classification of wear mechanisms/models'. *Proceedings of the Institution of Mechanical Engineers, Part J: Journal of Engineering Tribology* 216.6 (June 2002), pp. 349–355.

[153] Varenberg, M. 'Towards a unified classification of wear'. *Friction* 1.4 (December 2013), pp. 333–340.

[154] Bosman, R. and Schipper, D. J. 'Mild Wear Prediction of Boundary-Lubricated Contacts'. *Tribology Letters* 42.2 (May 2011), pp. 169–178.

[155] Atkins, P. and Paula, J. de. *Physical chemistry*. 8th editio. Oxford, UK: Oxford University Press, 2006, p. 1072.

[156] Spikes, H. A. 'Friction Modifier Additives'. *Tribology Letters* 60.1 (October 2015), p. 5.

[157] Lansdown, A. R. *Lubrication and Lubricant Selection: a Practical Guide*. Pergamon Press, 2003, p. 320.

[158] Spikes, H. A. 'Stress-augmented thermal activation: Tribology feels the force'. *Friction* 6.1 (2018), pp. 1–31.

[159] Beyer, M. K. and Clausen-Schaumann, H. 'Mechanochemistry: The Mechanical Activation of Covalent Bonds'. *Chemical Reviews* 105.8 (August 2005), pp. 2921–2948.

[160] He, X. and Kim, S. H. 'Mechanochemistry of Physisorbed Molecules at Tribological Interfaces: Molecular Structure Dependence of Tribochemical Polymerization'. *Langmuir* 33.11 (2017), pp. 2717–2724.

[161] Tysoe, W. 'On Stress-Induced Tribochemical Reaction Rates'. *Tribology Letters* 65.2 (2017), pp. 1–16.

[162] Spikes, H. A. and Tysoe, W. 'On the Commonality Between Theoretical Models for Fluid and Solid Friction, Wear and Tribochemistry'. *Tribology Letters* 59.1 (July 2015), p. 21.

[163] Hsu, S. M. and Gates, R. S. 'Boundary lubricating films: Formation and lubrication mechanism'. *Tribology International* 38.3 (2005), pp. 305–312.

[164] Gellman, A. J. and Spencer, N. D. 'Surface chemistry in tribology'. *Proceedings of the Institution of Mechanical Engineers, Part J: Journal of Engineering Tribology* 216.6 (January 2002), pp. 443–461.

[165] Allen, C. and Drauglis, E. 'Boundary layer lubrication: monolayer or multilayer'. *Wear* 14.5 (November 1969), pp. 363–384.

[166] Spikes, H. A. 'The History and Mechanisms of ZDDP'. *Tribology Letters* 17.3 (October 2004), pp. 469–489.

[167] Barnes, A. M., Bartle, K. D. and Thibon, V. R. 'A review of zinc dialkyldithiophosphates (ZDDPS): characterisation and role in the lubricating oil'. *Tribology International* 34.6 (June 2001), pp. 389–395.

[168] Fujita, H. and Spikes, H. A. 'The formation of zinc dithiophosphate antiwear films'. *Proceedings of the Institution of Mechanical Engineers, Part J: Journal of Engineering Tribology* 218.4 (January 2004), pp. 265–278.

[169] Crobu, M., Rossi, A., Mangolini, F. and Spencer, N. D. 'Tribochemistry of Bulk Zinc Metaphosphate Glasses'. *Tribology Letters* 39.2 (August 2010), pp. 121–134.

[170] Vengudusamy, B., Green, J. H., Lamb, G. D. and Spikes, H. A. 'Tribological properties of tribofilms formed from ZDDP in DLC/DLC and DLC/steel contacts'. *Tribology International* 44.2 (February 2011), pp. 165–174.

[171] Gosvami, N. N., Bares, J. A., Mangolini, F., Konicek, A. R., Yablon, D. G. and Carpick, R. W. 'Mechanisms of antiwear tribofilm growth revealed in situ by single-asperity sliding contacts'. *Science* 348.6230 (April 2015), pp. 102–106.

[172] Crobu, M., Rossi, A. and Spencer, N. D. 'Effect of Chain-Length and Countersurface on the Tribochemistry of Bulk Zinc Polyphosphate Glasses'. *Tribology Letters* 48.3 (December 2012), pp. 393–406.

[173] Zhang, J. and Spikes, H. A. 'On the Mechanism of ZDDP Antiwear Film Formation'. *Tribology Letters* 63.2 (August 2016), p. 24.

[174] Naveira-Suarez, A., Tomala, A., Grahn, M., Zaccheddu, M., Pasaribu, H. R. and Larsson, R. 'The influence of base oil polarity and slide-roll ratio on additive-derived reaction layer formation'. *Proceedings of the Institution of Mechanical Engineers, Part J: Journal of Engineering Tribology* 225.7 (July 2011), pp. 565–576.

[175] Naveira Suarez, A., Grahn, M., Pasaribu, H. R. and Larsson, R. 'The influence of base oil polarity on the tribological performance of zinc dialkyl dithiophospate additives'. *Tribology International* 43.12 (December 2010), pp. 2268–2278.

[176] Akchurin, A. and Bosman, R. 'A Deterministic Stress-Activated Model for Tribo-Film Growth and Wear Simulation'. *Tribology Letters* 65.2 (June 2017), p. 59.

[177] Ghanbarzadeh, A., Parsaeian, P., Morina, A., Wilson, M. C. T., Van Eijk, M. C. P., Nedelcu, I., Dowson, D. and Neville, A. 'A Semi-deterministic Wear Model Considering the Effect of Zinc Dialkyl Dithiophosphate Tribofilm'. *Tribology Letters* 61.1 (2016).

[178] Andersson, J., Larsson, R., Almqvist, A., Grahn, M. and Minami, I. 'Semi-deterministic chemo-mechanical model of boundary lubrication'. *Faraday Discussions* 156 (2012), p. 343.

[179] Bosman, R. and Schipper, D. J. 'Running-In of Systems Protected by Additive-Rich Oils'. *Tribology Letters* 41.1 (January 2011), pp. 263–282.

[180] Bosman, R. and Rooij, M. B. de. 'Transient Thermal Effects and Heat Partition in Sliding Contacts'. *Journal of Tribology* 132.2 (2010), p. 021401.

[181] Rabinowicz, E. 'The Determination of the Compatibility of Metals through Static Friction Tests'. en. *A S L E Transactions* 14.3 (January 1971), pp. 198–205.

[182] Dwyer-Joyce, R. S. 'The Effects of Lubricant Contamination on Rolling Bearing Performance'. PhD thesis. University of London, 1993.

[183] Nikas, G. K. 'Theoretical modelling of the entrainment and thermomechanical effects of contamination particles in elastohydrodynamic contacts'. PhD thesis. Imperial College, 1999, pp. 1–342.

[184] Nevosad, A., Azhaarudeen, S., Doerr, N., Zacharias, H., Klarner, J. and Badisch, E. 'Initial Damage Mechanism and Running-In Behaviour of Phosphate Conversion Coatings'. *Key Engineering Materials* 721.December (December 2016), pp. 356–361.

[185] Archard, J. F. 'Elastic Deformation and the Laws of Friction'. *Proceedings of the Royal Society A: Mathematical, Physical and Engineering Sciences* 243.1233 (December 1957), pp. 190–205.

[186] Bosman, R. and Schipper, D. J. 'On the transition from mild to severe wear of lubricated, concentrated contacts: The IRG (OECD) transition diagram'. *Wear* 269.7-8 (2010), pp. 581–589.

[187] Rajan, K., Deshpande, P. and Narasimhan, K. 'Effect of heat treatment of preform on the mechanical properties of flow formed AISI 4130 Steel Tubes—a theoretical and experimental assessment'. *Journal of Materials Processing Technology* 125-126 (September 2002), pp. 503–511.

[188] Jackson, R. L., Krithivasan, V. and Wilson, W. E. 'The pressure to cause complete contact between elastic—plastic sinusoidal surfaces'. *Proceedings of the Institution of Mechanical Engineers, Part J: Journal of Engineering Tribology* 222.7 (July 2008), pp. 857–863.

[189] Manners, W. 'Plastic deformation of a sinusoidal surface'. *Wear* 264.1-2 (January 2008), pp. 60–68.

[190] Almqvist, A. 'On the Effects of Surface Roughness in Lubrication'. PhD thesis. Lulea University of Technology, 2006.

[191] Gao, Y., Bower, A., Kim, K.-S., Lev, L. and Cheng, Y. 'The behavior of an elastic–perfectly plastic sinusoidal surface under contact loading'. *Wear* 261.2 (July 2006), pp. 145–154.

[192] Ernens, D., Rooij, M. B. de, Schipper, D. J., Pasaribu, H. R., Riet, E. J. van and Haaften, W. M. van. 'Mechanical Characterization and Single Asperity Scratch Behaviour of Dry Zinc and Manganese Phosphate Coatings'. *17th Nordic Symposium on Tribology*. Hämeenlinna, 2016.

[193] API. *Petroleum and natural gas industries - Procedures for testing casing and tubing connections (ISO 13679:2011) Industries*. Tech. rep. Geneva: International Organization for Standardization, 2011.

[194] Hertz, H. 'Ueber die Beruehrung fester elastischer Koerper'. *Journal für die reine und angewandte Mathematik* 92 (1882), pp. 156–171.

[195] API. *5CT: Specification for casing and tubing*. Tech. rep. American Petroleum Institute, 2001.

[196] Rooij, M. de, Linde, G. van der and Schipper, D. 'Modelling material transfer on a single asperity scale'. *Wear* 307.1-2 (September 2013), pp. 198–208.

[197] Linde, G. van der. 'Predicting galling behaviour in deep drawing processes'. PhD thesis. University of Twente, 2011.

[198] Singerling, B. F. 'de PATAT'. PhD thesis. University of Twente, 2002.

[199] Oliver, W. and Pharr, G. 'An improved technique for determining hardness and elastic modulus using load and displacement sensing indentation experiments'. *Journal of Materials Research* 7.06 (June 1992), pp. 1564–1583.

[200] Kjer, H. M. and Wilm, J. 'Evaluation of surface registration algorithms for PET motion correction Bachelor thesis'. PhD thesis. Technical University of Denmark, 2010.

[201] Besl, P. and McKay, N. D. 'A method for registration of 3-D shapes'. *IEEE Transactions on Pattern Analysis and Machine Intelligence* 14.2 (February 1992), pp. 239–256.

[202] Chen, Y. and Medioni, G. 'Object modeling by registration of multiple range images'. *Proceedings. 1991 IEEE International Conference on Robotics and Automation*. 3. IEEE Comput. Soc. Press, 1992, pp. 2724–2729.

[203] Bosman, R. 'Mild microscopic wear in the boundary lubrication regime'. PhD thesis. University of Twente, 2011.

[204] Polonsky, I. A. and Keer, L. M. *Fast Methods for Solving Rough Contact Problems: A Comparative Study*. January 2000.

[205] Carslaw, H. S. and Jaeger, J. C. *Conduction of heat in solids*. 2nd. Clarendon Press, 1959, p. 510.

This page has been intentionally left blank.

Part II.

Appended Papers

A. Mechanical characterization and single asperity scratch behaviour of dry zinc and manganese phosphate coatings

D. Ernens[a,b], M.B. de Rooij[a], H.R. Pasaribu [b], E.J. van Riet[b], W.M. van Haaften[b], D.J. Schipper[a]

[a]*Laboratory for Surface Technology and Tribology, Department of Engineering Technology, University of Twente, P.O. Box 217, 7500 AE Enschede, The Netherlands*

[b]*Shell Global Solutions International BV, Innovation, Research & Development, Wells R & D, Kessler Park 1, 2288 GS Rijswijk, The Netherlands*

Abstract The goal of this study is to characterise the mechanical properties of zinc and manganese phosphate coatings before and after running in. The characterisation is done with nano-indentation to determine the individual crystal hardness and single asperity scratch tests to investigate the deformation behaviour at the single asperity level. The nano-indentation and scratch tests reveal brittle deformation behaviour for the as received coatings. Under uni-directional sliding both layers reduce to a powder which is subsequently compacted to a so called glaze layer. The smooth and brittle glaze layer has a higher hardness compared to the as received coating and its properties can be satisfactorily described by models normally used for a hard coating on a soft substrate.

Latest version available on-line: `https://doi.org/10.1016/j.triboint.2017.04.034`

A.1. Introduction

Phosphate conversion coatings are often used to facilitate the running-in phase of machine elements [1]. In the oil and gas industry these coatings are, amongst others, used as corrosion protection [2–5] of casing connections during storage. An added benefit of the coatings is the improved galling resistance in the assembly phase [6].

The casing connections contain a metal-to-metal seal to ensure pressure integrity of the created conduit after installation. The sealing performance of metal-to-metal seals has been shown to be determined by the surface texture and changes thereof [7–10]. Phosphate coatings, therefore, play an important role in the seal ability of the casing connections.

Typically zinc and manganese coatings consist of respectively hopeite [11] and hureaulite [12] crystals. The crystal hardness is reported by [13] to be 3.2 and 5 on the Mohs scale. Others report 2.5 - 3 Mohs and 3.5 Mohs respectively [1]. As the Mohs scale is ordinal, this only says that hureaulite is harder than hopeite. The equivalent Vickers hardness is 102 - 229 HV.

Kumar et al. [14] characterized zinc phosphate using micro hardness indentations, wear experiments and corrosion experiments. They determined the micro hardness of the layer to be 50 HV and found that the needle structure of zinc phosphate crystals plays an important role in the wear behaviour of medium alloy low carbon steel. The experimentally observed wear increase was attributed to the roughening of the surface and the subsequent increase in local contact stress. They found that the phosphate process introduces considerable compressive residual stresses in the substrate reducing fretting resistance. Furthermore, they observed an increase in the coefficient of friction (COF) compared to bare steel attributed to the increased contact area due to the softer layer. Finally, they concluded that zinc phosphate is not effective in increasing wear resistance.

The authors of this paper attribute the introduction of compressive stresses to epitaxy. In [1] a misfit of -7 % between the hopeite lattice and α-Fe lattice is reported which indeed leads to tensile stresses in the coating and thus compressive stresses in the substrate. Interestingly the misfit of hureaulite is -1 % and should thus lead to less issues with wear resistance of the coating.

Previous work on the mechanical characterization of manganese phosphate coatings was conducted by [15]. They derived a bulk behaviour law for manganese phosphate based on micro hardness indentations combined with a finite element model. The finite element analysis is used to match the experimental indentation data to provide the stress – strain curves assuming a non-layered material. The combined data is fitted to a modified Ludwick model. The procedure yields a continuous material model that incorporates the coating to bulk transition. The surface hardness was measured to be 125 HV.

The wear characteristics as function of the applied phosphating process were first investigated by [3]. The findings were that a thin fine grained coating gives superior wear performance. A more elaborate study on the relation between the coating process and the seizure behaviour of manganese phosphate was done by [16]. Considerable improvements were obtained by fine tuning the cleaning, refining and phosphating parameters. They also showed that the carbon content of the substrate plays a significant role. Next to that they found that annealing

the coating yields considerable improvements in seizure resistance related to improved oil retaining properties and increased surface hardness from 125 HV to 300 HV [15, 17].

The general conclusion for the previous research was that the COF goes down with increasing load and repeated sliding. This is attributed to the formation of a flat and smooth glaze layer after sustained sliding [1]. It is also suggested in [1, 13] that the phosphate layers have a certain directionality or anisotropy owing to the crystal growth and aforementioned epitaxy leading to slight differences in deformation behaviour.

The cited investigators focused on long running systems and characterization of the friction and wear at the macroscopic level. However, the metal-to-metal seal undergoes a maximum total sliding length of <0.5 meter during assembly [18]. Short running systems, like casing connections, and the deformation mechanism at the asperity level that gives rise to the macroscopic friction and wear observations have not been investigated. In order to properly model the phosphate coatings in a contact and wear model [19] to predict its influence on seal ability a characterisation of their properties needs to be performed. This study aims to characterize the deformation mechanism(s) of the phosphate coatings before and after formation of a glaze layer.

A.2. Methods

In order to obtain fundamental insight in the effect of phosphate coatings on surface evolution and thus sealing performance it is important to characterise the initial phosphate layer as well as the evolution of the phosphate layer. For the deformation behaviour nano-indentation and scratch experiments are performed. The wear mode is determined according to the works of [20, 21]. The scratch tests will also be used to determine layer hardness and shear strength using the method introduced by Tayebi, Conry and Polycarpou (TCP) [22].

A.2.1. Phosphated specimens

The phosphated specimens were prepared from quenched and tempered AISI4130 steel by water jetting 70 x 70 x 2 mm coupons from 100 mm bar material. These were subsequently ground on both sides to a surface finish of $R_a = 0.1\,\mu\mathrm{m}$. The substrate hardness was measured prior to phosphating by the method of Section A.2.3 at 500 mN resulting in a hardness of 1.96 $\pm$ 0.3 GPa.

After grinding, the specimens were cleaned, degreased and water rinsed before they were dipped in the zinc or manganese phosphate bath. See Table A.1 for an overview of the process parameters. The resulting coating weights are reported in the final row. Note, however, that due to the morphology a coating thickness is difficult to define [1]. Therefore absolute depths are reported in the results.

SEM micrographs of the coating are shown in Figure A.2. The morphology for the zinc phosphate is the distinct needle shape [1] in agreement with its orthorombic dipyramidal unit cell [11]. The morphology for manganese phosphate is the characteristic plate structure

Table A.1.: Overview of the phosphate conversion coating process for the AISI4130 substrate.

Step	Treatment	Zinc phosphate	Manganese phosphate
1	Degreasing	Gardoclean® 349, $50g/l$, $75°C$, 10 min dip	
2	Rinsing	cold water	
3	Activation	Gardolene® V6522, $2g/l$, $40°C$, 1 min dip	Gardolene® V6563, $4g/l$, $40°C$, 1 min dip
4	Phosphating	Gardobond® Z3300, $75°C$, 5 min dip time, Free acid: 18, Total acid: 112, Fe++: $0.9g/l$	Gardobond® G4098 + $5g/l$ Gardobond®Additive H7050, $90°C$, 5 min dip time, Free acid: 18; Total acid: 119; Fe++: $1g/l$
5	Rinsing	cold water & demineralized water	
6	Drying	oven $95°C$	
-	Coating weight	$4.5g/m^2$	$10.95g/m^2$

[1] coming from its monoclinic prismatic unit cell [12]. The manganese phosphate process produces a much denser and more refined coating compared to zinc phosphate. The surface roughness of the coatings was measured using a confocal microscope (Keyence VK-9700) and is shown in Figure A.1. This shows that zinc phosphate produces a much rougher surface compared to manganese phosphate.

X-ray diffraction (XRD) measurements were performed to characterize the phosphate crystal type. The measurements were performed on 2 different positions on the sample surface. For the manganese phosphate coatings, an additional measurement with a measurement time of 3600 s/frame was performed. The measurement settings are reported in A.4. The XRD characterization of the specimens confirms that the crystal structure for zinc phosphate is predominantly hopeite [11] while for manganese phosphate it is hureaulite [12], see Figure A.3.

A.2.2. Experimental design of the scratch experiments

The scratch experiments are designed according to the work of [20]. The relations used to dimension the scratch pins are as follows and assume plastic deformation,

$$\theta = \arctan\sqrt{\frac{h(2r-h)}{r-h}} \tag{A.1}$$

$$h_{sliding} = \frac{F_n}{\pi r H}. \tag{A.2}$$

Where θ is the attack angle, h is the penetration depth and $h_{sliding}$ the penetration depth during sliding. Based on equation (A.1) and assuming a constant hardness, H, of 50 HV0.005 of the coating layer according to [14] two scratch pins with different round off radii were selected.

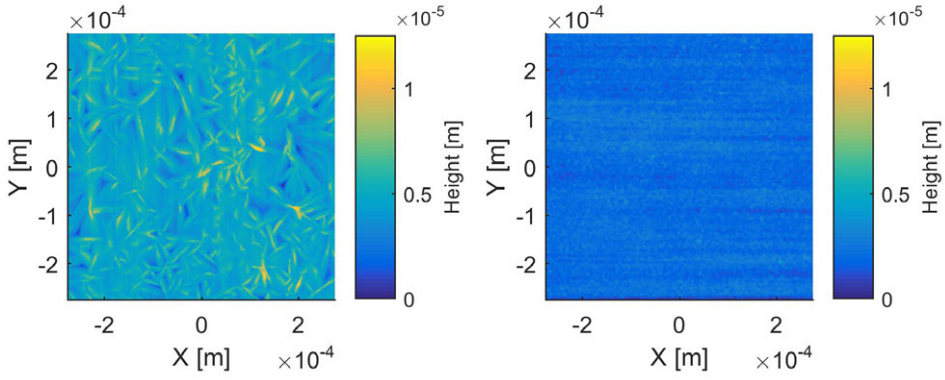

(a) (b)

Figure A.1.: Height maps using confocal microscopy for both coatings. Figure A.1a shows the topology of zinc phosphate and Figure A.1b for manganese phosphate. Height is scaled to the maximum of zinc phsophate.

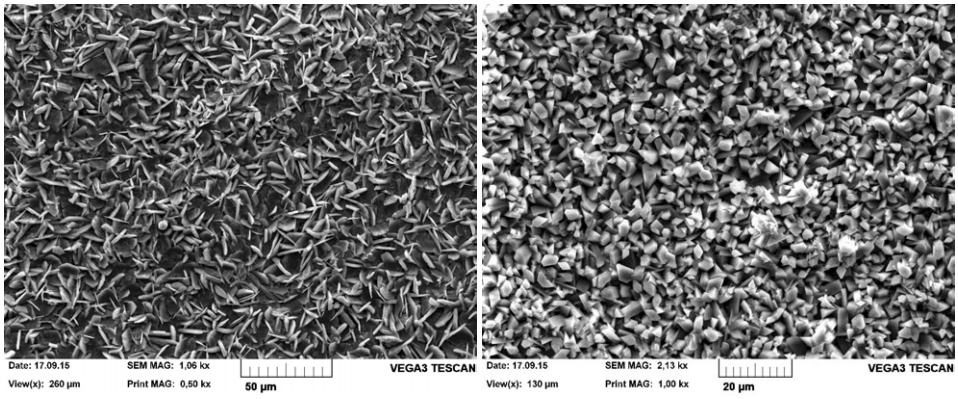

(a) (b)

Figure A.2.: SEM micrographs of the phosphate coatings and the crystals that they contain. Figure A.2a shows zinc phosphate with is characteristic needle structure. Figure A.2b is manganese phosphate with its characteristic plate structure. Note the difference in magnification between the zinc and manganese phosphate specimens.

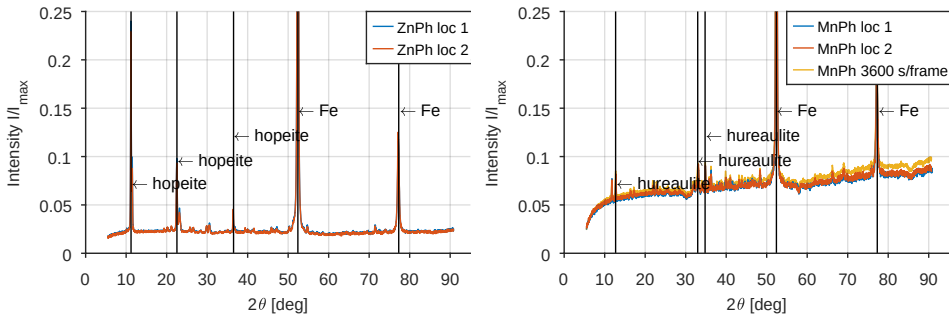

(a) (b)

Figure A.3.: X-ray diffractogram for zinc and manganese phosphate coated specimens. The intensity is normalized by the maximum intensity. The peaks at $52.4\,\mathrm{deg}$ and $77.3\,\mathrm{deg}$ are from the iron in the substrate. The remaining diffractogram is in agreement with hopeite for zinc phosphate and hureaulite for manganese phosphate. Note that the second XRD measurement for manganese phosphate was performed at $3600 s/frame$.

A sharp indenter made of quenched and tempered Sverker21 steel with a round-off radius, r, of 100 µm which connects in a continuous manner to a 90° conical section [20]. The surface hardness is 700 HV and the surface finish is polished with an $R_a = 0.01\,\mu\mathrm{m}$. A ball was used for lower contact angles at higher contact loads and larger contact areas. The ball is made of AISI52100 steel with a radius of $1500\,\mu\mathrm{m}$, a surface hardness of 700 HV, and a polished surface finish of $R_a = 0.01\,\mu\mathrm{m}$. The sliding velocity, v, is chosen as low as possible to minimize thermal effects. Scratch tests with constant load and with increasing load were performed to respectively determine the deformation behaviour, scratch hardness and shear strength of the layers. The tribofilms generated with the ball in the constant load experiments were subsequently used to determined the hardness of the layer and deformation behaviour after run in. The experimental variation is determined by the round-off radius and applied load. The experiments and their resulting attack angle, penetration depth and sliding lengths are summarized in Table A.2.

Prior to all the experiments the scratch pins and balls were ultrasonically cleaned in acetone for 15 minutes, subsequently dried with nitrogen and wiped with lens paper.

The tests were performed on two tribotesters. The ploughing asperity tester [20] and a Bruker UMT-3. The ploughing asperity tester is a dedicated test set-up for single asperity tests. The machine was used for the single unidirectional scratches. The Bruker UMT-3 is a universal mechanical tester which was used in the pin on disc mode. In this case the scratch tracks are placed in an arc. The machine was used for the scratch hardness and the single and repeated unidirectional scratches on a single wear track.

Next to the tribotester (UMT-3) depth measurement, the wear track width and depth are measured using a confocal microscope. The height of the deposition on the pins is also measured using a confocal microscope. A subset of the pins were inspected using a SEM to identify the deposition using EDX.

Table A.2.: Overview of experiments

Experiment	Passes	r	F_n	Loading	l	θ	$h_{sliding}$	v
	(#)	(μm)	(N)	(-)	(mm)	(deg)	(μm)	(mm/s)
Unidirectional	1	100	0.1−5	constant	5	16−45	0.6 − 32	0.1
	1	1500	5 − 45	constant	5	3 − 9	2 − 20	0.1
	10	1500	5 − 45	constant	5	3 − 9	2 − 20	0.1
Scratch hardness	1	100	0.1−5	ramp	1.8	16−45	0.6 − 32	0.1

A.2.3. Nano-indentation

Nano-indentation is used to determine the surface hardness of the phosphate coating before and after the generation of the tribofilm or glaze layer [1] in the unidirectional sliding experiments. The goal of the nano-indentation is threefold: to determine the surface hardness of the coatings; to determine the deformation behaviour of the coatings and to determine the transition from coating hardness to substrate hardness as function of penetration depth. These results will then be used to characterize the layers and can serve as input for a layered contact or wear model.

The structure (Figure A.2) of both phosphates gives a rough non-uniform surface (Figure A.1). The indentation results reported here were all placed in the needles for zinc phosphate and in random locations for manganese phosphate. Furthermore, indents were performed in a wear track after 10 passes to investigate how the compaction of the phosphate layers changes the surface hardness and deformation behaviour.

The equipment used for these experiments is the universal nano-mechanical tester (UNAT) built by Asmec. The nano-indentation was carried out using a diamond Berkovich tip. The loads applied ranged from 1 - 500 mN. Each test was repeated 15 times, tests with fracture events were discarded. The load was applied in 10 s, the hold time was 15 s and unloading was performed in 4 s. The tip geometry and measurement set-up were validated prior to the measurements using a sapphire reference. To establish a datum for the indentation tests, an indentation at 0.1 mN is made prior to the measurement. Processing of the force-displacement curves is done according to the method of [23].

A.2.4. Determination of scratch hardness and shear strength

The hardness and shear strength will be determined from the measured normal, F_n, and tangential force, F_t, with the method of [22], here abbreviated as TPC method, by solving the

following system of equations,

$$F_t = Hr^2\left[\alpha - \sin(\alpha)\cos(\alpha)\right] + 2sr^2\left[\int_0^{\pi/2}\int_0^{\alpha}\sin(\zeta)\sqrt{\sin^2(\xi)+\cos^2(\xi)\cos^2(\zeta)}d\zeta d\xi\right] \tag{A.3}$$

$$F_n = \frac{\pi}{2}Hr^2\sin^2(\alpha) - sr^2\left[\sin(\alpha) - \cos^2(\alpha)\ln\left(\frac{1}{\cos(\alpha)} + \tan(\alpha)\right)\right] \tag{A.4}$$

$$\alpha = \theta = \arctan\sqrt{\frac{h(2r-h)}{r-h}} \tag{A.5}$$

Where H is compound surface hardness, s is the shear stress opposite to the sliding direction, α is defined as the angle of a line from the centre of the sphere to the point of first contact with the layer equivalent to the attack angle [20] and ζ, ξ are integration variables. The difference with [22] is the use of the measured depth from the tribometer instead of calculating the depth by adding a modelled elastic deformation to the measured plastic deformation. This choice was made because of the difficulty of establishing a datum on these rough surfaces. Note that this equation assumes bulk properties and is therefore only valid for relatively small depth/coating thickness ratios.

A.3. Results & discussion

A.3.1. Nano-indentation as received coatings

The nano-indentation force – displacement curves at 3 mN are presented in Figure A.4. Comparing the indentation depths it can be seen that zinc phosphate (ZnPh, Figure A.4a) has a lower indentation depth than manganese phosphate (MnPh, Figure A.4b). The indentation curves show instability during the indentation phase and large variability in indentation depth. This is most apparent for MnPh. In certain cases the coating failed in the hold phase. The instability and variability indicates brittle material behaviour and subsequent failure of the coating and is confirmed by the absence of elastic recovery.

The processed results in Figure A.5 show the indentation hardness and depth for all applied normal loads. Indeed zinc phosphate is measured as having a higher hardness than manganese phosphate. Multiple indentations reveal a rather large spread in the observed crystal hardness as shown in Figure A.5a. This is attributed to the brittleness combined with the discrete crystals that the coating consists of. Based on the crystal hardness found in literature [1, 13] this result is unexpected and can be explained by the following.

First, the approximate point of transition to the substrate hardness from Figure A.5b is used to estimate the coating thickness. The zinc phosphate coating has an average thickness of >6 µm and the manganese phosphate coating >5 µm. This is supported by the coating weight [1].

Second, the area function for the Berkovich indenter is $A = 24.56h^2$. This gives for the zinc phosphate 3 mN indentation with h = 0.3 µm an A = 2.2 µm^2 or an equivalent length (square root of the area) of 1.5 µm. The manganese phosphate 3 mN indentation with h = 0.7 µm an A

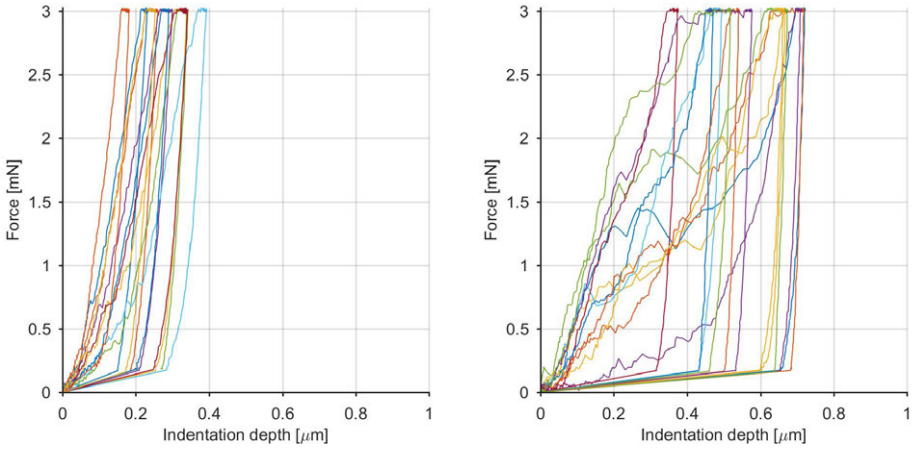

(a) (b)

Figure A.4.: Nano indentation results for both coating layers. The 3 mN load was applied in 10 s, the hold time was 15 s and unloading was performed in 4 s. Figure A.4a shows the results for zinc phosphate and Figure A.4b manganese phosphate.

= 12 µm^2 gives an equivalent length of 3.5 µm. The lengths are compared to the crystal sizes using the microscopy in Figure A.2 and topography in Figure A.1.

For zinc phosphate the hardness decreases with increasing load which is explained by the roughness and long and narrow needle structure. Under increasing load the contact area will grow beyond the width of the needles reducing the support for the indenter and increasing the measured penetration depth. The results in Figure A.5a support this hypothesis showing decreasing hardness for increasing load and a much lower hardness than expected close to the substrate.

For manganese phosphate the reverse is happening, the hardness increases with load. Potential explanation are that the coating is considerably softer and thinner than thought. Or because of the small crystal size the indenter is cleaving the crystals. This is exemplified by the instability during indentation as can be seen in Figure A.4b. As the indentation depth increases more crystals participate in the contact recovering the phosphate bulk hardness. Taking into account the thickness estimation the results in Figure A.5a support the latter hypothesis.

Considering the above, the validity of instrumented hardness measurements and the application of the Oliver & Pharr method [23] for these coatings should be called into question. Therefore the observations are only used qualitatively for the deformation behaviour.

The hypotheses above imply that the effective bulk hardness will be lower than the nano-hardness for zinc phosphate and higher for manganese phosphate. Based on Figure A.1, for zinc phosphate the area covered by the higher needles is about a third. The large needle structure of the zinc phosphate coating will first bear the load. This lowers the effective hardness of the coating. Hence the bulk hardness will depend on two coupled properties: the amount of

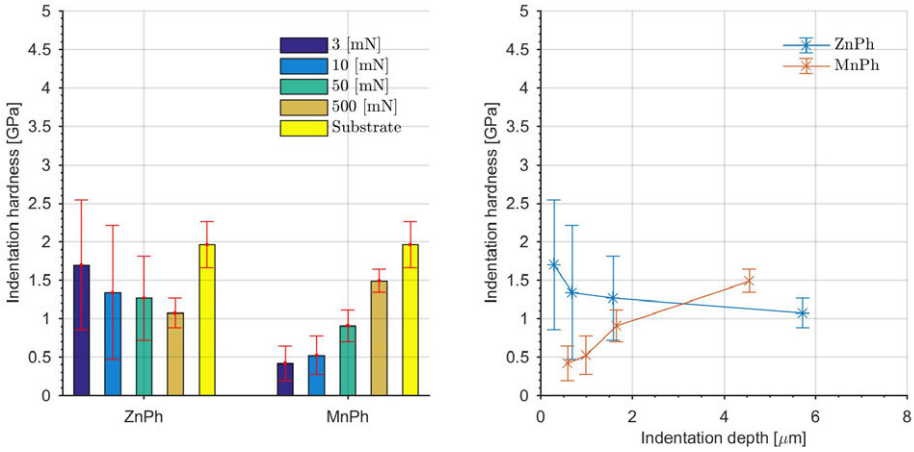

(a) (b)

Figure A.5.: Statistical results of nano-indentation. Figure A.5a gives an overview of the average results for each coating, the error bar indicates the standard deviation. Figure A.5b shows the hardness versus indentation depth

crystals present on the surface and the size of these crystals. Where the size is dependent on the initial amount of crystal nucleation sites as the growth is restricted by neighbouring crystals [1]. Then the following can be written for the bulk hardness,

$$H_c = \frac{F_n}{A_{indenter}} \tag{A.6}$$

$$H_b = \frac{A_{true}}{A_{total}} H_c \tag{A.7}$$

$$\frac{A_{true}}{A_{total}} = \rho_c A_c \tag{A.8}$$

Where H_c is the single crystal hardness as measured with nano-indentation, H_b is the bulk hardness derived from the ensemble of single crystals with area A_c and coverage ρ_c in crystals/square meter defining the true area A_{true} relative to the total area A_{total}.

Applying equation (A.7) to the zinc phosphate example results in a bulk hardness of 600 MPa based on the single crystal hardness of 1800 MPa which is close to the earlier reported value of 50 HV in [14]. For manganese phosphate this is much less of an issue, almost the full area will be in contact owing to the smoothness of the surface. In both cases it means that for high bulk hardness the coating coverage needs to be maximum, advocating a fine and dense coating.

To obtain bulk coating properties from nano-identation of individual crystals the following is proposed. The crystal density and single crystal size can easily be obtained using image recognition software or as is done here the true area can be measured directly from surface topography measurement using a height cut-off filter.

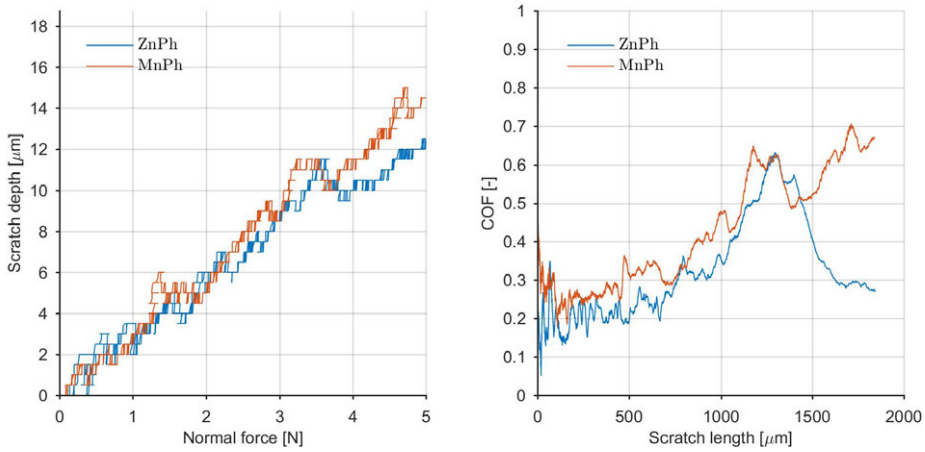

(a) (b)

Figure A.6.: Results of scratch testing with r = 100 µm radius tip. Figure A.6a shows depth as function of normal force during sliding. Figure A.6b shows the COF versus scratch length.

A.3.2. Scratch hardness and shear strength from ramped load tests

The measured scratch depth versus scratch length and the corresponding COF are depicted in Figure A.6. For both coatings the depth is initially increasing at a similar rate, see Figure A.6a. For zinc phosphate the indenter is reaching the substrate earlier evidenced by the change in penetration rate. Comparing the results in Figure A.6b zinc phosphate has a lower COF than manganese phosphate indicating easier removal of the coating.

Using equation (A.3) the resulting scratch hardness and shear strength are computed and the result is shown in Figure A.7. As with the nano-indentation the crystal density, $\rho_{crystal}$, and associated roughness make it complicated to perform a stable measurement on the specimens. The properties are determined at 10 % of the respective coating thickness. The resulting scratch hardness averages around 1.2 GPa and is in agreement with the nano-indentation results of Figure A.5. The shear strength of zinc phosphate averages at 25 MPa which is lower than manganese phosphate at 50 MPa.

The reason for the difference in shear strength is threefold: complete ZnPh needles (see Figure A.8a) are removed, the higher roughness of ZnPh and thus the varying amount of material in front of the indenter and misfit of the ZnPh crystal lattice leading to tensile stresses in the coating. This matches and explains the introductory remarks related to zinc phosphate having lower wear resistance than manganese phosphate.

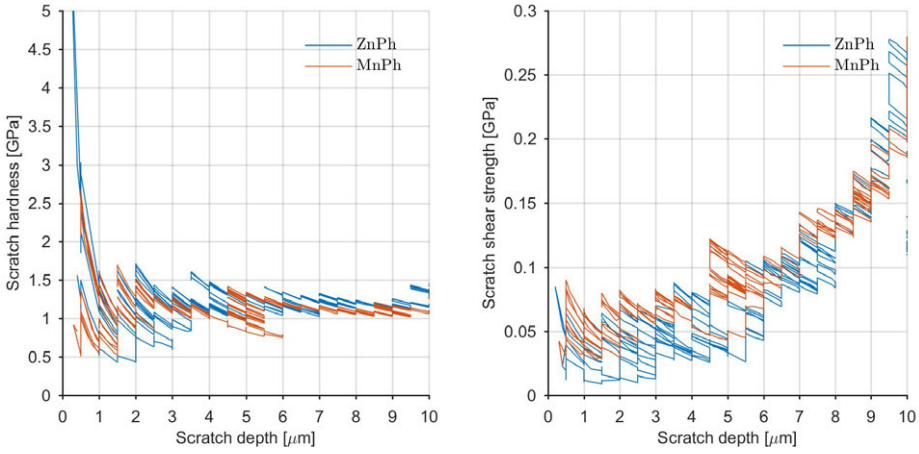

(a) (b)

Figure A.7.: Figure A.7a shows the computed hardness and Figure A.7b the computed shear strength from the scratch experiments. The results are truncated at 10 µm scratch depth for comparison with Figure A.5. As shown in [22] the hardness converges with increasing depth to the substrate value.

A.3.3. Deformation behaviour based on constant load tests

The following qualitative observations are made during the constant load tests and are representative for the full set of experiments. Figure A.8 shows the balls after the 35 N tests. Both zinc Figure A.8a and manganese Figure A.8b phosphate adhere strongly to the counter surface. The transfered layer could not be removed by wiping or ultrasonic cleaning. Note that the angle of attack will be reduced by the presence of the lump of transferred material on the pin similar to the observations of [20]. Figure A.8c and Figure A.8d show the measurement of the average height of the lump on the respective balls. The lumps, disregarding the loose debris, are approximately 10 µm heigh after removal of the sphere.

It is further interesting to note the shape of the transfer layer formed by the transferred phosphate. The shape exactly resembles the contact area during fully plastic sliding, see for instance [24, 25] justifying the choice for equation (A.1). Next to that, the debris particles indicate a brittle material. Reinforcing the notion of the coating being crushed by a brittle failure mode. After crushing, the debris is subsequently compacted in the contact to form the lump. When using a sharp asperity having higher contact angles this is not observed. In that case complete crystals are lifted from the surface comparable to the wedging mode as described by [21].

In Figure A.9 a SEM micrograph is shown of the zinc phosphate transfer layer on the ball. Upon closer inspection brittle fracture lines can be observed in the deposition confirming the earlier observations. Furthermore the layer has the appearance of a densely packed powder which has been polished to a very smooth surface finish. The EDX analysis confirms that the transferred material is indeed consisting of zinc, phosphorus and oxygen.

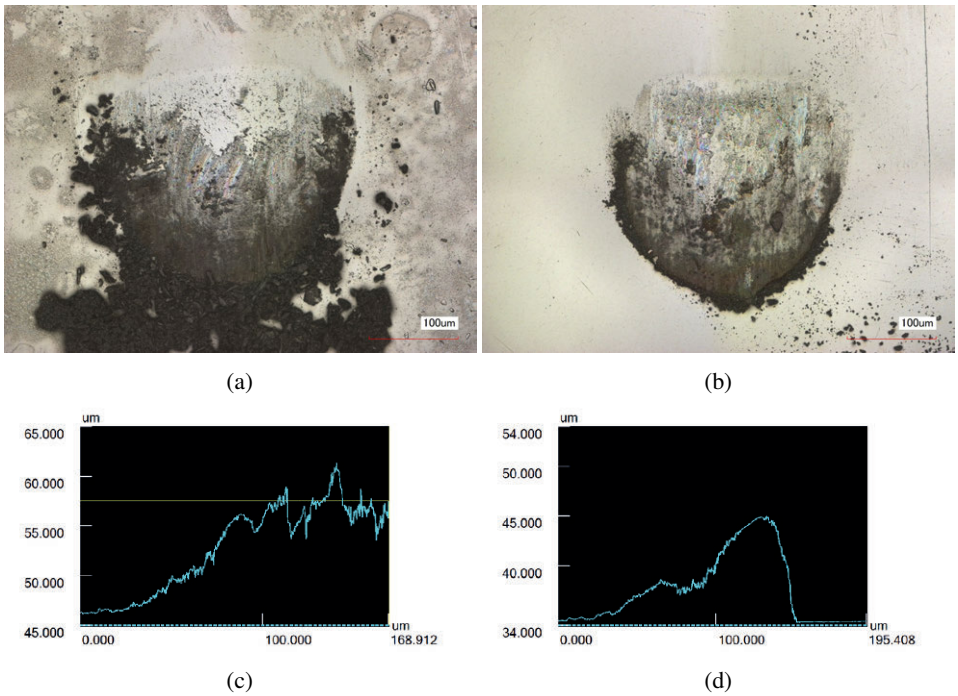

Figure A.8.: Comparison between zinc phosphate in Figure A.8a and manganese phosphate in Figure A.8b at a normal load of 35 N. Microscopy is taken before cleaning. Images are representative for the complete set. Figure A.8c is the measured lump height after subtracting the sphere for Figure A.8a. The same is done for manganese phosphate Figure A.8b in Figure A.8d.

.

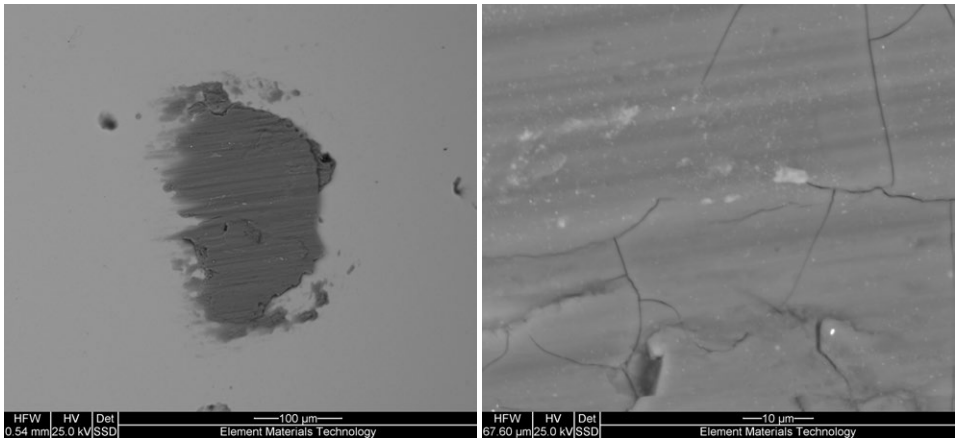

(a) (b)

Figure A.9.: SEM recording of zinc phosphate transfer layer. Overview on the left, zoom in on the right. The normal force during sliding was 30 N. Clearly visible are what seem to be brittle fractures in the otherwise very smooth transfer film.

However, transfer of lumps of phosphate is not always observed. Shown in Figure A.10 are two examples of instances where no transfer occurred, one for each phosphate type. Figure A.10a shows the counter surface after running against zinc phosphate. Figure A.10b shows the counter surface is shown after running against manganese phosphate for which the same observations are made. A silver coloured turning to brown deposition can be observed which is confirmed with EDX to be a thin film of zinc or manganese phosphate.

The lack of transfer is explained by the different orientation of the pins with the surface during sliding. Until now all experiments were performed with the direction of grinding of the plate. In this case the wear track described a circular path and thus traversed the ridges of the underlying roughness. Upon traversing material from the pin is deposited in the valleys as described in the previous section.

A.3.4. Wear tracks

A comparison of two wear tracks is shown in Figure A.11. Figure A.11a and Figure A.11c are zinc phosphate and Figure A.11b and Figure A.11d are manganese phosphate. The lower 2 tracks are after a single scratch experiment, the top two tracks are after 10x repeated unidirectional scratch experiments. Note how initially only the peaks of the zinc phosphate are flattened, after 10x repeated sliding the roughness is filled with the debris which is subsequently compacted and polished. Pile up of removed material is visible at the sides of the wear track. In the manganese phosphate case this is less pronounced due to the smaller crystal size, however, the same mechanism is at play here based on the earlier observations of deposition on the balls.

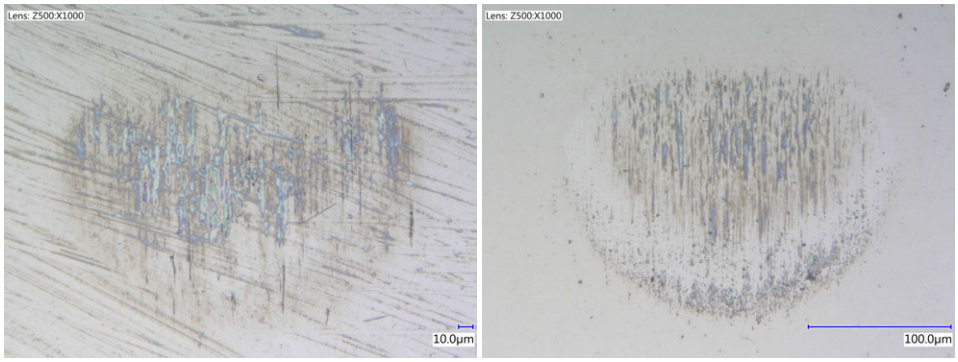

(a) (b)

Figure A.10.: Overview of the wear scars for dry experiment without transfer to pin. Figure A.10a shows zinc phosphate and Figure A.10b is manganese phosphate. The thin film was confirmed to be zinc or manganese phosphate using EDX.

Further, after formation of a so called glaze layer [1] the wear process enters a second phase of wearing through the formed layer. In this case the layer is thinned until small pieces start to break out according to a mechanism similar to delamination which exposes the underlying substrate. Some of which is starting to occur in Figure A.11a.

A.3.5. Nano-indentation of formed tribofilm or glaze layer

The topmost wear tracks shown in Figure A.11 were indented with the same loads as previous indentations to investigate the properties of the glaze layer. The results are shown in Figure A.12 and it is observed that the glaze layer possesses a significantly higher surface hardness over a longer depth range compared to the as received coatings. This indicates also a high cohesion between the individual debris particles. Which supports the earlier hypothesis on the formation of a compacted layer of small debris particles under the sliding contact.

A fit of the average indentation results versus depth is made with the following models. The work of [26] states the compound hardness as follows

$$H = H_s + (H_l - H_s)\exp^{-\frac{\beta h_c}{t}}. \tag{A.9}$$

Where H is the compound indentation hardness, H_s is the substrate hardness, H_l is the layer hardness, β is a constant that depends on the elastic modulus and yield strength of the layer and substrate, h_c is the indentation depth and t is the coating thickness. Korsunsky [27] derived the following relation for the layer to substrate hardness transition

$$H = H_s + \frac{H_l - H_s}{1 + k\left(\frac{h_c}{t}\right)^2}. \tag{A.10}$$

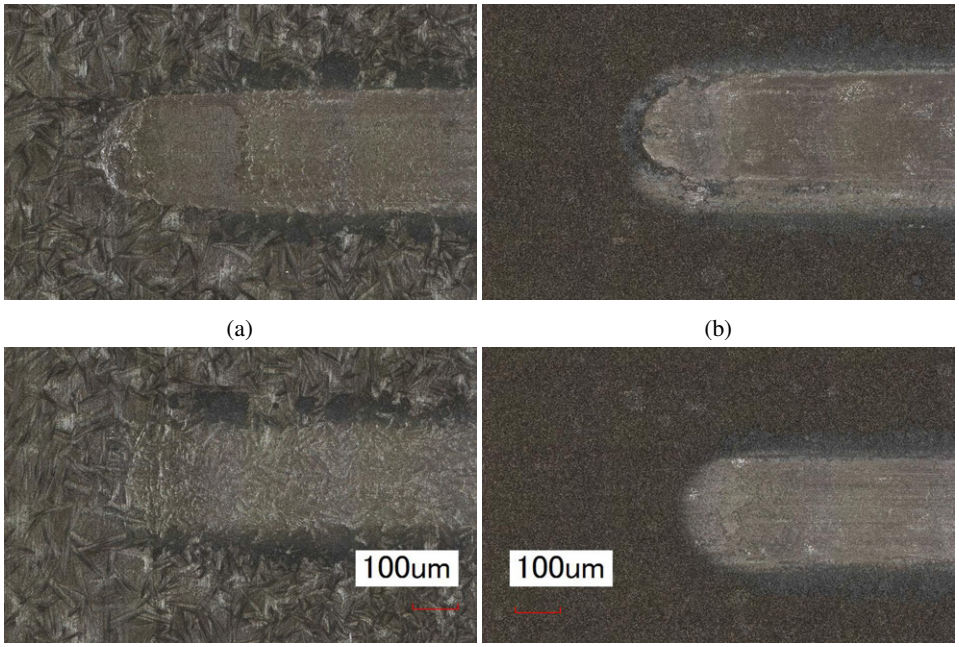

(a) (b)

(c) (d)

Figure A.11.: Comparison of two wear tracks made with a $3mm$ ball. Bottom after one pass at $45N$, top after 10 passes at $35N$. Location is at the end of the tracks. Figure A.11a and Figure A.11c are zinc phosphate and Figure A.11b and Figure A.11d are manganese phosphate. Notice how after one pass the underlying crystal structure is still visible. After 10 passes the layer is compacted and the previously rough crystallographic topology has been polished. Pile up is visible next to the wear tracks.

Table A.3.: Results of the fitting process using the models (A.9) and (A.10).

Coating	t (µm)	Model (A.9), [26] β	Model (A.9), [26] H_l (GPa)	Model (A.10), [27] k	Model (A.10), [27] H_l (GPa)
ZnPh	6	3.1	3.18	14.47	3.06
MnPh	5	1.3	3.47	2.74	3.36

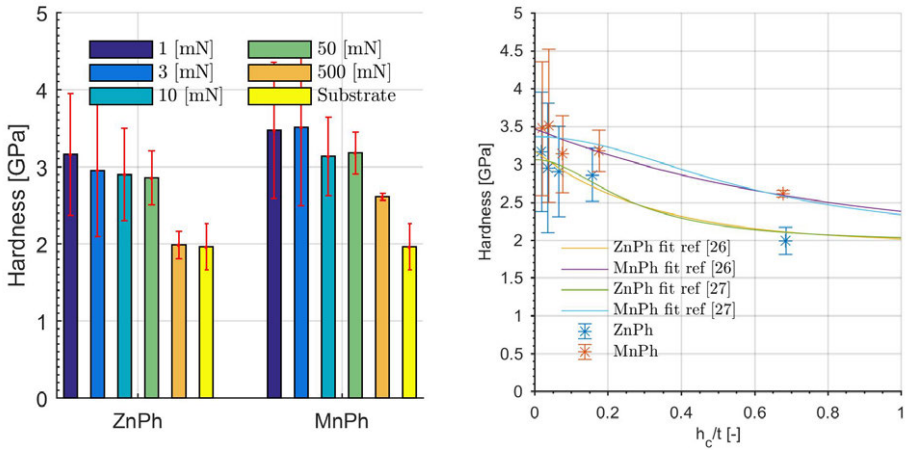

(a) (b)

Figure A.12.: Statistical results of nano-indentation on the glaze layer. Figure A.12a gives an overview of the average results for each coating, the error bar indicates the standard deviation. Figure A.12b shows the hardness versus indentation depth compared with a fit using (A.9) and (A.10).

Where k depends on whether the deformation is plasticity of fracture dominated. Here H_l and β or k are used as fitting parameters. The result is shown in Figure A.12b. The values found from the fitting procedure are shown in Table A.3. It shows that the glaze layer exhibits typical behaviour for a hard layer on soft substrate. Care should be taken though because of the large spread on the indentation results.

Note further that even though AISI4130 exhibits plastic strain hardening [28], the hardness increase is entirely attributed to the compaction of the phosphate into a glaze layer. This is supported by the results because at deeper penetration the hardness converges to the "as received" substrate value.

A.3.6. Implications for the full scale system

Previous investigators [1, 3, 14–17] found that zinc phosphate coated systems have a higher wear rate than manganese phosphate. As shown zinc phosphate will in practice exhibit a lower

hardness because of a reduced contact area owing to its roughness coming from its dendritic crystal structure. As a consequence the counter surface will penetrate deeper in the coating layer which, combined with its lower shear strength, leads to higher wear.

The mechanism that allows the formation of a glaze layer [1] in phosphated systems was shown to be as follows. The attack angle of the asperity is kept low due to the formation of a lump. Therefore the system remains in the ploughing regime. By keeping the attack angle low, the counter surface compacts and polishes the phosphated surface. Furthermore there is a supply of phosphate to fill gaps in the surface topology which is also subsequently compacted and polished. In contrast, the sharp asperity removed complete crystals from the surface. This advocates the use of phosphates on one surface rubbing against a smooth, hence asperities with low attack angle, counter surface.

A.4. Conclusions

The mechanical properties and wear characteristics of dry zinc and manganese phosphate coatings were investigated using nano-indentation and a pin-on-disc tribometer. The hardness of the as received coating layers and the formed glaze layer were determined using a Berkovich indenter. Further, the scratch hardness and shear strength of the layers were determined using single asperity scratch tests with a 100 µm and 1500 µm round off asperity.

1. The hardness tests of the as received coatings revealed brittle material behaviour and fracture events. The zinc phopshate nano-hardness was higher compared to manganese phosphate because of the difference in crystal structure.

2. The scratch tests further confirmed the brittle material behaviour. The computed shear strength showed that zinc phosphate has a lower shear strength than manganese phosphate because of complete removal of the needle shaped crystallites.

3. The formation of the glaze layer in phosphate coatings was shown to be related to crushing and compaction of phosphate debris combined with a low attack angle and the formation of a lump on the counter surface. The lump lowered the attack angle keeping the system in the ploughing regime allowing for the counter surface to polish the glaze layer. The lump acts as a reservoir to fill up any gaps in the surface topology leading to a homogeneous and flat glaze layer.

4. The glaze layer has a significantly higher hardness compared to as received coating due to compaction of the worn phosphate crystals in the sliding contact. The layer is brittle owing to the base coating properties as shown by nano-indentation, SEM and the contact area shape. The hardness of the layered system can be satisfactorily described by standard models normally used for metallic layers.

Acknowledgements

The authors are grateful for the financial support for this work by Shell Global Solutions International BV. Dr. Frank Hollmann and Ralf Schneider of Chemetall GmbH are acknowledged for sharing their knowledge on phosphate conversion coatings and the preparation of the lab specimens.

XRD settings

The crystallographic characterization of the phosphate is performed with a Bruker D8 Discovery HTS diffractometer equipped with a Vantec 2000 detector and a Co2K source. The following measurement parameters were used: Snout: $0.5[mm]$, $\theta_1 = 5$, $\theta_2 = 15$, Frames : 3 with a frame width of 28 each, Scan axis: Coupled, Mode: step, Sample oscillation: None, Measurement time/frame: $1200[s]$, Slit width: $1.2[mm]$ line/$0.5[mm]$ point. Before the start of the measurements, a reference corundum sample (1776, NIST) is measured to check the alignment of the detector.

References

[1] Rausch, W. *The phosphating of metals*. Metals Park, Ohio, USA; Teddington, Middlesex, England: ASM International; Finishing Publications Ltd., 1990, p. 406.

[2] Burke, D. 'The Sliding Friction of Bonded Solid Lubricants'. PhD thesis. University of central Lancashire, 2005.

[3] Khaleghi, M., Gabe, D. and Richardson, M. 'Characteristics of manganese phosphate coatings for wear- resistance applications'. *Wear* 55.2 (August 1979), pp. 277–287.

[4] Totik, Y. 'The corrosion behaviour of manganese phosphate coatings applied to AISI 4140 steel subjected to different heat treatments'. *Surface and Coatings Technology* 200.8 (January 2006), pp. 2711–2717.

[5] Weng, D., Jokiel, P., Uebleis, A. and Boehni, H. 'Corrosion and protection characteristics of zinc and manganese phosphate coatings'. *Surface and Coatings Technology* 88.1-3 (January 1997), pp. 147–156.

[6] Ertas, A. 'Experimental Investigation of Galling Resistance in OCTG Connections'. *Journal of Manufacturing Science and Engineering* 114.1 (February 1992), p. 100.

[7] Pérez-Ràfols, F., Larsson, R., Riet, E. J. van and Almqvist, A. 'On the flow through plastically deformed surfaces under unloading: A spectral approach'. *Proceedings of the Institution of Mechanical Engineers, Part C: Journal of Mechanical Engineering Science* 232.5 (March 2018), pp. 908–918.

[8] Pérez-Ràfols, F., Larsson, R., Lundström, S., Wall, P. and Almqvist, A. 'A stochastic two-scale model for pressure-driven flow between rough surfaces'. *Proceedings of the Royal Society A: Mathematical, Physical and Engineering Science* 472.2190 (June 2016).

[9] Pérez-Ràfols, F., Larsson, R. and Almqvist, A. 'Modelling of leakage on metal-to-metal seals'. *Tribology International* 94 (February 2016), pp. 421–427.

[10] Inose, K., Sugino, M. and Goto, K. 'Influence of Grease on High-Pressure Gas Tightness by Metal-to-Metal Seals of Premium Threaded Connections'. *Tribology Online* 11.2 (2016), pp. 227–234.

[11] Hill, R. and Jones, J. 'The crystal structure of hopeite'. *American Mineralogist* 61 (1976), pp. 987–995.

[12] Moore, P. B. and Araki, T. 'Hureaulite: lts Atomic Arrangement'. *American Mineralogist* 58.3-4 (1973), pp. 302–307.

[13] KozŁowski, A. 'Dry friction of manganese phosphate coatings on steel and cast iron'. *Electrodeposition and Surface Treatment* 2.2 (January 1974), pp. 109–122.

[14] Kumar, A., Bhola, S. and Majumdar, J. D. 'Microstructural characterization and surface properties of zinc phosphated medium carbon low alloy steel'. *Surface and Coatings Technology* 206.17 (April 2012), pp. 3693–3699.

[15] Hivart, P., Hauw, B., Dubar, L. and Bricout, J. P. J. 'Numerical identification of bulk behavior law of manganese phosphate coatings. Comparison with tribological properties'. *Journal of Coatings Technology* 75.942 (July 2003), pp. 37–44.

[16] Hivart, P., Hauw, B., Bricout, J. and Oudin, J. 'Seizure behaviour of manganese phosphate coatings according to the process conditions'. *Tribology International* 30.8 (July 1997), pp. 561–570.

[17] Hivart, P., Hauw, B., Crampon, J. and Bricout, J. 'Annealing improvement of tribological properties of manganese phosphate coatings'. *Wear* 219.2 (September 1998), pp. 195–204.

[18] Stewart, F., Le, H., Williams, J., Leech, A., Bezensek, B. and Roberts, A. 'Characterisation of friction and lubrication regimes in premium tubular connections'. *Tribology International* 53 (September 2012), pp. 159–166.

[19] Bosman, R., Hol, J. and Schipper, D. 'Running-in of metallic surfaces in the boundary lubrication regime'. *Wear* 271.7-8 (July 2011), pp. 1134–1146.

[20] Rooij, M. de, Linde, G. van der and Schipper, D. 'Modelling material transfer on a single asperity scale'. *Wear* 307.1-2 (September 2013), pp. 198–208.

[21] Hokkirigawa, K. and Kato, K. 'An experimental and theoretical investigation of ploughing, cutting and wedge formation during abrasive wear'. *Tribology International* 21.1 (February 1988), pp. 51–57.

[22] Tayebi, N., Conry, T. F. and Polycarpou, A. a. 'Determination of hardness from nanoscratch experiments: Corrections for interfacial shear stress and elastic recovery'. *Journal of Materials Research* 18.09 (September 2003), pp. 2150–2162.

[23] Oliver, W. and Pharr, G. 'An improved technique for determining hardness and elastic modulus using load and displacement sensing indentation experiments'. *Journal of Materials Research* 7.06 (June 1992), pp. 1564–1583.

[24] Masen, M. and Rooij, M. de. 'Abrasive wear between rough surfaces in deep drawing'. *Wear* 256.6 (March 2004), pp. 639–646.

[25] Masen, M., Rooij, M. de and Schipper, D. 'Micro-contact based modelling of abrasive wear'. *Wear* 258.1-4 (January 2005), pp. 339–348.

[26] Bhattacharya, A. and Nix, W. 'Analysis of elastic and plastic deformation associated with indentation testing of thin films on substrates'. *International Journal of Solids and Structures* 24.12 (January 1988), pp. 1287–1298.

[27] Korsunsky, A., McGurk, M., Bull, S. and Page, T. 'On the hardness of coated systems'. *Surface and Coatings Technology* 99.1-2 (February 1998), pp. 171–183.

[28] Rajan, K., Deshpande, P. and Narasimhan, K. 'Effect of heat treatment of preform on the mechanical properties of flow formed AISI 4130 Steel Tubes—a theoretical and experimental assessment'. *Journal of Materials Processing Technology* 125-126 (September 2002), pp. 503–511.

This page has been intentionally left blank.

B. The role of phosphate conversion coatings in make-up and seal ability of casing connections

D. Ernens[a,b], E.J. van Riet[b], M.B. de Rooij[a], H.R. Pasaribu [b], W.M. van Haaften[b], D.J. Schipper[a]

[a]*Laboratory for Surface Technology and Tribology, Department of Engineering Technology, University of Twente, P.O. Box 217, 7500 AE Enschede, The Netherlands*

[b]*Shell Global Solutions International BV, Innovation, Research & Development, Wells R & D, Kessler Park 1, 2288 GS Rijswijk, The Netherlands*

Abstract Phosphate-conversion coatings are widely used on (premium) casing connections for protection against corrosion. These coatings provide galling protection in conjunction with lubricant. The friction and wear that occur during makeup and subsequent load cycling strongly influence the sealing performance of the metal/metal seal. Therefore, phosphate-conversion coatings play an important role in the sealing performance of metal/metal seals. An extensive test program was set up to investigate the role of phosphate coatings during makeup and in the subsequent sealing of the metal/metal seal. With pin-on-disk, anvil-on-strip, and ring-on-ring tests, the interactions between the substrate, lubricant, and phosphate coating were investigated. A comparison was made between uncoated and coated specimens using base greases and formulated greases: API-modified lubricant and two commercially available yellow dopes. The results indicate a strong influence of the phosphate coating leading to damage-free makeup, low wear, and less dependence on the lubricant for optimal sealing ability. This is attributed to the formation of a hard and smooth dissimilar surface, the ability to adsorb the lubricant, and the generation of a transfer layer on the uncoated counter-surface. It is concluded that taking the interaction with phosphates into account could enable lubricants to be tailored for sealing performance, and thus can ease the transition to environmentally friendly rated lubricants.

Latest version available on-line: `https://doi.org/10.2118/184690-PA`

B.1. Introduction

Phosphate conversion coatings [1, 2] were initially applied on (premium) casing connections for protection against corrosion during storage. A side effect of the presence of the phosphate coatings was improved galling resistance [3]. Phosphate conversion coatings therefore play an important role in proper make-up of casing connections and their subsequent sealing performance.

The premium connection and, for this paper, its metal-to-metal seal should be considered as a (tribo)system [4, 5]. It is defined as the combination of lubricant (dope), coating, surface finish, and casing material grade under sliding conditions. The contact conditions are determined by the interference of pin and box and the mechanical properties of the pipe material. Next to that, it is important to realize that a connection undergoes sliding in two directions. Make-up (sliding) is predominantly in circumferential direction and micro sliding in axial direction. The micro sliding occurs after make-up because of axial, pressure or thermal load cycling in the well. The performance of a connection design under these conditions is typically verified using ISO 13679 [6] testing.

The work of [7, 8] indirectly assesses the influence of phosphate coatings on the galling behavior of connections during make-up. The coating was applied on the specimens to avoid galling in their screening tests. Implicitly they show that all the fully formulated lubricants show no galling with phosphated surfaces up to extremely high contact stresses. Whereas some of these lubricants normally show galling on bare metal surfaces at very low contact stresses as shown by [8, 9]. No link, however, was made with the subsequent seal ability performance which will be attempted in this paper.

In general the crystalline phosphate layer provides a chemically incompatible surface with large surface area [1, 2]. The large surface area and high surface energy facilitates the adsorption of a lubricant to protect the surface [10–12]. Further, the coating can deform slightly to even out high pressure peaks in the contact and improve conformity of the surfaces [11]. Under sliding conditions the phosphate crystals are crushed and compacted leading to the formation of a hard and smooth glaze layer [13]. Furthermore, because of the properties mentioned it can also serve as a base layer for corrosion inhibitors [14]. In other applications it is used to reduce wear, circumvent galling, and improve running in [15] or as a base layer for paint and organic coatings [10, 16].

Sealing performance of contacting elements has been shown to be determined by the surface texture, its orientation and changes thereof [17–20], the shape distortion [21], the interaction with the lubricant [22] and degradation thereof [17]. The work of [19] shows for instance a significant difference in seal ability between a turned and a sand blasted surface topography. The turned surface topography seals much better because of the highly localized circumferential line contacts as a consequence of the waviness. The work of [17] compares lubricant influence (API modified [23] vs an environmentally friendly grease) on seal ability performance. They show that a connection can be successfully made-up but fail during load cycling because of thermal degradation of the lubricant. This exposed the surface directly to the hard inorganic particles contained in the environmentally friendly grease. The particles subsequently abraded the surface leading to formation of scratches and/or galling in the seal area reducing its sealing

performance. In addition, the surfaces generally showed higher wear because of the presence of these abrasive particles.

The initial configuration (turned vs. sand blasted) and subsequent evolution because of friction and wear of the tribosystem is thus important for successful sealing. Moreover the wear should be minimized to stay as close as possible to the initial configuration and the intended design contact stresses of the connection manufacturer. Hence a low wearing turned surface against a flat surface can be defined as "the optimal sealing configuration".

Therefore, it was hypothesized that phosphate conversion coatings not only inhibit corrosion and avoid galling but also play an important role in creating and maintaining an optimal sealing configuration in today's casing connections in conjunction with the lubricant. Based on the literature this is not considered as part of connection or lubricant design.

An extensive test program of three different experiment types was set-up to test this hypothesis. Small scale pin-on-disc tests were performed to simulate the casing connection at the micro level, up to a ring-on-ring set-up simulating the complete metal-to-metal seal of a casing connection. Care was taken to run the test with similar parameters as in the real connection.

The goal of this paper is to provide understanding of the role of phosphate coatings on casing connections and its contribution to sealing, propose a new direction for connection (tribo) system design, and ease the transition to environmentally friendly pipe dopes.

B.2. Methods

Real connections are manufactured on a lathe, resulting in a characteristic spiralling turning profile around the circumference. The surface texture thus has a certain directionality or lay. The pitch and amplitude are determined by the feed rate and cutting depth. When taking a cross section in axial direction a wavy line profile emerges comparable to the turned texture shown in Figure B.1. As discussed in the introduction, a connection sees two types of relative motion. Make-up or circumferential direction resulting in a velocity vector oriented parallel to the waviness and micro-sliding or axial direction resulting in a velocity vector perpendicular to the waviness. This was mimicked in the tests.

The design of the tests and related cumulative sliding lengths is in accordance with ISO 13679 [6] CALIV (Connection Assessment Level) dictated make/break tests and load cycling. Assuming a 9-5/8" 53.5# connection with the seal at mid wall and that the metal-to-metal seal fully engages in 1/3 of a turn the cumulative sliding length for 3 make/breaks is ~1.5 meter. To give an indication of the contact conditions the Hertzian [24] contact stresses were calculated using the mechanical properties of the substrate with a Young's modulus of 210 GPa and Poisson ratio of 0.3.

First, the pin-on-disc tests are designed to investigate make-up sliding by sliding parallel to the waviness. Next to that, the relatively small stroke length gives insight in the lubricant behavior during micro sliding. The applied contact stresses are equivalent to those in the metal-to-metal seal of a premium connection. The test is used for screening purposes and to gain understanding of the friction and wear properties at the micron scale.

Table B.1.: Chemical composition used steel grades.

Chemical composition (wt%)										
	C	Si	Mn	P	S	Cr	Ni	Cu	Mo	V
API 5CT P110	-	-	-	$\leq$ 0.02	$\leq$ 0.01	-	-	-	-	-
Typical P110	0.26− 0.35	0.17− 0.37	0.40− 0.70	$\leq$ 0.02	$\leq$ 0.01	0.80− 1.10	$\leq$ 0.20	$\leq$ 0.20	0.15− 0.25	$\leq$ 0.08
AISI4130	0.28− 0.33	0.15− 0.35	0.40− 0.60	$\leq$ 0.035	$\leq$ 0.04	0.80− 1.10	-	-	0.15− 0.25	-
AISI52100	0.95− 1.10	0.15− 0.30	$\leq$ 0.25	$\leq$ 0.03	$\leq$ 0.025	1.30− 1.60	-	-	-	-

Secondly, the strip test is used for contact stresses and sliding velocities equivalent to those in the connection metal-to-metal seal. The contact is elliptical which is closer to the circumferential [19] line contact in the seal area. The test, however, is limited to unidirectional sliding parallel to the waviness.

Finally, the ring-on-ring test provides circumferential line contact at equivalent contact stresses and sliding velocities as they occur in metal-to-metal seals. After make-up sliding a seal ability test can be performed. The details will be given in the following sections.

B.2.1. Materials

The pin on disc tests are carried out using an R = 5 mm bearing steel (AISI52100) ball against a quenched and tempered steel (AISI4130) disc. The chemical composition is reported in Table B.1. The ball is polished and has a surface roughness of S_a = 0.01 µm and a surface hardness of 700 HV. The disc is produced by grinding and has a surface roughness of S_a = 0.10 µm and a surface hardness of 240 HV. See Figure B.1 for a measurement of the surface texture. The disc is subsequently zinc or manganese phosphated.

The strip tests are done using a steel (P110) anvil against a steel (P110) strip. The anvils and strips are manufactured from a 4” diameter P110 tubing. The chemical composition is reported in Table B.1. The anvil is turned and has a surface roughness of S_a=1.6 µm and a surface hardness of 320 HV. The strip has the waviness applied by planing (mimicking a turned surface finish) with a cutting element in sliding direction and has a surface roughness of S_a=1.6 µm and a surface hardness of 320 HV. See Figure B.1 for a measurement of the surface textures. These surface properties are common for casing connections. The anvil is subsequently manganese phosphated.

The ring-on-ring tests are performed using steel (P110) "box" against a steel (P110) "pin". The box is flat; the pin has a round-off radius of 80 mm. The box and pin are manufactured from 4” diameter P110 tubing. The chemical composition is reported in Table B.1. The box and pin

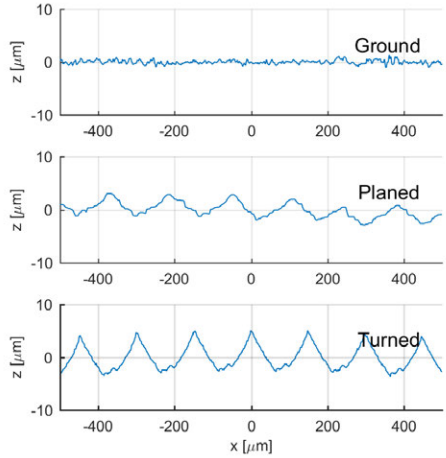

Figure B.1.: Surface textures of specimens before phosphating.

contacting surfaces are manufactured by turning. The surface roughness is S_a =1.6 µm and the surface hardness 306 HV. The box is subsequently zinc or manganese phosphated.

Note: that in all cases the sliding direction is perpendicular to the "paper" in Figure B.1 or parallel to the waviness. Next to that, only the planed and turned surface textures are representative for the metal-to-metal seal surface texture of a casing connection.

B.2.2. Lubricants

To investigate the influence of the separate components of the dope a comparison is made using base oils and base greases versus fully formulated (yellow) dopes. These are listed in Table B.2. The de facto standard dope and reference compound is API modified [23] containing heavy metals. Chemicals are divided into black, red, yellow, and green categories by the Norwegian Pollution Control Authority (SFT) according to their biodegradability in relation to discharge in the marine environment [25]. The most hazardous substances belong in the black category (API mod), while the green category indicates fully biodegradable. Yellow compounds have acceptable environmental properties but still need discharge permission.

B.2.3. Phosphating

After manufacturing, the specimens were cleaned, degreased and water rinsed before they were dipped in the zinc or manganese phosphate bath. The process was carried out under laboratory conditions to ensure maximum uniformity and repeatability for the specimens. See Table I.3 for an overview of the process parameters. The resulting coating weights are reported in the final row. Note, however, that because of the morphology a coating thickness is difficult to define [1]. Therefore, weight per unit area is reported in the results.

Table B.2.: Overview of lubricants used in the test program.

Short hand	Full name	Base oil	Thickener	Additives
BO	API mod base oil	Mineral based	-	-
Al bg	Aluminium base grease	Mineral based	Aluminium complex	-
Li bg	Lithium base grease	Mineral oil	Lithium complex	-
API mod	API modified	Mineral based	Lithium complex	Lead, copper, zinc, graphite
YD1	Yellow dope 1	Ester oil	Undisclosed	Undisclosed
YD2	Yellow dope 2	Mineral oil	Undisclosed	Undisclosed

Table B.3.: Overview of the phosphate conversion coating processes for the AISI4130 and P110 substrate.

Step	Treatment	Zinc phosphate	Manganese phosphate
1	Degreasing	Gardoclean® 349, 50 g L^{-1}, 75 °C, 10 min dip	
2	Rinsing	cold water	
3	Activation	Gardolene® V6522, 2 g L^{-1}, 40 °C, 1 min dip	Gardolene® V6563, 4 g L^{-1}, 40 °C, 1 min dip
4	Phosphating	Gardobond® Z3300, 75 °C, 5 min dip time, Free acid: 18, Total acid: 112, Fe++: 0.9 g L^{-1}	Gardobond® G4098 + 5 g L^{-1} Gardobond®Additive H7050, 90 °C, 5 min dip time, Free acid: 18; Total acid: 119; Fe++: 1 g L^{-1}
5	Rinsing	cold water & demineralized water	
6	Drying	oven 95 °C	
-	Coating weight	4.5 g m^{-2}	10.95 g m^{-2}

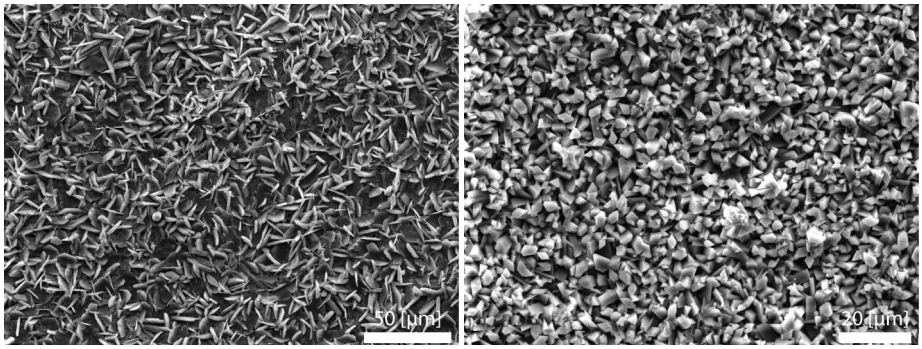

(a) (b)

Figure B.2.: SEM micrographs of the phosphate crystal sizes. Note the difference in magnification. Figure B.2a shows zinc phosphate with is characteristic needle structure. Figure B.2b is manganese phosphate with its characteristic plate structure.

SEM micrographs of the coating are shown in Figure B.2. Note the difference in magnification. The morphology for the zinc phosphate is the distinct needle shape [1] in agreement with its orthorhombic dipyramidal unit cell. The morphology for manganese phosphate is the characteristic plate structure [1, 26] coming from its monoclinic prismatic unit cell. The manganese phosphate process produces a much denser and more refined coating compared to zinc phosphate because of its smaller crystal size [1]. The difference in morphology leads to higher wear for zinc phosphate because of the looser structure as shown in [13]. However, both coatings do form a glaze layer with their wear debris in the sliding contact.

B.2.4. Pin on disc

The pin-on-disc experiments are performed with a Bruker UMT-3 shown schematically in Figure B.3a. The UMT-3 is a modular universal mechanical tester capable of applying a normal load, F_N, of up to 1000 N. The load range and measurement accuracy are determined by the installed load cell. In this case a six degrees of freedom load cell (TFH-50) is installed.

The reciprocating tests are performed at a maximum Hertzian contact stress, P_{max}, of 1 GPa by applying 10 N normal load. The contact spot diameter is approximately 140 µm at this stress. The imposed reciprocating sliding length is 500 µm at a frequency of 0.5 Hz or linear velocity, v, 0.5 mm/s. With 1000 cycles the equivalent sliding length is 1000 mm. Both dry and lubricated experiments are executed. Prior to each lubricated experiment the lubricant is applied with a cotton swab on the disc and pin surface. For comparison, a set of reference tests are done on a non-phosphated specimen.

B.2.5. Anvil-on-strip

The strip tests are performed with a Quiri tribometer, see Figure B.3b for a schematic of the set-up. In this case, unidirectional sliding tests are performed. The strip is mounted in a tensile tester. On each side of the strip an anvil is pressed at a prescribed load. The strip is then pulled up at a prescribed velocity while measuring the resultant friction force. The sliding tests are performed at a maximum Hertzian contact stress of 1.4 GPa by applying 20 kN normal load. For the as machined tests, a load ramp is applied over the first 5 strokes. The reason for this was the difficulty of distinguishing the performance of the different dopes when applying a constant load, i.e. they were all equally bad. The load ramp and thus milder conditions provided better differentiation. The contact spot is elliptic and approximately 5.7 mm x 1.1 mm. The sliding velocity is 24 mm/s. Up to 50 strokes were made with a sliding length of 31 mm which sums up to 1550 mm cumulative sliding length for the anvil. Here also a set of reference tests on bare specimens are performed for comparison.

B.2.6. Ring-on-ring tester

The ring-on-ring tests are performed in an in-house developed test set-up, see Figure B.3c for a schematic of the specimen. Sliding tests are performed with continuous contact equivalent to the make-up of a casing connector. The contact configuration of the rings is flat against a round-off of R = 80 mm line contact. The contact line diameter is 70 mm and the contact width approximately 1 mm. The sliding tests are performed at a maximum Hertzian contact stress of 0.25 GPa by applying 30 kN normal force. The sliding velocity is 24 mm/s. The total sliding length is 1 revolution. At predefined sliding lengths, the specimen is broken apart and a replica of the surface texture is taken to monitor surface evolution. The lubricant is removed and reapplied at each of these steps. Reference tests in as machined versus as machined configuration were performed for comparison.

After make-up sliding the specimen inner diameter was filled with thermal oil, assembled, and subjected to a 120 kN normal force or a 0.37 GPa maximum Hertzian contact stress. On the outside the specimen was submerged in a glass chamber filled with glycol which acted as leak detection fluid. The glass chamber was connected with a tube to a beaker on a balance to monitor displacement of the glycol by the thermal oil. Then an internal pressure of 700 bar was applied using a Resato pump. When a steady state was reached the load was gradually lowered in a stepwise manner and displacement was monitored for 15 minutes per step until a leak was observed.

B.2.7. Microscopy & metrology

The resulting wear scars are investigated with a Keyence VHX5000 digital light microscope and a Bruker NPFLEX white light interferometer. Scanning electron microscopy (SEM) was performed using a Tescan Vega3 equipped with an Energy-Dispersive X-ray Spectroscopy (EDS/EDX) detector. Intermediate states of the surfaces were captured with a Struers RepliSet-T3. To ensure maximum retention of generated surface layers the specimens are prepared for

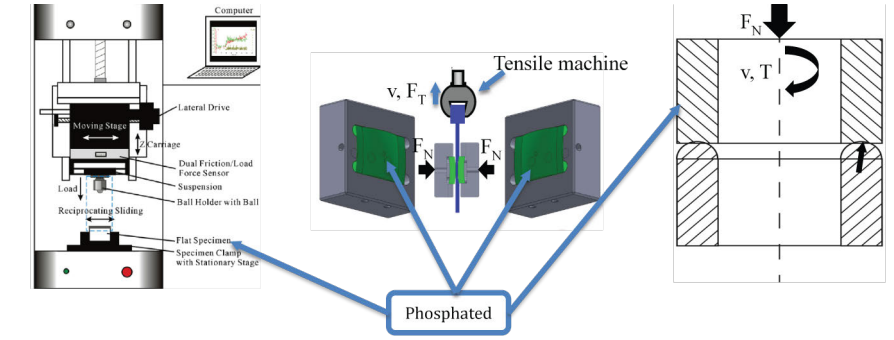

P_{max} = 1.0 GPa (145 ksi)
v = 0.5 mm/s (0.02 inch/s)
L = 1.0 m (39.37")
(a)

P_{max} = 1.4 GPa (203 ksi)
v = 24.0 mm/s (0.95 inch/s)
L = 1.55 m (61.02")
(b)

P_{max} = 0.37 GPa (68 ksi)
v = 24.0 mm/s (0.95 inch/s)
L = 0.22 m (8.66")
(c)

Figure B.3.: Overview of the test set-ups used for the results presented in this paper. (a) Bruker UMT-3 pin-on-disc set-up. (b) Strip test set-up. The end of the strip is mounted in a tensile machine and a prescribed load is applied on the anvils. The strip is then pulled up under position control leading to a certain friction force. (c) Ring-on-ring schematic. Note: the round-off radius R is exaggerated.

microscopy by flushing the grease from the surface with heptane. Final rinsing was done by flushing with acetone and drying to air. For the subsequent measurement of the wear scars with the interferometer the specimens are ultrasonically cleaned in acetone for 5 minutes and wiped dry.

B.2.8. Data processing pin-on-disc

The measured reciprocating friction data from the pin-on-disk tests is processed to get continuous graphs of the coefficient of friction. The locations of the peaks are detected of the absolute values of the measured COF using Matlab® built in findpeaks. Next a moving average is taken of the resulting data with a 1 s window to get smooth trends.

B.3. Results and discussion

B.3.1. Pin-on-disc & anvil-on-strip

The reference test results using pin-on-disc are shown in Figure B.4. In Figure B.4a the processed friction traces are shown. The base greases are not able to protect the surface leading to galling as indicated by the high coefficient of friction. This is confirmed by the resulting wear scar as shown for the lithium base grease in Figure B.4b. It is clear that material was pulled out of the surface and transferred to the ball. The transferred material (lump)

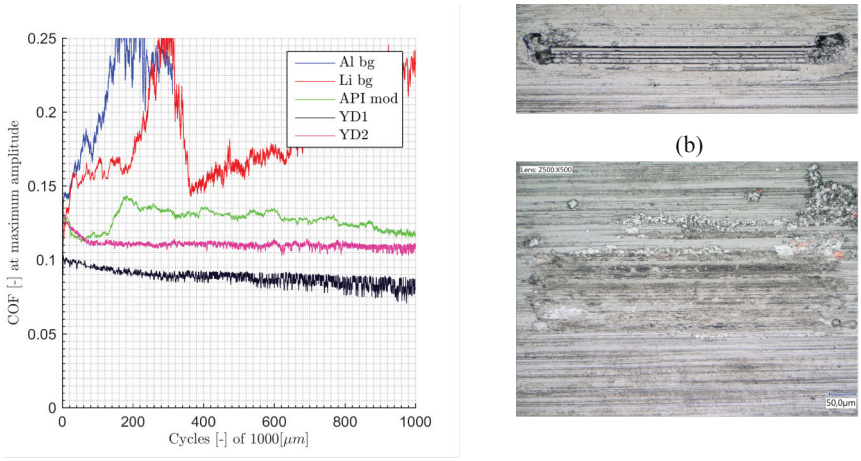

Figure B.4.: Reference pin-on-disc experiments in uncoated system. Note: the y-axis was truncated to improve visibility. In Figure B.4a the friction traces versus cycle are shown for the various lubricants. Figure B.4b shows an example of the galling damage after the test with the lithium base grease. Figure B.4c shows the result of a test with API modified.

subsequently created grooves in the disc surface. The failure is typically immediate and results in large surface damage. The friction coefficient does return to a lower value further in the test. This is, however, because the lump finished cutting the groove and widening of the contact lowering the contact stress.

In contrast, the fully formulated greases provided protection either by (metallic) particles and graphite or by forming a reactive tribofilm. This is shown for API modified in Figure B.4c. Based on the colors, a combination of zinc, lead and graphite formed a protective film on the surface. Copper does not seem to contribute to the protective film of the sliding contact. This was confirmed using SEM-EDX.

The reference test results using the strip test set-up are shown in Figure B.5. Under the harsher (higher velocity) test conditions all lubricants fail in galling as indicated by the high initial friction coefficient in Figure B.5a. The lubricants that failed in pin-on-disc perform also the worst in the strip test. In all cases the failure was initiated because the lubricants cannot build up the protective film that was found in the pin-on-disc test which results in adhesive wear leading to galling [27].

Two of those failed specimens are shown in Figure B.5b for Li bg and Figure B.5c for API mod. The results were close to identical on each side. Therefore, the wear scars of anvil and strip are shown for one side of the strip. In each case galling was severe; however, the Li bg shows the largest surface damage with big chunks of material being removed. API modified is more well behaved only showing deep scratching of the surface. Again the friction coefficient goes down with subsequent strokes because of widening of the contact lowering the contact stress.

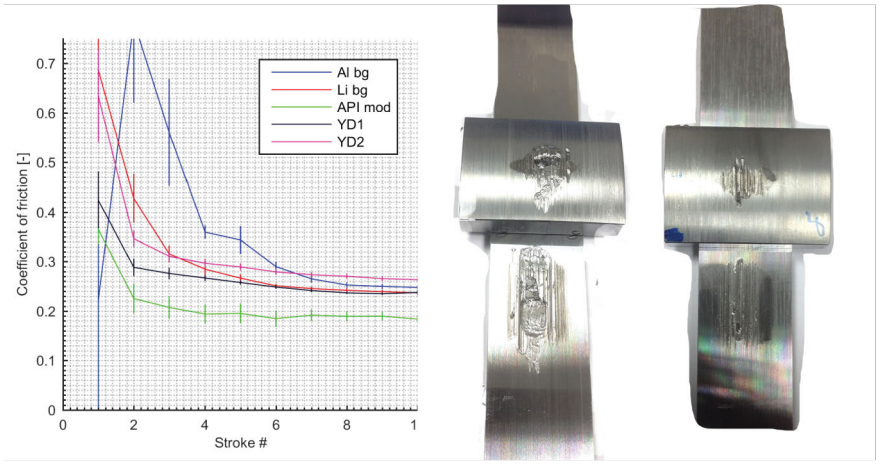

(a) (b) (c)

Figure B.5.: Reference strip test experiments in uncoated system. In Figure B.5a the friction traces versus stroke are shown for the various lubricants. Figure B.5b shows a macrograph of a galled Li bg specimen. Figure B.5c shows a macrograph of the galled API mod specimen.

For easy comparison and brevity, the results above will be summarized using the maximum friction coefficient, observations from light microscopy and interferometry, and scanning electron microscopy hereafter.

The summary for the pin-on-disc and strip tests are shown in Figure B.6. For clarity, a coefficient of friction of 1 indicates galling based on the combination of the friction trace and observations of the wear scar. Figure B.6a shows the summary of the friction traces as shown in Figure B.4a including the zinc and manganese phosphate results. As discussed the base greases fail by galling and the full formulation greases give acceptable friction and wear results.

When changing to a zinc or manganese phosphate disc the earlier failing lubricants show low friction and wear behaviour. Even the base oil that is used to formulate the aluminium base grease produces acceptable results. Furthermore, the coefficient of friction is not varying a lot between the different lubricants.

The same set of lubricants was tested using the strip tester. Here a higher contact stress is combined with a higher sliding velocity. The results are summarized in Figure B.6b. As discussed (Figure B.5), in the uncoated tests all lubricants fail in galling which is attributed to the more realistic test conditions. In all cases failure is immediate; the first stroke will directly indicate the galling resistance. This is in line with the observations of previous investigators [3, 8, 9] as discussed in the introduction.

As before, coating one of the surfaces (anvil here) with manganese phosphate changes the behavior drastically. Now all lubricants protect the surface in conjunction with the manganese phosphate coating. No galling was observed. As in the pin-on-disc tests, the maximum

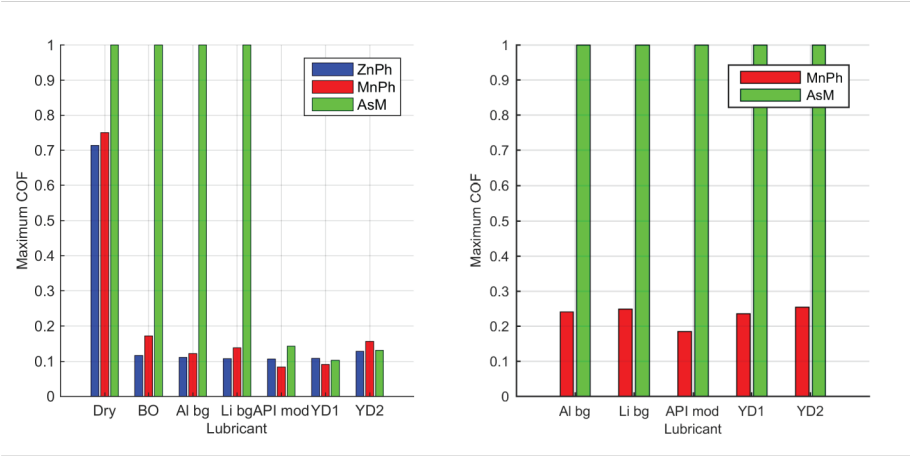

(a) (b)

Figure B.6.: Summarized results for pin-on-disc and strip tests. Figure B.6a shows the results of the pin-on-disc tests for as machined (AsM), and zinc (ZnPh) and manganese (MnPh) phosphated discs. Note that a COF of 1 indicates galling. Figure B.6b shows the results of the striptests for as machined and manganese phosphated anvils.

coefficient of friction is approximately the same for all tests which indicates that the sliding behavior is dominated by the base oil and the manganese phosphate coating. Next to that, comparing pin-on-disc with anvil-on-strip the trends in maximum COF are the same.

B.3.2. Ring-on-ring

The results of the ring-on-ring tests cannot be satisfactorily captured in a friction trace. Typically (onset of) galling is not detected in the torque signal because of the localized nature versus the relatively large surface area of the specimen. Therefore, only the surface damage or lack thereof is assessed.

The outcome of the reference test for the ring-on-ring set-up is shown in Figure B.7. The specimen was made-up with API modified. Large areas of surface damage are visible due to galling particularly in the region marked by C. Note that the observation is made after one revolution. No lubricant was to be found in the galled areas indicating that lubricant squeeze out started the galling process. Even though a substantial area was galling, the onset was not observed on the torque measurements. This shows the inability of detecting (onset of) galling during full connection (including threads) make-up based on only the torque-turn graph.

In Figure B.8 the results are shown after make-up sliding with zinc phosphate specimens (Figure B.8a/b) and manganese phosphate specimens (Figure B.8c/d) against as machined pins. The conditions were the same as for the specimen in Figure B.7. The surfaces are burnished and show no signs of surface damage or galling. On the phosphated box specimens

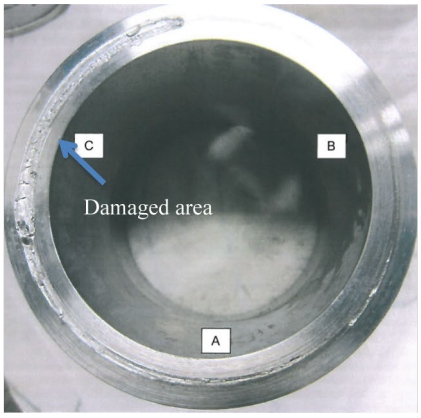

Figure B.7.: Results of the as machined reference test. Surface damage after make-up sliding with API modified. Letters indicate orientation of specimen to match with the counter surface.

a smooth and flat glaze layer is formed in the sliding contact. On the as machined pin specimens transfer of material can be observed.

The generation of the glaze layer was tracked using replicas. The surface evolution is shown in Figure B.10 for the zinc phosphate specimen as function of cumulative sliding length. This set is representative for the glaze layer formation in general. With increasing cumulative sliding length gradually the glaze layer emerges. Here the formation starts at about 37.5 mm or the 4^{th} image in the sequence.

The profiles of the surfaces in Figure B.8 before and after running are shown at the top 2 rows of Figure B.11. In addition, the profiles of the ZnP – MnP combination and the results after running in with base oil are shown in the rows below. In the AsM cases it is clear that minimal wear has occurred on the pin side and the wavy structure of the turning profile remains. On the phosphate side the surface has become smoother and flatter by the formation of the glaze layer. This keeps the contact situation localized increasing the likelihood of sealing. As expected, there is an appreciable difference in wear between API mod and base oil. This is because of the lack of wear reducing additives like graphite, zinc and lead. Nonetheless, just base oil and phosphate already gives a low wearing system. The ZnP – MnP combination does not show this result, both surfaces have an irregular rough appearance. In contrast with the AsM – phosphate results, this will lead to a random contact stress distribution and probably lower seal ability performance.

This is confirmed by the seal ability results reported in Figure B.12. Shown are the calculated contact intensity (measured normal load divided by contact circumference) at onset of measured leak for the different surface finishes and lubricant combinations. The ZnP – MnP combination performs the worst of the set. Having a wavy texture on a flat (Figure B.11) increases seal ability dramatically as shown by the results with API mod and base oil. The influence of the lubricant and in particular the solids contained within it is shown to be minimal judging by the similar seal ability results for API mod and base oil. The differences are probably mostly coming from the differences in wear and the resulting lower localized contact stresses.

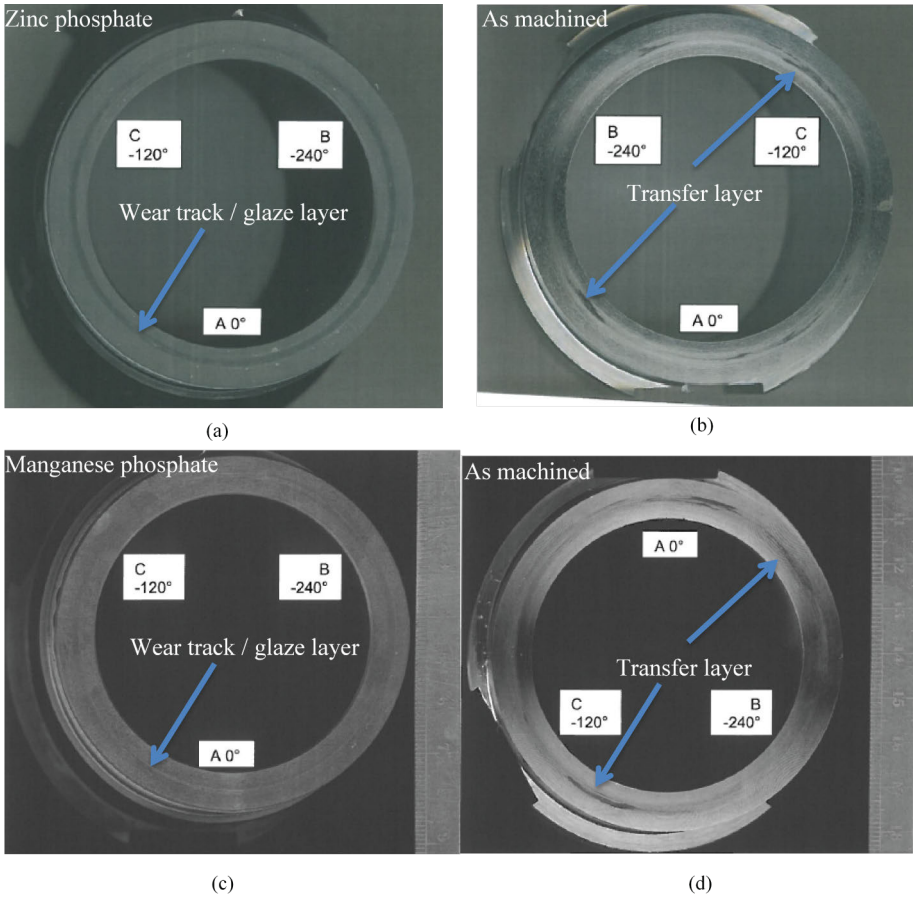

Figure B.8.: Surface after make-up sliding with phosphate specimens lubricated by API modified. Letters indicate orientation of specimen to match with the counter surface. Figure B.8a and Figure B.8b show the result of a zinc phosphate box against an as machined pin. Figure B.8c and Figure B.8d show the results of a manganese box against an as machined pin. Sliding conditions were the same: 1 full revolution at 24 mm/s. No galling is observed.

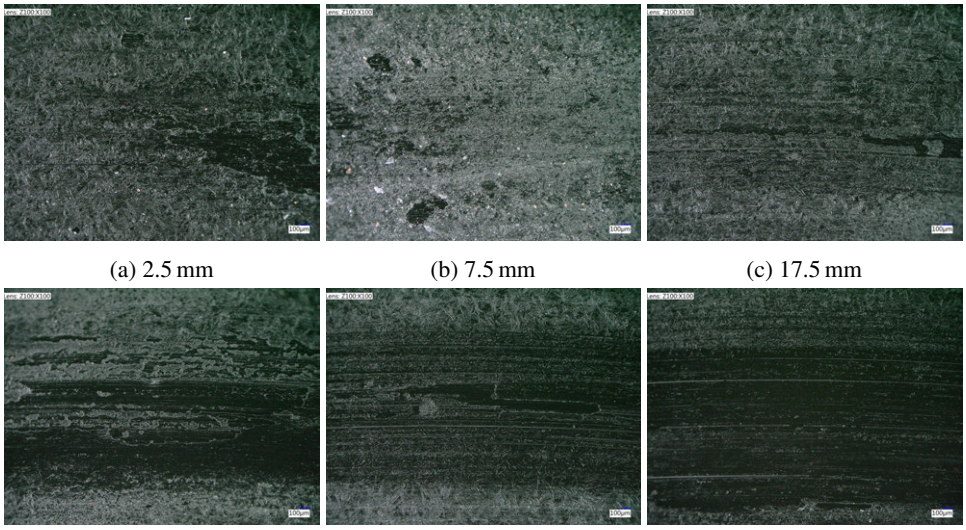

(a) 2.5 mm (b) 7.5 mm (c) 17.5 mm

(d) 37.5 mm (e) 77.5 mm (f) 155.5 mm

Figure B.9.: Surface evolution using intermediate replicas of the zinc phosphate surface (Figure B.8a) up to 72% of a full revolution. The cumulative sliding length is reported under the micrographs.

Figure B.10.: Surface evolution using intermediate replicas of the zinc phosphate surface (Figure B.8a) up to 72% of a full revolution. The cumulative sliding length is reported under the micrographs.

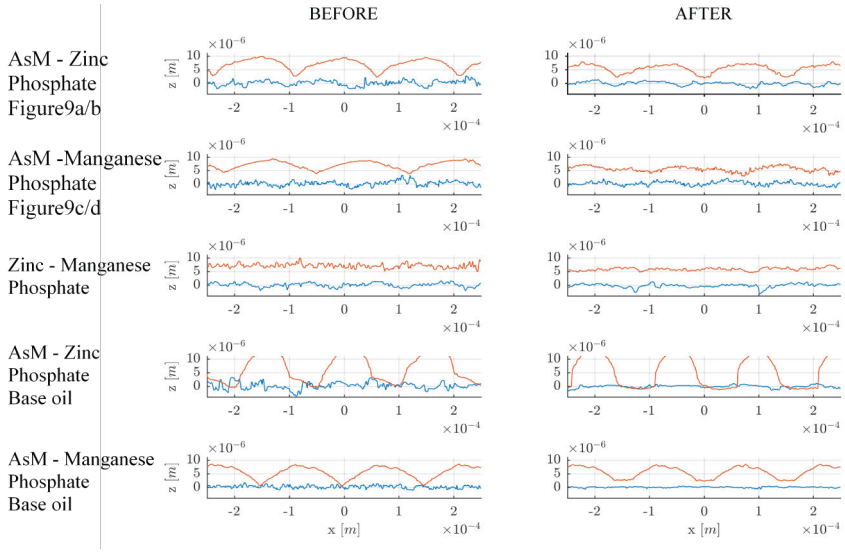

Figure B.11.: Line profiles of ring-on-ring specimens after make-up sliding with API modified, The graphs show profile height (Z) versus seal width (X). A comparison is made between the state before and after for the combination of pin (top profile) and box (bottom profile) in each graph.

B.4. Discussion

Combining the observations from pin-on-disc (Figure B.4 and Figure B.6a), anvil-on-strip (Figure B.5 and Figure B.6b), and ring-on-ring (Figure B.8, Figure B.10, Figure B.11 and Figure B.12) the following can be deduced.

Phosphate conversion coatings play a critical role in damage free make-up and subsequent micro sliding of a casing connection. In all tests the phosphate coating reduces the likelihood of galling significantly, regardless of the lubricant. The coating also provides a low wearing tribosystem which was shown to be beneficial for seal ability. Using the observations from literature and the tests presented in this paper the reason for this is as follows:

1. Phosphate coatings provide a dissimilar surface to the bare steel counter surface [1] which minimizes adhesion and thus avoids galling.
2. Phosphate coatings provide a reservoir for the lubricant which replenishes the contact [1].
3. Generation of a glaze layer [13] on the phosphate surfaces results in a smooth and dense interfacial layer.
4. Generation of a tribolayer on the bare steel counter surface.

As discussed in the introduction, make-up sliding strongly influences the initial sealing configuration and thus performance. The combination of the above leads to a low wearing tribosystem

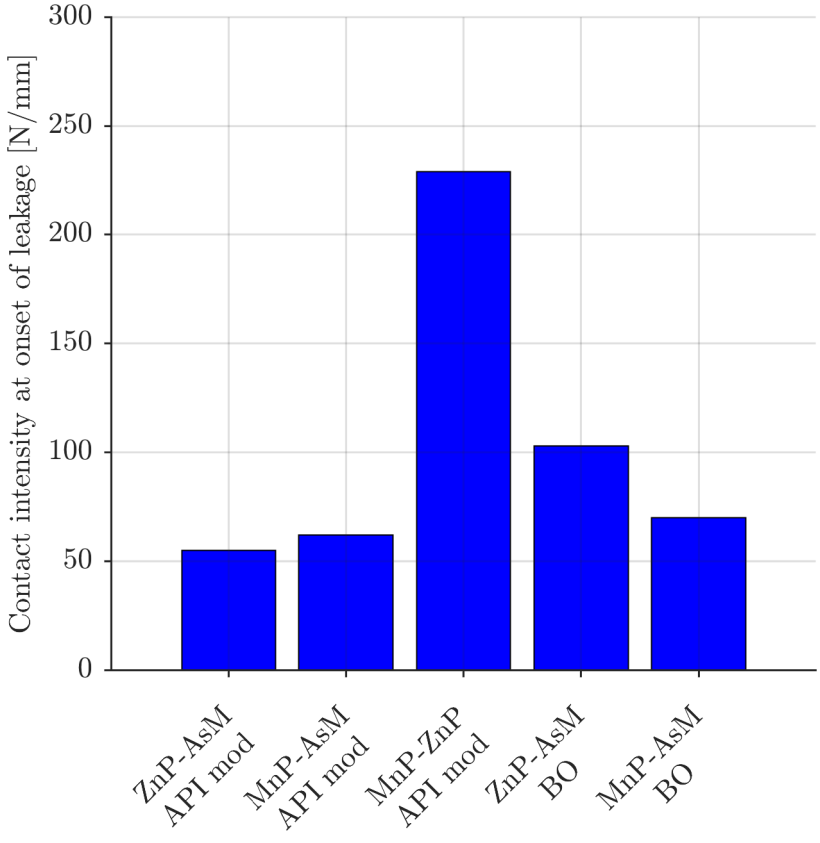

Figure B.12.: Seal ability results as function of the various surface finishes (Figure B.11) and lubricant combinations. Seal ability is measured by the amount of contact intensity at the onset of leakage. Lower contact intensity at the onset of leakage thus means better seal ability performance.

keeping the original waviness in tact (Figure B.11) which leads to higher localized contact stresses and, as a result, a better sealing surface [18–20]. This was confirmed in the seal ability tests (Figure B.12) and can be achieved with phosphate and a simple base oil alone.

B.5. Conclusions

The role of phosphate coatings on make-up and seal ability of casing connections was investigated using pin-on-disc anvil-on-strip, and ring-on-ring tests. From the results in this paper it is clear that this role is crucial for reliable performance of casing connections. This has been recognized by the industry judging by the extensive use of phosphating on casing connections. The results outlined in this paper should give this scientific support.

The results indicate the following role for the phosphate coatings in make-up and subsequent seal ability performance:

1. The phosphate coating:
    a. Provides a dissimilar surface compared to the steel counter surface that ensures no adhesion preventing galling.
    b. Provides a large surface area that lets the coating be an adsorbent for the lubricant.
    c. Provides a pre-applied tribolayer protecting the surface from the onset, allowing galling free make-up of surfaces with highly localized contact stresses.
    d. Provides independence of the lubricant for galling prevention.
2. The phosphate coating achieves this by:
    a. Generating a tribolayer on the bare countersurface under make-up sliding and microsliding.
    b. Generating a smooth flat glaze layer under make-up sliding.
3. The importance of the lubricant formulation is reduced, which does not necessarily need (hard) solids or additives to provide good make-up and seal ability performance.
4. Best seal ability was achieved with surface combinations that generate highly localized contact stress profiles, i.e. as machined vs phosphate.
5. The combination of glaze layer, tribolayer and synergy with the lubricant results in a low wearing system providing, when combined with an as machined countersurface, an ideal configuration for sealing.

The conclusion opens the door for lubricants that are tailored for sealing performance alone by taking advantage of the presence of a phosphate coating. To the best of the author's knowledge this is not done today. Most (yellow) dopes just mimic API modified by replacing the metallic particles with (hard) mineral particles. It was shown by other investigators that these can be destructive [17] for the sealing surfaces. This work shows that these solids are not needed and the authors would actually advice against it as it will destroy the glaze- and tribolayers that are

formed. Furthermore, as the lubricant composition can be simplified it can ease the transition to environmentally friendly rated lubricants.

Acknowledgements

We would like to thank Shell Global Solutions BV for giving us the opportunity to publish our work, OCAS NV for performing anvil-on-strip and ring-on-ring the experiments and Chemetall GmbH for sharing their expertise on phosphate conversion coatings.

References

[1] Rausch, W. *The phosphating of metals*. Metals Park, Ohio, USA; Teddington, Middlesex, England: ASM International; Finishing Publications Ltd., 1990, p. 406.

[2] Narayanan, T. S. N. S. 'Surface pretreatment by phosphate conversion coatings - A review'. *Reviews on Advanced Materials Science* 9.2 (2005), pp. 130–177.

[3] Ertas, A. 'Experimental Investigation of Galling Resistance in OCTG Connections'. *Journal of Manufacturing Science and Engineering* 114.1 (February 1992), p. 100.

[4] Salomon, G. 'Application of Systems Thinking to Tribology'. *A S L E Transactions* 17.4 (January 1974), pp. 295–299.

[5] Czichos, H. and Winer, W. O. *Tribology: A Systems Approach to the Science and Technology of Friction, Lubrication and Wear (Tribology Series, 1)*. Vol. 100. Elsevier, 1978, p. 513.

[6] API. *Petroleum and natural gas industries - Procedures for testing casing and tubing connections (ISO 13679:2011) Industries*. Tech. rep. Geneva: International Organization for Standardization, 2011.

[7] Ertas, A., Cuvalci, O. and Carper, H. J. 'Determination of Friction Characteristics of J-55 OCTG Connections Lubricated with Environmentally Safe Thread Compound'. *Tribology Transactions* 42.4 (January 1999), pp. 881–887.

[8] Carper, H. J., Ertas, A., Issa, J. and Cuvalci, O. 'Effect of Some Material, Manufacturing, and Operating Variables on the Friction Coefficient in OCTG Connections'. *Journal of Tribology* 114.4 (October 1992), p. 698.

[9] Carper, H. J., Ertas, A. and Cuvalci, O. 'Rating Thread Compounds for Galling Resistance'. *Journal of Tribology* 117.4 (October 1995), p. 639.

[10] Burke, D. 'The Sliding Friction of Bonded Solid Lubricants'. PhD thesis. University of central Lancashire, 2005.

[11] Khaleghi, M., Gabe, D. and Richardson, M. 'Characteristics of manganese phosphate coatings for wear- resistance applications'. *Wear* 55.2 (August 1979), pp. 277–287.

[12] Weng, D., Jokiel, P., Uebleis, A. and Boehni, H. 'Corrosion and protection characteristics of zinc and manganese phosphate coatings'. *Surface and Coatings Technology* 88.1-3 (January 1997), pp. 147–156.

[13] Ernens, D., Rooij, M. B. de, Pasaribu, H. R., Riet, E. J. van, Haaften, W. M. van and Schipper, D. J. 'Mechanical characterization and single asperity scratch behaviour of dry zinc and manganese phosphate coatings'. *Tribology International* 118 (February 2018), pp. 474–483.

[14] Totik, Y. 'The corrosion behaviour of manganese phosphate coatings applied to AISI 4140 steel subjected to different heat treatments'. *Surface and Coatings Technology* 200.8 (January 2006), pp. 2711–2717.

[15] Westberg, H. J., Nilsson, P. H., Rosén, B.-G. and Stenbom, B. 'Manganese Phosphating of Gears and Surface Roughness Consequence'. *Proceedings of the 26th Leeds-Lyon Symposium on Tribology*. 2000, pp. 145–153.

[16] Pokorny, P., Szelag, P., Novak, M., Mastny, L. and Brozek, V. 'Thermal stability of phosphate coatings on steel'. *Metalurgija* 54.3 (2015), pp. 489–492.

[17] Inose, K., Sugino, M. and Goto, K. 'Influence of Grease on High-Pressure Gas Tightness by Metal-to-Metal Seals of Premium Threaded Connections'. *Tribology Online* 11.2 (2016), pp. 227–234.

[18] Pérez-Ràfols, F., Larsson, R. and Almqvist, A. 'Modelling of leakage on metal-to-metal seals'. *Tribology International* 94 (February 2016), pp. 421–427.

[19] Pérez-Ràfols, F., Larsson, R., Lundström, S., Wall, P. and Almqvist, A. 'A stochastic two-scale model for pressure-driven flow between rough surfaces'. *Proceedings of the Royal Society A: Mathematical, Physical and Engineering Science* 472.2190 (June 2016).

[20] Pérez-Ràfols, F., Larsson, R., Riet, E. J. van and Almqvist, A. 'On the flow through plastically deformed surfaces under unloading: A spectral approach'. *Proceedings of the Institution of Mechanical Engineers, Part C: Journal of Mechanical Engineering Science* 232.5 (March 2018), pp. 908–918.

[21] Ledoux, Y., Lasseux, D., Favreliere, H., Samper, S. and Grandjean, J. 'On the dependence of static flat seal efficiency to surface defects'. *International Journal of Pressure Vessels and Piping* 88.11-12 (December 2011), pp. 518–529.

[22] Murtagian, G. R., Fanelli, V., Villasante, J. A., Johnson, D. H. and Ernst, H. A. *Sealability of Stationary Metal-to-Metal Seals*. July 2004.

[23] API. *Recommended Practice on Thread Compounds for Casing, Tubing, and Line Pipe*. Tech. rep. Washington: American Petroleum Institute, 2015.

[24] Hertz, H. 'Ueber die Beruehrung fester elastischer Koerper'. *Journal für die reine und angewandte Mathematik* 92 (1882), pp. 156–171.

[25] Johnsen, S., Frost, T., Hjelsvold, M. and Utvik, T. R. 'The Environmental Impact Factor - a proposed tool for produced water impact reduction, management and regulation'. *SPE International Conference on Health, Safety and Environment in Oil and Gas Exploration and Production*. Society of Petroleum Engineers, April 2000.

[26] Moore, P. B. and Araki, T. 'Hureaulite: lts Atomic Arrangement'. *American Mineralogist* 58.3-4 (1973), pp. 302–307.

[27] Stachowiak, G. and Batchelor, A. W. *Engineering Tribology*. Butterworth-Heinemann, 2013, p. 884.

C. Characterization of the adsorption mechanism of manganese phosphate derived tribofilms

D. Ernens[a,b], G. Langedijk[b,c], P. Smit[c] , M.B. de Rooij[a], H.R. Pasaribu[b], D.J. Schipper[a]

[a]*Laboratory for Surface Technology and Tribology, Department of Engineering Technology, University of Twente, P.O. Box 217, 7500 AE, Enschede, The Netherlands*

[b]*Shell Global Solutions International BV, Innovation, Research & Development, Wells R & D, 2288 GS, Kessler Park 1, Rijswijk, The Netherlands*

[c]*The Hague University of Applied Sciences, Faculty of Technology, Innovation & Society, Engineering Physics, Delft, The Netherlands*

Abstract Casing connections in the oil and gas industry are typically coated with zinc and / or manganese phosphate for corrosion protection during storage. The presence of phosphate coatings is also known to give beneficial tribological performance. The coating allows the system to run without problems long after it is worn off. This is because of two mechanisms. Glaze layer formation on the coated surface and, as will be shown, tribofilm formation on the uncoated counter-surface. An investigation into the mechanism behind this tribofilm formation is presented in this paper. The aim is to develop lubricants that exploit these mechanisms. A pin-on-disc set-up was used to investigate the interaction of a manganese phosphated disc and bare counter surface. Six base oils with different polarity and viscosity were used. The resulting tribofilms were analysed using optical microscopy, scanning electron microscopy, X-ray diffractometry, X-ray photoelectron spectroscopy, focused ion beam, and atomic force microscopy. The tribofilm is robust, amorphous, only forms in the presence of a lubricant under sliding conditions and adsorbs on substrates with a large variation in chemical composition. It is concluded that the tribofilm consists of physisorbed manganese phosphate and formation is shear stress activated.

Latest version available on-line: `https://doi.org/10.1007/s11249-018-1082-2`

C.1. Introduction

Casing connections (Figure C.1) in the oil and gas industry are used to connect 12 meter sections of pipe by means of a threaded male (pin) and female (box) member to fortify the bore hole during drilling [1]. The connections are (typically the box) coated with zinc and / or manganese phosphate for corrosion protection during storage. The presence of phosphate coatings is also known to give beneficial tribological performance [2–4].

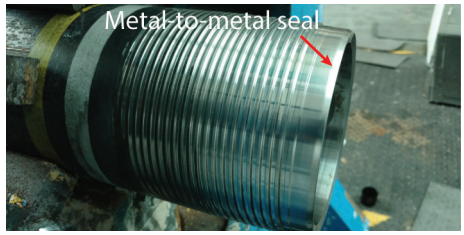

Figure C.1.: Male or "pin" member of a premium casing connection assembly. The pin is connected to a female or "box" member by the thread. At the final moment of assembly the metal-to-metal seal engages ensuring a gas tight connection. Picture: Rob Keeris.

The phosphate coating has mostly been ignored in the design of lubricants for the oil and gas industry. In the search for environmentally friendly lubricants the presence of phosphate coatings should be exploited [3]. This can remove the high temperature break down issues with currently available products as shown for instance in [5].

The protective properties on the coated side of the tribosystem have been shown to come from the formation of a hard and smooth glaze layer [2, 3, 6, 7]. However, this is not the full explanation. It was observed that on the uncoated counter surface a tribofilm was formed under unidirectional sliding conditions in [2, 3].

The authors are not aware of a study investigating the formation of tribofilms in phosphate conversion coated tribosystems. In all cases the changes on the coated member are monitored [8] or of the system altogether for instance on the basis of the seizure resistance [9]. This is probably because it is mainly seen as a running-in coating [10] for long running systems. However, in a casing connection and the metal-to-metal seal the sliding lengths during assembly are short (<1 m) and the sliding velocities are low (<30 mm/s). Given the low total sliding distance, the phosphate coating and its associated generated tribofilms affect the wear process strongly [3, 11]. The wear changes the surface topology of the metal-to-metal seal [12] and thus influences the subsequent seal ability [5, 13–15]. The mechanism behind the formation of this tribofilm, its properties, and the influence of the base oil on these properties with the aim of developing an environmentally friendly lubricant is the subject of this paper.

C.2. Background

The phosphate coatings of interest consist of stable crystals of hopeite [16] (zinc phosphate, ZP) or hureaulite [17] (manganese phosphate, MP). The crystals have been formed under a conversion process involving an acidic solution with phosphate ions reacting with the steel substrate. Subsequently, the crystalline coating precipitates [6, 18]. The focus in this investigation is on manganese phosphate because of its more isotropic crystallites. However, similar tribofilm formation was observed in zinc phosphate [2].

The formation of tribofilms is important in contacts running in the boundary or mixed lubrication regime. Typically the tribofilm is the last line of defence and if it fails the system transitions from mild wear to severe wear [19]. The film is formed by adsorption on and / or chemical reaction at the surfaces of the contacting members [20]. This is can be initiated and accelerated by shear or thermal influences or a combination thereof [21]. According to a recent review there is a wide range of additives employing one or a combination of these mechanisms to form the tribofilm [22]. Fatty acids, amides and functionalised polymers for instance are physically adsorbed. On the other hand, stearic acid forms iron stearate with iron oxide by chemical adsorption. The simplest chemical reaction derived film is formed by sulphur which reacts with freshly exposed iron once the oxide layer is removed by wear [23]. In general, on steels, the generation of chemically reacted tribofilms is governed by temperature while this is typically not the case for ceramics [24]. Surface engineering on the other hand aims to modify the surface by applying a coating or make deliberate changes to the surface texture using for instance laser technology to functionalize the surface. Nano-composite coatings aim to do both: promote tribofilm growth and provide high hardness [25].

A well-known example of the interaction of phosphate chemistry with steel surfaces [26] and / or the properties of the base oil [27] is zinc dialkyldithiophosphate (ZDDP) which is widely used as anti-wear additive [28]. The growth rate is governed by the applied (shear) stress [29], base oil polarity [30], and bulk temperature which could be satisfactorily described by an Arrhenius growth model [29]. Still, the formation relies on contact between the sliding members and stops when the film thickness is significantly greater than the roughness i.e. the contact operates in the elastohydrodynamic lubrication (EHL) regime [31].

Following the approach of previous investigators, tribofilm growth because of rubbing against a manganese phosphate conversion coating is investigated in this paper. The working hypothesis was that tribofilm growth is governed by a chemical reaction and influenced by base oil polarity. To understand the mechanisms behind its growth the thickness of the tribofilm is monitored as function of the normal load, sliding length, velocity, bulk temperature and base oil polarity.

C.3. Experimental

The conditions during assembly of a casing connection have been studied in a contact situation where the pin is represented by a ball that slides against a phosphated flat representing the box [3]. Here only the assembly of the metal-to-metal seal is considered. During assembly the pin and box are in continuous contact. The pin seal sees a stationary contact, whereas the box

Table C.1.: Properties of the used commercial base oils ranked by polarity.

Base oil name	Type	Polarity ranking	Aniline point (°C)	Dynamic viscosity (22 °C, 500 1/s) (Pa s)	Density (15 °C) (kg/m³)
A	Group V	1	<20.0*	0.166	915
B	PAG	2	30.0	0.383	1019
C	Group I	3	104.2	3.320	943
D	Group I	4	117.9	1.520	958
E	Group II	5	125.6	0.245	866
F	PAO	6	170.0	3.000	853

* Taken from technical data sheet.

seal sees a moving contact because of the thread pitch. By subsequently selecting the right reciprocating amplitude the continuous contact and the ratio of sliding lengths between the pin and the box can be properly simulated.

The reciprocating set-up has been chosen to easily simulate the assembly process for the study of the rate of formation and removal of the protective tribofilms on the uncoated ball surface under influence of sliding length, sliding velocity, contact stress, bulk temperature, base oil viscosity and base oil polarity. The combination of parameters will give insight in the particular adsorption or reaction mechanism responsible for the tribofilm formation. Next to that, the ball chemistry was varied to confirm the found adsorption mechanism of the tribofilm. For instance, if the mechanism is chemisorption or a chemical reaction on the bare steel surface no tribofilm formation is expected on stainless steels or ceramics [23].

C.3.1. Lubricants

The influence of the base oil polarity is studied with commonly used base oils to select the base stock which maximizes the tribofilm formation. The relevant properties of the model fluids and base oils are listed in Table C.1. The polarity was determined using the aniline point [32]. The dynamic viscosities were determined using the rheometer protocol listed in Section C.3.3.

C.3.2. Materials

The experiments were performed using a 10 mm ball on flat configuration. The balls are polished and made from AISI52100 bearing steel, AISI316 stainless steel, aluminium oxide or silicon nitride. For the preparation of the flat, the same procedure as in [2] was used. The flat is made from quenched and tempered AISI4130 which was subsequently ground and then dip coated with manganese phosphate. The bare flat is made from the same material and polished. The properties of these materials are listed in Table C.2. The choice for AISI4130 is because it has the same chemical composition as most oil field quenched and tempered casing material grades [3].

Table C.2.: Summary of used materials and their properties.

Material name (-)	Surface finish Ra (µm)	Young's Modulus (GPa)	Surface hardness (GPa)
AISI316L	0.01	160	2
AISI4130-1	0.01	210	3
AISI4130-2	0.10	210	3
AISI52100	0.01	213	7
Si3N4	0.03	300	35
Al2O3	0.03	360	20

C.3.3. Rheometer

The base oil dynamic viscosities were measured using a Haake Mars III rheometer. The measurement geometry was bob (CC25) in cup (CCB25). Temperature was controlled using the Peltier module (TM-PE-C). The dynamic viscosity was measured by imposing a shear rate sweep of 0.01 – 500 1/s at a temperature of 22°C. In all cases the fluids showed Newtonian behaviour. The results of those measurements are also listed in Table C.1.

C.3.4. Pin-on-disc tribometer

The formation of the protective tribofilm is investigated using a Bruker UMT-3 pin-on-disc tribometer. Loads were measured with the 6D load cell (TFH-50). Two drive modules were used for the experimental program. The low velocity (0.05 – 0.5 mm/s) and high temperature (200°C) reciprocating tests were performed with the slider of the tribometer combined with the high temperature module (S35HE-350). The high velocity (>0.5 mm/s) reciprocating tests were performed with a dedicated reciprocating drive module (RF33FE).

C.3.5. Experimental design

First it was checked that the formation is indeed shear stress induced or if contact stress alone could initiate tribofilm growth by a 24h static (no movement, constant load) test at a constant contact stress of 1 GPa. The static tests were performed with base oil E. Next, the mechanism of formation is studied under variation of sliding length, sliding velocity, contact stress, base oil viscosity and base oil polarity. The tribofilm is formed under reciprocating gross sliding conditions with a fixed stroke length of 0.5 mm. This gives a similar sliding length ratio as the pin to box sliding ratio during make-up of the metal-to-metal seal. The experimental design is summarized in Table C.3. The sliding velocity is relatively low and the related temperature increase under the testing conditions was computed to be negligible using [33]. Each data point is obtained with a fresh ball on a fresh patch of coating. Prior to the experiments the

ball was cleaned in acetone and heptane using an ultrasonic bath and subsequently wiped dry. The disc was only flushed with acetone and heptane to avoid removal of the coating by the sonication process and subsequently blown dry with nitrogen. After the experiment the ball was flushed with acetone and heptane to remove the base oil and blown dry with nitrogen. From selected experiments the ball with generated tribofilm was used on a bare polished disc to investigate the durability of the tribofilm.

Table C.3.: Overview of the range of experimental parameters used to study the formation of the tribofilm with a fixed stroke length of 0.5 mm.

Normal force	Cumulative sliding length	Sliding velocity	Bulk temperature	Base oil aniline point	Base oil dynamic viscosity at 20°C and 500 1/s	Maximum Hertzian contact stress	Hertzian contact area
(N)	(mm)	(mm/s)	(°C)	(°C)	(Pa s)	(GPa)	(10^{-3} mm^2)
2.5 – 10	1 – 8000	0 – 10	22 – 200	20 – 170	0.245 – 3.3	0.47 – 1.0	3 – 15

C.3.6. Analyses

The resulting tribofilms were investigated using a digital light microscope (Keyence VHX-5000) and measurements were taken with the accompanying software, X-ray Diffractometry (XRD, PANalytical Empyrean diffractometer, Cu anode, focusing optics: 0.1 and 0.3 mm monocapillary), Scanning Electron Microscopy (SEM, Tescan Vega 3) combined with Energy-dispersive X-ray spectroscopy (EDX), X-ray Photoelectron Spectroscopy (XPS, Kratos Axis Nova with 15kV Al Kα source), focused ion beam (FIB, FEI Helios NanoLab 650) and Atomic Force Microscopy (AFM, NanoSurf Flex-Axiom in tapping mode with ACTA cantilever). The analytical techniques were used to determine the following properties of the formed tribofilm: The area coverage, thickness, surface topography, (crystal) structure and composition as function of the experimental parameters (Table C.3).

C.3.7. Thickness determination based on thin film interference

The maximum thickness of the tribofilms was determined by the colour scheme coming from the complex thin film interference using the optical microscope [34]. The method was calibrated with AFM and FIB/SEM measurements. Other methods including ellipsometry and interferometry were attempted, however, they either failed or were not precise enough because of the curvature and roughness of the ball or the complex thin film interference. The current method based on optical microscopy was determined to be accurate to $\pm$100 nm. Therefore the method is only used to reveal trends.

C.3.8. Data processing

The measured data is post processed using Matlab® and the Curve Fitting Toolbox v2017a. The build in power law model `power1` is used to fit

$$h(t) = at^b \tag{C.1}$$

to the data where indicated. Where h is the determined thickness in nanometers, t the rubbing time in seconds and a, b the fitting parameters. To determine tribofilm growth rates the resulting fit is differentiated with respect to time.

From the measurements of coefficient of friction (COF), μ, normal force, F_n, and tribofilm area coverage, A_{cov}, an average shear stress can be computed according to

$$\tau = \frac{\mu F_n}{A_{cov}}. \tag{C.2}$$

C.4. Results

In the static tests no tribofilm growth was observed. Next to that, the uncoated system is taken as a reference for tribofilm durability tests later in this section. For all base oils the system failed within 0.10 m of sliding because of galling. When a base oil and sliding was included, tribofilm formation was subsequently consistently and repeatedly observed.

C.4.1. Friction

The average COF for the ambient temperature experiments is shown in Figure C.2. The average COF was determined in the growth region of the tribofilm formation in Figure C.4 to be able to compute meaningful shear stresses that (could) correlate with growth rate in Figure C.7. As shown the COF was consistent for all base oils and sliding lengths with relatively small variance. The number of observations, N, per base oil differed, however, N>20 for each base oil.

C.4.2. Tribofilm formation as a function of sliding length or rubbing time

The formation of the tribofilm was first studied as function of sliding length or rubbing time at a constant reciprocating velocity of 0.5 mm/s and 22 °C. Figure C.3 shows the light microscopy of the balls as function of the cumulative sliding length (columns) and base oil (rows). The reciprocating sliding is in horizontal direction. The top row shows the dry sliding experiments as a reference.

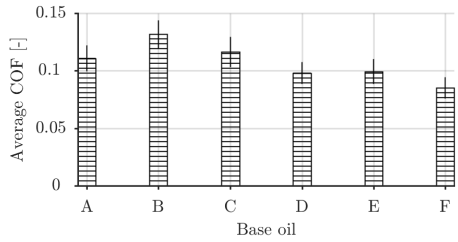

Figure C.2.: Average friction coefficients for all base oils. The error bars indicate 1 standard deviation for N>20 for each base oil.

The following can be observed. In dry sliding conditions, no tribofilm is formed and complete hureaulite crystals are transferred. Furthermore, the system quickly wears through the phosphate coating and transitions to adhesive wear in line with previous investigators [11]. In lubricated conditions, a tribofilm readily forms for all base oils. The tribofilm has a patchy appearance. Based on the thin film interference different tribofilm thickness and derived growth rates are observed for each base oil. In all cases an increase in surface area coverage can be observed which could be indirectly used to compare the wear rates of the phosphate coating as function of the different lubricants.

Using the results of Figure C.3 the thickness of the film can be determined based on the thin film interference (Section C.3.7). The results of this are shown in Figure C.4 for each base oil. This gives the influence of the base oil on the layer thickness versus rubbing time and its power law fit (C.1). The fastest growth is observed for base oil B and the slowest for base oil F. All films grow to a similar limiting thickness before wear balances the growth. After that tribofilm wear reduces the thickness. Next to that, the counter surface phosphate coating also wears out. This reduces the supply of phosphate particles and therefore the growth rate up to the point that the ball is rubbing on bare steel (base oil A at 1 m in Figure C.3).

The growth rates for 10 N at 0.5 mm/s were determined by differentiating the fitting results of Figure C.4 against rubbing time and the maxima and mean values are shown in Figure C.5. The mean was determined in the region where $\frac{\mathrm{dh}}{\mathrm{dt}} > 0$.

The measured tribofilm surface coverage as function of sliding length is shown in Figure C.7a. The increase of the area covered by the tribofilm is because of wear on the coated side of the tribosystem. This is shown for base oil B in Figure C.6 by the wear scar evolution as function of sliding length. The wear scar width corresponds to the tribofilm width for base oil B in Figure C.3. The ball sinks deeper in the coating increasing its area of contact. The increase in coverage is thus proportional to the wear of the coating on the disc. The measurements indicate that the initial wear is similar for all base oils and diverges after the maximum tribofilm thickness (Figure C.4) is reached. The divergence is because of removal of the tribofilm and coating at the heart of the contact which has seen most sliding length, see again for instance base oil A at 1 m in Figure C.3. This is compensated by tribofilm formation at the edges of the contact. The balance seems to be affected by the initial growth rate. The exclusive presence of the tribofilm in rubbed areas confirms the static test results and indicates a shear stress activation mechanism.

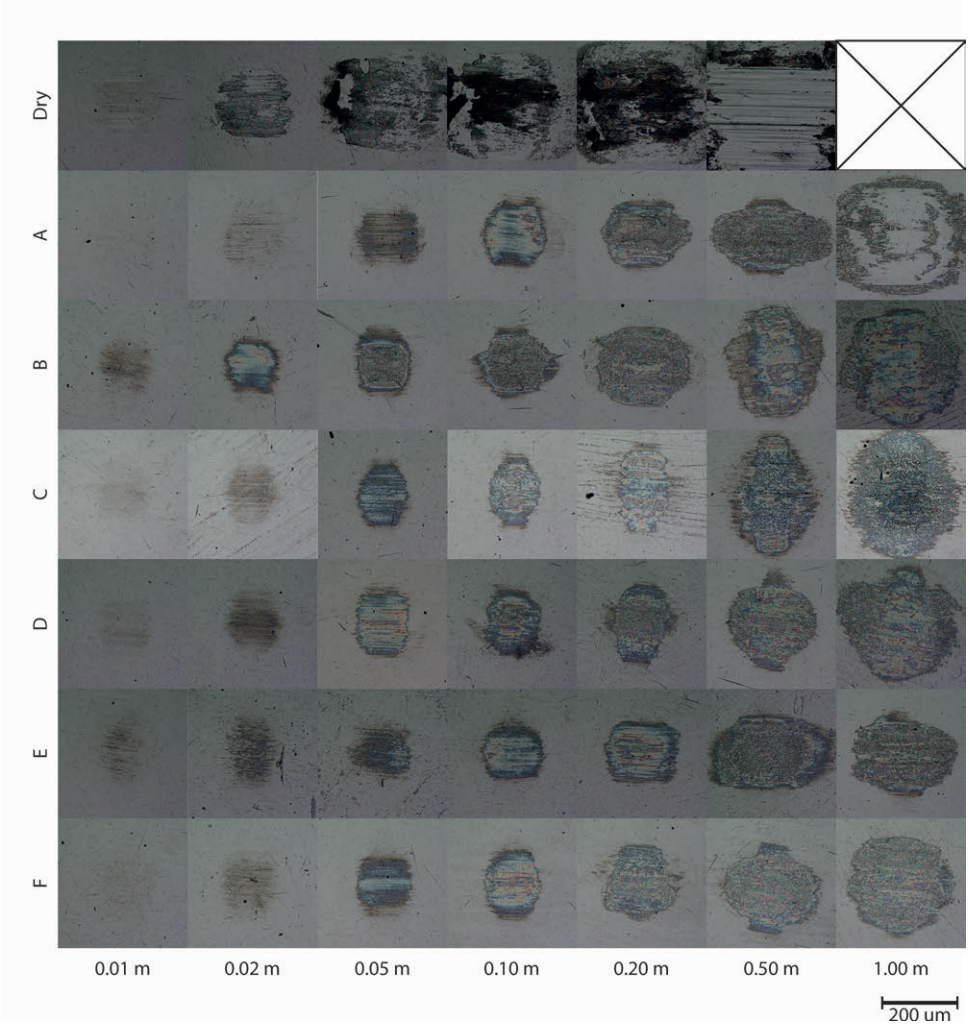

Figure C.3.: Overview of tribofilm formation as function of cumulative sliding length and base oil at a sliding velocity of 0.5 mm/s and temperature of 22 °C. Reciprocating sliding direction is horizontal.

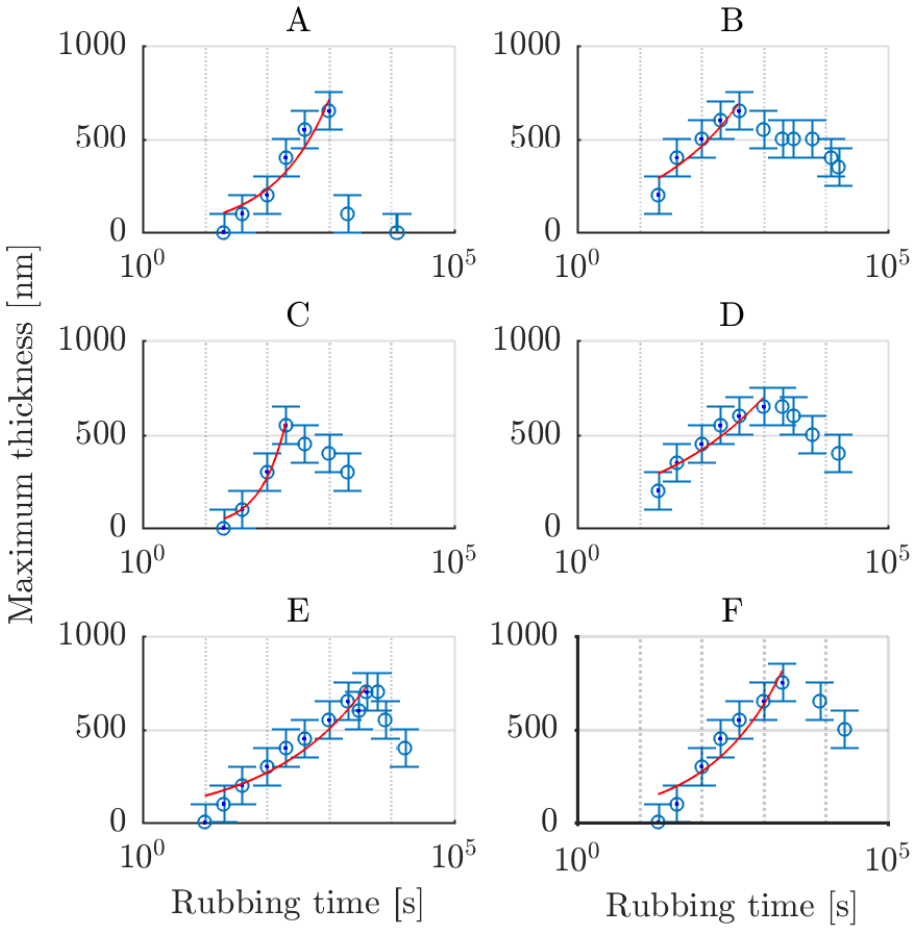

Figure C.4.: Tribofilm thickness evolution versus rubbing time at 0.5 mm/s and temperature of 22 °C with a power law fit in the growth region for all base oils. Closed points were used for the fit. The measurements up to 2000 s are corresponding with the images in Figure C.3.

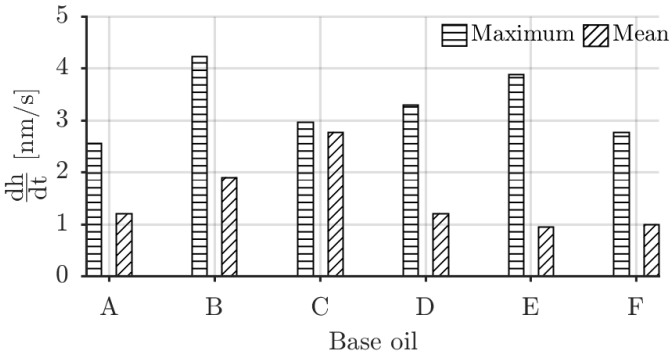

Figure C.5.: Maximum and mean tribofilm growth rate for all baseoils based on the derivative of the curve fits in Figure C.4.

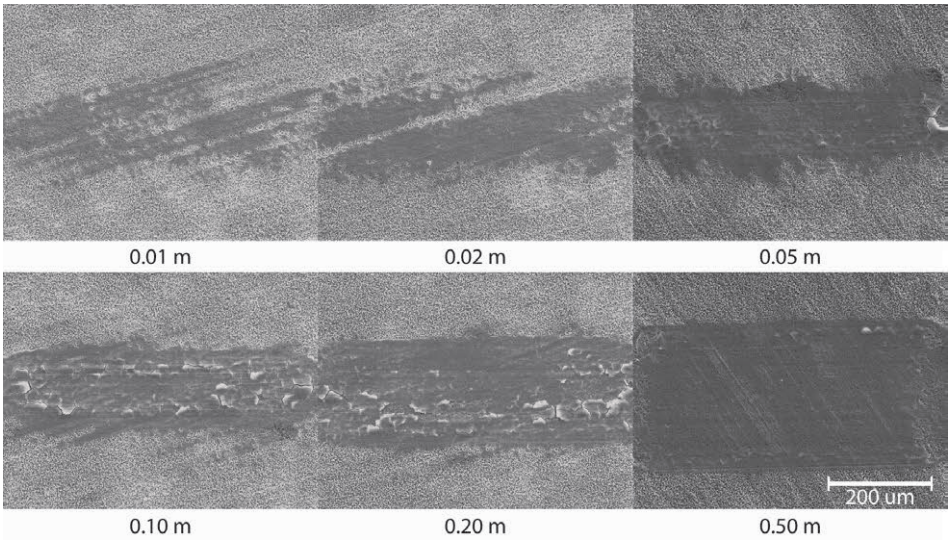

Figure C.6.: Secondary electron (20 kV) images of the wear scar for base oil B as function of cumulative sliding length at a sliding velocity of 0.5 mm/s and temperature of 22 °C. The wear scars correspond to the tribofilms shown in Figure C.3.

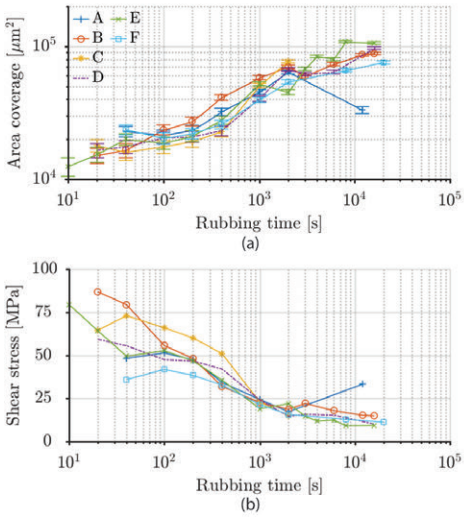

Figure C.7.: (a) Tribofilm surface coverage versus rubbing time. (b) Resulting calculated instantaneous shear stress as function of rubbing time.

The shear stress activation hypothesis is tested by assuming that only rubbed area is covered by tribofilm. This allows computing of an average instantaneous shear stress using the measured friction and covered surface area data with equation (C.2). The result is shown in Figure C.7b as function of rubbing time. It is clear for instance that the high shear stress of base oil B and the low shear stress of base oil F correlate with their observed growth rates in Figure C.5. Next to that the shear stress is highest at the start of the rubbing experiment and reduces because the contact area grows as a consequence of the wear on the disc side. This matches the earlier assertion of wear balancing the growth, however, this is thus mainly because the shear stress goes down.

The tribofilm formation as function of force, temperature and velocity was further investigated with the oils presenting the highest (base oil B) and lowest (base oil F) growth rate hereafter.

C.4.3. Tribofilm formation as function of force, temperature and velocity

The stress activation mechanism and its influence on the tribofilm growth was investigated by varying the normal force. The results are shown in Figure C.9a. The thickness versus time measurements show a large influence in the first 100 seconds, particularly for base oil B. The influence is relatively small for base oil F. Converting the data to shear stress as shown in Figure C.8 indicates a similar result as Figure C.7b. The larger tribofilm thickness for base oil B is entirely because of the initially higher shear stress. After that the shear stresses are comparable and the curves collapse on each other as shown in Figure C.8. The shear stress does

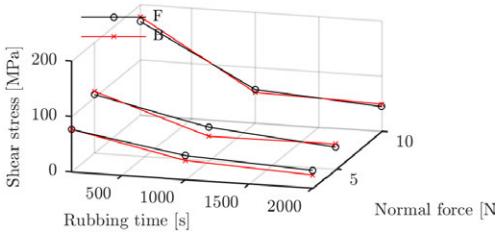

Figure C.8.: Calculated instantaneous shear stress as function of rubbing time and normal force at 0.5 mm/s and 22 °C.

increase with increased applied normal force explaining the increase in tribofilm thickness in Figure C.9a and further confirming the stress activation hypothesis.

The influence of bulk temperature on the tribofilm growth was investigated by increasing the bulk temperature of the disc and pin. The results are given in Figure C.9b. No acceleration of tribofilm formation by increasing temperature is observed for both base oils.

The results for increasing velocity are shown in Figure C.9c. The reduced tribofilm thickness for increasing velocities can entirely be attributed to increased wear at higher velocities of the tribofilm and the phosphate coating. In other words it is not because of the shorter test duration giving less time for growth. Note further that this is not a thermal effect as discussed in Section C.3.5.

C.4.4. Tribofilm topology and thickness

The surface topology of the tribofilm of a ball after 8 m equivalent sliding with base oil E at 0.5 mm/s, 10 N and 22 °C shown in Figure C.10a was measured using AFM. This particular experiment was chosen because in the middle of the ball part of the tribofilm was removed showing the underlying ball surface. The measurement was performed at the edge of this opening in the tribofilm. The result is shown in Figure C.10b. The surface is still smooth indicating that roughening of the surface is not part of the tribofilm growth mechanism. It further confirms the earlier observations of a patchy tribofilm. After 8 m of sliding the film had a maximum thickness of 466 nm. The surface was protected successfully either by the film itself or the separation that it created between disc and ball.

In addition a cross section was made by FIB on another ball after 0.5 m equivalent sliding with base oil E at 0.5 mm/s, 10 N and 22 °C. The cross section was investigated with SEM and shown in Figure C.10c and a zoom in of the tribofilm in Figure C.10d. The thickness is about 400 nm. No particular structure can be discerned in the tribofilm indicating a homogeneous composition throughout the thickness.

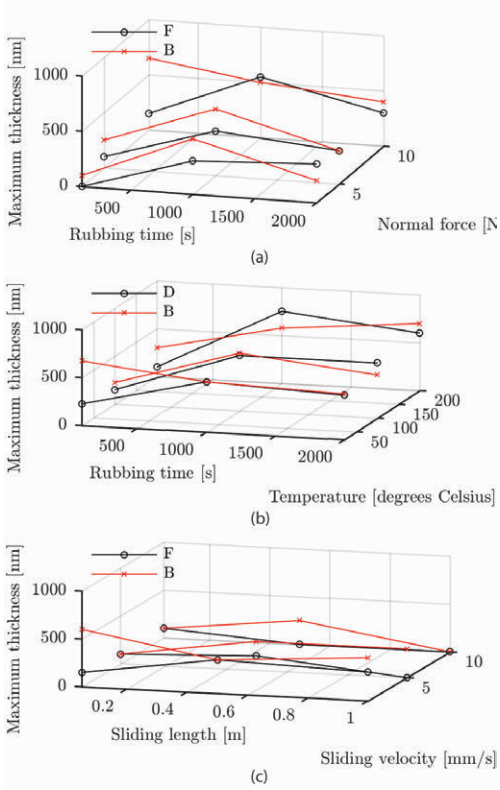

Figure C.9.: Tribofilm thickness as function of rubbing time and: (a) normal load at 0.5 mm/s and 22 °C, (b) bulk temperature at 0.5 mm/s and (c) sliding velocity at 22 °C. Note: Error bars of $\pm$ 100 nm removed for clarity of presentation.

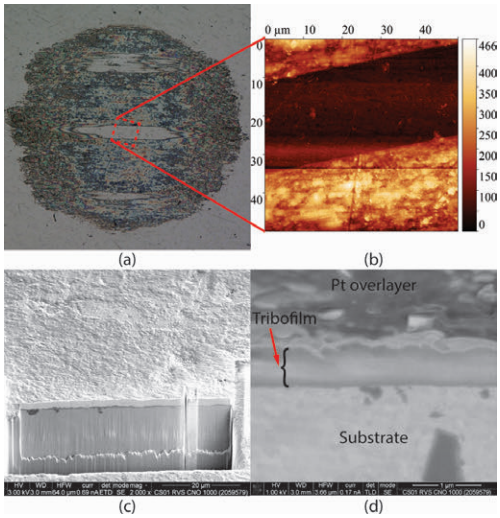

Figure C.10.: Surface topology and internal structure of the tribofilm. Figure C.10a and b show a LM image and AFM measurement of a tribofilm formed with base oil E after 8 meter sliding at 0.5 mm/s, 10 N and 22 °C. Note: approximate location is indicated. Figure C.10c and d show a SEM micrograph of the cross section made by FIB after 0.5 m equivalent sliding with base oil E at 0.5 mm/s, 10 N and 22 °C

C.4.5. Tribofilm composition

The X-ray diffractogram is shown in Figure C.11. The untouched coating on the disc was taken as a reference to compare to the tribofilm on the ball. The disc diffractogram shows the characteristic Bragg reflections for hureaulite [17]. The reflections are sharp, corresponding to an avarage crystalite size of more than 100 nm (according to Scherrer's equation, [35]). The tribofilm shows no Bragg reflections except for a strong Fe peak at 44.6° coming from the underlying AISI52100 steel. If the hureaulite would have been broken up into crystal fragments of a few nanometer coherent length (i.e. approximately 5-10 unit cells), there still should be recognizable reflections in the diffraction pattern. This indicates that there are no crystalline phases present in the tribofilm which can therefore be considered to have an X-ray amorphous structure.

To validate the measurement method used for the tribofilm on top of the ball, a test sample was made by lightly dusting the top of a clean reference ball with rutile (TiO_2) powder. Data collection using optical elements to selectively irradiate an area of approximately 0.3 mm radius resulted in a diffraction pattern where the applied titania phase could be readily identified.

SEM-EDX shows (Figure C.12) that the tribofilm comprises of phosphorous, oxygen and manganese. The result is normalized with the oxygen content. Multiple ball surfaces were probed in regions with a thin film (<100 nm) and a thick film (>400 nm) generated with base oil B, base oil D and base oil F. It was observed that the absolute concentrations depended on the thickness but that the ratios were independent of thickness. No differences were observed

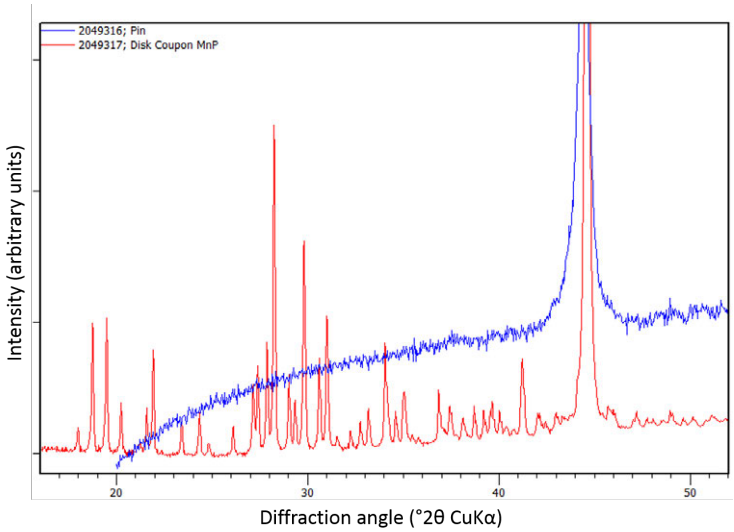

Figure C.11.: X-ray diffraction measurements of as received manganese phosphate coating compared with the tribofilm on the ball.

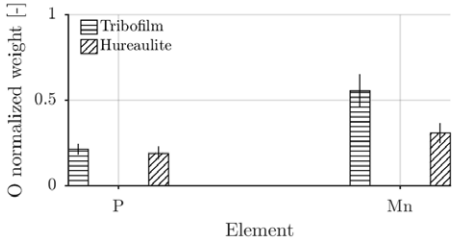

Figure C.12.: EDX measurement normalized by the respective oxygen weight content for the tribofilm on the ball and hureaulite on the disc surface.

between the base oils. The tribofilm P/O ratios matched the as received P/O ratio. This probably indicates that the tribofilm is still containing phosphate. A difference can be observed, however, for the manganese weight content (Mn_{film}/Mn_{coat}=1.8) that could not be solely explained by the added manganese content of the underlying AISI52100. Even though this does not say anything about the molecular structure of the tribofilm and EDX is semi-quantitative it was interesting to note the ratio difference in the light of the possibility of a chemisorption or chemical reaction.

The assertions of SEM-EDX were confirmed and made more precise using XPS. A line profile was taken across the centre line of the film including the bare AISI316L steel surface on each side. The spectrum is measured on the tribofilm. Therefore, mainly the elements Mn, P, O, C are measured and to a lesser extent the elements Fe, Cr, N and Si. The spectra of the Mn2p, P2p, O1s and C1s peaks are given in Figure C.13. The binding energy and the shape of the

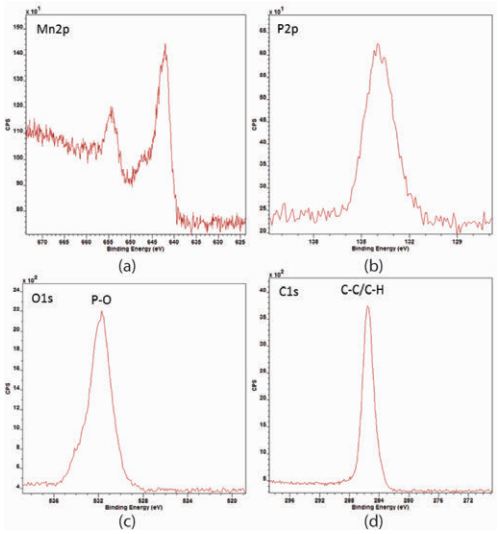

Figure C.13.: XPS measurement using a line scan of the first monolayers of a tribofilm generated with base oil E on a AISI316L ball.

Mn2p peak indicate a 2+ oxidation state of Mn (Figure C.13a). The P2p peak indicates the presence of one P-containing component. The binding energy of the peak can be associated with a phosphate phase (Figure C.13b). The O1s peak indicates the presence of more than one O-containing component. The main peak at a binding energy of 531.7eV could be associated with the phosphate phase (Figure C.13c). The C1s peak indicates the presence of only one component (Figure C.13d).

The line profile revealed a high C surface concentration. This probably comes from adsorbed base oil or solvent. For comparison of concentrations the composition was calculated leaving the c signal out. The result is the line profile in Figure C.14. The line profile reveals a Mn/P ratio of 0.8. If a simple correction [36] is made for the carbon-overlayer and the Mn/P ratio becomes 1.3. Which is a similar ratio between these elements as the EDX (Figure C.12) of hureaulite and it is now clear that the tribofilm consists of a phosphate. It was concluded based on the Mn/P ratio, the 2+ oxidation state and knowledge of the source of the tribofilm that this is probably hureaulite with the molecular formula of $Mn_5^{2+}(PO_3OH)_3(PO_4)_2 \cdot 4\,H_2O$ [17]. Another candidate could be $Mn_3(PO_4)_2$, which is the simplest phosphate molecule fitting the findings.

The observations with the initial line profile were confirmed by sputtering the tribofilm for a certain amount of time after which the composition is measured. Sputtering was done using 5kV Argon ions. The sputtered area was 1 x 1 mm, hence covering the entire tribofilm and part of the untouched ball surface.

The tribofilm was sputtered in three steps. The resulting spectra are shown in Figure C.15. The initial spectrum (0 s) shows the earlier discussed overwhelming C1s peak. After 120 seconds of sputtering the C1s peak has decreased in intensity considerably. The sputtering has

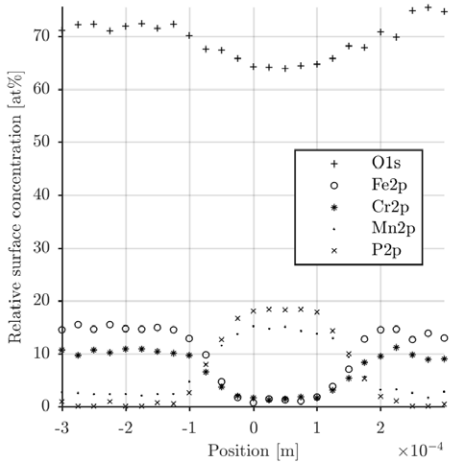

Figure C.14.: XPS linescan result belonging to Figure C.13.

removed the carbon containing top layer revealing the layer underneath. Before sputtering the binding energies of Fe2p and Cr2p indicated most of the Fe and Cr is present in an oxidised state. After sputtering only the metallic state of both elements is observed. The spectrum after 240 seconds is similar to the 120 seconds spectrum. The Mn2p and P2p peaks decreased in intensity and the Fe2p and Cr2p peaks increased in intensity. After 1740 seconds the Mn2p and P2p peaks disappeared from the spectrum indicating complete removal of the tribofilm. This was confirmed by optical microscopy. This rapid removal was surprising and indicated a 4 to 8 times higher sputter yield than anticipated.

Comparing the 0, 120 and 240 seconds results and using the knowledge of the higher sputter yield, and thus larger steps in depth, it is clear there are no compositional differences throughout the thickness. This is in line with the FIB/SEM observations in Figure C.10d.

C.4.6. Tribofilm durability

The durability of the tribofilm was investigated by generating a tribofilm with a lubricant. The tribofilm was generated over 0.5 m equivalent sliding at 0.5 mm/s, 10 N and 22 °C. The disc was subsequently exchanged for an uncoated and polished disc to test the durability. An example is shown for a tribofilm generated with base oil A. The test on the uncoated disc was run for 0.05 m with the same parameters and lubricant. The result is shown by the comparison between before and after in Figure C.16. The tribofilm has seen limited wear and shows that once the film is formed it is protecting the tribosystem successfully. This was repeated for all base oils and longer sliding lengths without tribosystem failure.

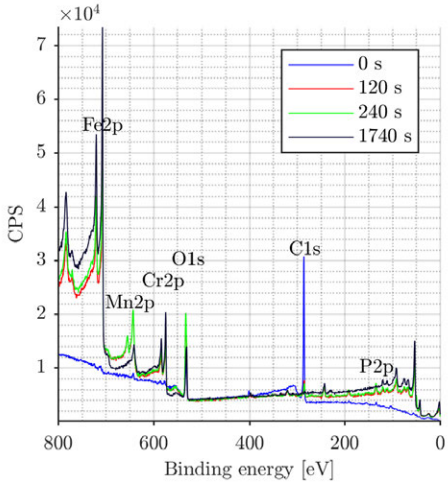

Figure C.15.: XPS depth spectra after sputtering.

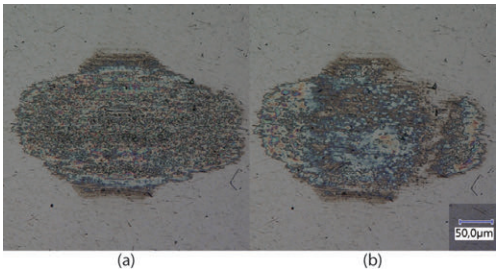

Figure C.16.: Tribofilm growth (a) on the phosphated disc after 0.5 m sliding at 0.5 mm/s, 10 N and 22 °C. Removal (b) on the polished disc for base oil A after 0.05 m sliding at 0.5 mm/s, 10 N and 22 °C.

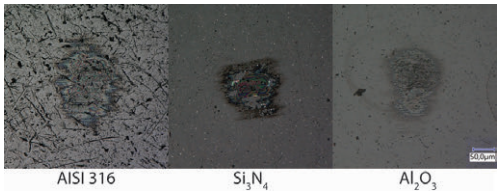

Figure C.17.: Tribofilm growth after 50 cycles with base oil B for different surface chemistries.

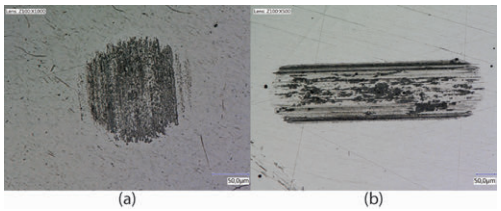

Figure C.18.: Pin and disc wear mark after sliding with harvested phosphate particle rich oil.

C.4.7. Tribofilm growth on stainless steel and non-metallic surfaces

The growth of the tribofilm was not unique for carbon steel surfaces. Meaning that the presence of (an) iron (oxide) is not a necessary condition for tribofilm growth. The results after rubbing for 50 cycles with base oil B for a selection of materials is shown in Figure C.17. It is observed that it forms readily on stainless steel (AISI 316) or non-metallic surfaces (Si3N4 / Al2O3) surfaces. However, the growth rates were lower compared to carbon steel.

C.4.8. Tribofilm growth with phosphate rich oil

Based on the previous results it is interesting to investigate if tribofilms grow on polished uncoated steel discs using the harvested base oil with phosphate particles. If this is the case these particles could also be considered as additives by adding them to the oil and remove the need for phosphating altogether.

To obtain base oil with dispersed particles the phosphated discs were washed after each experiment with ethanol. The solution of ethanol, base oil and particles was collected in a beaker. Next, the beaker was placed in an oven at 90 °C to evaporate the ethanol. The phosphate rich oil was subsequently used to lubricate a polished disc versus polished ball contact using the same experimental settings as before. The results were rather disappointing, no tribofilm formation was observed with any of the base oils. Figure C.18 shows the result after sliding 50 cycles. Signs of adhesive wear and scuffing can be clearly seen on disc and pin indicating that no protective film was formed. In addition, the same results were obtained with bought manganese phosphate powder (Sigma Alderich).

To confirm that particles are dispersed a set of samples were left in the oven until all the base oil was evaporated. The result is shown in Figure C.19. It clearly shows that debris particles

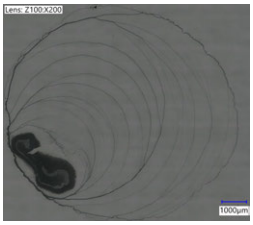

Figure C.19.: Results after evaporating the base oil from harvested oil from the rubbing experiment.

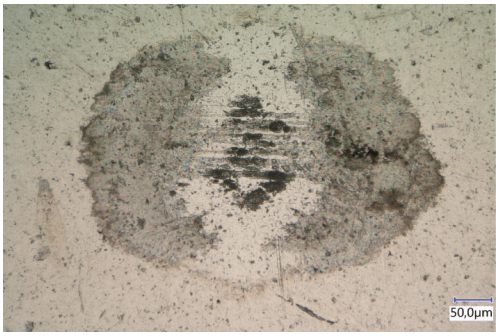

Figure C.20.: Tribofilm (or lack thereof) after sliding with base oil C on a thicker manganese phosphate coating after 0.5 m sliding at 0.5 mm/s, 10 N and 22°C.

were dispersed in the oil and are most probably responsible for the tribofilm growth.

C.4.9. The role of the phosphate coating

The thickness of the phosphate coating on the counter surface turned out to be an important factor in successful tribofilm growth. Tribofilms would only grow on the ball with coatings that were $<3\,\mathrm{g\,cm^{-2}}$. On thicker coatings large chunks of coating were removed because of ploughing and delamination [2]. This was because a thicker coating bears the subsurface stresses [37]. A ball surface after sliding on a thicker coating is shown in Figure C.20 for an AISI316 ball and base oil C. Hence for the mechanisms described in the previous chapters to occur the phosphate coating needs to act as a shear layer.

C.5. Discussion

The tests results shown here support the hypothesis that tribofilm growth in a lubricated bare against phosphate conversion coated contact is governed by the applied shear stress in two ways. First it breaks off small particles from the phosphate coating which get dispersed in the base oil (that is why the static tests did not yield a film). Second it stress activates the particle

such that it adsorps to the ball. The lubricant polarity was proven to not play a significant role in the tribofilm growth. However, the growth rate is inversely affected by velocity as shown in Figure C.9c. This was attributed to the increased wear of the tribofilm and the coating on the disc.

It is known that for proper dispersion of particles in a solvent the particle polarity should be matched with the polarity of the solvent. Next to that, polar particles are dispersed by polar solvents and vice versa and incompatibility of particle and solvent leads to flocculation or agglomeration [38]. The role of the base oil polarity could be that, when it is properly matched (base oil B) it promotes dispersion of the generated particles and counters agglomeration. This maximizes the (re)activity and availability of the particles. On the other hand in an apolar solvent (base oil F), the particles tend to agglomerate which reduces their (re)activity and availability until a certain saturation threshold is reached.

The film formation is observed to only happen in the presence of a lubricant, the onset to be most rapid for (low viscosity) polar base oils and follows a power law as function of sliding length. Once the film is formed the thickness and growth rates converge to similar values indicating that once the surface is covered and the concentration of dispersed manganese phosphate particles is high enough the base oil is not influencing the growth any more. This is confirmed in the subsequent tests with a variation in load, velocity or temperature. In all cases the film thickness stopped increasing at 600 - 700 nm. This is probably because an equilibrium is reached between growth and removal similar to observations in ZDDP derived films by [39]. The question is: can the formation be fully attributed to high friction (shear) and is this because of the low viscosity or the polarity?

The found maximum rates (Figure C.5) are plotted against base oil aniline point, COF, dynamic viscosity and maximum shear stress in Figure C.21. Starting with aniline point (Figure C.21a) no correlation was found in the data. Observational evidence (Figure C.3) did show early initiation for base oil B which might be attributed to its molecular structure instead of its polarity when taking into account the performance of base oil A (poly alkalyne glycol vs adipate ester). There is a clear correlation with COF in Figure C.21b. This can weakly be attributed to the difference in base oil dynamic viscosity (Figure C.21c). The main effect though is because of the stress activation mechanism, the shear stress (and thus the COF) gives a clear correlation with the maximum growth rate as shown in Figure C.21d.

The tests with varying load, temperature and velocity (Figure C.9) confirm this and show that growth is directly proportional to shear stress and therefore indicates a stress activation mechanism. No acceleration was found when the bulk temperature was increased which rules out a chemisorption or chemical reaction mechanism. Therefore the tribofilm formation is probably driven by physisorption.

The gradient of Figure C.21d can be used to estimate the interaction volume using the stress-promoted thermal activation equation following the work by [40] to speculate about the reactive group driving the physisorption. The equation is written as,

$$Rate = A \exp\left(\frac{-(E - N\tau\Delta v)}{RT}\right) \tag{C.3}$$

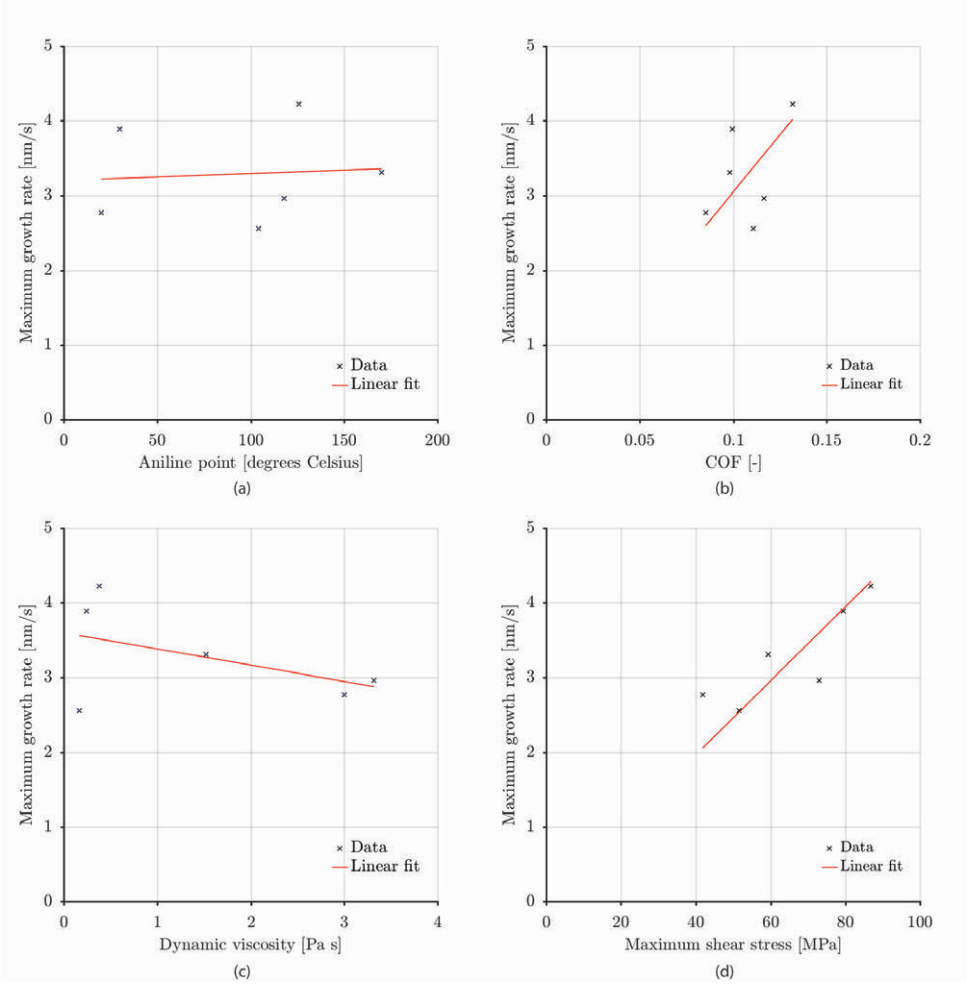

Figure C.21.: Correlation of maximum growth rate with the aniline point, COF, dynamic viscosity and maximum shear stress.

where A is the pre-constant, E the molar thermal activation energy, N Avogadro's constant, τ the shear stress, Δv the activation volume, R the gas constant, and T the temperature. As no thermal activation was found equation (C.3) can be simplified to

$$Rate = A \exp\left(\frac{N\tau\Delta v}{RT}\right). \tag{C.4}$$

Now the build up rate of the hureaulite tribofilm should be related to shear stress by taking the $\log$ of equation (C.4) such that

$$\log(Rate) = \log(A) + \frac{N\Delta v}{RT}\tau. \tag{C.5}$$

The activation volume is found from the slope of the shear stress against a log(maximum growth rate) plot and calculated to be $0.052\,\mathrm{nm}^3$. If a typical bond length of $0.2\,\mathrm{nm}$ is considered, the molecular area over which the shear stress acts is $0.26\,\mathrm{nm}^2$. The most plausible functional groups in the hureaulite molecule are the phosphate group, PO_4^{3-}, and the hydroxide group, OH^-. Using the bond lengths reported in [17] and the Van der Waals radii of the atoms these groups yield a molecular area of roughly $0.29\,\mathrm{nm}^2$ and $0.23\,\mathrm{nm}^2$ respectively. In addition, the activation can be from deforming or stretching a single P-O bond in the phosphate group giving an area of $0.07\,\mathrm{nm}^2$. As discussed, for adsorption to happen particles need to be generated first. A crystal has a tendency to split along crystallographic structural planes because of relative weakness in the crystal which is known as cleavage. In other words, a preferential fracture plane. For hureaulite this is perpendicular to the a-axis [17] in the unit cell abc-reference system and also denoted as $\{100\}$-plane [41] which will expose phosphate groups. Hence the most plausible explanation for the adsorption of hurealite is deformation or stretching of (a bond in) the exposed phosphate group. This will make the non-polar phosphate group slightly more polar leading to adsorption on the ball surface.

The experiments with harvested base oil or adding manganese phosphate powder to the base oil (Section C.4.8) confirm this (re)activity and shows that this is lost if the oil with particles is isolated and reused on another disc. This is probably because the particles are quickly oxidized or hydrolised and explains why the tribofilm is only formed in situ. This is also why the manganese phosphate powder does not work as stabilizing agents are added during grinding to avoid agglomeration.

These assertions are further fortified by the patchy (Figure C.10) and amorphous (Figure C.10d, Figure C.11) structure, the unchanged chemical composition of the film (Figure C.12, Figure C.13, Figure C.15), and the formation of tribofilms on carbon steel (Figure C.3), stainless steel and ceramic surfaces (Figure C.17).

The durability of the films (Figure C.16) is unexpected for physisorption, particularly at elevated temperatures. However it is an important and interesting property for the application at hand. The casing connections need to maintain seal ability at elevated temperatures under micro sliding conditions. The presence and generation of a durable tribofilm can be beneficial for their performance. However attention should be paid to the phosphate coating thickness. If the coating is not acting as a shear layer, tribofilm formation is limited or non-existent.

C.6. Conclusions

The formation of tribofilms in a phosphate conversion coated tribosystem was investigated for the first time. Phosphate based tribofilms derived from the hureaulite crystals on the disc were created on the ball counter surface in a pin-on-disc tribometer under variation of normal force, sliding length, sliding velocity, bulk temperature and base oil polarity.

The results indicate the following:

1. When rubbing against a manganese phosphate (hureaulite) coating under lubricated conditions an amorphous and durable tribofilm that consists of hureaulite is created.
2. The hureaulite particles are generated by cleavage along the {100}-plane which exposes phosphate groups. These are subsequently activated by shear stress which deforms or stretches the P-O bond(s). This leads to a more polar functional group which adsorbs at the ball surface forming a tribofilm.
3. Therefore the formation of the tribofilm is activated by shear stress and the rate of formation of the tribofilms is strongly correlated with the magnitude of the shear stress in the tribological contact.
4. The initiation of the tribofilm is weakly correlated with the base oil polarity.
5. Tribofilm growth is only observed in-situ.
6. The adsorption mechanism is physisorption, confirmed by the tribofilm formation on carbon steel, stainless steel, silicon nitride and aluminium oxide, the unchanged chemical composition / structure and the absence of thermal acceleration.
7. No tribofilm formation was observed on thick (>3 g cm^{-2}) phosphate coatings.

The conclusions fortify those in our earlier work [3]. Phosphate conversion coatings are a fact of life in the oil and gas industry and can be used as engineering parameters to develop the next generation environmentally friendly lubricants and ensure seal ability of casing connections.

Acknowledgements

The authors are grateful to Shell Global Solutions International BV for permission to publish this work, dr. ir. Rob Bosman for the insightful discussions on the film formation, dr. Huub Kooijman for the discussions on the tribofilm structure and XRD analyses, dr. Marco de Ridder for the XPS analyses, and drs. Edward Worthington and Shell Global Solutions Germany GmbH for providing the polarity data of the lubricants.

References

[1] Bommer, P. *A Primer of Oilwell Drilling*. 7th. Austin: The University of Texas at Austin, 2008.

[2] Ernens, D., Rooij, M. B. de, Pasaribu, H. R., Riet, E. J. van, Haaften, W. M. van and Schipper, D. J. 'Mechanical characterization and single asperity scratch behaviour of dry zinc and manganese phosphate coatings'. *Tribology International* 118 (February 2018), pp. 474–483.

[3] Ernens, D., Riet, E. J. van, Rooij, M. B. de, Pasaribu, H. R., Haaften, W. M. van and Schipper, D. J. 'The Role of Phosphate-Conversion Coatings in the Makeup and Sealing Ability of Casing Connections'. *SPE Drilling & Completion* (October 2018).

[4] Ertas, A. 'Experimental Investigation of Galling Resistance in OCTG Connections'. *Journal of Manufacturing Science and Engineering* 114.1 (February 1992), p. 100.

[5] Inose, K., Sugino, M. and Goto, K. 'Influence of Grease on High-Pressure Gas Tightness by Metal-to-Metal Seals of Premium Threaded Connections'. *Tribology Online* 11.2 (2016), pp. 227–234.

[6] Rausch, W. *The phosphating of metals*. Metals Park, Ohio, USA; Teddington, Middlesex, England: ASM International; Finishing Publications Ltd., 1990, p. 406.

[7] Nevosad, A., Azhaarudeen, S., Doerr, N., Zacharias, H., Klarner, J. and Badisch, E. 'Initial Damage Mechanism and Running-In Behaviour of Phosphate Conversion Coatings'. *Key Engineering Materials* 721.December (December 2016), pp. 356–361.

[8] Perry, J. and Eyre, T. 'The effect of phosphating on the friction and wear properties of grey cast iron'. *Wear* 43.2 (June 1977), pp. 185–197.

[9] Hivart, P., Hauw, B., Bricout, J. and Oudin, J. 'Seizure behaviour of manganese phosphate coatings according to the process conditions'. *Tribology International* 30.8 (July 1997), pp. 561–570.

[10] Neville, A., Morina, A., Haque, T. and Voong, M. 'Compatibility between tribological surfaces and lubricant additives—How friction and wear reduction can be controlled by surface/lube synergies'. *Tribology International* 40.10-12 (October 2007), pp. 1680–1695.

[11] Azhaarudeen, S., Faruck, A. A. M. and Nevosad, A. 'Tribological behaviour and wear mechanisms of manganese phosphate coatings under dry reciprocating sliding contact conditions'. *Tribology International* 122.February (June 2018), pp. 189–199.

[12] Le, H. R., Stewart, F. and Williams, J. A. 'A Simplified Model of Surface Burnishing and Friction in Repeated Make-Up Process of Premium Tubular Connections'. *Tribology Letters* 59.2 (August 2015), p. 35.

[13] Pérez-Ràfols, F., Larsson, R. and Almqvist, A. 'Modelling of leakage on metal-to-metal seals'. *Tribology International* 94 (February 2016), pp. 421–427.

[14] Pérez-Ràfols, F., Larsson, R., Lundström, S., Wall, P. and Almqvist, A. 'A stochastic two-scale model for pressure-driven flow between rough surfaces'. *Proceedings of the Royal Society A: Mathematical, Physical and Engineering Science* 472.2190 (June 2016).

[15] Pérez-Ràfols, F., Larsson, R., Riet, E. J. van and Almqvist, A. 'On the flow through plastically deformed surfaces under unloading: A spectral approach'. *Proceedings of the Institution of Mechanical Engineers, Part C: Journal of Mechanical Engineering Science* 232.5 (March 2018), pp. 908–918.

[16] Hill, R. and Jones, J. 'The crystal structure of hopeite'. *American Mineralogist* 61 (1976), pp. 987–995.

[17] Moore, P. B. and Araki, T. 'Hureaulite: lts Atomic Arrangement'. *American Mineralogist* 58.3-4 (1973), pp. 302–307.

[18] Narayanan, T. S. N. S. 'Surface pretreatment by phosphate conversion coatings - A review'. *Reviews on Advanced Materials Science* 9.2 (2005), pp. 130–177.

[19] Bosman, R. and Schipper, D. J. 'Mild Wear Prediction of Boundary-Lubricated Contacts'. *Tribology Letters* 42.2 (May 2011), pp. 169–178.

[20] Stachowiak, G. and Batchelor, A. W. *Engineering Tribology*. Butterworth-Heinemann, 2013, p. 884.

[21] Beyer, M. K. and Clausen-Schaumann, H. 'Mechanochemistry: The Mechanical Activation of Covalent Bonds'. *Chemical Reviews* 105.8 (August 2005), pp. 2921–2948.

[22] Spikes, H. A. 'Friction Modifier Additives'. *Tribology Letters* 60.1 (October 2015), p. 5.

[23] Lansdown, A. R. *Lubrication and Lubricant Selection: a Practical Guide*. Pergamon Press, 2003, p. 320.

[24] Hsu, S. 'Boundary lubrication: current understanding'. *Tribology Letters* 3.1 (March 1997), pp. 1–11.

[25] Erdemir, A. 'Review of engineered tribological interfaces for improved boundary lubrication'. *Tribology International* 38.3 (March 2005), pp. 249–256.

[26] Crobu, M., Rossi, A., Mangolini, F. and Spencer, N. D. 'Tribochemistry of Bulk Zinc Metaphosphate Glasses'. *Tribology Letters* 39.2 (August 2010), pp. 121–134.

[27] Barnes, A. M., Bartle, K. D. and Thibon, V. R. 'A review of zinc dialkyldithiophosphates (ZDDPS): characterisation and role in the lubricating oil'. *Tribology International* 34.6 (June 2001), pp. 389–395.

[28] Spikes, H. A. 'The History and Mechanisms of ZDDP'. *Tribology Letters* 17.3 (October 2004), pp. 469–489.

[29] Gosvami, N. N., Bares, J. A., Mangolini, F., Konicek, A. R., Yablon, D. G. and Carpick, R. W. 'Mechanisms of antiwear tribofilm growth revealed in situ by single-asperity sliding contacts'. *Science* 348.6230 (April 2015), pp. 102–106.

[30] Naveira Suarez, A., Grahn, M., Pasaribu, H. R. and Larsson, R. 'The influence of base oil polarity on the tribological performance of zinc dialkyl dithiophospate additives'. *Tribology International* 43.12 (December 2010), pp. 2268–2278.

[31] Fujita, H. and Spikes, H. A. 'The formation of zinc dithiophosphate antiwear films'. *Proceedings of the Institution of Mechanical Engineers, Part J: Journal of Engineering Tribology* 218.4 (January 2004), pp. 265–278.

[32] Zhmud, B. 'Beyond the aniline point: Critical solution point for the oil/aniline system as a measure of oil solubility'. *Fuel* 86.16 (November 2007), pp. 2545–2550.

[33] Bosman, R. and Rooij, M. B. de. 'Transient Thermal Effects and Heat Partition in Sliding Contacts'. *Journal of Tribology* 132.2 (2010), p. 021401.

[34] Kasap, S. O. *Optoelectronics & Photonics:Principles & Practices: International Edition*. 2nd. Upper Saddle River, NJ 07458: Pearson Education Prentice Hall, 2013, p. 550.

[35] Cullity, B. and Stock, S. *Element of X-Ray Diffraction*. 3rd. Pearson Education, 2001, p. 664.

[36] Smith, G. C. 'Evaluation of a simple correction for the hydrocarbon contamination layer in quantitative surface analysis by XPS'. *Journal of Electron Spectroscopy and Related Phenomena* 148.1 (July 2005), pp. 21–28.

[37] Holmberg, K. and Matthews, A. *Coatings tribology : properties, mechanisms, techniques and applications in surface engineering*. 2nd Editio. Elsevier Science, 2009, p. 576.

[38] Shibata, J., Fujii, K., Murayama, N. and Yamamoto, H. 'Dispersion and Flocculation Behavior of Fine Metal Oxide Particles in Various Solvents'. *KONA Powder and Particle Journal* 20.20 (2002), pp. 263–269.

[39] Fujita, H. and Spikes, H. A. 'Study of Zinc Dialkyldithiophosphate Antiwear Film Formation and Removal Processes, Part II: Kinetic Model'. *Tribology Transactions* 48.4 (October 2005), pp. 567–575.

[40] Zhang, J. and Spikes, H. A. 'On the Mechanism of ZDDP Antiwear Film Formation'. *Tribology Letters* 63.2 (August 2016), p. 24.

[41] Ashcroft, N. W. and Mermin, N. D. *Solid State Physics*. Cengage Learning, Inc, 1976, p. 848.

D. On the glaze layer formation in zinc and manganese phosphate coatings

D. Ernens[a,b], M.B. de Rooij[a], H.R. Pasaribu [b], D.J. Schipper[a]

[a]*Laboratory for Surface Technology and Tribology, Department of Engineering Technology, University of Twente, P.O. Box 217, 7500 AE Enschede, The Netherlands*

[b]*Shell Global Solutions International BV, Innovation, Research & Development, Wells R & D, Kessler Park 1, 2288 GS Rijswijk, The Netherlands*

Abstract Phosphate conversion coatings form a glaze layer in sliding tribological contacts. Earlier work has shown that in dry sliding contacts the glaze layer attains a substantial surface hardness. This is, however, not observed when sliding under lubricated conditions. On glaze layers generated in ring-on-ring and pin-on-disc test it is shown for the first time with nano-indentation and atomic force microscopy that the hardness difference comes from a significant difference in particle size. This is substantiated with a particle interaction model taking into account the difference in interaction coming from the environment and the particle size. It is concluded that the main reason for higher hardness after dry sliding comes from the smaller particle sizes because of the more effective grinding in the contact.

To be submitted to Tribology International.

D.1. Introduction

Casing connections (Figure D.1) in the oil and gas industry are used to connect 12 meter sections of pipe to fortify the bore hole during drilling [1]. The connections are typically coated with zinc (ZP) and/or manganese phosphate (MP) for corrosion protection during storage. The presence of phosphate coatings is also known to give beneficial tribological performance [2–6].

(a) (b)

Figure D.1.: Casing strings are connected by screwing together a male and female part also known as a pin shown in Figure D.1a and a box shown in Figure D.1b. Indicated is the location of the metal-to-metal seal.

In a casing connection the sliding lengths during assembly are short (<1 m) and the sliding velocities are low (<30 mm/s). Therefore the phosphate coating and its associated generated glaze layer affect the wear process strongly [3]. The wear changes the surface topology of the metal-to-metal seal [7] and thus influences the subsequent seal ability [8–10].

In a previous paper the macroscopic mechanism behind the formation of hard layers in dry phosphated steel surfaces was described [4]. This so called glaze layer [11] formed under sliding conditions by crushing and compacting the phosphate crystals in the contact. The resulting glaze layer had a higher hardness, up to 3.5 GPa, than its phosphate crystal constituents and typical steel substrates. As will be shown in this paper it turned out that hard glaze layers are not always formed. In particular after lubricated sliding conditions such as those in [3]. In this paper, therefore, an investigation is presented on the mechanism behind the formation of the (hard) glaze layer on the phosphated side of the tribosystem.

As said before, small-sized phosphate particles are generated in the sliding contact [4]. It was hypothesised that these particles agglomerate readily because of their size and thus high surface energy combined with the applied contact stress. This compacted agglomerate of nano-particles, the glaze layer, is thought to be the source of the high hardness.

The strength of inter particle bonds is governed by Van der Waals forces, electrostatic repulsion forces [12, 13] and capillary forces [14, 15]. The interaction forces are modified by the surface energy, the size of the particles, and the environment. For instance, a particle will generate a stronger interaction in a humid environment because of the presence of capillary forces coming from adsorbed water [16]. On the other hand, exchanging the water for oil in the system will lower the interaction forces because of its weaker interaction potential and capillary effect

[12–14]. Furthermore, it is well known that the interaction between particles grows stronger when particle size goes down [13].

The increasingly stronger interaction leads to agglomeration in particle based systems [17] which can be exploited in for instance the manufacturing of pills [18]. The tensile strength and by extension the hardness [19] of such an agglomerate was first modelled by [20] based on the aforementioned inter particle interactions and the porosity of the agglomerate. The work of [20] forms the basis for modelling the strength of pills [18, 21], energy needed to deagglomerate particles in high shear mixing [22, 23] and grinding [24] and the mechanical properties of powders [25].

To investigate if particle agglomeration lies at the basis of the high hardness, glaze layers were generated in dry and lubricated conditions in a pin-on-disc set-up. These experiments were designed to explain the lower hardness observed in specimens from lubricated experiments [3]. The surface hardness was determined after the test using nano-indentation. Next, the particle size was investigated using AFM for each condition. Finally, using the particle interaction model of [20], the origin of the hardness differences is discussed and explained.

D.2. Methods

The conditions during assembly of a casing connection have been studied in two experiments. The ring-on-ring test provides a circumferential line contact at equivalent contact stresses and sliding velocities as they occur in metal-to-metal seals. This is where the initial observations of lower glaze layer hardness under lubricated conditions were done.

Subsequent work was done in a pin-on-disc set-up to investigate the influence of the lubricant on the mechanical properties of the glaze layer. The contact situation is as follows, the pin is represented by a ball that slides against a phosphated flat representing the box (Figure D.1).

The pin-on-disc set-up has been chosen to easily simulate the assembly process for the study of the formation of the glaze layer in lubricated conditions and the influence of lubrication on the mechanical properties. The details will be given in the following sections.

D.2.1. Lubricants

The lubricant used in the ring-on-ring test is Jet-Lube (JLu) API modified [26]. The compound consist of a mineral base oil, a lithium soap thickener and metallic particles. On visual inspection the compound has a black colour and the metallic particles are clearly visible. The ASTM D-217 penetration is 310 - 340. In the pin-on-disc test the influence of a lubricant on the glaze layer hardness is studied with Shell Ondina 933 base oil.

Table D.1.: Chemical composition used steel grades

	Chemical Composition (%)									
	C	Si	Mn	P	S	Cr	Ni	Cu	Mo	V
API 5CT P110	–	–	–	≤ 0.020	≤ 0.010	–	–	–	–	–
Typical P110	$0.26 - 0.35$	$0.17 - 0.37$	$0.40 - 0.70$	≤ 0.020	≤ 0.010	$0.80 - 1.10$	≤ 0.20	≤ 0.20	$0.15 - 0.25$	≤ 0.08
AISI4130	$0.28 - 0.33$	$0.15 - 0.35$	$0.40 - 0.60$	≤ 0.035	≤ 0.04	$0.80 - 1.10$	–	–	$0.15 - 0.25$	–
AISI52100	$0.95 - 1.10$	$0.15 - 0.30$	≤ 0.25	≤ 0.030	≤ 0.025	$1.30 - 1.60$	–	–	–	–

Table D.2.: Summary of used materials and their properties.

Material name (-)	Surface finish Ra (μm)	Young's Modulus (GPa)	Surface hardness (GPa)
AISI4130	0.01	210	3
P110	1.6	210	3
AISI52100	0.01	213	7

D.2.2. Materials

The ring-on-ring tests specimens are manufactured from quenched and tempered steel taken from 4" diameter P110 tubing. The chemical composition is reported inTable D.1. The contacting surfaces are manufactured by turning resulting in a surface roughness of Ra = 1.6 μm. The top sample has a round-off radius of 80 mm and the bottom sample is flat. The box is subsequently zinc or manganese phosphated according to the procedure in [4]. The surface topographies before the test are shown in Figure D.2. The mechanical properties are listed in Table D.2.

The pin-on-disc experiments are performed using a 3 mm and 10 mm ball on flat configuration. The balls are polished and made from bearing steel (AISI52100). The flat is made from quenched and tempered steel (AISI4130) which was subsequently ground and then dip coated with zinc or manganese phosphate according to the procedure in [4]. The mechanical properties are listed in Table D.2.

D.2.3. Ring-on-ring tester

The ring-on-ring [3] tests are performed in an in-house developed test set-up. Concentric sliding tests are performed with continuous contact, equivalent to the make-up of a casing connector. The contact configuration of the rings is flat against a radius of R = 80 mm leading to a circumferential line contact. The contact line diameter is 70 mm and the contact width approximately 1 mm. The sliding tests are performed at a maximum Hertzian contact stress of 0.25 GPa by applying a 30 kN normal force. The sliding velocity is 25 mm/s. The total sliding length is 1 revolution.

The properties of the specimens under investigation are summarized in Table D.3. The set consists of 2 experiments designated as pairs in the table. The surface evolution tests are

Table D.3.: Overview of ring-on-ring specimens investigated. The test results are summarized by sliding length l and maximum Hertzian contact stress P_{max} during sliding.

Pair #	Specimen ID (-)	Material (-)	Ra (µm)	Coating (-)	Lubricant (-)	l (mm)	Sliding velocity (mm s^{-1})	P_{max} (GPa)
1	65275	P110	1.2	ZP	JLu API mod	219,75	25	0.25
	65267	P110	1.6	None				
2	65273	P110	1.3	MP	JLu API mod	219,75	25	0.25
	65259	P110	1.6	None				

summarized by sliding length, l, and maximum Hertzian contact stress during sliding, P_{max}.

D.2.4. Contact stresses for pin-on-disc tests

To come to realistic contact stresses for the pin-on-disc tests the contact stress in the ring-on-ring test was determined using a semi-analytical method (SAM) based contact solver [27, 28]. This method takes deterministic (measured) roughness as input together with the mechanical properties (Table D.2) to solve for the contact problem. Plasticity is handled by an elastic-perfect plastic material behaviour assumption and implemented by a hardness cut-off for the maximum allowable contact stress.

A full width section of the initial surface topography of the rin-on-ring tests was measured and used to this end. A cross section of the topographies is shown in Figure D.2a and Figure D.2b for the top and bottom specimen respectively. The contact stress solution for the 30 kN normal load at assembly is shown in Figure D.2c. The conclusion was that the contact stresses reach the material hardness of 3 GPa on the top of the waviness. This was subsequently used to select the pin-on-disc loading.

D.2.5. Pin-on-disc tribometer

The formation of the glaze layer under dry and lubricated conditions was investigated using a Bruker UMT-3 pin-on-disc tribometer. The load was measured with the 6D load cell (TFH-50). The low velocity (0.1 mm/s) uni-directional sliding tests were performed with a 3 mm ball using the slider of the tribometer combined with the high temperature module (S35HE-350). One pass was made, hence on the disc the sliding length is equal to the Hertzian contact width of 140 µm. The test is shown schematically in Figure D.3a and summarized in Table D.4. The unidirectional tests are the same as [4].

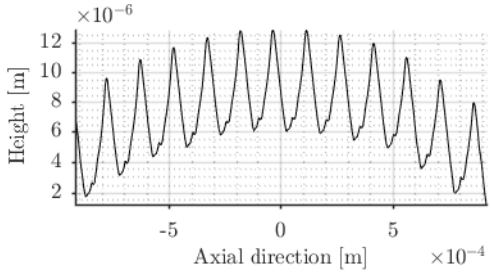

(a) Top

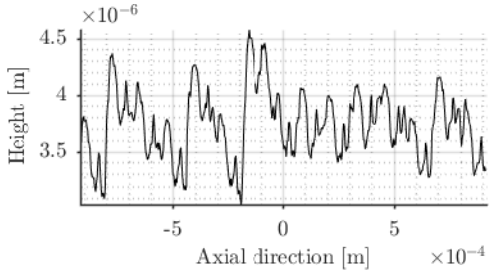

(b) Bottom

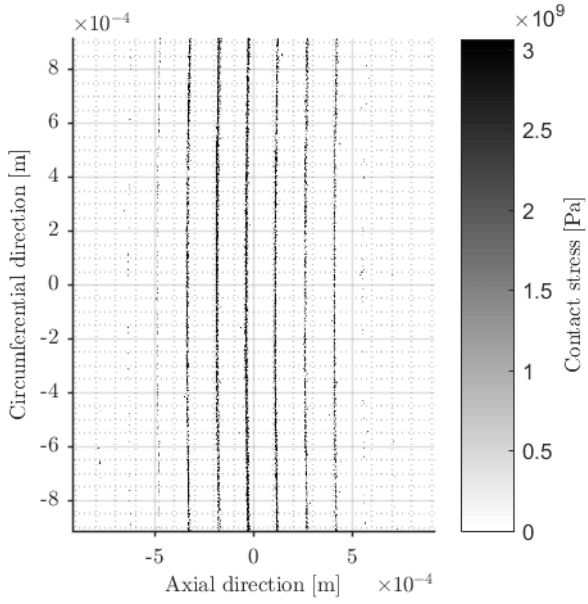

(c) Contact stress

Figure D.2.: Surface topographies before the ring-on-ring test for the top specimen in Figure D.2a and the bottom specimen in Figure D.2b. The resulting contact stress when applying 30 kN normal load is shown in Figure D.2c and obtained with the method of [27].

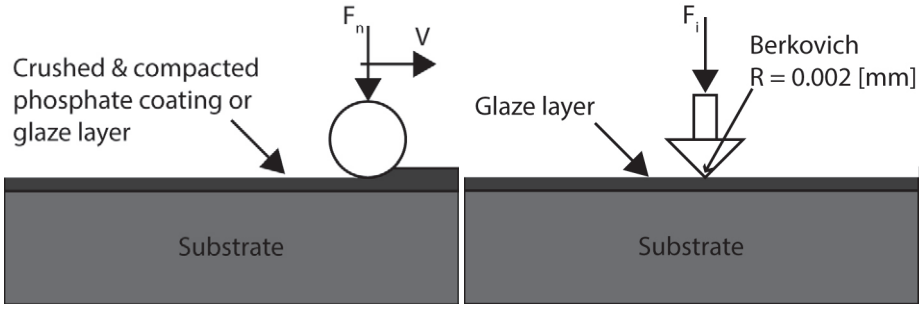

(a) pin-on-disc (b) nano-indent

Figure D.3.: Schematic overview of the pin-on-disc tests. First the glaze layer is created by uni-directional sliding with a 3 mm ball as shown in Figure D.3a. This is followed by nano-indentation using a Berkovich indenter as depicted in Figure D.3b.

D.2.6. Analyses

Before the test the surface topography of the ring specimens was measured with a white light interferometer (Bruker NP-Flex, at 0.8 µm lateral resolution). After the tribological test, the rings and the discs were prepared for further analysis by rinsing of the lubricants with heptane and acetone and subsequent drying with nitrogen. The resulting glaze layers were investigated using a nano-indenter (UNAT, Asmec), Scanning Electron Microscopy (SEM, Tescan Vega 2), X-ray Diffractometry (XRD, PANalytical Empyrean diffractometer, Cu anode, focusing optics: 0.1 and 0.3 mm monocapillary), and Atomic Force Microscopy (AFM, NanoSurf Flex-Axiom in tapping mode with ACTA cantilever). The analytical techniques were used to determine the following properties of the formed glaze layer: The indentation hardness, surface topography and particle size as function of the experimental parameters.

D.2.7. Nano-indentation

The nano-indentation depicted in Figure D.3b was carried out using a diamond Berkovich tip. The loads applied ranged from 1 - 500 mN, see also Table D.4. Each test was repeated 15 times, tests with fracture events were discarded. The load was applied in 10 s, the hold time was 15 s and unloading was performed in 4 s. The tip geometry and measurement set-up were validated prior to the measurements using a sapphire reference. To establish a datum for the indentation tests, an indentation at 0.1 mN is made prior to the measurement. Processing of the force-displacement curves to become an indentation hardness is done according to the method of [29].

D.2.8. Particle size measurement

The average particle sizes were determined using the phase output of the AFM measurements. The phase is sensitive for slope changes. This information was used to find the particle

Table D.4.: Overview of the range of experimental parameters used to study the formation of the glaze layers.

Geometry (-)	Experiment	Normal force (N)	l (mm)	Sliding velocity (mm s^{-1})	P_{max} (GPa)	Hertzian contact area (10^{-3} mm^2)
Ball 3 mm	uni-directional	5 - 45	0.14	0.1	1.8 - 3.74	5 - 20
Berkovich 2 µm	nano-indentation	0.001 - 0.5	N/A	N/A	N/A	N/A

boundaries in a line profile. The average particle size is subsequently found by dividing the line length by the boundary crossings.

D.3. Results

An overview of the initial phosphate coatings and the generated glaze layers after dry uni-directional sliding are shown for zinc phosphate in Figure D.4 and manganese phosphate in Figure D.5 using backscatter electron imaging (BSE). The results on an untouched section of the phosphated discs are shown in Figure D.4a and Figure D.5a (Note the difference in magnification when comparing). The crystal surface of zinc phosphate (Figure D.4a) shows a rough texture coming from the needle shape which is typical for hopeite crystals [30]. The needle can grow well over 50 µm in length with a width of 10 µm. The crystal surface of manganese phosphate (Figure D.5a) is smooth, its shape is jagged typical for hureaulite crystals [31]. An individual crystallite is approximately 2 µm in size in all directions.

Upon comparison with the untouched phosphate (Figure D.4a, Figure D.5a) the formation of a glaze layer can be clearly observed in Figure D.4b and Figure D.5b. The glaze layer forms because of the crushing and compaction of the crystals in the sliding contact as observed in earlier investigations [3–5].

Zooming in on the center of the glaze layers in Figure D.4c and Figure D.5c it is clear that the zinc phosphate glaze layer has a different character compared to manganese phosphate. This is attributed to the difference in precursor material (hopeite vs hureaulite crystals). Flattened needles can be observed in zinc phosphate with the valleys next to them filled with crushed debris. Manganese phosphate shows a much smoother surface mainly because it starts with much smaller crystals which are all crushed and compacted into a smooth layer. This is in line with our earlier work [4].

These glaze layers and their counterparts formed under lubricated conditions were subsequently indented using a Berkovich indenter to investigate the differences in surface hardness.

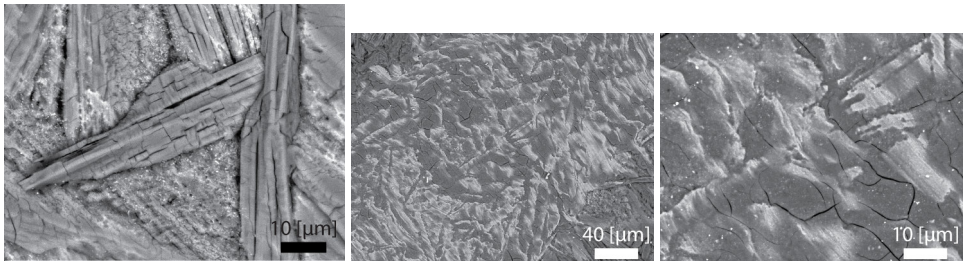

(a) (b) (c)

Figure D.4.: SEM BSE (20 kV) images of the initial crystalline zinc phosphate coating in Figure D.4a and the resulting glaze layer at two levels of magnification in Figure D.4b and Figure D.4c respectively.

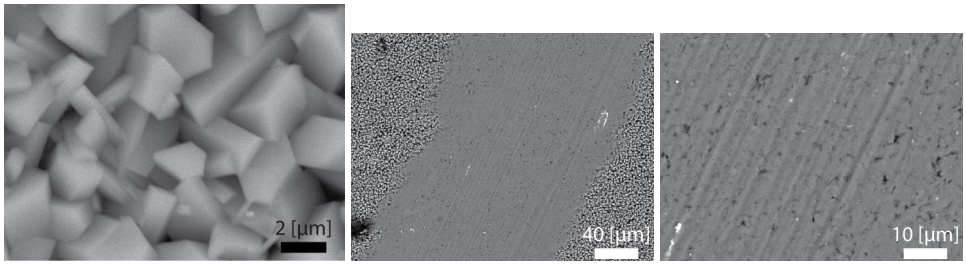

(a) (b) (c)

Figure D.5.: SEM BSE (20 kV) images of the initial crystalline manganese phosphate coating in Figure D.5a and the resulting glaze layer at two levels of magnification in Figure D.5b and Figure D.5c respectively.

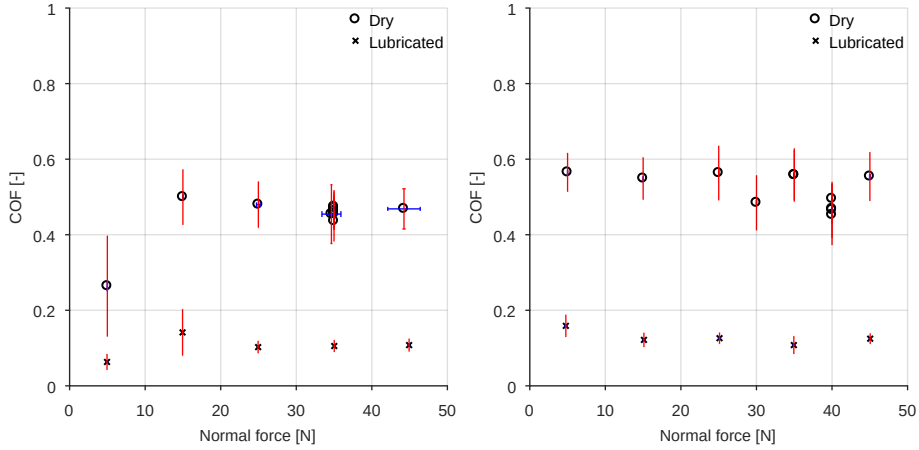

(a) ZP (b) MP

Figure D.6.: Coefficient of friction as function of normal load and lubrication condition with 3 mm ball. Figure D.6a shows the results for zinc phosphate and Figure D.6b for manganese phosphate. Error bars correspond to 1 standard deviation of COF.

D.3.1. Coefficient of friction

The coefficient of friction (COF) for both conditions and coatings are reported in Figure D.6. This shows a substantial difference between dry and lubricated conditions for both ZP (Figure D.6a) and MP (Figure D.6b). This will become important for the discussion later in this paper. Comparing dry versus lubricated, the friction is a factor 5-6 lower and more stable in lubricated conditions judge by the error bars. Comparing the coating types, ZP has slightly lower friction in dry conditions compared to MP. Both coatings manifest a constant COF over a large normal force range.

D.3.2. Crystal structure of pin-on-disc generated glaze layer

X-ray diffraction data were collected on the wear track using focusing optics, resulting in elliptical irradiated area of 0.14 × 0.55 mm. The glaze layers were generated in the pin-on-disc experiments. A reference measurement was made on a section of untouched MP using the same optics and diffraction geometry.

The representative resulting diffractograms are compared in Figure D.7. The reflections from the supporting metal are stronger in the pattern of the wear track. This is consistent with the expectation that removal of hureaulite will result in a reduced absorption of X-radiation in the beam path and therefore in a stronger signal. Both patterns show additional reflections that can all be attributed to hurealite. Since the irradiated area is not sharply delimited, the hureaulite signals could originate from the untouched MP material at the very edge of the wear track. Although the relative intensities differ, a detailed investigation shows that both patterns

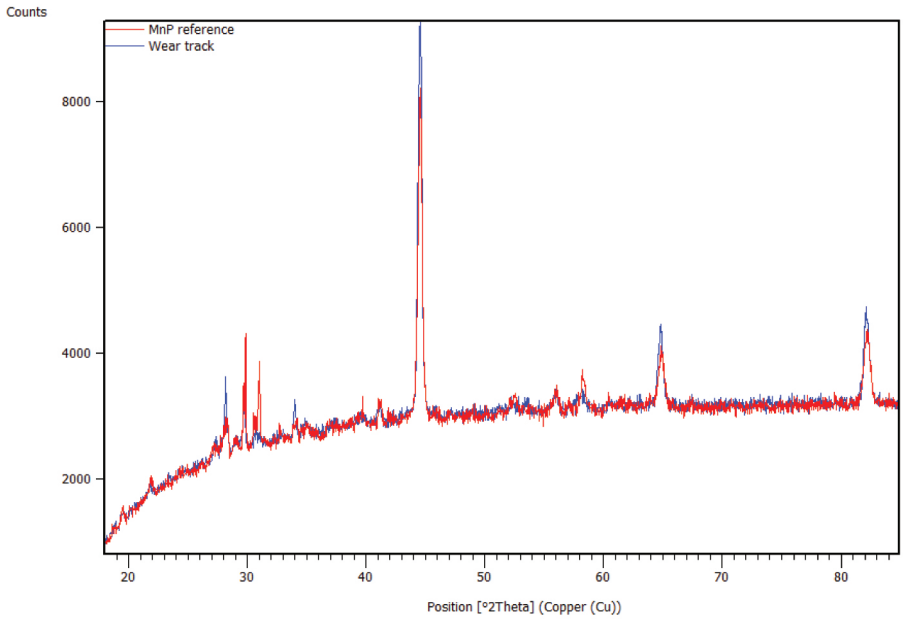

Figure D.7.: X-ray diffractogram of the as received manganese phosphate compared to crushed and compacted manganese phosphate in the glaze layer.

contain the same set of reflections. There is therefore no indication of the presence of a new crystalline phase in the wear track.

D.3.3. Hardness of the glaze layer

The load carrying capacity of the glaze layer generated in the ring-on-ring test [3] was investigated using nano-indentation and compared to the results of [4]. The results are shown in Figure D.8 and numbered according to specimen ID presented in Table D.3. The indentations were placed along the centreline of the glaze layer at multiple normal loads as indicated by the legend. The indentation hardness of the glaze layer for the previous work are shown in Figure D.8b designated as "Dry". The results of the lubricated pin-on-disc test of the present work are designated with "O933". This is compared to the lubricated test in the ring-on-ring in Figure D.8a. The glaze layer exhibits a substantial lower hardness compared to the dry sliding experiments of [4]. The indentation hardness averages 1-2 GPa when formed with zinc phosphate and 1-1.5 GPa when formed with manganese phosphate. The lower hardness after lubricated sliding is reproduced in the pin-on-disc test with Ondina 933 in Figure D.8b. This indicates that lubrication negatively affects the hardness of the formed glaze layers.

Normalizing the hardness of the dry sliding experiments with the lubricated experiments of Figure D.8b results in Figure D.9. This reveals hardness differences of up to 4.5 times between the two conditions.

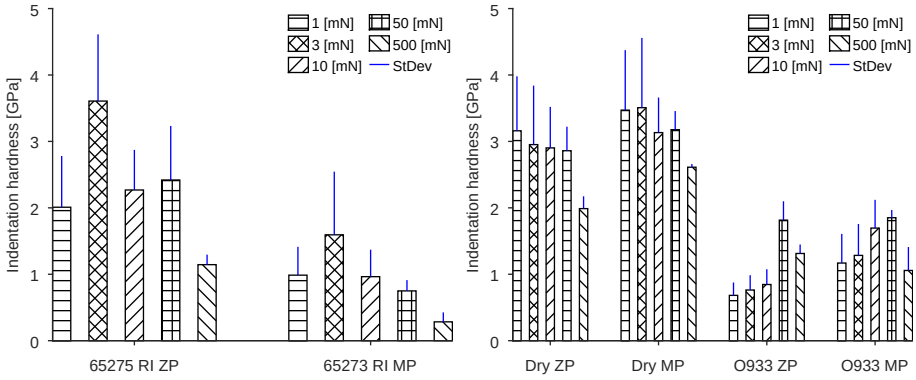

(a) Ring-on-ring (b) Pin-on-disc

Figure D.8.: Nano-indentation results using a Berkovich indenter at increasing normal loads. Figure D.8b shows the results for the glaze layer hardness after dry sliding [4] and lubricated sliding with Ondina 933. Figure D.8a shows the results after lubricated sliding in the ring-on-ring tests [3].

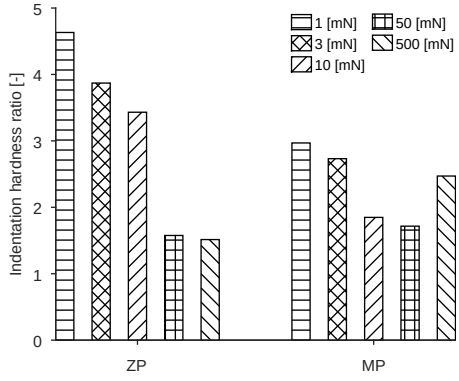

Figure D.9.: Ratio of indentation hardness between dry and lubricated sliding taken from Figure D.8b.

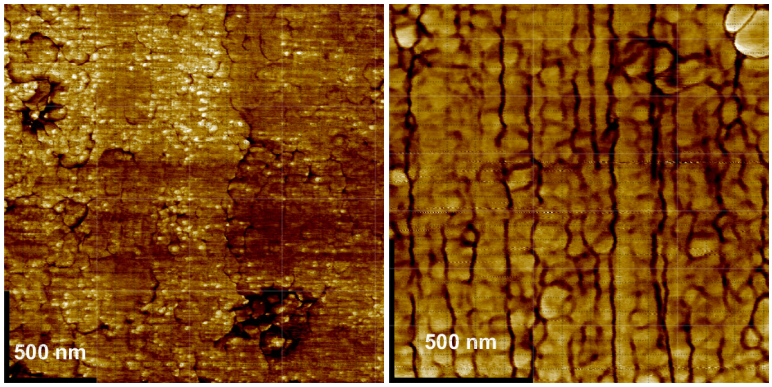

(a) ZP Dry (b) ZP Lubricated

Figure D.10.: AFM phase images of the zinc phosphate glaze layer at high magnification. Figure D.10a shows the result after dry sliding and Figure D.10b after lubricated sliding.

In the following, the surface topology and structure of the glaze layers is investigated with AFM. The aim was to get a better understanding of the structure of this glaze layer and the reason for the observed hardness ratios between lubricated and dry sliding.

D.3.4. AFM of glaze layer

The AFM was performed in tapping mode with the cantilever intermittently contacting the surface of the glaze layer. The result is a height map and information about the change in amplitude and phase of the cantilever when interacting with the surface. The phase is sensitive for changes in slope of the substrate and effective in detecting edges [32]. Therefore the phase images are presented here as a means to detect particles and from that determine particle size. No differences were observed between the uni-directional and reciprocating tests. Representative results are shown here for brevity.

Figure D.10 shows the phase images of the zinc phosphate glaze layer formed in dry (Figure D.10a) and lubricated (Figure D.10b) sliding conditions. Judging by the AFM results the glaze layer consists of tightly packed nano-particles. A clear difference in size can be observed between the dry and lubricated sliding conditions. The dry condition shows much smaller particles compared to lubricated.

The same observations were made for the manganese phosphate glaze layers shown in Figure D.11. Also here a distinct difference in particle size could be observed. Again, the dry condition in Figure D.11a shows a smaller particle size than the lubricated condition in Figure D.11b.

Comparing the zinc and manganese glaze layers it is clear that the zinc phosphate layer consists of slightly larger particles after dry sliding and slightly smaller particles after lubricated sliding conditions. Using the method described in Section D.2.8 the particles were identified and their average size subsequently measured. This could only be reliably done for the lubricated

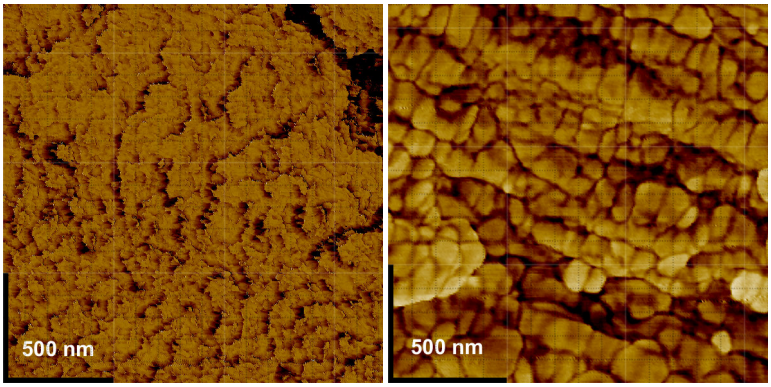

(a) MP Dry (b) MP Lubricated

Figure D.11.: AFM phase images of the manganese phosphate glaze layer at high magnification. Figure D.11a shows the result after dry sliding and Figure D.11b after lubricated sliding.

condition. The average particle diameter after lubricated sliding for zinc phosphate was 100 nm and for manganese phosphate 92 nm. In the following an attempt is made to explain why this is important and how it gives rise to differences in glaze layer hardness.

D.4. Discussion

From the results of AFM it is clear that the glaze layers comprise of phosphate crystals that are crushed into particles. The particle size is modified by the presence of the lubricant which could explain the difference in the measured surface hardness by nano indentation. In this section the origin of the difference in hardness between the dry and lubricated condition will be discussed using a model for particle deagglomeration.

The agglomerate is defined by a hierarchy of scales. For this, inspiration is drawn from the model of [22]. Here the primary particles, denoted by subscript 0, are representing the phosphate unit cells that make up the primary aggregates denoted by subscript a. These bonds are hard to break and are assumed to require considerable mechanical force which will determine the minimum size of the primary aggregates.

In this investigation the size and compaction of the primary aggregates are thought to determine the mechanical properties of the glaze layer. Furthermore, as shown (Section D.3.4) the presence of a lubricant can modify the glaze layer by generating different size primary aggregates. In the following, a model is discussed which is based on inter particle interactions to explain how this can give rise to differences in glaze layer hardness. The model is based on the work of [12, 13, 20].

Before presenting the model, it is good to list the underlying assumptions.

1. Primary particles and primary aggregates are spherical and have equal radius [16, 20].

2. The aggregates are in contact, hence the surface-to-surface distance is 4 Å [16, 20].
3. The particles are densely random packed [33].
4. The agglomerate is stressed as a whole and also fails as a whole. This rules out cracking. Note: this overestimates the strength of the agglomerate [34].
5. Aggregates are strongly compacted and thus in full contact, therefore the electrostatic force is zero [16, 22].
6. Another consequence of the full contact situation is the absence of capillary effects [15, 16].

The inter particle strength can be seen as their tendency to stick together and is governed by the amount of atoms or molecules contained in the particle [16]. This results in van der Waals forces, F, and electrostatic repulsion forces considered to be zero here. The sum of both gives the strength of the inter particle interaction. The van der Waals forces between primary particles are calculated using the result of [13] for two equally sized particles as

$$F = -\frac{AL_0}{48d^2}. \tag{D.1}$$

Where L_0 is taken here as the phosphate unit cell diameter, A is the effective Hamaker constant and d represents the surface to surface distance.

Assuming now that the agglomerate is stressed as a whole and fails by rupture, the tensile strength of the agglomerates can be defined as [20],

$$\sigma_{\mathrm{T}} = 1.1\frac{1-\bar{\epsilon_{\mathrm{a}}}}{\bar{\epsilon_{\mathrm{a}}}}\frac{F}{L_{\mathrm{a}}^2} \tag{D.2}$$

where $\bar{\epsilon_{\mathrm{a}}}$ is the average porosity of the agglomerates and L_{a} the diameter of the agglomerates.

Finally, a measure of the porosity as function of particle size needs to be introduced to conclude the computation of the agglomerate tensile strength. This is done using the result of [33],

$$\bar{\epsilon_{\mathrm{a}}} = 1 - \left(0.394 + 0.606\exp\left(-0.4L_{\mathrm{a}}^{0.468}\right)\right). \tag{D.3}$$

However, the average porosity is approaching 0 when the particle size is <100 nm [33]. Hence the influence will be minimum.

Combining equations (D.1), (D.2), and (D.3) the tensile strength of agglomerates can be determined. This shows that the tensile strength is linearly dependent on the environment (A) and inversely quadratically dependent on the particle size (L_{a}) for particles <100 nm.

It is thus clear that because of the stronger inter particle interaction an agglomerate produced under dry conditions possesses a higher tensile strength compared to lubricated conditions. However, the most pronounced influence comes from the difference in agglomerate size as a result of the crushing of the phosphate crystals during sliding. This ties the lower observed hardness of Section D.3.3 together with the larger observed particle size for the lubricated experiments in Section D.3.4. This can also explain why zinc phosphate while consisting of the softer mineral hopeite [30] exhibits a hardness close to that of manganese phosphate which

consists of the harder hureaulite [31]. This difference is explained by the difference in particle size.

The glaze layers generated in lubricated conditions show considerable lower hardness compared to their counterparts generated in dry conditions. Even though the contact stress differed considerably between ring-on-ring and pin-on-disc, the lower hardness under lubricated conditions could be reproduced in pin-on-disc. This shows that the hardness is or has become contact stress independent. This behaviour is also observed in the pressing of tablets where the tensile strength starts to stabilize after a certain amount of compressive force [21, 35].

It was shown with AFM (Section D.3.4) that the difference between the glaze layers is the size of the agglomerated particles that constitute them. Clearly dry sliding produced the smallest particles. This is predominantly because of the stronger adhesion of the particles to the AISI52100 ball [36] and as a consequence a higher amount frictional energy available in the contact to break up the crystals. In short, the grinding was more effective compared to the lubricated condition.

Using considerations from inter particle interactions it was shown that the tensile strength is considerably lower for the lubricated condition as grinding is more effective in the dry conditions. The lubricated condition causes weaker inter particle bonding and thus lower adhesion to the ball. This leads to lower frictional energy and less effective grinding of the crystals. Which results in larger particles which gives rise to weaker inter particle bonds and thus a lower glaze layer hardness.

D.5. Conclusions

Previous work showed that a hard glaze layer is formed under dry sliding conditions in zinc and manganese phosphate coatings by crushing and compacting phosphate debris particles. The formation of glaze layers on phosphated surfaces was investigated in this paper by generating them in a ring-on-ring set-up and on the smaller scale in a pin-on-disc set-up. The generated glaze layers were investigated using SEM, nano-indentation, XRD and AFM. To explain the observations an inter particle interaction model was used. The results indicate the following:

- The mechanism behind glaze layer formation on phosphate conversion coatings was investigated for the first time with SEM, nanoindentation, XRD and AFM.
- A higher indentation hardness is obtained for glaze layers formed under dry sliding conditions compared to lubricated conditions.
- The hardness difference is explained by a difference in the particle size that make up the glaze layer. A hard glaze layer is obtained with small particles.
- The particle size is related to the COF and, consequently, the effectiveness of grinding in the sliding contact.

- Based on the consideration of the forces acting at the particle scale, the hardness is predominantly governed by particle size and in addition the resulting particle interactions by Van der Waals forces modified by the presence of water (dry sliding) and oil (lubricated sliding).
- The mechanisms were successfully reproduced in a pin-on-disc test.
- The higher glaze layer hardness in dry sliding is thus because of a higher COF leading to smaller debris particles giving rise to stronger inter particle interactions.

The application of this could be to improve the wear resistance of phosphate conversion coatings by applying a dry sliding pre-burnishing step. The hard glaze layer can subsequently reduce the coating wear in lubricated sliding.

Acknowledgements

The authors are grateful to Shell Global Solutions International BV for permission to publish this work. We thank dr. ir. Rob Bosman for the discussions on the AFM results, dr. Huub Kooijman for the discussions on the glaze layer structure, and dr. Frank Hollmann & Frank Schneider of Chemetall GmbH for the discussions on phosphate conversion coatings and preparation of the phosphated specimens.

References

[1] Bommer, P. *A Primer of Oilwell Drilling*. 7th. Austin: The University of Texas at Austin, 2008.

[2] Azhaarudeen, S., Faruck, A. A. M. and Nevosad, A. 'Tribological behaviour and wear mechanisms of manganese phosphate coatings under dry reciprocating sliding contact conditions'. *Tribology International* 122.February (June 2018), pp. 189–199.

[3] Ernens, D., Riet, E. J. van, Rooij, M. B. de, Pasaribu, H. R., Haaften, W. M. van and Schipper, D. J. 'The Role of Phosphate-Conversion Coatings in the Makeup and Sealing Ability of Casing Connections'. *SPE Drilling & Completion* (October 2018).

[4] Ernens, D., Rooij, M. B. de, Pasaribu, H. R., Riet, E. J. van, Haaften, W. M. van and Schipper, D. J. 'Mechanical characterization and single asperity scratch behaviour of dry zinc and manganese phosphate coatings'. *Tribology International* 118 (February 2018), pp. 474–483.

[5] Nevosad, A., Azhaarudeen, S., Doerr, N., Zacharias, H., Klarner, J. and Badisch, E. 'Initial Damage Mechanism and Running-In Behaviour of Phosphate Conversion Coatings'. *Key Engineering Materials* 721.December (December 2016), pp. 356–361.

[6] Ertas, A. 'Experimental Investigation of Galling Resistance in OCTG Connections'. *Journal of Manufacturing Science and Engineering* 114.1 (February 1992), p. 100.

[7] Le, H. R., Stewart, F. and Williams, J. A. 'A Simplified Model of Surface Burnishing and Friction in Repeated Make-Up Process of Premium Tubular Connections'. *Tribology Letters* 59.2 (August 2015), p. 35.

[8] Pérez-Ràfols, F., Larsson, R. and Almqvist, A. 'Modelling of leakage on metal-to-metal seals'. *Tribology International* 94 (February 2016), pp. 421–427.

[9] Pérez-Ràfols, F., Larsson, R., Lundström, S., Wall, P. and Almqvist, A. 'A stochastic two-scale model for pressure-driven flow between rough surfaces'. *Proceedings of the Royal Society A: Mathematical, Physical and Engineering Science* 472.2190 (June 2016).

[10] Pérez-Ràfols, F., Larsson, R., Riet, E. J. van and Almqvist, A. 'On the flow through plastically deformed surfaces under unloading: A spectral approach'. *Proceedings of the Institution of Mechanical Engineers, Part C: Journal of Mechanical Engineering Science* 232.5 (March 2018), pp. 908–918.

[11] Rausch, W. *The phosphating of metals*. Metals Park, Ohio, USA; Teddington, Middlesex, England: ASM International; Finishing Publications Ltd., 1990, p. 406.

[12] Krupp, H. 'Particle adhesion theory and experiment'. *Advances in Colloid and Interface Science* 1.2 (May 1967), pp. 111–239.

[13] Hamaker, H. 'The London—van der Waals attraction between spherical particles'. *Physica* 4.10 (October 1937), pp. 1058–1072.

[14] Israelachvili, J. N. *Intermolecular and surface forces*. 3rd. Academic Press, 2011, p. 704.

[15] Pakarinen, O. H., Foster, A. S., Paajanen, M., Kalinainen, T., Katainen, J., Makkonen, I., Lahtinen, J. and Nieminen, R. M. 'Towards an accurate description of the capillary force in nanoparticle-surface interactions'. *Modelling and Simulation in Materials Science and Engineering* 13.7 (October 2005), pp. 1175–1186.

[16] Israelachvili, J. *Intermolecular and Surface Forces*. Elsevier, 2011.

[17] Hartley, P., Parfitt, G. and Pollack, L. 'The role of the van der Waals force in the agglomeration of powders containing submicron particles'. *Powder Technology* 42.1 (April 1985), pp. 35–46.

[18] Coury, J. and Aguiar, M. 'Rupture of dry agglomerates'. *Powder Technology* 85.1 (October 1995), pp. 37–43.

[19] Cahoon, J. R., Broughton, W. H. and Kutzak, A. R. 'The determination of yield strength from hardness measurements'. *Metallurgical Transactions* 2.7 (1971), pp. 1979–1983.

[20] Rumpf, H. 'Die Wissenschaft des Agglomerierens'. *Chemie Ingenieur Technik - CIT* 46.1 (January 1974), pp. 1–11.

[21] Adolfsson, Å., Gustafsson, C. and Nyström, C. 'Use of Tablet Tensile Strength Adjusted for Surface Area and Mean Interparticulate Distance to Evaluate Dominating Bonding Mechanisms'. *Drug Development and Industrial Pharmacy* 25.6 (January 1999), pp. 753–764.

[22] Bałdyga, J., Makowski, Ł., Orciuch, W., Sauter, C. and Schuchmann, H. P. 'Deagglomeration processes in high-shear devices'. *Chemical Engineering Research and Design* 86.12 (December 2008), pp. 1369–1381.

[23] Rwei, S. P., Manas-Zloczower, I. and Feke, D. L. 'Observation of carbon black agglomerate dispersion in simple shear flows'. *Polymer Engineering and Science* 30.12 (June 1990), pp. 701–706.

[24] Kwade, A. and Schwedes, J. 'Breaking characteristics of different materials and their effect on stress intensity and stress number in stirred media mills'. *Powder Technology* 122.2-3 (January 2002), pp. 109–121.

[25] Bika, D. G., Gentzler, M. and Michaels, J. N. 'Mechanical properties of agglomerates'. *Powder Technology* 117.1-2 (June 2001), pp. 98–112.

[26] API. *Recommended Practice on Thread Compounds for Casing, Tubing, and Line Pipe*. Tech. rep. Washington: American Petroleum Institute, 2015.

[27] Bosman, R. and Rooij, M. B. de. 'Transient Thermal Effects and Heat Partition in Sliding Contacts'. *Journal of Tribology* 132.2 (2010), p. 021401.

[28] Almqvist, A., Sahlin, F., Larsson, R. and Glavatskih, S. 'On the dry elasto-plastic contact of nominally flat surfaces'. *Tribology International* 40.4 (April 2007), pp. 574–579.

[29] Oliver, W. and Pharr, G. 'An improved technique for determining hardness and elastic modulus using load and displacement sensing indentation experiments'. *Journal of Materials Research* 7.06 (June 1992), pp. 1564–1583.

[30] Hill, R. and Jones, J. 'The crystal structure of hopeite'. *American Mineralogist* 61 (1976), pp. 987–995.

[31] Moore, P. B. and Araki, T. 'Hureaulite: lts Atomic Arrangement'. *American Mineralogist* 58.3-4 (1973), pp. 302–307.

[32] Magonov, S., Elings, V. and Whangbo, M.-H. 'Phase imaging and stiffness in tapping-mode atomic force microscopy'. *Surface Science* 375.2-3 (April 1997), pp. L385–L391.

[33] Yu, A., Feng, C., Zou, R. and Yang, R. 'On the relationship between porosity and interparticle forces'. *Powder Technology* 130.1-3 (February 2003), pp. 70–76.

[34] Hobbel, E. F. 'Cohesion and interparticle forces'. PhD thesis. Delft University of Technology, 1988.

[35] Pitt, K. G. and Heasley, M. G. 'Determination of the tensile strength of elongated tablets'. *Powder Technology* 238 (April 2013), pp. 169–175.

[36] Ernens, D., Langedijk, G., Smit, P., Rooij, M. B. de, Pasaribu, H. R. and Schipper, D. J. 'Characterization of the Adsorption Mechanism of Manganese Phosphate Conversion Coating Derived Tribofilms'. *Tribology Letters* 66.4 (December 2018), p. 131.

This page has been intentionally left blank.

E. The mechanisms leading to galling initiation during make-up of casing connections

D. Ernens[a,b], M.B. de Rooij[a], H.R. Pasaribu [b], D.J. Schipper[a]

[a]*Laboratory for Surface Technology and Tribology, Department of Engineering Technology, University of Twente, P.O. Box 217, 7500 AE Enschede, The Netherlands*

[b]*Shell Global Solutions International BV, Innovation, Research & Development, Wells R & D, Kessler Park 1, 2288 GS Rijswijk, The Netherlands*

Abstract Assembly of casing connection in the oil and gas industry is performed with grease or thread compound. An often occurring failure mechanism during assembly is galling. This leads to costs associated with lost productivity and when undetected compromises the metal-to-metal sealing performance in the well. It is known from literature that galling initiates at relative low contact stress with thread compound in uncoated oil and gas steel grades. However, the mechanisms leading to galling have not been described. This paper presents a study that explains the underlying mechanisms with the aim to design environmentally friendly alternatives for the currently lead containing standard compound American Petroleum Institute (API) modfied. It was found with face seal, interference seal and pin-on-disc experiments that galling initiates because of squeezing out of the lubricant and its tribofilm. The initiation is exacerbated by the combination of the typically turned surface topograhpy, sliding parallel to the lay of the topography, the inert environment created by the compound and the relatively weak interaction of the additives with the substrate. Together this leads to the thread compound only adding 60 mm of sliding length till failure compared to a plain mineral oil.

Article in preparation for submission to a journal.

E.1. Introduction

The assembly of (casing) connections in the oil and gas industry is performed with grease, also called thread compound. The base greases are typically made with a mineral base oil and metal soaps or metal complex soaps [1]. Additives are subsequently added in the form of metallic, mineral or metallic oxide based particles. Thread compounds are thus relatively simple grease formulations. What is special about them is the high solids content of up to 50-60 wt% [2]. TThe function of the grease and the added particles is said to be threefold: it provides repeatable friction for a predictable assembly torque response [3], provide surface protection [4] and aids in the seal ability of the system by blocking or bridging potential leak channels [5–7].

Cold welding and subsequent material transfer also known as galling is an often occurring failure mechanism of the connections in the assembly phase. Such failures lead to delays in the manufacturing of the well and therefore additional costs. It is further of great interest because the initial seal ability of the metal-to-metal seal is determined here [5]. It is known from previous studies that even at mild loads galling initiation happened on uncoated surfaces lubricated with a thread compound [4, 5, 8]. The mechanisms, however, are poorly understood and are important as design input for the development of environmentally friendly thread compounds. The galling initiation mechanisms are investigated in this paper.

The standard thread compound is API modified [2]. The compound was formulated over 70 years ago [9] and is still the most widely used thread compound in the oil and gas industry [2]. It contains a base grease made with a heavy mineral oil and a metal soap thickener combined with graphite, lead, zinc and copper. Several explanations for its success in protecting the surface during assembly and sealing ability are given. The work of [8] attributes it mainly to the lead particles that form a protective film. While zinc and copper are said to be added to control the friction coefficient. In addition, the copper particles are the largest and probably aid in thread sealing [9, 10]. Finally the graphite is not of lubrication grade and therefore acts mainly as filler [8]. This, together with the broad particle size distributions of the metallic additives [9], should also help in the sealing ability [6, 7]. The work of [4] found that this protection is limited to the rather low contact stress of 303 MPa in typical oil industry steel grades [8]. Nowadays a contact stress of up to 2000 MPa is common. This is probably because API modified was originally designed as a thread sealing compound [9]. However, the mechanism behind the failures, also with other compounds [5], has not been explained. This needs to be understood to replace the lead containing API modified for an environmentally friendly thread compound.

In deep drawing, galling is the main cause for tool failure. In lubricated conditions these failures where related to the desorption of the lubricant [11] by local flash temperatures [12] as postulated by [13] and shown by [14, 15]. The work of [16–18] investigates the non-lubricated condition and relates it to increased adhesion as a consequence of local flash temperatures. However, forming of plate materials typically happens at linear sliding velocities in the order of 0.1-1 $\mathrm{m\,s^{-1}}$ while casing connections are assembled at a velocity of 0.01 $\mathrm{m\,s^{-1}}$.

In order to understand the mechanisms a program was set up to investigate the role of the components present in API modified. In addition, a hypothesis revolving around the aforementioned local flash temperatures leading to desorption of the lubricant was tested as possible galling initiation mechanism [14, 15]. To study the mechanisms of API modified, the full formulation

Table E.1.: Properties of mother material used for manufacturing the SSMUR specimens. Properties were obtained according to ISO6892-1:2009.

Pipe ID	Yield stress Rp0.2 [MPa]	Ultimate tensile strength Rm [MPa]	Uniform plastic elongation Ag [%]	Fracture elongation A5 [%]	Hard-ness HV10
51876	861	947	6.3	18.8	306

thread compound and variations on this formulation with single particle compounds was studied to understand their effect on friction and wear.

The results of [4] were reproduced in the anvil-on-strip test in our earlier paper [5]. The focus in this paper is on the explanation of the mechanisms behind the failure using observations in our Shell Sealing Mock-Up Rig (SSMUR). A follow-up investigation was carried out with reciprocating tests in a pin-on-disc tribometer. Reciprocating tests were chosen to simulate the continuous contact in a casing connection. It also allows for (debris) particles to get caught in the contact. The influence of roughness was investigated by performing the same experiments on polished and ground discs. In addition, a comparison was made with anvil-on-strip and SSMUR. Real connections salvaged from the field were finally used to validate the scaled test findings.

E.2. Methods

Casing connections are assembled at rotational velocities of 2 - 5 RPM and thread pitches are in the order of 5 mm rev^{-1}. This results in circumferential and axial velocities in the order of 10 mm s^{-1} and 0.1 mm s^{-1} respectively. As such the pin progresses into the box with a velocity vector mainly pointed in the circumferential direction. It means further that the pin is always contacting on the same surface area while the box surface sees the pin sliding past in axial direction. The seal engages at the final moments of assembly giving a short sliding length of about 0.2-0.6 m in circumferential direction. In this short length a peak contact stress in the order of 1 GPa is build up by the increasing interference of the pin and box seal area. These conditions were emulated with the following experimental methods.

E.2.1. Materials

SSMUR specimens were manufactured from thick walled P110 tubing [19] using a lathe. The mechanical properties of the tubular material are given in Table E.1. To ensure repeatable surface topography for the test campaign, special attention was given to the metal-to-metal seal area. This was achieved by specifying the dimensions of the carbide cutting element, setting a fixed feed rate and depth of cut and using a new cutting element for each specimen.

Table E.2.: Overview composition and basic properties base greases.

Sample - #	1	2	3	4	5	6	7
Short hand	API mod	bg	bg Cu	bg Zn	bg Pb	bg Zn Cu	API mod no Pb
Base oil	Mineral oil						
Thickener	Aluminium complex						
Penetration	310 -330	265 - 285	343	356	408	383	300
Graphite	X	-	-	-	-	-	X
Copper	X	-	X	-	-	X	X
Zinc	X	-	-	X	-	X	X
Lead	X	-	-	-	X	-	-

Table E.3.: Overview particle properties in the general API modified formulation

Material	Compatibility Fe [20]	UTS MPa	Morphology	Smallest mesh size µm [2]
Lead	0.125	18	Sphere	<44
Zinc	0.5	$28 - 246$	Flake	<44
Copper	0.32	$210 - 360$	Flake	<44

E.2.2. Lubricants

API modified was used as the reference. The variations on the full formulation are given in Table E.2. These variations are created by adding the same weight percent of an additive as in the full formulation to the base grease. This resulted in a difference in consistency, however the same experimental results were obtained after balancing the formulation to come to the same consistency as the full product. For the discussion later in this paper the properties of the particles are listed in Table E.3. This includes the compatibility with iron according to the work of [20].

E.2.3. Shell Sealing Mock-up rig

The Shell Sealing Mock-up Rig (SSMUR) is an in-house build test set-up for research into running-in and metal-to-metal sealing of casing connections. Two specimen configurations are possible in this apparatus. A face seal configuration and an interference seal configuration. An overview is given in Figure E.1. Both will be explained hereafter. The performed tests are summarized in Table E.4.

The face seal set-up or ring-on-ring test [5] (Figure E.1a and Figure E.1c) provides circumferential line contact at equivalent contact stresses, sliding lengths and sliding velocities as they

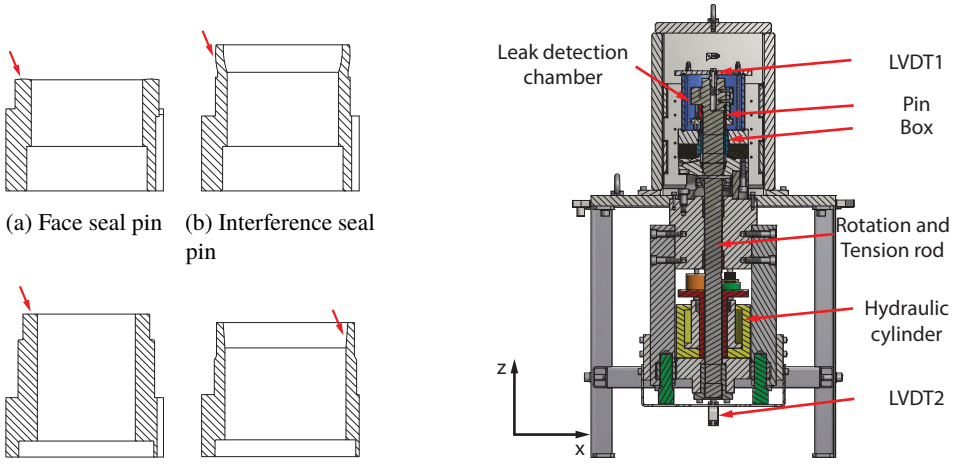

(a) Face seal pin (b) Interference seal pin (c) Face seal box (d) Interference seal box (e) Load frame

Figure E.1.: Figure E.1a shows a pin cross section and Figure E.1c shows a box cross section for the face seal specimens. Figure E.1b shows a pin cross section and Figure E.1d shows a box cross section for the interference seal specimens. The contact locations are indicated with an arrow. Figure E.1e shows the load frame that is used to execute the experiments on these specimens with the most important parts indicated.

occur in metal-to-metal seals. Sliding tests are performed with continuous contact equivalent to the assembly of a casing connector. After "assembly" a seal ability test can be performed.

The contact configuration is flat against a radius of R = 80 mm line contact. The contact line diameter is approximately 70 mm and the contact width approximately 1 mm. Sliding was performed with a contact intensity (CI) of 136 N mm^{-1} resulting in a maximum Hertzian contact stress, p_{max}, of 0.25 GPa. The sliding velocity is 24 mm s^{-1}. The goal was to reach a total sliding length is 1 revolution or 220 mm. The specimens were rotated stepwise with the following sequence 2.5-5-10-20-40-70.4-70.4 mm. In between steps the specimen was cleaned, surface replicas (Struers RepliSet-T3) were taken, and fresh lubricant was applied for the next sliding step. Important for later reference is that the sliding direction was parallel (face seal) or predominately parallel (interference seal) respectively to the turned roughness.

The interference seal set-up (Figure E.1b and Figure E.1d) provides radial line contact at equivalent contact stresses, sliding lengths and sliding velocities as they occur in metal-to-metal seals. The specimen can be assembled-disassembled using a position controlled process by mounting it on a threaded rod which screws into a nut. The screw thread has a pitch of 3 mm rev^{-1}.

The contact configuration is a round-off of 39 mm against a conical flat with a taper angle of 4 degrees. Assembly is performed over approximately 0.5 revolution resulting in a monotonically increasing contact stress. At the maximum interference position a maximum contact stress of 700 MPa is generated. The sliding velocity is 24 mm s^{-1}. The aim was to reach a

Table E.4.: Overview of the experiments performed with the face and interference seal set-up.

Set #	Box	Coating	Pin	Coating	Thread compound	Average COF (-)	CI make up ($N\,mm^{-1}$)	Sliding length (mm)
Face seal								
FG01[a]	65282	AsM	65248	AsM	API mod	0.08	136	220
FG02[b]	65300	AsM	65298[b]	AsM	O933	0.2	136	37.5
FG03[c]	65270	AsM	65258	AsM	O933	0.23	136	20
Interference seal								
IG01	64726	AsM	64715	AsM	API mod	0.15	0-190	116

a Galling observed in friction data after 77.5 mm.
b Galling observed in friction data after 20 mm.
c Rotated in one step to reported sliding length, small galling spot observed which is depicted in Figure E.6.

circumferential sliding length of approximately 1100 mm on the pin and approximately 363 mm on the box.

E.2.4. Pin-on-disc

The pin-on-disc experiments were performed with a Bruker UMT-3. The UMT-3 is a modular universal mechanical tester capable of applying a normal load, F_N, of up to 1000 N. The load range and measurement accuracy are determined by the installed load cell. In this case a six degrees of freedom load cell (TFH-50) is installed. The reciprocating tests are performed at a p_{max} of 1 GPa by applying 10 N normal load. The contact spot diameter is approximately 140 µm at this stress. The imposed reciprocating stroke length is 50 µm or 500 µm (will be indicated in the text) at a frequency of 0.5 Hz or linear velocity, v, 0.5 $mm\,s^{-1}$. With 1000 cycles the equivalent sliding length is 100 µm or 1000 mm respectively.

E.2.5. Analyses

The resulting specimens were investigated with a Keyence VHX5000 digital light microscope, White Light Interferometry (WLI, Bruker NP-FLEX), Scanning Electron Microscopy (SEM, Tescan Vega 3, Jeol JSM-7001F SHL) combined with Energy-dispersive X-ray spectroscopy (EDX), SEM on cross sections prepared with Focused Ion Beam (FIB, SII NanoTechnology Inc. SMI3000TB) and Broad Ion Beam (BIB, Jeol IB-19510CP).

E.3. Results

E.3.1. Galling investigation API modified

The results of [4] were first reproduced in the SSMUR with both specimen configurations and API modified as the lubricant. Galling occurred early in the test, however, this was only observed when opening the specimen after a full revolution. The precise moment of onset was determined after post processing the torque signal. Therefore, the result shown in Figure E.2 is after a full revolution of sliding in CW-direction yielding substantial surface damage around the full circumference. Shown are the pin after cleaning in Figure E.2a and the box specimen still mounted in the machine before cleaning in Figure E.2b. Based on the torque signal, galling initiated after 77.5 mm cumulative sliding length (which is 33% of the circumference). This is in agreement with the extend of the surface damage which covers about 66% of the surface. Already at this macroscopic scale, lumps of (transferred) material could clearly be observed.

A tribofilm was formed on both pin and box between BA-AC. If a tribofilm was formed along the full circumference is hard to say, however, galling initiation could also be observed in areas with a tribofilm. Thus the tribofilm was not very effective at preventing metal-to-metal contact. The reason for galling thus seems to be removal of the lubricant or its derived tribofilm and subsequent cold welding of asperities leading to lump growth with galling as the outcome. Hence, because of the stepwise assembly process (Section E.2.3), it could be said that >40 mm of undisturbed sliding is enough for removal of the films. In can indeed be observed that the large lump in Figure E.2b was responsible for the severe damage in Figure E.2a.

Figure E.2d shows a detailed overview for the face seal specimen. Severe plastic deformation was observed on both surfaces and clear indications of material transfer were present as lumps on either side of the system. The EDX analysis on this part of the surface did not indicate any presence of the thread compound. However, elsewhere on the surface a tribofilm was found (Figure E.2e) which consisted of the constituents of the thread compound according to SEM/EDX summarized in Table E.5. To get better insight in the adsorption and structure of the tribofilm a focused ion beam cross section of the film was made in Figure E.2f. The tribofilm thickness was measured to be 1.5 µm. SEM/EDX mapping in Figure E.3 indicated also here that the tribofilm consisted of the constituents of the thread compounds. It can also be observed that the constituents are present as individual particles in the tribofilm indicating minimal smearing or churning of the components.

A follow up investigation was performed using the interference seal set-up. The hypothesis was that the combination of circumferential sliding with axial sliding would allow replenishment of the lubricant in the contact. Figure E.2c shows the results after 116 mm cumulative sliding length obtained in two steps of 58 mm. The results were similar to Figure E.2a, severe galling was observed with large lumps growing and damaging the counter surface. According to the torque signal galling was initiated after approximately 87 mm which is similar to the face seal result. The lump damaging the surface can be clearly seen in the center of Figure E.2c. The scratch in axial direction is because of pulling the pin out of the box after the assembly experiment. This indicates that the lump had a substantial height and thus the extend of material transfer.

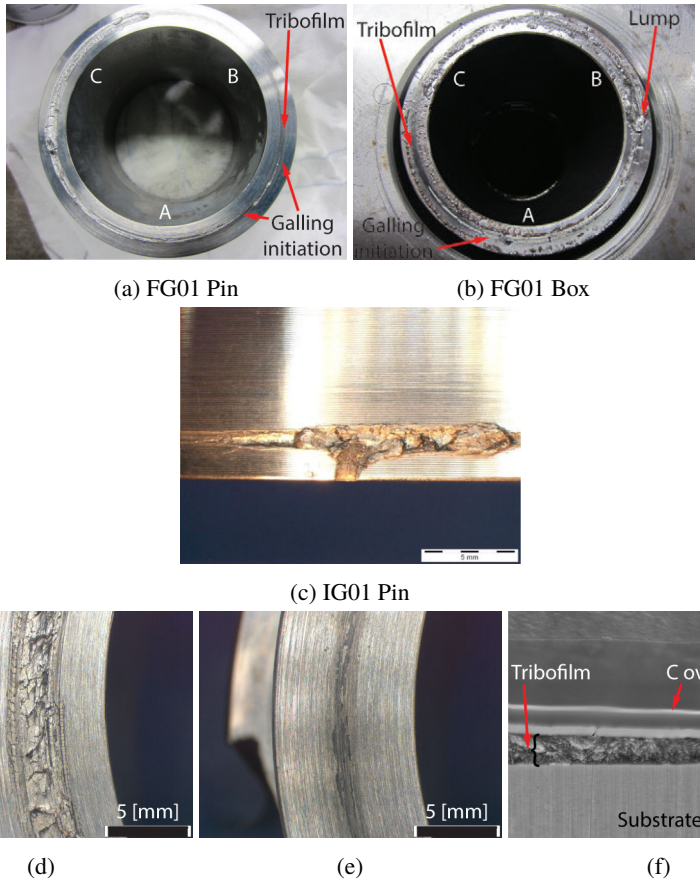

(a) FG01 Pin (b) FG01 Box

(c) IG01 Pin

(d) (e) (f)

Figure E.2.: Surface damage after make-up sliding with API modified for set FG01. Letters indicate orientation of specimen to match with the counter surface. Hence when in contact the pin and box are paired as A-A, B-C and C-B (pin-box). Figure E.2a shows the pin surface after cleaning and Figure E.2b the box surface before cleaning. Figure E.2c image of the contact area of interference seal specimen IG01 that failed during make-up sliding with API modified because of galling. The row below shows a detailed investigation with LM and SEM/FIB. Figure E.2d shows a macroscopic view of the galled area. Figure E.2e shows a tribofilm on another part of the same surface. SEM/EDX was also captured of this area and is presented in Table E.5. Figure E.2f shows the FIB cross sectioning result imaged by secondary electrons at 20 kV on the tribofilm shown from the top in Figure E.2e. The EDX mapping results can be found in Figure E.3.

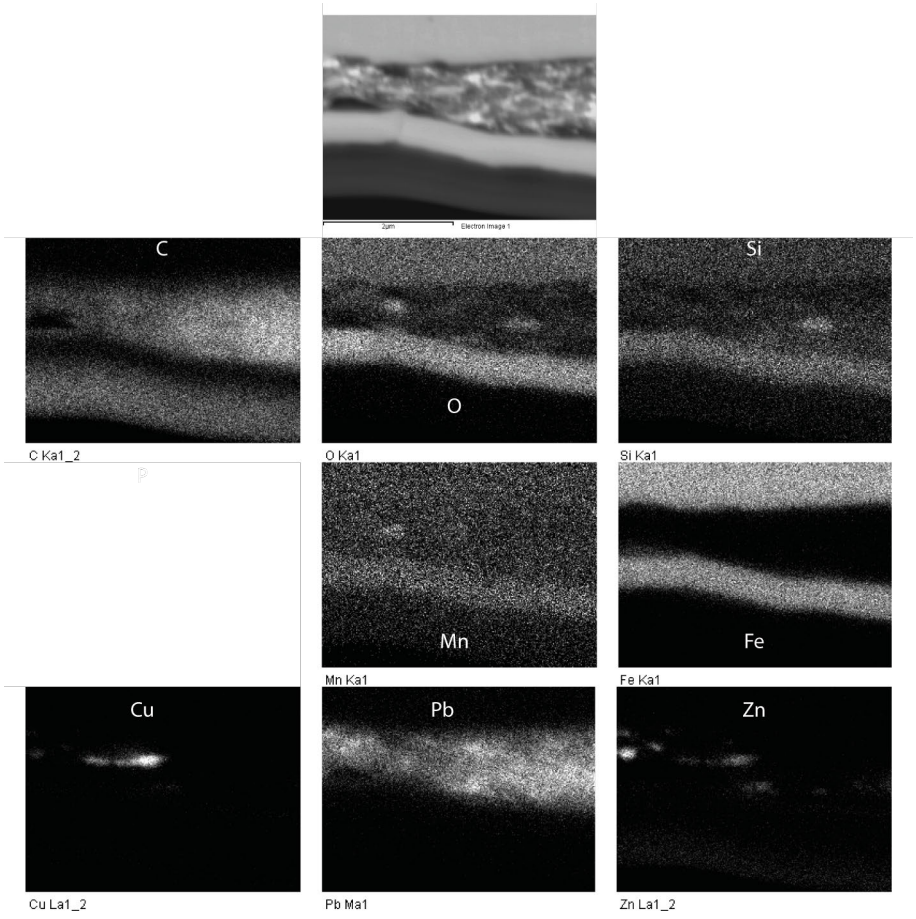

Figure E.3.: Backscatter electron image and EDX mapping at 20 kV corresponding to the secondary electron image of Figure E.2f.

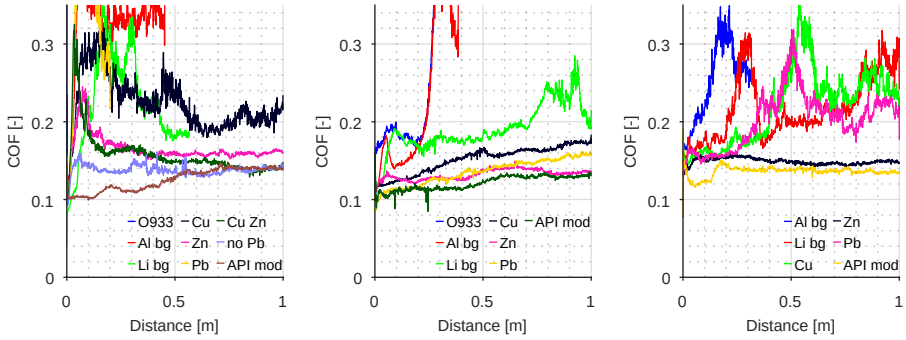

(a) Polished (b) Ground perpendicular (c) Ground parallel

Figure E.4.: Comparison of the COF versus cumulative sliding length for all tested base greases. The y-axis is truncated at COF=0.35 for clarity of the presentation. Figure E.4a shows the evolution of COF versus cumulative sliding length on a polished disc. Figure E.4b shows a comparison of the COF when sliding perpendicular to the roughness versus cumulative sliding length for all tested (base) greases. Figure E.4c shows a comparison of the COF when sliding parallel to the roughness versus cumulative sliding length for all tested (base) greases.

E.3.2. Pin-on-disc results

The results of the SSMUR were followed up by a detailed investigation into the role of the particles using a pin-on-disc set-up. The summary of the results in terms of the COF for the reciprocating tests are shown in Figure E.4. These results will be discussed hereafter in combination with microscopy of the wear scars. The results for polished discs are shown in Figure E.4a which are compared to Figure E.4b and Figure E.4c showing the COF for sliding perpendicular and parallel to the ground roughness respectively.

Upon comparing the data sets the following can be observed. In the parallel (Figure E.4c) case the results are similar to the polished disc (Figure E.4a). None of the base greases performed well except for the zinc containing formulation. Note further that the COF starts higher compared to the perpendicular case for the particle containing compounds. This indicates that the orientation of the roughness has a big influence on the lubricity of the compounds. This is confirmed with the perpendicular case, all previously failing compounds are performing well. No excessive friction is measured even after 1 m cumulative sliding length.

To explain the frictional results an overview of the wear scars is discussed hereafter. Figure E.5 shows the wear scars of the reference tests after 1 m cumulative sliding length with the aluminium complex base grease and the full formulation API modified. Shown from left to right in each row are the results for the polished disc and the ground disc with the sliding oriented perpendicular and parallel to the lay.

Figure E.5a, Figure E.5b and Figure E.5c are the results after sliding with just the base grease. In all cases deep scratches are visible at the surface. Initial damage is because of the material transfer, the lumps subsequently scratched the disc surface. Based on the sharp increase in COF in Figure E.4 galling occurred early in the reciprocating test. It is clear that the base

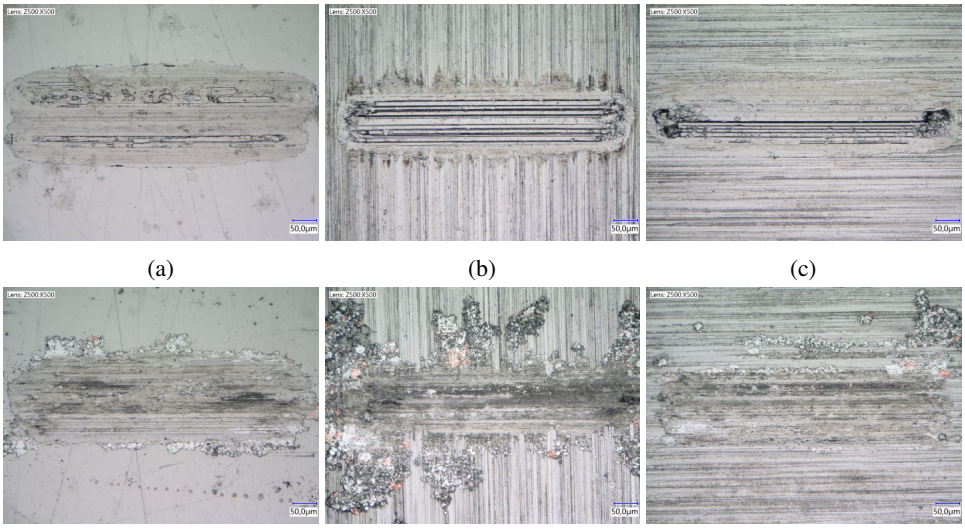

(a) (b) (c)

(d) Polished (e) Perpendicular (f) Parallel

Figure E.5.: Comparison of wear scars on a polished and ground disc perpendicular and parallel to the waviness with 500 µm stroke after 1 m cumulative sliding length with a 10 mm AISI52100 ball at 1 GPa. First row: base grease. Second row: API modified.

grease does not provide enough surface protection to avoid catastrophic failure because of galling.

Figure E.5d, Figure E.5e and Figure E.5f shows the full formulation API modified results. A large amount of zinc or lead particles, judged by colour, are visible in and around the wear scar in Figure E.5d. Virtually no copper seems to enter the contact. The COF is steady and slightly increasing over the full test duration probably because the contribution to the interfacial shear strength of the growing metallic film becomes more significant. In the perpendicular case (Figure E.5e) a large amount of particles gets embedded and based on the colour zinc/lead, copper and graphite are in the generated film. The difference with parallel sliding (Figure E.5f) is striking. Upon comparison, the thickness of the tribofilm and the amount of embedded particles is less. Furthermore it seems that only lead/zinc and in lower amounts graphite is in the tribofilm. In all cases no surface damage is visible because of the protective tribofilm that was deposited in the contact.

The base grease and API modified results were compared to single particle base greases. The results could be categorized into two categories. Severe galling or protective film formation, quite similar to the results in Figure E.5. The friction traces of Figure E.4 show that only zinc particles gave a consistently low COF. Both copper and lead did not enter the contact in the polished and perpendicular to the roughness tests and would only form a film when sliding perpendicular. Zinc particles thus play an important role in the protection of the surface based on the previous results. This is further exemplified by the results with copper and zinc added to the base grease which shows a similar result as the experiment with only zinc.

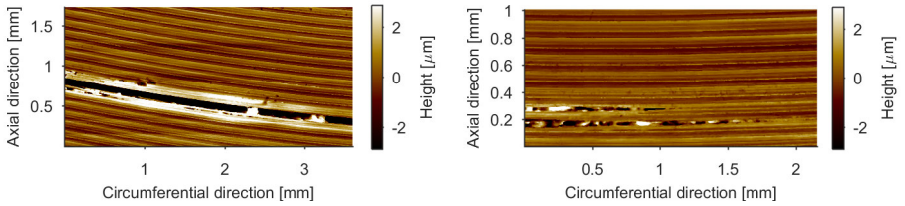

Figure E.6.: Interferometer measurement of the surface damage on the box of set FG03. Figure E.6a shows an overview of the scratch and Figure E.6b a detail of the initiation location. Initiations happens at the peaks of the waviness.

E.3.3. Galling initiation with mineral oil

Additional tests were performed using the mineral oil Shell Ondina 933 (O933) to get a clearer handle on the galling behaviour, to rule out contaminants and to test the thermal desorption hypothesis. This base oil is known to desorp at 130 °C [14]. Two tests were performed, set FG02 and FG03 (Table E.4). In FG02 a stepwise make-up was performed according to the sequence 2.5-5-10-20 mm and galling was observed during the 20 mm step. Based on the torque signal galling initiated after approximately 20 mm cumulative sliding. Therefore, a second specimen was assembled in a single step for 20 mm to capture the initiation of galling. The results of this test are shown in Figure E.6. It was found, not entirely unexpected, that galling initiates at the peaks of the waviness as shown in Figure E.6b. Next to that, if no formulated lubricant is used initiation starts after approximately 17.5-20 mm. Which means API modified adds only about 60 mm of additional sliding length before initiation of failure which is not sufficient for a typical casing connection.

The galling initiation mechanism was further investigated using fretting experiments in pin-on-disc. Fretting experiments were chosen because they mimic the continuous contact and they force the contact to run with the additives captured at initial contact, analogous to the observations in the metal-to-metal seal. The hypothesis was that galling is initiated because of wear of the protective oxide skin after removal of the lubricant. Two discs were prepared for the experiments a polished disc and a polished disc from the same batch that was tempered at 80 °C for 90 minutes to increase the oxide thickness. The stroke length was 50 µm and the sliding velocity 0.05 mm s^{-1}, far below any thermally initiated failure.

The results of the experiment are shown in Figure E.7 and clearly show the influence of the oxide thickness (designated "ox" in the legend) on the initiation of galling. The results of API mod were erratic depending on if a particle of lead, zinc or copper was captured in the initial contact.

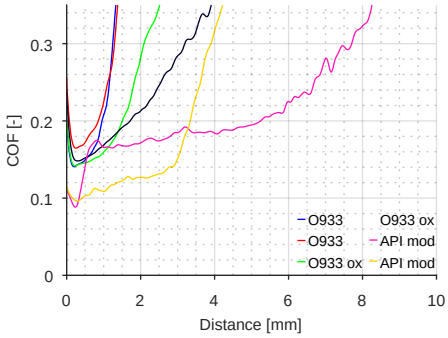

Figure E.7.: Fretting experiments with 50 µm stroke at 0.05 mm s^{-1} to investigate the effect of oxide thickness on the initiation of galling with Ondina 933 and API modified. Initiation was delayed by increasing the oxide thickness using tempering at 80 °C.

(a) (b) (c)

Figure E.8.: Macroscopic images of the metal-to-metal seal area of a section cut from a salvaged VAM 21 connection. The contact was opened gently to investigate the distribution of the thread compound (here API modified). The contact area has a much lower concentration of particles compared to the surrounding non-contact area. The BSE image in Figure E.8c and EDX results in Table E.5 at 20 kV confirmed these observations.

E.4. Observations in real connections

A set of VAM21 connections [21] were salvaged from the field and cut to inspect the seal area. One side of this tribosystem was manganese phosphated to avoid the issues described above and in [5]. Figure E.8 shows a macroscopic overview of the seal just after opening the contact. The contact clearly has a lower concentration of particles compared to the surrounding non-contact area. This confirms the observations in the previously presented investigations.

The macroscopic observations were confirmed with SEM/EDX in Figure E.8c and Table E.5. The contact area has a lower wt% of (smeared) metallic particles based on the lead, zinc and copper content. Focussing on the particles, predominantly lead and zinc are present. This is in line with the observations in the SSMUR and pin-on-disc investigation.

Table E.5.: EDX results in wt% for presented figures. Trace elements like Si, Al and Ca have been left out for clarity of the presentation without recalculating the wt%.

					wt%				
Figure / location	C	O	Cr	Mn	Fe	Co	Cu	Zn	Pb
Figure E.2d base metal	2.7		0.9	0.8	94.6	0.7			
Figure E.2d	4.2		1.0	0.9	93.0	0.6			
Figure E.2e	32.9	2.6			4.6		3.2	6.3	50.6
Figure E.8c 1	10.2	35.1	0.9		33.9		0.1	10.6	1.4
Figure E.8c 2	11.5	19.4	1.0		54.9			5.1	2.9
Figure E.8c 3	12.7	8.0	0.7		68.9		0.1	2.2	4.7
Figure E.8c 4	13.4	4.8	0.9		64.4		0.2	2.1	11.4
Figure E.8c 5	15.9	8.0	0.9		62.5		0.2	2.6	7.5

E.5. Discussion

The assembly results in SSMUR indicate that API modified is not a very effective lubricant at the high contact stress conditions in a connection. In both the face seal and interference seal configuration immediate failure was observed despite the formation of tribofilms on the surface (Figure E.2). The failure mode is clearly cold welding followed by material transfer (Figure E.2d). The resulting lumps damage the surfaces by higher localized contact stresses repeating the cold welding process and subsequent scratching of the surface by the transferred material [22]. Judged by the SEM and EDX analysis on the FIB cross section (Figure E.2f) the tribofilm was created during initial contact. This is evidenced by the presence of individual particles in Figure E.3. These films when running with API modified can also be observed in the macroscopic photos in the work by [23]. Hence the film is created by trapping the grease and its constituents upon initial contact. The film is not able to withstand long sliding lengths as shown by the results in Figure E.2.

Desorption of the lubricant by local flash temperatures as the initiation mechanism [14, 15] was ruled out using the thermal model by [24]. The model uses a contact model based on the Boussinesq-Cerruti half-space assumption [25] combined with a solution for a uniform square heat source taken from [26]. The heat source is the frictional heating which is a product of COF, velocity and local contact stress. Even though the maximum contact stress is equal to the material hardness, the local flash temperatures do not exceed 4 °C at these sliding velocities as shown in Figure E.9.

This means that the galling observed is initiated by another mechanism. This was shown with fretting experiments in pin-on-disc with varying oxide thickness (Figure E.7). The failure is initiated because of the rubbing off of the lubricant and its derived tribofilm, the oxide layer is subsequently the only line of defence which protects the surface for a short while until fresh steel surfaces are exposed. Both the mineral oil and API modified shield the surface from oxygen and have no active ingredients (like sulfur [27]) restoring the oxide layer. The fresh steel surfaces will thus cold weld, the subsequent junctions are broken which leads to lump growth and finally galling [28, 29].

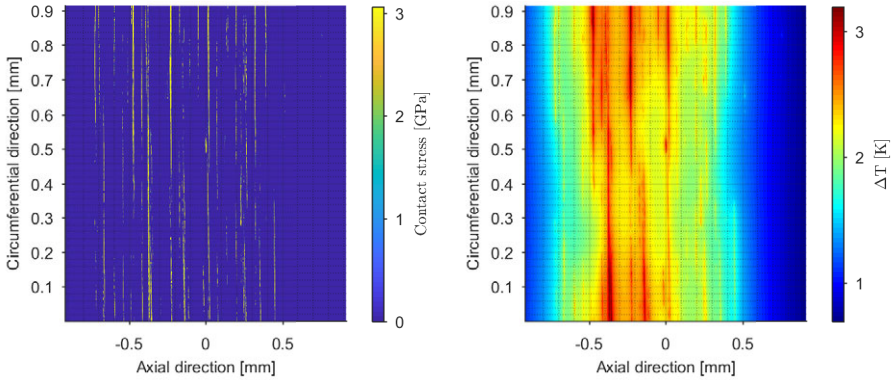

(a) Contact stress (b) Contact temperatures

Figure E.9.: Contact stresses and resulting flash temperatures using the model of [24]. Figure E.9a shows the contact stress distribution using the measured roughness of pin and box at location C-B (Figure E.2). The resulting flash temperatures are shown in Figure E.9b using a velocity of 24 m s^{-1} and a COF of 0.1 at a Fourier number >100 or steady state conditions.

The pin-on-disc results showed that there is a difference in the effectiveness of each additive in the API modified formulation. Both copper and lead do not sustain a film when no mechanical locking by roughness is possible. In contrast zinc forms and sustains a film in all cases. This difference can be for two reasons, either lead and copper do not enter the contact at all or they are rubbed off because they interact weakly with the steel surface (either by affinity [20] or roughness). Interestingly, lead and copper differ considerably in mechanical strength (Table E.3) with zinc right in the middle of the two. Hence it cannot be attributed to the shear strength differences. Next to that, in principle, the same sized particles are present in the formulation according to the mesh size (Table E.3). There is a difference in interaction with iron according to [20] as listed in Table E.3. This can explain both hypotheses as the interaction also plays a role in capturing the particle in the contact.

The particle size and mechanical properties were shown to play an important role in entrapment of a particle in a sliding or sliding-rolling contact by [30, 31]. In addition, if a particle is not trapped it can block the inlet leading to locally starved lubrication conditions resulting in potential surface damage. In support of the discussion in the previous paragraph a simple entrapment model was therefore derived and used qualitatively in conjunction with the particle properties (Table E.3) to explain the results presented. The derivation of the particle trapping model is inspired by seminal work of [30] and [31]. The size of the particles that are taken up by the sliding contact was determined by solving the force balance for the free body diagram in E.6.

In Figure E.10 the sensitivity to the choice for μ_2, or disc friction, and a fixed ball friction ($\mu_1 = 0.12$) is investigated for a maximum ball radius of 5 mm. A larger friction factor leads to trapping of larger particles or, of interest in this paper, mechanical locking ($\mu_2 \gg \mu_1$) by roughness leads to a higher chance of trapping of (larger) particles.

From the model it is clear that mechanical locking (increasing μ_2, perpendicular case) increases

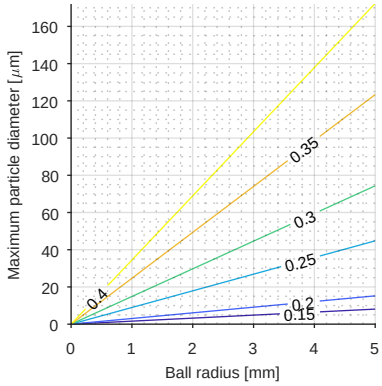

Figure E.10.: Maximum size of particles that will enter the contact for $\mu_1 = 0.12$ and as function of μ_2 and ball radius.

the likelihood of (larger) particles entering the contact. If this is not possible (polished and parallel cases) strong surface interaction (high friction) will give the highest chance of trapping a particle (zinc, Table E.3). Otherwise the particle size that can be captured is extremely small (Figure E.10).

The assertions were confirmed with the investigation of the real connection metal-to-metal seal area. Also in real connections hardly any particles were found in the contact area. In contrast, next to the contact large particles could be observed. The particles that were found in the contact were relatively small and consisted mainly of lead and zinc.

The combined results of pin-on-disc, our previous anvil-on-strip [5], SSMUR specimens and the real connection lead to the following mechanism initiating galling in casing connections. All have a turned roughness profile and assembly happens mainly in parallel orientation hence particles are not captured and there is no mechanical locking. Next to that the contact stress distribution promotes removal of grease from the contact. Hence in the SSMUR face seal case the amount of thread compound is determined at initial contact and quickly depleted because particles are not trapped and any film that has formed is squeezed out. This is also supported by the method of stepwise assembly and intermediate replenishment of the lubricant. In the SSMUR interference seal and the real connection a similar mechanism is present, however, one would expect replenishment by the movement in axial direction. This is not the case as shown and has probably to do with the large circumferential velocity component entraining the grease and ejecting the particles [32]. This explains why shot blasting the connection reduces the galling susceptibility considerably [Shell Connection QA/QC team, pers. comm.] as this promotes particle locking. However, this is not beneficial for sealing ability [5, 33, 34].

Finally, as discussed, the particles seem to play a relatively minor role in the contact defining the metal-to-metal seal and thus in sealing ability. Smearing of lead and zinc is observed, which can close or repair micro channels. However, not to an extent that is expected to make an impact. The presence of large amount of thread compound and particles before and after the seal, however, can make an impact by bridging and sealing the area. This is similar to how thread sealing works [9] and what API mod was designed for. In this scenario the metal-to-

metal seal contact acts as a barrier against which the particles are compressed by the pressure differential.

E.6. Conclusions

It was shown that a soft metallic tribofilm is formed by the initial contact which squeezes the particles into a film. This film subsequently is squeezed out of and rubbed off the concentrated contact on the waviness. The tribosystem then wears off the oxide layer until fresh steel is exposed initiating cold welding, material transfer and ultimately galling.

- Desorption of the lubricant because of exceeding local flash temperatures is not the initiation mechanism of galling.
- Galling was induced at a relatively moderate contact stress of 300 MPa. It was shown this happens because of interacting mechanisms which can be generalized to other thread compounds:
    1. Squeeze out and wear of at initial contact formed soft (metallic) tribofilms.
    2. Lack of strong adsorption of the thread compound or its tribofilm to the steel.
    3. Particle size.
    4. Waviness/roughness orientation with respect to the dominating sliding direction.
    5. Affinity of the particle towards the substrate.
    6. Creation of an inert atmosphere by the thread compound combined with the continuous contact such that no oxide layer recovery can happen.
    7. Wearing out the oxide layer which subsequently exposes bare steel initiating galling.

Acknowledgements

The authors are grateful to Shell Global Solutions International BV for permission to publish this work.

Patricle entrapment model

The derivation of the particle trapping model is inspired by seminal work of [30] and [31]. The size of the particles that are taken up by the sliding contact was determined by solving the force balance for the free body diagram in Figure E.11. The particle just got in contact with

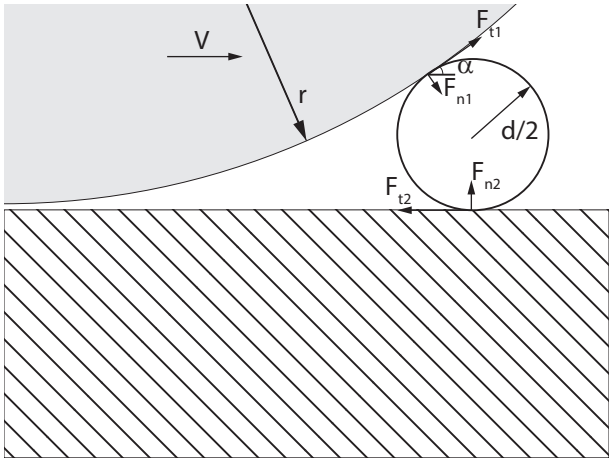

Figure E.11.: Free body diagram for the particle trapping model.

the sliding ball and stationary counter surface. The force balance becomes,

$$\sum F_x = 0 : F_{n1}\sin(\alpha) + F_{t1}\cos(\alpha) - F_{t2} = 0 \tag{E.1}$$

$$\sum F_y = 0 : -F_{n1}\cos(\alpha) + F_{n2} + F_{t1}\sin(\alpha) = 0. \tag{E.2}$$

Where F_n indicates the force normal to the ball and particle surface, F_t is the force tangent to the surfaces and α the angle of the tangent line with the y-axis. Now define,

$$F_{t1} = \mu_1 F_{n1} \tag{E.3}$$

$$F_{t2} = \mu_2 F_{n2}, \tag{E.4}$$

and substitute in equation (E.2) to obtain

$$\sum F_x = 0 : F_{n1}\sin(\alpha) + \mu_1 F_{n1}\cos(\alpha) - \mu_2 F_{n2} = 0 \tag{E.5}$$

$$\sum F_y = 0 : -F_{n1}\cos(\alpha) + \mu_1 F_{n1}\sin(\alpha) + F_{n2} = 0. \tag{E.6}$$

Next, the angle α can be expressed in the particle diameter, d, and ball radius, r, as

$$\tan\alpha = \frac{\sin\alpha}{\cos\alpha} = \frac{\sqrt{2rd}}{r - \frac{d}{2}}. \tag{E.7}$$

Finally substituting (E.6) into (E.5) and subsequently substituting (E.7) results in

$$F_{n1}\sqrt{2rd} + \mu_1 F_{n1}\left(r - \frac{d}{2}\right) - \mu_2\left(F_{n1}\left(r - \frac{d}{2}\right) - \mu_1 F_{n1}\sqrt{2rd}\right) = 0. \tag{E.8}$$

The normal force, F_{n1}, can now be divided out of the expression to yield a function that is only dependent on particle diameter, ball radius and the two COF's, viz

$$\sqrt{2rd} + \mu_1\left(r - \frac{d}{2}\right) - \mu_2\left(\left(r - \frac{d}{2}\right) - \mu_1\sqrt{2rd}\right) = 0. \tag{E.9}$$

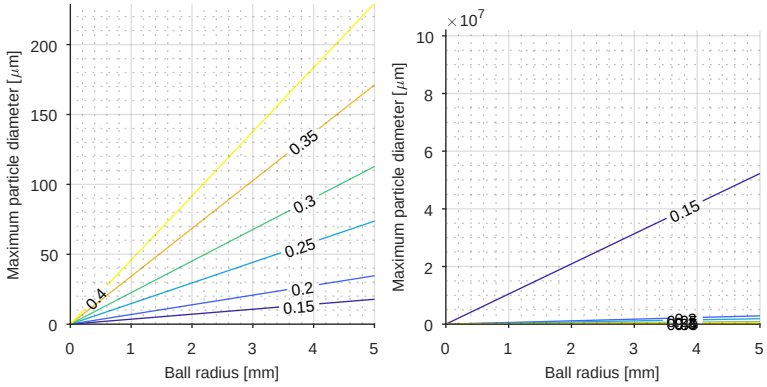

(a) Root 1 (b) Root 2

Figure E.12.: Maximum size of particles that will enter the contact.

Solving for the particle diameter using the Matlab® Symbolic Toolbox gives an expression that can be used to determine the maximum particle size that can be captured by a certain ball inlet size. Note that equation (E.9) is quadratic in d and thus yields two roots. The result of a parameter study is shown in Figure E.12. It is clear that the second root gives unrealistic results for the particle diameter. The isolines correspond to μ_2 with $\mu_1 = 0.08$. Note that for $\mu_1 = \mu_2$ no particles are captured in the contact, hence the surface interaction with each surface is important for trapping.

References

[1] Lugt, P. M. *Grease Lubrication in Rolling Bearings*. Oxford, UK: John Wiley & Sons Ltd, December 2012.

[2] API. *Recommended Practice on Thread Compounds for Casing, Tubing, and Line Pipe*. Tech. rep. Washington: American Petroleum Institute, 2015.

[3] Carper, H. J., Ertas, A., Issa, J. and Cuvalci, O. 'Effect of Some Material, Manufacturing, and Operating Variables on the Friction Coefficient in OCTG Connections'. *Journal of Tribology* 114.4 (October 1992), p. 698.

[4] Carper, H. J., Ertas, A. and Cuvalci, O. 'Rating Thread Compounds for Galling Resistance'. *Journal of Tribology* 117.4 (October 1995), p. 639.

[5] Ernens, D., Riet, E. J. van, Rooij, M. B. de, Pasaribu, H. R., Haaften, W. M. van and Schipper, D. J. 'The Role of Phosphate-Conversion Coatings in the Makeup and Sealing Ability of Casing Connections'. *SPE Drilling & Completion* (October 2018).

[6] Hoenig, S. and Oberndorfer, M. 'Tightness Testing of Environmentally Friendly Thread Compounds'. *SPE Europec/EAGE Annual Conference and Exhibition*. Vol. 1. Society of Petroleum Engineers, April 2006, pp. 473–480.

[7] Murtagian, G. R., Fanelli, V., Villasante, J. A., Johnson, D. H. and Ernst, H. A. *Sealability of Stationary Metal-to-Metal Seals*. July 2004.

[8] Ertas, A. 'Experimental Investigation of Galling Resistance in OCTG Connections'. *Journal of Manufacturing Science and Engineering* 114.1 (February 1992), p. 100.

[9] API. *WI 2317 : Tech Report on LTC / BTC Performance Properties and Leak Resistance*. Tech. rep. American Petroleum Institute, 2006, pp. 1–14.

[10] Teodoriu, C. and Badicioiu, M. 'Sealing Capacity of API Connections–Theoretical and Experimental Results'. *SPE Drilling & Completion* 24.01 (March 2009), pp. 96–103.

[11] Spikes, H. A. and Cameron, A. 'Scuffing as a Desorption Process—An Explanation of the Borsoff Effect'. *A S L E Transactions* 17.2 (January 1974), pp. 92–96.

[12] Blok, H. 'The flash temperature concept'. *Wear* 6.6 (November 1963), pp. 483–494.

[13] Blok, H. 'The postulate about the constancy of scoring temperature'. *Interdisciplinary Approach to Friction and Wear*. Ed. by Ku, P. Troy, New York: NASA SP-237, 1969, pp. 153–248.

[14] Drogen, M. van. 'The Transition to adhesive wear of Lubricated Concentrated Contacts'. PhD thesis. University of Twente, 2005.

[15] Heide, E. van der and Schipper, D. J. 'Galling initiation due to frictional heating'. *Wear* 254 (2003), pp. 1127–1133.

[16] Gåård, A., Hallbäck, N., Krakhmalev, P. and Bergström, J. 'Temperature effects on adhesive wear in dry sliding contacts'. *Wear* 268.7-8 (March 2010), pp. 968–975.

[17] Gåård, A., Krakhmalev, P., Bergström, J., Hirvonen Grytzelius, J. and Zhang, H. M. 'Experimental study of the relationship between temperature and adhesive forces for low-alloyed steel, stainless steel, and titanium using atomic force microscopy in ultrahigh vacuum'. *Journal of Applied Physics* 103.12 (June 2008), p. 124301.

[18] Gåård, A., Krakhmalev, P. V., Bergström, J. and Hallbäck, N. 'Galling resistance and wear mechanisms - Cold work tool materials sliding against carbon steel sheets'. *Tribology Letters* 26.1 (2007), pp. 67–72.

[19] API. *5CT: Specification for casing and tubing*. Tech. rep. American Petroleum Institute, 2001.

[20] Rabinowicz, E. 'The Determination of the Compatibility of Metals through Static Friction Tests'. en. *A S L E Transactions* 14.3 (January 1971), pp. 198–205.

[21] Sugino, M., Ugai, S., Nakamura, K., Yamaguchi, S. and Hamamoto, T. *VAM ® 21, an Innovative High-performance Premium Threaded Connection for OCTG*. Tech. rep. 107. Nippon Steel & Sumitomo Metal Corporation, 2015.

[22] Rooij, M. de, Linde, G. van der and Schipper, D. 'Modelling material transfer on a single asperity scale'. *Wear* 307.1-2 (September 2013), pp. 198–208.

[23] Inose, K., Sugino, M. and Goto, K. 'Influence of Grease on High-Pressure Gas Tightness by Metal-to-Metal Seals of Premium Threaded Connections'. *Tribology Online* 11.2 (2016), pp. 227–234.

[24] Bosman, R. and Rooij, M. B. de. 'Transient Thermal Effects and Heat Partition in Sliding Contacts'. *Journal of Tribology* 132.2 (2010), p. 021401.

[25] Johnson, K. L. *Contact Mechanics*. Cambridge University Press, 1987, p. 452.

[26] Carslaw, H. S. and Jaeger, J. C. *Conduction of heat in solids*. 2nd. Clarendon Press, 1959, p. 510.

[27] Lansdown, A. R. *Lubrication and Lubricant Selection: a Practical Guide*. Pergamon Press, 2003, p. 320.

[28] Rooij, M. B. de and Schipper, D. J. 'Analysis of Material Transfer From a Soft Workpiece to a Hard Tool: Part I—Lump Growth Model'. *Journal of Tribology* 123.3 (2001), p. 469.

[29] Rooij, M. B. de and Schipper, D. J. 'Analysis of Material Transfer From a Soft Workpiece to a Hard Tool: Part II—Experimental Verification of the Proposed Lump Growth Model'. *Journal of Tribology* 123.3 (2001), p. 474.

[30] Nikas, G. K. 'Theoretical modelling of the entrainment and thermomechanical effects of contamination particles in elastohydrodynamic contacts'. PhD thesis. Imperial College, 1999, pp. 1–342.

[31] Dwyer-Joyce, R. S. 'The Effects of Lubricant Contamination on Rolling Bearing Performance'. PhD thesis. University of London, 1993.

[32] Nikas, G. K. 'Particle Entrainment in Elastohydrodynamic Point Contacts and Related Risks of Oil Starvation and Surface Indentation'. *Journal of Tribology* 124.3 (2002), p. 461.

[33] Pérez-Ràfols, F., Larsson, R., Lundström, S., Wall, P. and Almqvist, A. 'A stochastic two-scale model for pressure-driven flow between rough surfaces'. *Proceedings of the Royal Society A: Mathematical, Physical and Engineering Science* 472.2190 (June 2016).

[34] Pérez-Ràfols, F., Larsson, R. and Almqvist, A. 'Modelling of leakage on metal-to-metal seals'. *Tribology International* 94 (February 2016), pp. 421–427.

This page has been intentionally left blank.

F. Evaluation of the elevated temperature performance and degradation mechanisms of thread compounds

D. Ernens[a,b], D. Westerwaal[b], R.F.H. Roijmans[b], E.J. van Riet[b], S. Daegling[c], A. Wheatley[c], E. Worthington[c], H. Kramer[d], W.M. van Haaften[b] M.B. de Rooij[a], H.R. Pasaribu[b]

[a]*Laboratory for Surface Technology and Tribology, Department of Engineering Technology, University of Twente, P.O. Box 217, 7500 AE, Enschede, The Netherlands*

[b]*Shell Global Solutions International BV, Innovation, Research & Development, Wells R & D, 2288 GS, Kessler Park 1, Rijswijk, The Netherlands*

[c]*Shell Global Solutions Germany GmbH, Innovation, Research & Development, Hamburg, Germany*

[d]*Nederlandse Aardolie Maatschappij, Assen, The Netherlands*

Abstract Thread compounds play an important role in the sealing ability of casing connections in the oil and gas industry. Next to their role during assembly, most of these thread compounds make use of non-biodegradable or persistent particle additives to aid in the sealing ability. Soon, these additives need to be replaced by benign alternatives as agreed in the proceedings of the Oslo-Paris Commission. This is, however, a challenge in high temperature (>150°C) well environments. This paper presents an investigation of the high temperature failure mechanisms of thread compounds with the aim to develop biodegradable high temperature resistant thread compounds. To this end, the performance of commercially available, environmentally acceptable thread compounds was investigated with thermogravimetric analysis (TGA), differential scanning calorimetry (DSC), high temperature rheometry and high temperature pin-on-disc experiments. The compounds are assessed on their stability, consistency, lubricity, and the resulting wear at high temperature. The results indicated that, without exception, the commercially available thread compounds fail by adhesive and/or abrasive wear at around 150 degrees Celsius because of thermally induced degradation. To remedy this and to validate the mechanisms, a prototype thread compound was developed which exhibits strong film forming. The conclusion is that a successful high temperature resistant environmentally acceptable thread compound can be developed. The key property is the ability of the compound to form a tribofilm which protects the surface after the lubricant has lost its consistency.

Submitted to SPE Drilling & Completion.

F.1. Introduction

The assembly of (casing) connections is performed with grease; also called thread compound. The base greases are typically made with a mineral base oil, and metal soaps or metal complex soaps. Additives are subsequently added in the form of metallic, mineral or metallic oxide based particles. Thread compounds are thus relatively simple grease formulations. What is special about them is the high solids content of up to 50-60 wt% compared to regular greases [1]. The function of the grease and the added particles is threefold; it provides a repeatable coefficient of friction for a predictable assembly torque response [2], provides surface protection [3–6] and aids in the seal ability of the system by blocking or bridging potential leak channels [7–11].

After assembly the casing is lowered into the well bore for the purpose of fortifying the drilled hole. During its lifetime the casing will experience several stress states. For instance, when the well is flowed it will heat-up and the casing experiences a transition from tension to being loaded in compression because of thermal expansion; this leads to small movements in the metal-to-metal seal in the axial direction, which will be defined as micro sliding. The micro sliding is typically in the order of 0.5 mm and operates at extremely low velocities i.e. $\ll 0.01\,\mathrm{mm\,s^{-1}}$ and thus fully in the boundary lubrication regime [12]. As typical contact widths are >1.0 mm this can also be characterised as fretting [7].

The casing string and connections are thus subjected to substantial loads under high subsurface temperature conditions (up to 240 °C). The seal ability of the system needs to be guaranteed under the micro sliding conditions described previously; this means that lubricity needs to be guaranteed to avoid cumulative damage leading to seal failure. Therefore, the long term thermal stability of the grease and related tribofilms is of great importance for the metal-to-metal seal tribosystem. This is the reason why the *de facto* standard thread compound, API modified [1], still uses metallic lead in its formulation.

Initiatives are under way to ban the use of heavy metals in thread compounds and to push the industry to formulate fully biodegradable alternatives. These initiatives are led by the Norwegian and British regulatory bodies: the Norwegian Environment Agency (NEA) and the Centre for Environment Fisheries and Aquaculture Science (CEFAS) respectively. They execute the outcomes of the Oslo-Paris Commission for the protection of the Marine Environment of the North-East Atlantic (OSPAR) by implementing the Harmonised Offshore Chemicals Notification Format (HOCNF) [13]. HOCNF is a scheme to harmonize the regulation of chemicals used in the offshore industry in the North Sea and the North-East Atlantic. The aim is to minimize the risk of serious spills and damage to the local marine environment. The regulators define an environmental friendliness scale to categorize the chemicals for use offshore. The scale runs from readily biodegradable and non-bioaccumulative, designated as E or Green, to nonbiodegradable and bioaccumulative, designated as A or Black, by CEFAS and NEA respectively. API modified belongs in the A or black category. The goal of CEFAS and NEA is to push developments in the direction of E, or green category, thread compounds. In between are the yellow and red category respectively. Environmentally acceptable products are in the yellow category, which should have a biodegradability of at least 60 wt% over 28 days in sea water and have no components that bioaccumulate.

To replace API modified, the lubrication and sealing mechanisms needs to be understood. Furthermore, limited information is available about high temperature degradation of thread

compounds and the mechanisms that ultimately lead to the failure of the metal-to-metal seal. These mechanisms were investigated and are described in this paper. In addition, current thread compound qualification and test procedures [1] [1] are not pushing manufacturers enough to bridge the gap from black to green dope. A proposal for a test method which incorporates the high temperature degradation is also provided in this paper. The mechanisms and test method were validated by successfully developing a prototype thread compound that remedies the found thermal degradation issues with current environmentally acceptable thread compounds.

As discussed the standard thread compound is API modified [1]. The compound was formulated over 70 years ago [14] and is still the most widely used thread compound in the oil and gas industry [1]. It contains a base grease made with a heavy mineral oil and a metal soap thickener combined with graphite, lead, zinc and copper. Several explanations for its success in protecting the surface during assembly and sealing ability are given. The work by Ertas et al. [6] attributes this mainly to the lead particles that form a protective film. Zinc and copper are said to be added to control the friction coefficient. In addition, the copper particles are the largest and probably aid in thread sealing [9, 14]. Finally the graphite is not of lubrication grade and therefore acts mainly as a filler [6]. This, together with the broad particle size distributions of the metallic additives [14], helps in the sealing ability [6].

In a study by Murtagian et al. [11] it was shown that the presence of a thread compound has a strong influence on gas sealing ability performance of the metal-to-metal seal. The onset of leakage was at a lower seal contact intensity and instantaneous compared to experiments without thread compound. There is, however, a large difference in the sealing performance between the different commercial thread compounds, as shown by Hoenig et al. [10]. This was mainly attributed to imposed variations of the applied internal pressure, the type of gas, and the temperature cycling. Still, API modified holds up well against recently developed thread compounds, particularly under high temperature conditions.

Inose et al. [8] show that thermal degradation of the thread compounds plays a significant role in the reduction of the sealing performance of metal-to-metal seals. The researchers exposed API modified and an environmentally acceptable thread compound containing inorganic particles to temperatures of 180 °C and evaluated the sealing ability. It was concluded that API modified performed better compared to the environmentally acceptable thread compound. This was attributed to the mineral oil which performed better under elevated temperature conditions, and its soft metallic particles closed potential leak paths and thus improved sealing ability. They thus show that a connection can be successfully made-up but fail during load cycling because of thermal degradation of the lubricant. This exposed the surface directly to the hard inorganic particles contained in the environmentally acceptable thread compound. The particles subsequently abraded the surface leading to formation of scratches and/or galling in the seal area; reducing its sealing performance.

The surface topography and its orientation was shown to play an important role in our previous work by Ernens et al. [7]. This was also shown with a stochastic sealing ability model by Pérez-Ràfols et al. [15]. Damage of the surface because of scratching can bypass the seal contact, leading to diminished sealing performance. These studies suggest that the choice for base oil, thickener and additives needs to be balanced between tribology and sealing ability. How to design a high temperature, stable and environmentally friendly thread compound was however not tackled in these studies, which is investigated in this paper.

Table F.1.: Summary and overview of the used test protocol for the various screening methods.

Test type	Measurement geometry	Protocol	Atmosphere
TGA and DSC	100 µL Al open cup, 60 µL Au closed cup	Dynamic 30-250 °C at 10 °C min^{-1}, iso hold 30 min at 250 °C, dynamic 250-30 °C at -10 °C min^{-1}	Open cup 80 mL min^{-1} air or N_2
Rheometer 1	coaxial cylinder (PZ38) 50 mL	Perform shear stress sweep 1.5-800 Pa at 20-50-100-150-200 °C with 30 min temperature hold per step	Half-open pressure vessel N_2
Rheometer 2	coaxial cylinder (Z10)	Perform shear rate sweep 1.0-100 s^{-1} at 20-40-70-100-140-180-200°C with 30 min temperature hold per step, hold for 3 hours, perform another sweep at 180 °C	Open cup air
Pin-on-disc	10 mm AISI52100 ball on AISI4130 disc	Perform 250 reciprocating cycles at 1 GPa with stroke 500 µm at 30-70-100-150-200-250°C	Half-open drive air

F.2. Methodology

Thermal stability was assessed with thermogravimetric analysis (TGA) and differential scanning calorimetry (DSC). This was followed by rheometer experiments at increasing temperatures to investigate the changes in consistency as a consequence of the thermal degradation. The rheometer experiments were performed by imposing a shear stress sweep to also investigate yielding behaviour. The outcomes of TGA/DSC and rheometer experiments were subsequently used to explain the high temperature pin-on-disc experiments. The pin-on-disc experiments are designed to investigate make-up sliding and micro-sliding in a single experiment, and are the same as [7], except for the addition of elevated temperatures. The used test set-up is open to atmosphere, so components in the grease can evaporate or react with oxygen. This is not, or to a lesser extent, the case in a real connection. Therefore, the test is accelerating degradation and is a worst-case scenario for the thread compound. The experiments are summarized in Table F.1 and will be described in more detail hereafter.

F.2.1. Lubricants

The screened lubricants consist of off-the-shelf environmentally acceptable thread compounds that were compared to the reference compound API modified. The lubricants are listed in

Table F.2, because of trade secrets most commercial compounds have undisclosed compositions except for ingredients that need to be stated in the material safety data sheet (MSDS) or that are stated with a general description on the technical data sheet (TDS). The dropping point listed in the table indicates the upper temperature limit at which a grease retains its structure [16]. This depends on the type of thickener used. In addition, a clay based base grease was mixed in the laboratory with various additives to explore the feasibility of formulating a high temperature, environmentally acceptable thread compound based on the film forming hypothesis that will be developed in this paper. The final formulation was also mixed in a production facility, as indicated in Table F.2.

F.2.2. TGA/DSC

The thermal stability test entails a temperature sweep using a Mettler Toledo TGA/DSC 1 from ambient temperature (25 °C) to 250 °C, at a temperature increase rate of 10 °C min^{-1}, followed by a hold period of 30 minutes at the same temperature (250 °C). At the end of the hold period, a cooling rate of 10 °C min^{-1} was imposed to reduce the temperature from 250 °C back to room temperature. For the thread compounds the resistance to oxidation and their general thermal behaviour was investigated using:

1. Open cup vs. closed cup experiements.

2. Air vs. nitrogen atmosphere.

3. 3. Open cup and mixing the thread compound with approximately 2 mg iron oxide (hematite) to simulate wear particles.

The open cups were all loaded with approximately 62.5 mg of product, the closed cups were all loaded with approximately 61.5 mg of product.

F.2.3. Rheometry

The rheology characterisation was performed with a Haake Mars III rheometer. Two protocols were used. For protocol *rheometer 1*, the measurement geometry was a coaxial cylinder (PZ38) allowing measurements in a half-open (evaporation still happens) environment under N_2 conditions. The rheology measurements were carried out on a sample volume of 50 mL. Temperature was controlled using the Peltier module (TM-PE-C) up to a maximum temperature of 200 °C. The temperature set-points were 20-50-100-150-200°C. At each set-point a 30 min hold was followed by a stress-controlled test over the range 1.5-800 Pa. The sample was not refreshed between the temperature steps. Protocol *rheometer 2* used an open coaxial cylinder (Z10) performing a shear rate sweep 1.0-100 s^{-1} at 20-40-70-100-140-180-200°C with 30 min temperature hold per step. This was followed with a 180 °C hold for 3 hours and another sweep at 180 °C to investigate the degradation effects.

Table F.2.: Overview of the commercial thread compounds that were screened and the subsequent prototype compounds that were designed using the methods described in this paper. The data is obtained from the TDS and MSDS.

Short hand	Full name	Base oil	Thickener	Additives based on MSDS (particles)	Dropping point °C
		Commercial thread compounds			
API mod	API modified [1]	Mineral oil	Undisclosed	Lead, copper, zinc, graphite	>204
YD A	Yellow thread compound A	Synthetic PAO and ester	Undisclosed	Calcium fluoride, calcium sulphate, calcium carbonate, etc.	>288
YD B	Yellow thread compound B	Synthetic oil	Calcium complex	Calcium fluoride, titanium dioxide, calcium carbonate, etc.	>288
YD C	Yellow thread compound C	Synthetic ester	Undisclosed	Mineral fillers	>200
		Prototype thread compounds			
SA	Shell internal A	Mineral oil	Clay	Melamine cyanurate	>288
SB	Shell internal B	Mineral oil	Clay	Lubrication grade graphite	>288
SG	Shell internal G	Mineral oil	Clay	Calcium phosphate	>288
SJ	Shell internal J	Mineral oil	Clay	SA + SB	>288
SK	Shell internal K	Mineral oil	Clay	SB + SG	>288
SL	Shell internal L	Mineral oil	Clay	SB + SG diff. ratio	>288
SM	Shell internal M	Mineral oil	Clay	SA + SB + SG	>288
SN	Shell internal N	Mineral oil	Clay	SA + SB + SG mixed in grease plant	>288

F.2.4. High temperature Pin-on-disc

The tribological screening experiments were performed with a Bruker UMT-3 equipped with the 350 °C drive module (S35HE-350). In addition to room temperature experiments (like [7]), elevated temperature experiments were performed. The temperature set points were 30–70–100–150–200–250°C. Once the temperature set point was reached a 15 minute hold period followed to ensure the disc surface temperature also reached the set-point. Then 250 reciprocating cycles were made with a stroke of 500 µm. Hence a total of 1500 cycles were made for an equivalent sliding length of 1.5 m. The location on the disc, ball and lubricant were not changed or replaced during the temperature steps. However, the ball was taken out of contact by 1 mm during the hold periods to avoid an offset on the load measurement by thermal influences on the load cell.

F.2.5. Performance assessment

Based on the correlations between sealing and surface quality and the role of the thread compound [8, 15, 16], the results of the tests were assessed according to the following criteria:

1. High temperature stability (e.g. dropping point).
2. High temperature consistency (e.g. shear/temperature thinning behaviour).
3. High temperature lubricity (Coefficient of Frcition (COF)).
4. Surface damage (wear).

The assessment was done by combining observations on the change in consistency, appearance and surface texture after the experiments. In addition, the resulting wear scars were investigated with a digital light microscope and a scanning electron microscope.

F.2.6. Anvil-on-strip

The anvil-on-strip experiments on the prototype compound were performed with a Quiri tribometer and compared to the results of our previous paper [7]. In this case, unidirectional sliding experiments were performed. The strip was mounted in a tensile tester. On each side of the strip an anvil was pressed at a prescribed load. The strip was then moved up at a prescribed velocity while measuring the resultant friction force. The sliding experiments were performed at a maximum Hertzian contact stress of 1.4 GPa by applying 20 kN normal load on the anvils. For the experiments with as machined surfaces (no coating), a linear load ramp was applied over the first 5 strokes. The contact spot was elliptical and approximately 5.7 mmx1.1 mm. The sliding velocity was 24 mm s^{-1}. Up to 50 strokes were made with a sliding length of 31 mm which sums up to 1550 mm cumulative sliding length for the anvil.

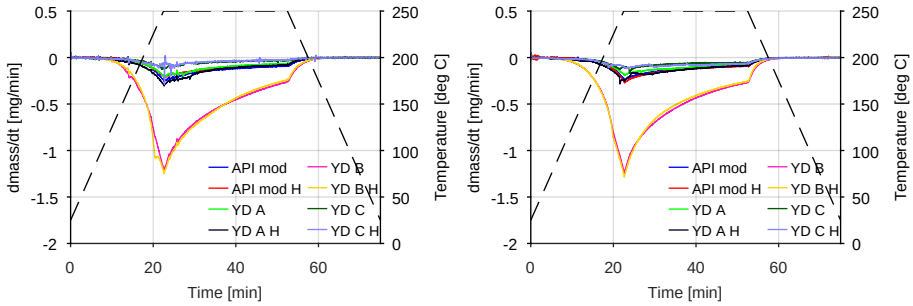

(a) Open cup N_2 (b) Open cup air

Figure F.1.: Overview of TGA experiments for open cup in nitrogen atmosphere in Figure F.1a and open cup in ambient air atmosphere in Figure F.1b. The mass loss was differentiated versus time for each experiment to obtain a mass loss rate. The dashed line belongs to the secondary y-axis displaying the heating and cooling program.

F.3. Results

F.3.1. TGA/DSC

The results of the TGA screening experiments are given in Figure F.1 by the rate of mass loss as a function of time. The results with a nitrogen atmosphere and an air atmosphere are shown in Figure F.1a and Figure F.1b respectively. The results for nitrogen and air show similar amounts of mass loss for the various compounds. There is one clear outlier in the set, YD B has a substantially higher mass loss compared to the other products. The onset of mass loss at a high rate is around 150 °C. The others display similar mass loss when YD B is left out of the comparison, with YD C having the lowest value. No significant differences were observed coming from the presence of hematite.

The DSC results are shown in Figure F.2 for closed cup, open cup in N_2 and open cup in air. In the closed cup experiments in Figure F.2a only YD B is undergoing permanent phase transitions with endothermic peaks around 150 °C and 200 °C. The first peak coincides with the onset of mass loss in Figure F.1. No measurable effect of hematite was observed. When performing the experiments in an open cup under both a nitrogen (Figure F.2b) and an air (Figure F.2c) atmosphere, evaporation and oxidation effects were found. In both cases all thread compounds show endothermic peaks at relatively low temperatures probably corresponding to lighter fractions evaporating. The endothermic peaks for YD B are more pronounced. In air indications of oxidation are present during the hold period with strong exothermic peaks for YD B and YD C which get more pronounced when hematite is added. API modified shows the highest thermal stability with no indications of a phase transition or reaction.

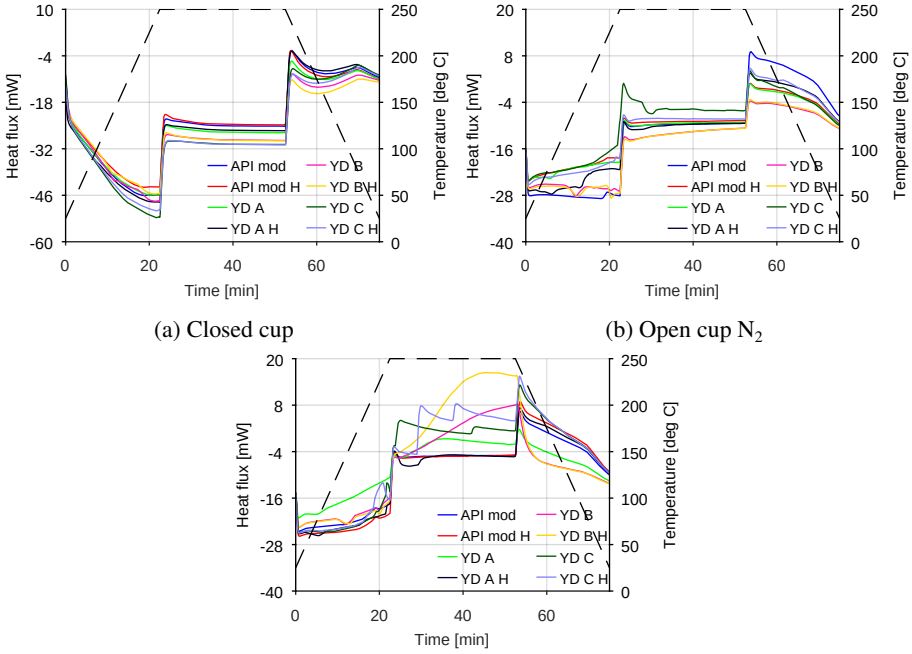

(a) Closed cup

(b) Open cup N_2

(c) Open cup air

Figure F.2.: Overview of the DSC experiments belonging to the TGA results in Figure F.1 for closed cup in Figure F.2a, open cup in nitrogen atmosphere in Figure F.2b and open cup in air atmosphere in Figure F.2c. The dashed line belongs to the secondary y-axis displaying the heating and cooling program.

F.3.2. Rheometry

The rheological characterisation as function of temperature is shown in Figure F.3 for the dynamic viscosity. API modified in Figure F.3a shows clear shear thinning behaviour as the viscosity drops monotonically with increasing shear rates. At high shear rates a plateau is reached which typically coincides with the base oil viscosity [17]. When observing the rheological experiment in an open version of the coaxial set-up indications of shear banding could clearly be seen [18, 19]. Shear banding means that only part of the fluid in the gap is entrained by the rotating cylinder and part of the fluid is stationary. Only above a certain threshold shear rate the complete gap will have uniform flow. Indications of this effect are observed in the flow curves of 20 °C and 50 °C. Where the 20 °C curve shows a relatively extended region, the 50 °C curve shows a shorter region because of temperature thinning of the lubricant. This is not a surprise as next to a thickener this thread compound contains 60% solids. At higher temperatures the effect is not observed as the elevated temperature has reduced the viscosity enough to develop a uniform flow immediately. Part of this could be attributed to gravimetric segregation of the metal particles which was observed after the test shown in Figure F.4a.

As discussed, the results for YD A were obtained with a different measurement geometry and protocol (rheometer 2, Section F.2.3). Consequently, limited information is available on the rheological behaviour. YD A exhibits clear shear thinning behaviour with a monotonically decreasing viscosity with increasing shear rate as shown in Figure 3b. Even though the measurement window is limited, the behaviour of YD A appears similar to YD C. The compound consistency is not negatively affected by temperature as the viscosity at 180 °C was measured twice at a 3 hour interval, in this protocol, which gave a repeatable result. This was also observed after the pin-on-disc experiment as shown in Figure F.4b.

YD B has a higher resistance to flow, as shown in Figure F.3c. The compound shows indications of a distinct yield point compared to the other thread compounds even though there is always flow according to [20]. Indications of shear banding were found up to 100 °C because of the higher initial viscosity. At 150 °C the temperature trend reversed compared to the other thread compounds, very little flow was observed. Therefore, the experiment was stopped, and the pressure chamber disassembled to investigate why this happened. It was found that the thread compound was completely dry explaining this behaviour, as shown in Figure F.4c. This agrees with the TGA/DSC observations in Figure F.1 and Figure F.2.

Figure F.3d shows the behaviour of YD C. At 20 °C a constant viscosity can be observed at low shear rates which has similarities with a Newtonian plateau region as observed by Cyriac et al. [21]. However, this typically happens at much lower shear rates, therefore here it is seen as part of the shear banding region. YD C has a high initial viscosity and is least affected by temperature thinning effects. Therefore, the effects of shear banding were observed up to the highest applied temperature. After the set-up cooled down to room temperature it was observed that the cylinder would not rotate any more, even though the last experiment (at 200 °C) showed fully developed flow. It was therefore decided to run an additional experiment at 20 °C on the aged product, which revealed similar behaviour as the 150 °C experiment of YD B. In Figure F.4d, it could be observed that the compound thickened into a clay-like substance.

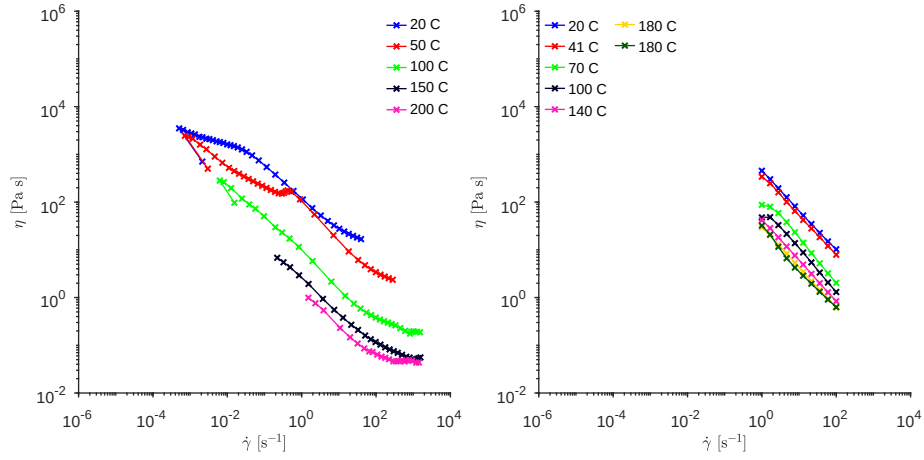

(a) API mod

(b) YD A

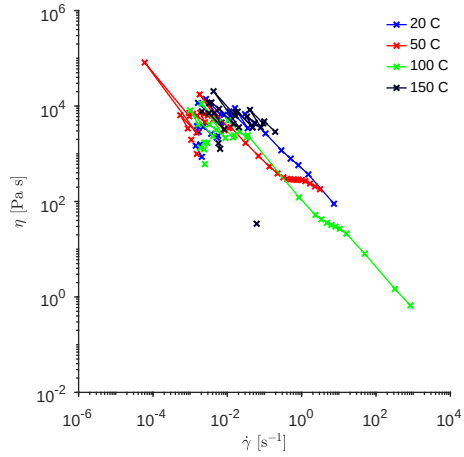

(c) YD B

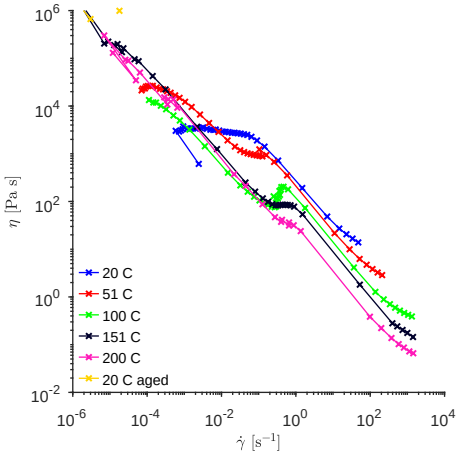

(d) YD C

Figure F.3.: Dynamic viscosity as function of the measured shear rate. Figure F.3a shows API modified, Figure F.3b shows yellow dope A, Figure F.3c shows yellow dope B, and Figure F.3d yellow dope C.

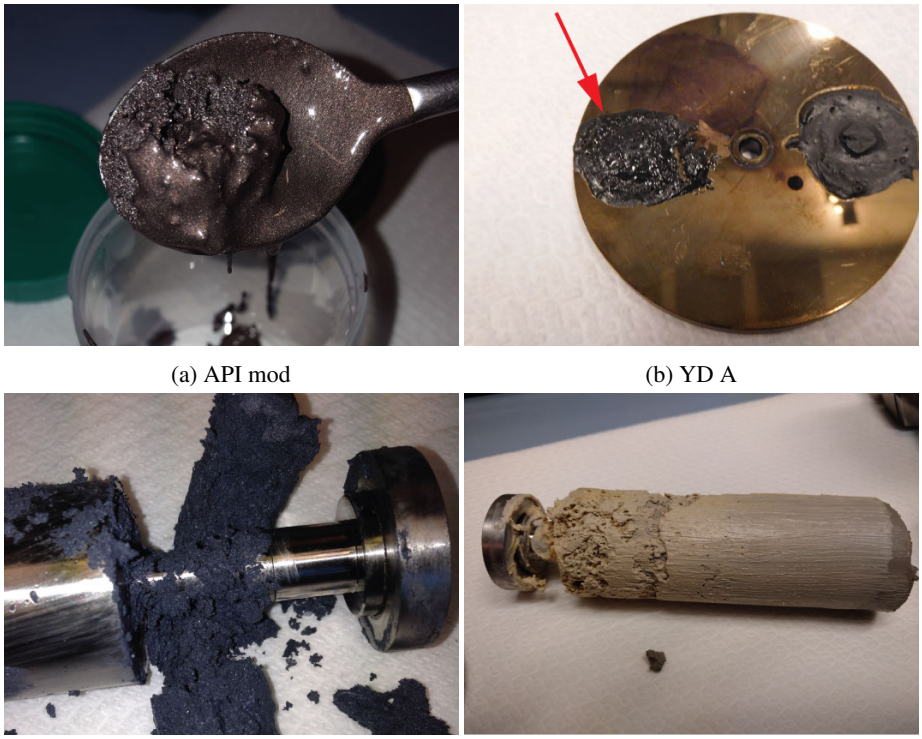

(a) API mod (b) YD A

(c) YD B (d) YD C

Figure F.4.: Observations after the high temperature rheology or pin-on-disc experiments. Figure F.4a shows the gravimetric segregation of particles observed in API mod. Figure F.4b shows the still greasy consistency of YD A indicated by the arrow. Figure F.4c shows the completely dried out YD B. Figure F.4d the observed thickening of YD C.

F.3.3. Pin-on-disc

The screening results of the pin-on-disc experiments are summarized for each temperature step comprising of 250 reciprocating cycles by their mean COF (bars), standard deviation (vertical lines) and maximum COF (dots) as shown in Figure F.5e. The COF was found to be a good indicator of thread compound failure. Based on the experiments performed a monotonically decreasing or constant COF with temperature typically indicated a well performing compound. If this trend showed an increasing COF this indicated a poor performing compound which failed because of adhesive and/or abrasive wear which was the case for the environmentally acceptable thread compounds tested, as observed in Figure F.5.

The observations after the experiments are shown by the wear scars in Figure F.5. API modified retained most of its consistency until the end of the experiment with some segregation of the base oil from the grease structure, as shown in Figure F.4a, which could indicate that the dropping point was reached. The microscopy of the wear scar in Figure F.5a revealed many particles in the contact, forming a protective film. This also explains the relatively constant COF as this is dictated by the interfacial shear strength of the metallic film.

The environmentally acceptable thread compounds (YD A-C) all showed degradation of their lubrication performance on or shortly after the 150 °C step. This can be observed in Figure F.5e from the increase in mean COF, its standard deviation and the maximum COF. The reason is different for each compound, however, for all it resulted in failure of the tribosystem, leading to scratched surfaces. YD A shows the earliest indications of imminent failure at 100 °C, followed by YD C at 150 °C, and then YD B at 250 °C.

F.4. Prototype thread compound based on strong film formation

Based on the presented findings a lubricant was designed with a strong film forming tendency. The idea was to form a tribofilm during make-up, and thus before the base oil has evaporated. The design was made using the high temperature pin-on-disc approach described previously.

For this a thermally stable mineral oil was selected designated "S" in Figure F.7a, which was combined with a clay thickener to yield a base grease with a high dropping point [22] and stable rheological behavior as shown in Figure F.7c. Additives (as per Table F.2) were subsequently added to the base grease with the same wt% across all specimens and tested using the room temperature and elevated temperature pin-on-disc method. The final selection of the components resulting in compound SM[1] (Table F.2) was based on the swelling of melamine cyanurate at elevated temperatures to aid in seal ability and the film forming of graphite and calcium phosphate. In addition, graphite and calcium phosphate are considered to Pose Little Or No Risk (PLONOR) to the environment by OSPAR [23]. The result with this compound after the pin-on-disc experiment is shown in Figure F.6a.

[1] Patent pending.

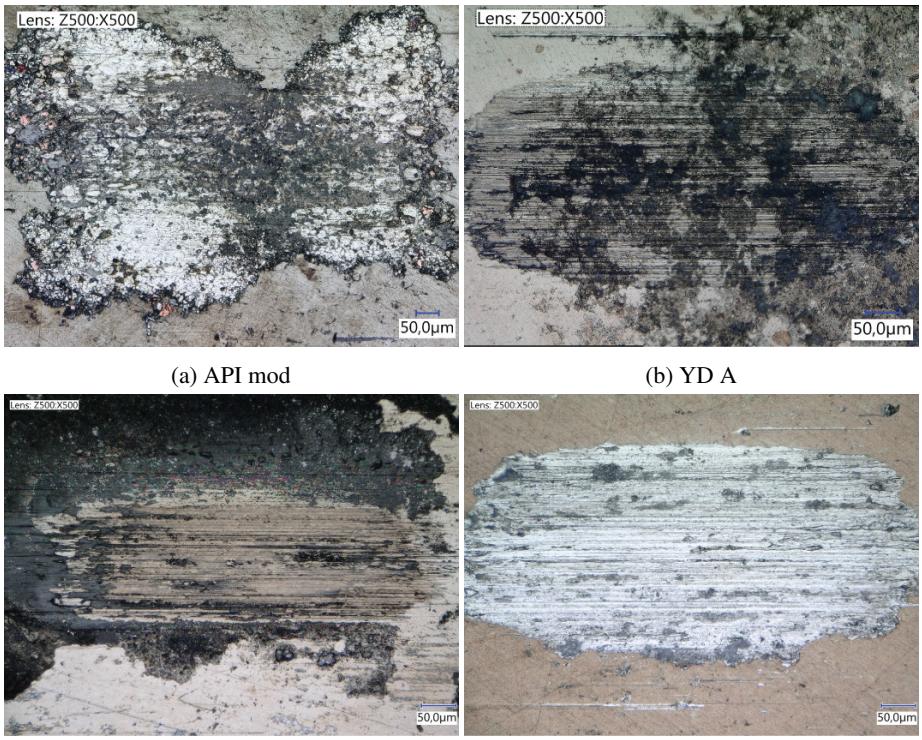

(a) API mod (b) YD A

(c) YD B (d) YD C

(e)

Figure F.5.: Wear scars after the pin-on-disc tests. All three environmentally thread compounds failed because of adhesive and/or abrasive wear as evidenced by the wear scars in Figure F.5b, Figure F.5c and Figure F.5d. The results of the PoD are shown in Figure F.5e. Each experiment is summarized by mean COF (bars), standard deviation (vertical lines) and maximum COF (dots).

The performance of compound SM was subsequently confirmed at ambient conditions in an As Machined (AsM) versus As Machined (no coatings) P110 tribosystem using the anvil-on-strip set-up and compared to previous results with the commercial thread compounds in [7]. This was the first thread compound of the ones tested that did not show galling in the AsM-AsM experiment as shown in Figure F.6d. The COF comparison with the results of our earlier work [7] are shown in Figure F.6d. The prototype mixture was subsequently manufactured professionally in a manufacturing plant, designated compound SN, which was used for assembly experiments. Before the assembly experiments, the performance was confirmed in pin-on-disc experiments which yielded equivalent results as compound SM (Figure F.5e). The assembly test entailed three make-ups and break-outs of a 5.5" 23# L8013Cr VAM TOP HT connection. This is a high chromium material (13 wt%) which is even more susceptible to galling, and therefore considered challenging for thread compounds. The connection box side is copper plated, and the pin side is AsM. Assembly was performed with a bucking unit, which means that assembly is performed at a low velocity (<1 RPM) and discontinuous because of the limited stroke length of the hydraulic arm. No galling was observed after multiple make-ups/break-outs as shown in Figure F.6c.

F.5. Discussion

In the investigation of commercially available thread compounds, none of the tested environmentally acceptable compounds meet the specifications needed for high temperature, high pressure oil and gas wells. Each of these compounds failed for different reasons in the tribological experiments. An overview of the TGA/DSC and rheology experiments is given in Figure F.7.

API modified showed the most stable elevated temperature behavior (Figure F.5e) with minimal weight loss in the TGA (Figure F.7a) and no indications of reactions or phase transitions in the DSC (Figure F.2). It also provided stable rheological behavior over the duration of the rheology experiment (Figure F.7b) with gravimetric segregation of its particles at the end of the experiment (Figure F.4a). However, this should not pose a problem in a metal-to-metal seal as only a thin film is applied in a narrow gap. In addition, at the end of the rheological experiments (Figure F.4a) and tribological experiments, it was observed that the base oil bled from the thread compound indicating that the dropping point was reached.

YD A failed earliest in the pin-on-disc experiments (Figure F.5e) even though TGA/DSC (Figure F.7a, Figure F.1 and Figure F.2) and rheology (Figure F.7) showed stable behavior for this compound. It still had its original consistency as observed after the pin-on-disc experiment (Figure F.4b). Therefore, it is possible that a film is formed initially, which is rubbed off over the course of the experiment and not replenished leading to failure.

YD B failed because of evaporation of the base oil. The onset of accelerated evaporation is around 150 °C, as found in the TGA/DSC and the rheology experiments in Figure F.7a and Figure F.7b respectively. In addition, the DSC (Figure F.2c) revealed oxidation of the compound in air. This resulted in a dry compound (Figure F.4c) which allowed no replenishment of the lubricant in the contact area, leading to starved conditions. In addition, as the base oil has evaporated, this leaves hard inorganic particles in the contact area, leading to abrasion.

(a) SM and SN

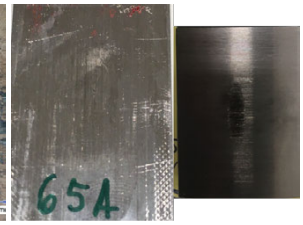

(b) SM

(c) SN

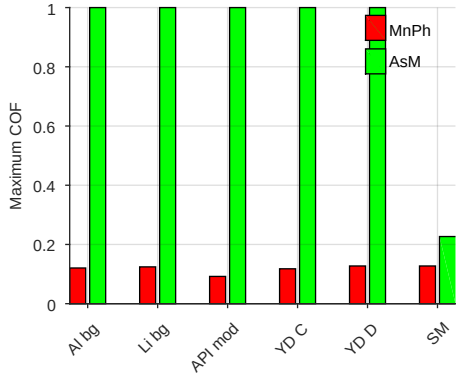

(d) SN

Figure F.6.: Prototype compound combining SA, SB and SG. Figure F.6a shows the pin-on-disc results after 250 reciprocating cycles per temperature step, for a total of 1500 at 1 GPa with a 10 mm AISI52100 ball on a AISI4130 flat. Strong film forming was observed, providing successful surface protection. The performance in the anvil-on-strip experiments was equally good with no galling observed in an AsM-AsM P110 tribosytem in Figure F.6b. Finally, the performance was confirmed by assembly tests of a 5.5" 23# L8013Cr VAM TOP HT connection which showed no galling after multiple make-up and break-outs as shown in Figure F.6c. Figure F.6d shows the summarized results for the anvil-on-strip experiments of [7] with the result of SM added. Note that a COF of 1 indicates galling. Results are shown for the anvil-on-strip experiments with as machined (indicated AsM) strips and anvils, and manganese phosphated (indicated MP) strips and AsM strips.

From this point onwards, the contact relies on the tribofilm formed in the earlier steps of which remnants can still be observed in Figure F.5c. Therefore, failure is only observed at 250 °C. These observations are similar to the ones by [8].

YD C showed the best performance in the TGA experiments (Figure F.7) with the lowest weight loss of all compounds. In the DSC reactions or phase transitions were observed under a nitrogen and air atmosphere (Figure F.2). These can probably be related to the thickening observed after the rheology experiments (Figure F.4d) and oxidation, as observed in the TGA/DSC experiment (Figure F.1 and Figure F.2). The compound reduced to a clay-like consistency after exposure to high temperatures for an extended period. In the tribological experiments this led to removal of the compound from the contact by mechanical action of the ball. No protective tribofilms were formed as failure followed relatively quickly and catastrophically, as observed from the wear scar in Figure F.5d.

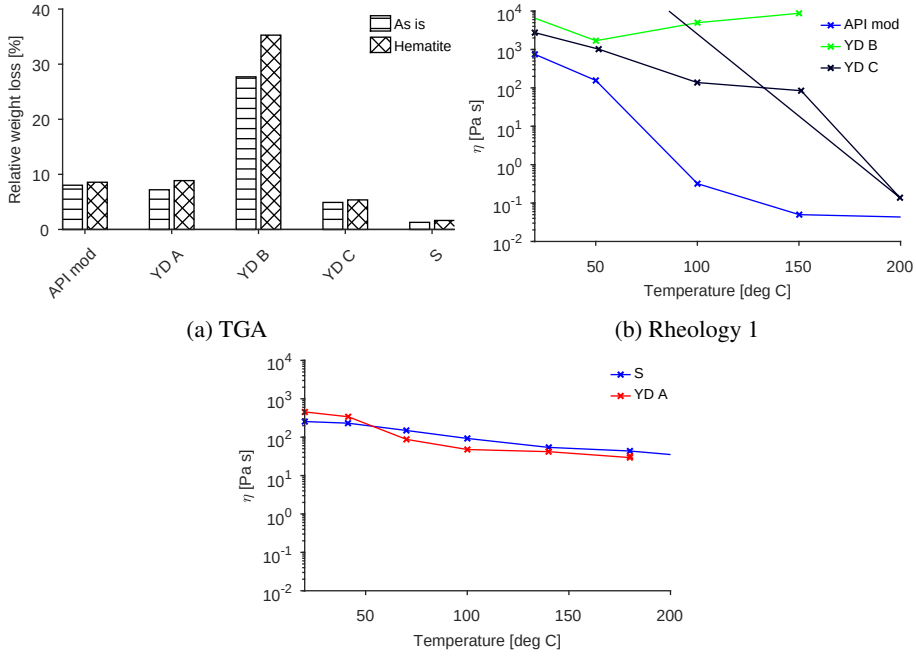

(a) TGA

(b) Rheology 1

(c) Rheology 2 YD A

Figure F.7.: Summary of TGA and rheology tests. Figure F.7a shows the relative mass loss for all tested compounds in a nitrogen atmosphere. Figure F.7b shows the effect of temperature on the viscosity at τ=50 Pa and, because of the different test protocol, Figure F.7c shows the effect of temperature on viscosity at $\dot{\gamma}$=1 s^{-1}.

In summary, the thermal degradation starts with evaporation, resulting in drying out of the compound. This is further exacerbated by oxidation, and in some cases thickening or bleeding of base oil (dropping point). The resulting increase in consistency leads to removal of lubricant from the contact by pushing the dry residue out. Subsequently, this leads to failure because

of adhesive wear and, finally, galling at the subsequent temperature steps. In some cases, the failure was accelerated by the presence of the (hard) inorganic particles that became abrasive once the consistency increased. It is clear though that even if the physical and chemical characteristics indicate stable behaviour, the tribological outcome is not necessarily the same.

Based on the experiments using commercially available compounds, the following challenges were identified:

1. The required biodegradability, leading to the use of lighter oils (e.g. esters) which compromises the high temperature stability and, with that, lubricity.

2. Use of inorganic (mineral) particles to replace soft metal particles leads to (sealing) surface damage, which was also observed by [8].

3. TGA/DSC or elevated temperature rheology based tests do not reveal the high temperature performance of a thread compound. High temperature tribological tests, however, do reveal this and are in line with earlier work by [8].

To validate the understanding of the mechanisms leading to failure and the high temperature pin-on-disc method, a prototype lubricant was designed that successfully mitigates the observed failure modes by film formation prior to degradation. The compound outperformed all the tested commercially available thread compounds.

F.6. Conclusion

A simple high temperature tribological test method was developed and validated using cross testing with TGA/DSC, high temperature rheometry, anvil-on-strip, and full-scale make-up/break-out experiments. The method was developed by using it to investigate the high temperature failure mechanisms of commercially available thread compounds. The method and mechanisms were successfully validated by designing a prototype thread compound. The results indicate the following:

- Relying on just TGA/DSC, or rheometry, or even a combination thereof is not sufficient for the development of thread compounds for high temperature (>150 °C) applications.

- The commercial environmentally acceptable thread compounds fail at elevated temperatures because of evaporation of the base oil combined with oxidation of the compound. This increases consistency, which leads to starved lubrication conditions. The remaining tribofilm is worn until the system fails because of adhesive wear. This is sometimes further enhanced by abrasive action coming from the inorganic particle additives.

- The identified mechanisms were solved with a prototype thread compound developed using the methodology described. This was achieved by increasing the film forming tendency of the lubricant before the base oil is evaporated. This film is then able to protect the surface long after the lubricant has lost its consistency.

- The performance of the thread compound was successfully validated against earlier anvil-on-strip experiments using P110 material and full-scale make-up and break-out test using L8013Cr material.

Acknowledgements

The authors are grateful to Shell Global Solutions International BV for permission to publish this work.

References

[1] API. *Recommended Practice on Thread Compounds for Casing, Tubing, and Line Pipe*. Tech. rep. Washington: American Petroleum Institute, 2015.

[2] Carper, H. J., Ertas, A., Issa, J. and Cuvalci, O. 'Effect of Some Material, Manufacturing, and Operating Variables on the Friction Coefficient in OCTG Connections'. *Journal of Tribology* 114.4 (October 1992), p. 698.

[3] Ekwaro-Osire, S. and Karpat, F. 'Experimental Studies on Galling Onset in OCTG Connections: A Review'. *Journal of Energy Resources Technology* 130.1 (March 2008), p. 014502.

[4] Cuvalci, O., Sofuoglu, H. and Ertas, A. 'Effect of surface coating and tin plating on friction characteristics of P-110 tubing for different thread compounds'. *Tribology International* 36.10 (October 2003), pp. 757–764.

[5] Carper, H. J., Ertas, A. and Cuvalci, O. 'Rating Thread Compounds for Galling Resistance'. *Journal of Tribology* 117.4 (October 1995), p. 639.

[6] Ertas, A. 'Experimental Investigation of Galling Resistance in OCTG Connections'. *Journal of Manufacturing Science and Engineering* 114.1 (February 1992), p. 100.

[7] Ernens, D., Riet, E. J. van, Rooij, M. B. de, Pasaribu, H. R., Haaften, W. M. van and Schipper, D. J. 'The Role of Phosphate-Conversion Coatings in the Makeup and Sealing Ability of Casing Connections'. *SPE Drilling & Completion* (October 2018).

[8] Inose, K., Sugino, M. and Goto, K. 'Influence of Grease on High-Pressure Gas Tightness by Metal-to-Metal Seals of Premium Threaded Connections'. *Tribology Online* 11.2 (2016), pp. 227–234.

[9] Teodoriu, C. and Badicioiu, M. 'Sealing Capacity of API Connections–Theoretical and Experimental Results'. *SPE Drilling & Completion* 24.01 (March 2009), pp. 96–103.

[10] Hoenig, S. and Oberndorfer, M. 'Tightness Testing of Environmentally Friendly Thread Compounds'. *SPE Europec/EAGE Annual Conference and Exhibition*. Vol. 1. Society of Petroleum Engineers, April 2006, pp. 473–480.

[11] Murtagian, G. R., Fanelli, V., Villasante, J. A., Johnson, D. H. and Ernst, H. A. *Sealability of Stationary Metal-to-Metal Seals*. July 2004.

[12] Stachowiak, G. and Batchelor, A. W. *Engineering Tribology*. Butterworth-Heinemann, 2013, p. 884.

[13] OSPAR. *Guidelines for Completing the Harmonised Offshore Chemical Notification Format (HOCNF)*. Tech. rep. OSPAR, 2015.

[14] API. *WI 2317 : Tech Report on LTC / BTC Performance Properties and Leak Resistance*. Tech. rep. American Petroleum Institute, 2006, pp. 1–14.

[15] Pérez-Ràfols, F., Larsson, R., Lundström, S., Wall, P. and Almqvist, A. 'A stochastic two-scale model for pressure-driven flow between rough surfaces'. *Proceedings of the Royal Society A: Mathematical, Physical and Engineering Science* 472.2190 (June 2016).

[16] Pérez-Ràfols, F., Larsson, R. and Almqvist, A. 'Modelling of leakage on metal-to-metal seals'. *Tribology International* 94 (February 2016), pp. 421–427.

[17] Lugt, P. M. *Grease Lubrication in Rolling Bearings*. Oxford, UK: John Wiley & Sons Ltd, December 2012.

[18] Delgado, M. A., Valencia, C., Sánchez, M. C., Franco, J. M. and Gallegos, C. 'Thermorheological behaviour of a lithium lubricating grease'. *Tribology Letters* 23.1 (2006), pp. 47–54.

[19] Britton, M. M. and Callaghan, P. T. 'Nuclear magnetic resonance visualization of anomalous flow in cone-and-plate rheometry'. *Journal of Rheology* 41.6 (November 1997), pp. 1365–1386.

[20] Barnes, H. A. and Walters, K. 'The yield stress myth?' *Rheologica Acta* 24.4 (July 1985), pp. 323–326.

[21] Cyriac, F., Lugt, P. M. and Bosman, R. 'Impact of Water on the Rheology of Lubricating Greases'. *Tribology Transactions* 59.4 (July 2016), pp. 679–689.

[22] Lugt, P. M. 'Modern advancements in lubricating grease technology'. *Tribology International* 97 (May 2016), pp. 467–477.

[23] Comission, O. *Ospar list of substances used and discharges offshore which are considered to pose little or no risk to te environment (PLONOR)*. Tech. rep. OSPAR Commission, 2013, p. 10.